Modélisation des transferts de chaleur couplés pour la simulation multi-physique des chambres de combustion

Chai Koren

To cite this version:

Chai Koren. Modélisation des transferts de chaleur couplés pour la simulation multi-physique des chambres de combustion. Other. Université Paris-Saclay, 2016. English. <NNT : 2016SACLC001>. <tel-01308531>

HAL Id: tel-01308531
https://tel.archives-ouvertes.fr/tel-01308531
Submitted on 28 Apr 2016

HAL is a multi-disciplinary open access archive for the deposit and dissemination of scientific research documents, whether they are published or not. The documents may come from teaching and research institutions in France or abroad, or from public or private research centers.

L'archive ouverte pluridisciplinaire **HAL**, est destinée au dépôt et à la diffusion de documents scientifiques de niveau recherche, publiés ou non, émanant des établissements d'enseignement et de recherche français ou étrangers, des laboratoires publics ou privés.

NNT : 2016SACLC001

THÈSE DE DOCTORAT DE L'UNIVERSITÉ PARIS-SACLAY,

préparée à CentraleSupélec.

ÉCOLE DOCTORALE N°579

Sciences mécaniques et énergétiques, matériaux et géosciences.

Spécialité Combustion.

Présentée par

M. Chaï KOREN

Modeling conjugate heat transfer phenomena for multi-physics simulations of combustion applications

Thèse soutenue à Châtenay-Malabry, le 04/04/2016.

Composition du jury:

M. Dupoirieux, Francis	Maître de recherche, ONERA	Rapporteur
M. Gicquel, Laurent. Y.M.	Chercheur senior, CERFACS	Rapporteur
Mme Domingo, Pascale	Directrice de recherche, CORIA	Examinatrice
Mme. Escudié, Dany	Directrice de recherche, CETHIL	Présidente
M. Moureau, Vincent	Chargé de recherche, CORIA	Invité
M. Duvert-Naudin, Alexandre	Ingénieur R&D, Air Liquide	Invité
M. Gicquel, Olivier	Professeur, CentraleSupélec	Directeur de Thèse
M. Vicquelin, Ronan	Maître de conférences, CentraleSupélec	Co-Encadrant de Thèse

Laboratoire d'Énergétique Moléculaire et Macroscopique, Combustion
CNRS, CentraleSupélec.

Remerciements

Cette thèse est le fruit d'une collaboration entre le laboratoire EM2C de l'école CentraleSupélec et la société Air Liquide dans le cadre d'une chaire industrielle et de recherche soutenue par l'Agence Nationale de la Recherche.

Je souhaite remercier tout d'abord les différents membres de mon jury et en particulier Lurent Gicquel et Francis Dupoirieux qui ont accepté d'être les rapporteurs de mon manuscrit, ainsi que pour leurs différentes remarques enrichissantes concernant le travail présenté. Merci également à Dany Escudié qui a accepté d'assumer le rôle de présidente du jury de ma soutenance, ainsi que Pascale Domingo et Vincent Moureau qui ont fait le déplacement pour y assister.

Bien entendu, je souhaite remercier les personnes ayant encadré et contribué à ce travail : Olivier Gicquel, mon directeur de thèse qui m'a donné la chance d'embarquer dans cette aventure. Merci aussi à Ronan Vicquelin qui a co-encadré cette thèse, et dont j'ai eu l'honneur d'être le premier doctorant à temps plein sur une période de 3 ans. J'ai énormément appris à vos côtés, et je pense notamment aux nombreuses séances d'échange ou de travail qui ont fait progressé cette thèse. Tous les deux m'ont permis d'arriver à bon port au bout de ces trois années. Sans vous, ça n'aura pas été pareil!

Je tiens également à remercier très chaleureusement Bernard Labégorre et Alexandre Duvert-Naudin qui ont suivi de près ces travaux du côté Air Liquide. Les discussion régulières avec Alexandre en particulier ont été très enrichissantes et ont également contribué au résultat final de cette thèse. Je remercie également Guillaume Mougin et Vincent Gourlaouen qui m'ont accueilli dans l'équipe simulation physique du groupe Mathématiques Appliquées du Centre de Recherche Paris-Saclay d'Air Liquide. Merci aussi aux différents membres de l'équipe, Dianna, Benjamin, Guillaume, Marie et bien d'autres pour le très bon accueil auquel j'ai toujours eu droit lors de mes passages au centre.

Je souhaite également remercier de tout coeur le personnel administratif et technique du laboratoire pour l'aide et le soutien qu'ils ont pu m'apporter pendant cette thèse. C'est grâce à eux que la machine tourne tous les jours, et qu'en tant de doctorant on peut travailler en toute sérénité! Nathalie, Anne-cécile, Virginie, Brigitte, Noï, Matthieu et Sébastien, merci ! Je pense également à Thierry Schuller et Benoit Fiorina qui m'ont donné la chance de pouvoir participer à l'enseignement à l'école. Ce fut une expérience très enrichissante et qui m'a beaucoup apporté.

Je passe maintenant aux remerciements plus "personnels". A commencer donc par mes trois co-bureaux : Benoit Latour, Jordane Soussi et Wafa Bendhaou. On a passé presque trois ans et demi tous les quatre dans notre magnifique bureau 6314A. Plein de moments agréables, de fous rires, de pauses café/thé le matin à 9h et de goûter à 16h. C'est aussi grâce à vous que la thèse se soit déroulée aussi bien, et que j'ai maintenant plein de bons souvenirs pour la vie. Du coup, en plus du titre de docteur, cette thèse m'a également apporté de nouveaux amis :)

Je pense aussi aux différentes personnes qui ont animé la vie du labo pendant mon passage et qui furent bien trop nombreux pour tous être cités ici. Je vais néanmoins en citer quelques un : Marien Simeni-Simeni, Adrien Lemal, Nicolas Dumont et Florence Drui pour en avoir assuré le poste de responsable séance de sport du vendredi. Vincent Leroy, Fabien Tholin, Laurent tranchant, laurent soucasse et florent saint, les vieux qui ont su bien accueillir les petits nouveaux. Puis ceux qui sont déjà partis, qui sont restés ou qui ne sont pas encore partis : Clément Mirat, Marie Zarrouati, Paul Jourdaine, Maxime Philip, Manuel Gonzalez, Maria Castela, Théa Lancien, Pedro Vulpiani, Pedro Rodrigues, Adrien Chatelier, Benjamin Robbes, Davy et bien d'autres...

Je vais finir par mes proches : Les amis du lycée qui ont toujours posé des questions et qui se sont intéressés malgré le fait que le sujet leur était complètement étranger: Zazou, Louisa, Jeannou, Titi, Raphou, Geoffrey, Edmée, Carina et tous les autres!. Merci aussi aux amis de Centrale pour l'intérêt et pour être venus à ma soutenance. Marjo, Flo, Willy et Aurélien, vous voyez, vous aviez raison en ce mois de septembre 2011, j'ai finalement fait une thèse à l'EM2C =). Et puis le meilleur pour la fin : Ma fiancée, ma famille et ma belle famille. Merci à tous d'avoir été la et de m'avoir soutenu pendant ces trois années. Merci d'avoir cru en moi, et merci d'avoir été la ! Et surtout un grand merci à Sophie pour m'avoir encouragé sur la dernière ligne droite mais aussi pendant les moments où j'en avais besoin. C'est aussi grâce à tout ce beau monde si le résultat présenté a pu être atteint !

Abstract

The work presented in this manuscript is a part of the Oxytec industrial chair which members are: Air Liquide, CentraleSupélec, CNRS and ANR. The goals include the study of oxygen based combustion processes in order to improve the understanding of the phenomena occurring inside the considered combustion chambers. The considered operating conditions are extreme: High pressure, high temperatures and water vapor enrichment.

The considered configurations are multiphenomena with strong interactions, which all must be accounted for: Combustion, turbulence, radiation and heat transfer. Hence, this thesis studied the possible ways to conduct multiphysics simulations, using code coupling with the objective of being able to conduct high-fidelity computations of such configurations.

The main issue dealt with in this work is the flow-wall coupling methodology. A new interface model based on a common Dirichlet boundary condition is developped. The use of the model allows for an automatic control of the unsteady coupling step size between flow and wall. This control algorithm is based on variable step integrators and PID controllers. The discrepancy of the different time scales is also dealt with with the help of an acceleration method toward the permanent state. The acceleration used is compatible with the coupling step control.

The coupling procedure is then applied to two configurations: A first one which is made of a flame-wall interaction which allowed for a first validation of the method. Secondly, a laboratory-scale burner located in the EM2C laboratory is studied which consists of hydrogen enriched confined flames. The obtained results show that the coupling methodology is able to correctly solve the flow-wall interaction while also providing a quantitative comparison between experimental and numerical fields.

Résumé

Cette thèse s'inscrit dans le cadre de la chaire Oxytec regroupant la société Air Liquide, l'école CentraleSupélec, le CNRS et l'ANR. Cette chaire a pour objectif l'étude des chambres d'oxycombustion afin d'améliorer la compréhension des phénomènes qui y ont lieu : Les conditions opératoires envisagées comprennent une haute pression, hautes températures ainsi qu'un milieu enrichi en vapeur d'eau.

Les configurations étudiées présentent des interactions non négligeables entre les différents phénomènes physiques considérés : Combustion, écoulements turbulents, rayonnement et conduction dans les parois. Le travail mené se concentre ainsi sur l'étude numérique de ces configurations dites multi-physiques en couplant plusieurs outils de simulation numérique distincts. Les outils utilisés sont instationnaires et permettent la réalisation de simulations haute-fidélité.

Un accent est mis sur la méthodologie concernant le couplage écoulement-paroi. Un modèle d'interface basé sur une condition limite commune de type Dirichlet est développé dans un premier temps. L'utilisation de ce modèle permet la mise en place d'un contrôle automatique du pas de temps de couplage des codes de simulation de l'écoulement et de la paroi. Ce contrôle est basé sur la théorie des contrôleurs PID. La problématique de la disparité des temps caractéristiques est ensuite traitée, et une méthode d'accélération de la convergence vers le régime établi, cohérente avec le modèle d'interface, est développée.

Enfin, ces méthodes sont appliquées à deux configurations étudiées expérimentalement. Une première concerne une interaction flamme paroi et permet une validation de la méthodologie de couplage sur un cas concret. La seconde configuration est la chambre Valogaz étudiée au laboratoire EM2C et où le rayonnement est également pris en compte pour les simulations. Les résultats observés démontrent la capacité de la méthodologie de couplage développée à capturer correctement l'interaction écoulement-paroi et fournit des comparaisons quantitatives de températures de paroi entre valeurs expérimentales et numériques.

Contents

Abstract vii

Résumé ix

Nomenclature xxvii

1 Global, industrial and scientific contexts 1
- 1.1 Global context . . . 2
- 1.2 Oxycombustion . . . 6
- 1.3 Thesis work . . . 14

2 Numerical codes used for multi physics simulations 19
- 2.1 Turbulent reactive flows . . . 20
- 2.2 Heat transfer in solids . . . 32
- 2.3 Radiation in semi-transparent gases . . . 38
- 2.4 Coupling: OpenPALM coupler . . . 41
- 2.5 Conclusion . . . 43

3 Coupling procedures for conjugate heat transfer 45
- 3.1 State of the art: Numerical methods for multi physics simulations . . . 46
- 3.2 Considered coupling boundary conditions . . . 54
- 3.3 Hybrid cell interface model for updating the boundary temperature . . . 64
- 3.4 Conclusion . . . 74

4 Coupling step size determination 75
- 4.1 Deriving a method to determine the size of the coupling time step . . . 76
- 4.2 1D validation of the coupling step size determination . . . 85
- 4.3 Conclusion . . . 96

5 Attaining the permanent regime for the temperature in coupled conjugate heat transfer computations 99
5.1 Computing the permanent regime for flow configurations . 100
5.2 Accurately describing the permanent regime using unsteady solvers 106
5.3 Conclusion 112

6 Numerical simulation of a three-dimensional configuration of flame-wall interaction 115
6.1 Simulated configuration 116
6.2 Non-coupled flow simulation 118
6.3 Coupled conjugate heat transfer simulations 124
6.4 Conclusion 136

7 Application of the Conjugate Heat Transfer methodology to a laboratory-scale combustor 139
7.1 Experimental test rig and available measurements 141
7.2 Numerical setup 143
7.3 Results 155
7.4 A first quantification of the radiative heat transfer 162
7.5 Conclusion 168

Conclusion 169

A $0D$ ODE solver for the coupling time step determination 173
A.1 Adams-Bashforth integration schemes 174
A.2 0D test case 175

References 185

Index 187

List of Tables

2.1 Experimental and numerical values for the laminar flame speed of premixed air/methane flame with an equivalence ratio of 0.83. Experimental values extracted from Egolfopoulos et al. (1989). 28

3.1 Parameters used for the MMS test case 72

4.1 Values used for the different gains, available in Gustafsson (1991), Söderlind (2003), for an integration scheme of order k. $\alpha = K_P + 2K_D$, $\beta = K_P + K_I + K_D$ and $\gamma = K_D$. 83

4.2 Properties of both media considered in 1D test cases in SI units: Thermal conductivity, density, thermal capacity at constant pressure. 86

4.3 Comparison of the total number of coupling steps with the number of rejected steps for $\eta = 1\%$, $f_{ext} = 100$ Hz and a simulated time of 60 periods. 86

7.1 Repartition of the available CPU cores between the different numerical codes used. LES stands for the flow solver YALES2, S-HTS for the steady heat transfer solver and U-HTS for the unsteady heat transfer solver. 155

List of Figures

1.1 Global greenhouse gases emissions repartition and responsible economical sectors. Extracted from Statistics (2014) 3
1.2 Global CO_2 emissions repartition and responsible economical sectors. Extracted from Statistics (2014) 3
1.3 Left: Comparison of the world primary energy supply between 1971 and 2012. Right: Temporal evolution of the total annual CO_2 emissions. Extracted from Statistics (2014) 4
1.4 Aerial view of the Total offshore platform located in Amenem (Niger's Delta). The natural gas obtained as a byproduct of the oil extraction is burnt (right side of the picture). (Pius Utomi Ekpei/AFP/Getty Images, www.theatlantic.com) 5
1.5 Lacq CO2 capturing facility. Extracted from Total (2015) . 7
1.6 Comparison of the 3 different approaches for CO_2 capturing: Post-combustion, Pre-combustion and Oxyfuel combustion. Source: Royal Society of Chemistry, United Kingdom. 8
1.7 CO_2 vs NO_x emissions as a function of the operating temperature. Extracted from www.topac.com (). 10
1.8 Oxytec industrial chair tasks and partners. (French) 11
1.9 Heat flux fluctuations over mean heat flux as a function of the Reynolds number. Extracted from Abe et al. (2004). . 13

2.1 Computational domain of the channel flow configuration where δ =0.1 m. The streamwise and spanwise lengths verify $L_x = 4\pi L_z$ and $L_y = 2\pi L_z$ respectively. 24
2.2 Mean velocity profile along the wall normal direction scaled by u_τ. Circles: Moser et al. (1999). Black plain line: Numerical results 26

2.3 Root-mean-square velocity fluctuations scaled by u_τ profile along the wall normal direction. Circles: u^{rms} from Moser et al. (1999). Black plain line: u^{rms} numerical results. Blue squares: v^{rms} from Moser et al. (1999). Blue plain line: v^{rms} numerical results. Red diamonds: w^{rms} from Moser et al. (1999). Red plain line: w^{rms} numerical results. 26

2.4 Mean temperature profile along the wall normal direction. Circles: Kasagi et al. (1992). Black plain line: Numerical results . . . 27

2.5 Root-mean-square temperature profile along the wall normal direction. Circles: Kasagi et al. (1992). Black plain line: Numerical results . . . 27

2.6 1D profiles of temperature, density, gas velocity, Y_{CH_4}, Y_{CO}, Y_{CO_2}, Y_{H_2O} and $\dot{\omega}_{CO_2}$ for a 1D DNS premixed flame of air/methane with an equivalence ratio of 0.83. The mass fractions and source term are scaled by their maximum value. . . . 29

2.7 Spatial 1D profiles of the temperature for the DNS flame (black plain line) and thickened flame (red dashed line). . . 32

2.8 1D profiles of temperature, CH_4, CO_2, H_2, CO, H_2O, CH_3 and HCO scaled by the maximum value of the DNS flame as a function of the progress variable Y_c. red circles: DNS flame, black plain line: thickened flame. . . . 33

2.9 Discretization of the 1D domain. Cells are all of the same length Δx. Finite volume balances are done over the i^{th} cell using the $(i+\frac{1}{2})^{th}$ and $(i-\frac{1}{2})^{th}$ fluxes. . . . 34

2.10 Temperature fields for aluminium ($\lambda = 236$, $\rho = 2\,708$ and $c_p = 896$ in SI units). Black circles: Analytical solution a $t = 10$ s. Black plain line: Numerical solution a $t = 10$ s. Red circles: Analytical solution a $t = 25$ s. Red plain line: Numerical solution a $t = 25$ s. . . . 35

2.11 Numerical L^2 integration error as a function of the time step size. Black plain line: Explicit forward Euler method. Red dashed line: Explicit mid-point method. Gray faced triangle: First order slope. Black faces triangle: Second order slope. . . . 36

2.12 Temperature fields inside an aluminium layer of thickness $L_s = 0.5$ cm, computed by the 3D HTS YALES2 solver and 1D diffusion code. Red circles: 1D diffusion code. Black plain line: 3D HTS solver of the YALES2 library. . . . 37

2.13 Temperature fields inside a quartz layer of thickness $L_s = 12$ mm, computed by the 3D steady HTS YALES2 solver. Black circles: Theoretical solution. Black plain line: 3D steady HTS solver. 38

2.14 A schematic description of radiation energy evolution over a distance ds. Extracted from Zhang (2013). 40

2.15 One dimensional fields for the 1D test case. Blue line: Imposed temperature profile. Red diamonds: Analytical radiative power field. Red line: Numerical solution obtained with the Monte-Carlo solver Rainier. 41

2.16 An example of an OpenPALM canvas extracted from the GUI for a multiphyiscal simulation accounting for turbulent reactive flows, radiation and heat transfer inside the walls. The lines represent the communications between the different solvers: Orange: Unsteady heat transfer solver. Blue: Reactive flow solver. Pink: Steady heat transfer solver. Purple: Radiation solver. 42

3.1 Sequential coupling procedure for conjugate heat transfer. Adapted from Duchaine et al. (2009) 52

3.2 Parallel coupling procedure for conjugate heat transfer. Adapted from Duchaine et al. (2009) 53

3.3 1D configuration of flow-wall boundary. Blue cells on the left: Flow domain. Brown cells on the right: Wall domain. 60

3.4 Initial temperature field over a fluid-solid domain. Dashed line stands for the boundary. Left side is the fluid's side and the wall is on the right. 62

3.5 Red cross: steady state temperature which should be obtained. Blue circles: Temperature field after several coupling steps for a large coupling step. Dashed line stands for the boundary. Left side is the fluid's side and the wall is on the right. 62

3.6 Evolution of the boundary heat flux over time, normalized by the steady state heat flux. 63

3.7 Fluid and solid domains used for a coupled simulation. Dashed triangles represent the mesh and both grey triangles represent the two cells which make the hybrid cell around the interface. 65

3.8 Left: Energy budget over the entire hybrid cell. Right: Energy budget over a fluid cell with a Dirichlet BC yielding a boundary flux, Φ_w, used by the solid cell as a Neumann BC. 67

3.9 Channel flow configuration studied by Tiselj et al. (2013). Periodical boundary conditions are used in the x and z directions. In the y direction periodical boundary conditions are imposed to the solid slab: the face situated in $y = h+d$ is linked to the one in $y = -h$. 68

3.10 Normalized temperature fluctuations at the fluid-solid interface scaled by the value of the normalized thermal fluctuations for standalone flow simulations with Neumann boundary conditions. Abscissa is thermal activity ratio K. Curves are given for several values of G. Channel flow configuration with $Re_\tau = 180$ and $Pr = 1$. Figure extracted from: Tiselj et al. (2013). 69

3.11 Effusivity Vs. Diffusivity map for three groups: Gas, Liquids and Metals. 70

3.12 Results for MMS test of the hybrid cell. Red circles: Analytical solution. Black line: Numerical solution. a) Solutions at time $t = 0$. b) Solutions at time $t = 25ms$. c) Zoom on the near boundary zone for $t = 25ms$. 73

4.1 Generic control loop to advance thefunction f^n to its value f^{n+1} with a numerical integration error ϵ_n below a given tolerance η by adapting the integration time step Δt^n. . . 78

4.2 Evolution of the optimal integration time step scaled by used integration time step as a function of the numerical integration error for different orders. Gray dashed line: k+1 =0. Black plain line: k=0. Red plain line: k=1. Blue plain line: k=2 81

4.3 One-dimensional test case configuration. The length L_f of the fluid part is 1 mm while the length L_s of the solid part is 1 cm. 85

4.4 Evolution of the accepted time step scaled by the fluid solver's time step (a) and corresponding numerical error (b) for the I (red dashed-dotted line), PI (blue dashed line) and PID (black plain line) controllers for $\eta = 1\%$ and $f_{ext} = 100$ Hz. 87

4.5 Example of temporal evolution of the difference of the boundary temperature T_{bnd} with its mean value, $\overline{T}_{bnd}$ for the reference solution (black squares) and the I (red dashed-dotted line), PI (blue dashed line) and PID (black plain line) controllers. $\eta = 5$ % and $f_{ext} = 5$ Hz. 89

4.6 Evolution of the coupling time step scaled by the fluid time step (a) and the corresponding numerical integration error (b) computed by the PID controller without considering step rejection. Case conditions: $\eta = 0.1\%$ and $f_{ext} =$ 100 Hz. 90

4.7 The mean coupling time step scaled by the fluid time step as a function of the prescribed tolerance η for $f_{ext} = 100$ Hz. Black plain line : PID controller. Blue dashed line : PI Controller. Black dotted line : $\alpha\eta^{1/(k+1)}$. 92

4.8 The root-mean-square (RMS) of the coupling time step scaled by the fluid time step as a function of the prescribed tolerance η for $f_{ext} = 100$ Hz. Black plain line : PID controller. Blue dashed line : PI Controller. Black dotted line : $\alpha\eta^{1/(k+1)}$. 92

4.9 The mean coupling time step scaled by the fluid time step computed by the PID controller as a function of the frequency f_{ext} for different values of the prescribed tolerance η: 0.05% (line and circles), 0.5% (line and squares) and 5% (line and diamonds). The frequency is scaled by the fluid domain cut-off frequency $f_c = 25a_f/(\pi L_f^2) = 200$ Hz . . . 93

4.10 The root-mean-square coupling time step scaled by the fluid time step computed by the PID controller as a function of the frequency f_{ext} for different values of the prescribed tolerance η: 0.05% (line and circles), 0.5% (line and squares) and 5% (line and diamonds). The frequency is scaled by the fluid domain cut-off frequency $f_c = 25a_f/(\pi L_f^2) =$ 200 Hz 94

4.11 Evolution of the boundary temperature root-mean-square, scaled by the maximal value measured for f_{ext} =5 Hz, fluctuations as a function of the exterior frequency f_{ext}. . . . 95

4.12 Contours map of the temperature root-mean-square fluctuations scaled by the input fluctuations levels, as a function of the position in the fluid layer and exterior frequency f_{ext}. Black plain lines: Values for the coupled configuration. Red dashed lines: Values for a semi-infinite fluid. 96

5.1 Operating scheme of the steady coupling done by Chemin (2006). Initial fluid and solid states are denoted by $\mathcal{F}_n$ and $\mathcal{S}_n$ respectively. New iterations are computed as long as the convergence is not achieved for both boundary temperature and heat flux. 101
5.2 Temperature RMS inside the wall, normalized by the reference case RMS amplitude at the fluid-wall interface. Circles: non-accelerated reference case. Red plain line: Neumann-Dirichlet coupling approach with a desynchronization factor $\alpha = 10$. Blue dashed line: Neumann-Dirichlet coupling approach with a desynchronization factor $\alpha = 100$. The x coordinate is normalized by the length of the solid domain and is centered at the interface position x_{bnd}. Case condition: $f_{ext} = 100$ Hz 104
5.3 One-dimensional test case configuration with three layers of lengths: L_f =1 mm for the fluid part, L_s =1 mm for the solid part and L_w =3 cm for the second gas layer. 105
5.4 Temperature RMS inside the wall, normalized by the reference case RMS amplitude at the fluid-wall interface. Circles: non-accelerated reference case. Red plain line: Neumann-Dirichlet coupling approach with a desynchronization factor $\alpha = 10$. Blue dashed line: Neumann-Dirichlet coupling approach with a desynchronization factor $\alpha = 100$. Case condition: $f_{ext} = 100$ Hz 106
5.5 Schematics of a combustion chamber with air cooling using perforations in the chamber walls. A: Flame. B: Hot convective eddies. ϕ^R: Radiative heat flux emitted by the flame and hot gases. 107
5.6 Scheme of the interface model for coupled unsteady conjugate heat transfer when using acceleration of the physical transient heating or cooling. 110
5.7 Temporal evolution of the mean component of the boundary temperature. Circles: non-accelerated reference case. Red plain line: Neumann-Dirichlet coupling approach with a desynchronization factor $\alpha = 10$. Blue dashed line: Neumann-Dirichlet coupling approach with a desynchronization factor $\alpha = 100$. Black plain line: the acceleration method based on the superposition principle. Case conditions: $f_{ext} = 100$ Hz and $\eta = 5\%$ for the hybrid cell approach. 111
5.8 Fluctuating components of the boundary temperature plotted against the time normalized by signal period. 113

6.1 Experimental setup studied by Singh et al. (2013) Lengths are in mm. 117

6.2 Experimental temperature (in K) measurements along the disc's radius on both hot (red color) and cold (blue color) sides. Circles: Measurements. Lines: data fits Green line: Computed heat flux (in W/m^2) using the temperature fits. Extracted from Singh et al. (2013) 118

6.3 Field cut of the gas temperature for the uncoupled large eddy simulation once the ignition kernel is placed. 120

6.4 Field cut of the gas mean temperature for the uncoupled simulation. A: Reaction zone delimited by the iso-line $\dot{\omega}_{Y_c} = 0.1\dot{\omega}_{Y_c}^{max}$. B: Dilution zones where the hot gases encounter the coflow of N_2. 122

6.5 Profile of the normalized temperature (red plain line), flame sensor S_f (blue dashed line) and progress variable source term $\dot{\omega}_{Y_c}$ (black dotted line) along the centerline axis. . . 123

6.6 CO molar fraction profile along the centerline axis as a function of the distance from the wall. Black plain line: numerical results. Black circles: Experimental measurements. 123

6.7 Comparison of the experimental (symbols, Singh et al. (2013)) and numerical (plain line) mean temperature in the near wall region along the centerline axis. 124

6.8 Cuts of fluid (yellow) and solid (green) meshes. (a) Injection burner, coflow and solid disc. (b) Zoom in the interface zone between the solid and fluid domains identified by the red square in Fig.(a). 125

6.9 Temporal evolution of the boundary temperature at the disc center for a non-accelerated coupled simulation 127

6.10 Temporal evolution of the coupling time step scaled by the flow solver limiting diffusive time step for the tolerance η =5% (black plain line) and 0.1% (grey dashed line) without any acceleration. Dashed black line: accelerated simulation from Sec. 5.3.4 with η =5%. 128

6.11 Temporal evolution of the computed mean contribution of the boundary temperature at the disc center for two acceleration methods: Hybrid cell interface model with acceleration based on superposition, $\eta = 5\%$ (black plain line); Neumann-Dirichlet coupling approach with a desynchronization factor $\alpha = 1000$ (blue dashed line). 129

6.12 Comparison between experimental and numerical data for the mean boundary temperature as a function of the distance from the center of the disc. Circles: experimental data Singh et al. (2013). Black plain line: Hybrid cell interface model with acceleration based on superposition, $\eta = 5\%$. Blue dashed line: Neumann-Dirichlet coupling approach with a desynchronization factor $\alpha = 1000$. . . . 130

6.13 Color map of the mean temperature field over the disc surface for the Hybrid cell interface model with acceleration based on superposition, $\eta = 5\%$ case. 130

6.14 Instantaneous colored maps of N_2 mass fraction in the pulsed configuration simulated with the hybrid cell interface model combined with acceleration, taken at 4 different instants and are spaced every $5\,ms$. 132

6.15 Color map: Temperature field. Black line indicates the flame position as in Fig. 6.4. simulated with the hybrid cell interface model combined with acceleration. 133

6.16 Radial profiles of the disc temperature RMS computed by the accelerated hybrid cell approach (black plain line) and by the accelerated Neumann-Dirichlet coupling with a desynchronization factor $\alpha = 1000$ (blue dashed line). . . 133

6.17 Radial profiles of the relative wall heat flux RMS computed by the accelerated hybrid cell approach (black plain line) and by the accelerated Neumann-Dirichlet coupling with a desynchronization factor $\alpha = 1000$ (blue dashed line). . . 134

6.18 Temporal evolution of the boundary temperature at the center position of the disc computed with the hybrid cell interface model combined with acceleration. 135

6.19 Evolution of the coupling timpte step as a function of time. Time $t = 0$ is taken at the moment pulsations of the mass flow rate begin. Time is normalized by the inlet's mass flow rate fluctuation frequency. 135

7.1 Schematic of the Valogaz laboratory scale burner. 142

7.2 Typical M (left) and V (right) swirling methane/air flames for two different operating conditions. left: $\phi = 0.62$ and $\mathrm{U} = 12.2\,m \cdot s^{-1}$. Right: $\phi = 0.57$ and $\mathrm{U} = 12.1\,m \cdot s^{-1}$. Reproduced from Moeck et al. (2012). 143

7.3 Normalized Abel deconvoluted OH^* chemiluminescence corresponding to the zone of heat release. Extracted from Guiberti (2015). Left: M-shape flame. Right: V-shape flame. 144

7.4 Direct visualisation of the Valogaz burner studied by Guiberti (2015). Blue surfaces: Areas where the temperature was measured by LIP. Red zone: Temperature was measured using thermocouples. Extracted from Guiberti (2015). 144

7.5 Experimental temperature measurements along the steel bar using thermocouples. Extracted from Guiberti (2015). 145

7.6 LIP measurements on the quartz windows of the valogaz burner (Large blue zone in Fig. 7.4). Left: raw data with the location of the measurements points. Right: Reconstructed temperature field using linear interpolation. Extracted from Guiberti (2015). 145

7.7 Exterior heat transfer coefficient computed using natural convection correlations, along the the z coordinate on the quartz wall. 151

7.8 Fixed point algorithm used for the resolution of the steady heat transfer equation with a radiative flux boundary condition. T_{bnd} is the numerical value obtained for the boundary temperature, T_{bnd}^{est} is the temperature estimation and ϵ is the numerical tolerance used to check for the convergence. 152

7.9 Scheme of the coupling of the different numerical codes used for the simulation of the Valogaz burner. The codes are coupled through the OpenPalm coupler presented in chapter 2. 153

7.10 Left: Full meshes for both fluid and solid domain. Yellow is fluid, black is solid and red dashed line symbolize the interface. Right: A zoom on a section of the domain. . . . 154

7.11 Temporal evolution of the coupling time step during the simulation. 154

7.12 Up: mean temperature field inside the burner. Down: Mean velocity vector field inside the burner. Black dashed lines show the section for which wall temperature measurements are available. 156

7.13 Comparison of the mean normalized heat release field. Left: Mean normalized volumetric heat release. Right: Normalized Abel deconvoluted OH^* chemiluminescence corresponding to the zone of heat release. 157

7.14 Comparison of the mean normalized OH field. Left: Numerical mean normalized OH molar fraction. Right: Experimentally measured mean normalized OH molar fraction. 158

7.15 Comparison of the mean wall temperature $\overline{T}_{bnd}$ field on the quartz. Figure (a) shows the experimentally measured results while Fig. (b) shows the numerically computed field. 159

7.16 Relative and absolute errors for the wall temperature computed using coupled conjugate heat transfer. 160

7.17 Surface plot of the inner wall temperature T_{bnd} response to a modification of the outer boundary convective coefficient h_{ext}. T_{ext} is set to $293K$ and the radiation is taken into account with $\epsilon = 0.75$ for the quartz wall. 161

7.18 Mean mole fractions of the gaseous CO_2 (top) and water vapor (bottom) inside the studied burner. 161

7.19 Root-mean-square values for the temperature and heat flux inside the measurements zone. 162

7.20 Energy budget of the combustion chamber for the sensible enthalpy. Red: inlet's sensible enthalpy flux. Blue: outlet's sensible enthalpy flux. Black: wall heat flux. Green: Volume integrated heat release rate. 163

7.21 Instantaneous fields extracted from the radiation solver. From top to bottom: Temperature field. Radiative power, black line is the iso-contour for $P^{rad} = 0$. Rms radiative power scaled by the mean radiative power. Number of rays used at each point. Values obtained using the ERM method. 164

7.22 Comparison of the number of rays needed for the Monte-Carlo algorithm for the radiative power using the ERM method (upper figure) and the OERM method (lower figure). 165

7.23 Instantaneous radiative wall heat flux color map over the quartz walls. Flux showing is deactivated for the other walls. 166

7.24 1D configuration representative of the EM2C burner. The wall has a thickness e, and a thermal conductivity λ_s. T_c is the bulk temperature of the hot gases near inner walls, h_c is the heat transfer coefficient inside the chamber, T_w the wall temperature and ϕ^{rad} the radiative wall heat flux. T_{bnd} is wall's outer temperature, T_{ext} the atmosphere temperature, h_{ext} is the heat transfer coefficient outside the chamber and ϵ_{bnd} is the emissivity of the wall. 167

A.1 Left: Temploral evolution of the integration time step size. Right: Temporal evolution of the computed numerical solution. Blue plain line: $AB12$ solver. Green dotted line: $AB23$ solver. Red dashed line: $AB34$ solver. 175
A.2 Stability regions of the explicit Adams-Bashforth integration schemes, extracted from Hairer et al. (2008) 176

Nomenclature

Latin Characters :

c_p	Specific heat	u	Velocity
f	Frequency	T	Temperature
t	time	P	Pressure
$\dot{m}$	Mass flow rate	h	Enthalpy
a	Heat Diffusivity	h_s	Sensible enthalpy
b	Heat effusivity		

Greek Characters :

δ_0	Laminar flame thickness	ϕ	Heat flux
ρ	Density	ω	Pulsation
λ	Thermal conductivity	$\dot{\omega}_k$	Reaction rate for species k
ϵ	Integration error		
η	Integration error tolerance		

Superscripts :

n	Value at time $t = t_n$	$[k]$	k^{th} order integration scheme variable

Underscripts :

f	Flow variable	rhs	Right Hand Side term in an equation
s	Wall variable		
hyb	Hybrid cell variable	num	Numerical estimate
bnd	Boundary variable	opt	Optimal value
n	Value at time $t = t_n$	cpl	Coupling variable

Abbreviations :

LES	Large Eddy Simulation
DNS	Direct Numerical Simulation
RANS	Reynolds Averaged Navier Stokes
CHT	Conjugate Heat Transfer
RHS	Right Hand Side
BC	Boundary Condition
I	Integral
PI	Proportional-Integral
PID	Proportional-Integral-Derivative
NS	Navier Stokes
RTE	Radiative Transfer Equation

Chapter 1

Global, industrial and scientific contexts

1.1 **Global context** **2**
1.2 **Oxycombustion** **6**
  1.2.1 CO_2 capture 6
  1.2.2 NO_x reduction 9
  1.2.3 Oxytec Chair 9
  1.2.4 Positioning inside the Oxytec chair 10
  1.2.5 Conjugate Heat transfer 11
1.3 **Thesis work** **14**
  1.3.1 Goal of the thesis 14
  1.3.2 Manuscript structure 14
  1.3.3 Major contributions 16
  1.3.4 Communications 16

1.1 Global context

Global warming and climate change are one of the 21st century most important issues. With the COP21, 21^{th} Conference Of Parties on the United Nations Framework Convention on Climate Change (UNFCCC), organized in Paris, November 30^{th} to December 11^{th} 2015, the message is clear: Each and every country must contribute to the international effort. The goal is reaching an agreement on two major points:

- Reducing the greenhouse gas emissions in order to limit global warming
- How to adapt the different societies to the inevitable climate changes

The European Union chose to submit one single contribution for all 28 countries. The different goals are summarized in the document published by the European ec.europa.eu/clima/policies/strategies/2030/ (2015), and the goals to attain by 2030 are:

- -40% in greenhouse gas emissions in comparison to 1990
- At least 27% share for renewable energy
- $+27\%$ improvement in energy efficiency

To achieve the above-stated goals in terms of gas emissions reduction large efforts are needed. The considered gases include gases such as: CO_2, CO or nitrogen oxydes (N_2O and NO_x). Reducing either carbon or nitrogen based molecules' emissions requires either improving existing technologies or developing new and cleaner ones. In 2014, the energy and industrial sectors were responsible for 75 % of the global greenhouse gases emissions. Among the greenhouse gases, CO_2 is the main pollutant, while the second most present pollutant in terms of volume is methane, CH_4 (Fig. 1.1). In terms of greenhouse effect, a methane molecule has ten times the influence of a CO_2 molecule which means that both gases emissions have approximatively the same influence on the global greenhouse effect. When considering solely the CO_2 emissions, it appears that the industrial and electricity and heat generation sectors are responsible for nearly two thirds of the total emissions, Fig. 1.2, which when combined with the fact that 82 % of the world's energy supply is based on fossil ressources (1.3), and hence on combustion, shows the importance of improving the current technologies and industrial processes.

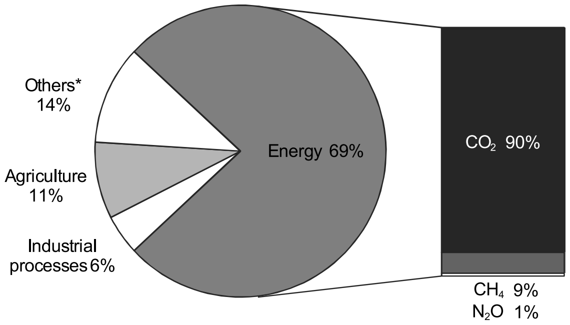

* Others include large-scale biomass burning, post-burn decay, peat decay, indirect N_2O emissions from non-agricultural emissions of NO_x and NH_3, Waste, and Solvent Use.

Figure 1.1: *Global greenhouse gases emissions repartition and responsible economical sectors. Extracted from Statistics (2014)*

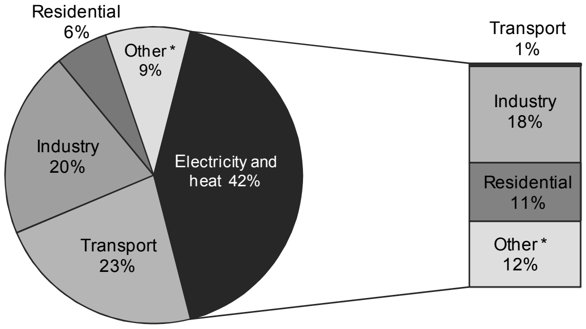

Note: Also shows allocation of electricity and heat to end-use sectors.

* Other includes commercial/public services, agriculture/forestry, fishing, energy industries other than electricity and heat generation, and other emissions not specified elsewhere.

Figure 1.2: *Global CO_2 emissions repartition and responsible economical sectors. Extracted from Statistics (2014)*

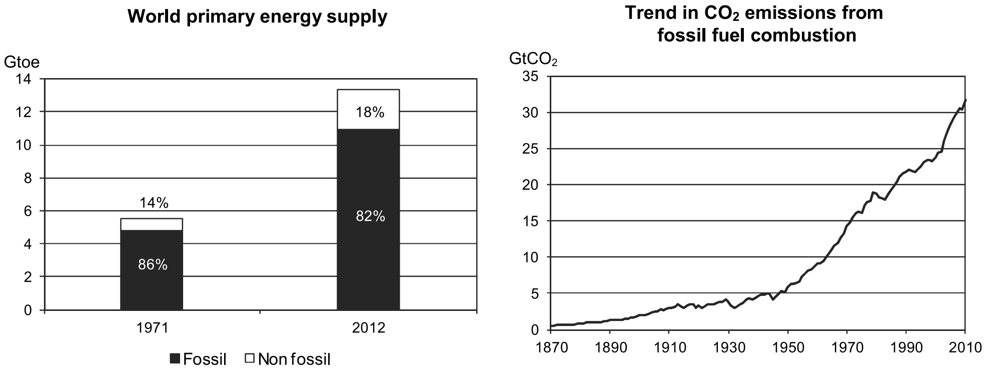

Figure 1.3: *Left: Comparison of the world primary energy supply between 1971 and 2012. Right: Temporal evolution of the total annual CO_2 emissions. Extracted from Statistics (2014)*

One of the considered approaches for reducing the greenhouse gases emissions is to develop what is called decarbonated energy production. One of the technological solution which are considered is the use of Oxycombustion instead of classical air combustion. Oxycombustion consists in replacing the air used as combustive in "classical" combustion systems with pure oxygen. The advantages of this technology are explained in the following section.

Another discussed aspect is the improvement in the global energy efficiency. This can be attained with the help of two main leverages: The first one is to increase the percentage of extracted fossile ressources from each well, while the second one is the improvement of the energy efficiency of the industrial processes.
When extracting crude oil from underground reservoirs, natural gas is also obtained. Yet, the quantity available in each reservoir is too small for it to be financially interesting to exploit. The cost of transporting the natural gas to the consumer is an obstacle for both gazoducs transport (70% of the global transported gas in the world) due to the construction and maintenance of the pipelines, and Liquid Natural Gas (*LNG*) tankers because of the cost of the liquefaction plants (30% of the global transported volume) IEA (2010). The issue with the first method is that it is expensive to construct, and the security of the pipelines is hard to ensure, in a global context of strife. For the *LNG* solution, the price is high because it implies constructing liquefaction plants at the extraction sites while also installing re-gazeifation plants at the harbors where the tankers unload their *LNG* cargo.

The complexity and high cost lead to a waste of fossil resources. As can be seen in Fig. 1.4, the obtained natural gas is burnt with the help of a torch. The global amount of gas burnt this way was of about 170 $Gm^3/year$ in 2009 (Kimmerlin (2010)). For example, in the same year, the total national consumption of France was of 45 Gm^3 !

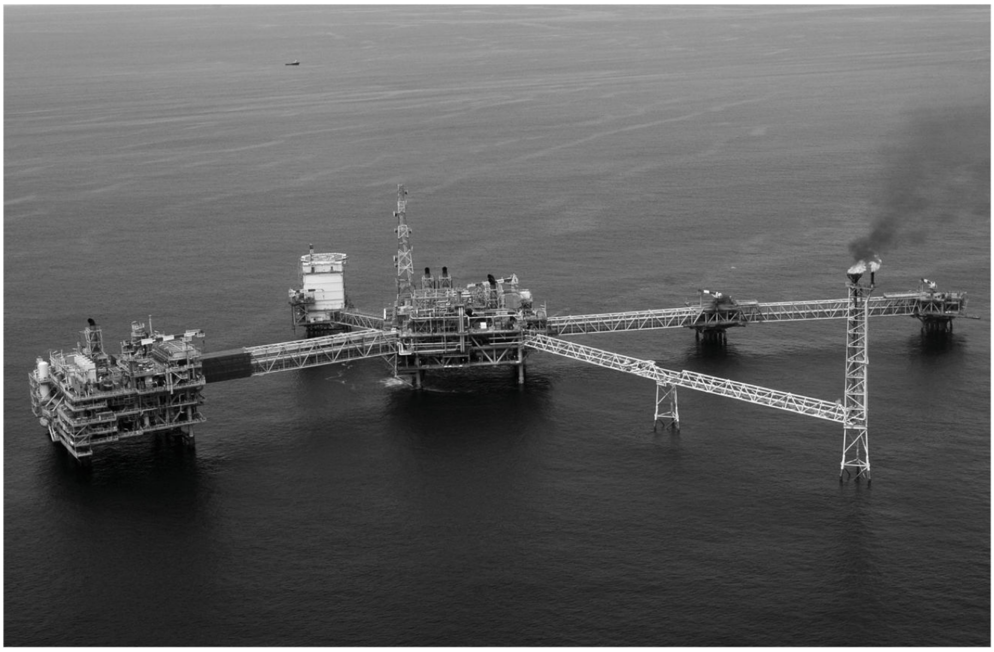

Figure 1.4: *Aerial view of the Total offshore platform located in Amenem (Niger's Delta). The natural gas obtained as a byproduct of the oil extraction is burnt (right side of the picture). (Pius Utomi Ekpei/AFP/Getty Images, www.theatlantic.com)*

A possible approach for reducing this loss of resources is to use high added-value transforming process such as fuel conversion techniques which will increase the efficiency of the reservoirs thanks to a higher profitability. The production of SynGas is one of the envisioned process but it requires large volumes of production for it to be interesting. Air Liquide produces SynGas with the help of well established classical combustion technologies such as Steam Methane Reforming (SMR), and oxygen-based combustion technologies such as Partial Oxidation (POX) and is currently developing the Auto Thermal Reforming (ATR) process for large volumes of production (Ulber (2015)). These processes are often part of the methanol production chain which is used in the chemical industry.

Concerning the energy efficiency of the industrial processes, it is improved by enhancing the temperature and pressure levels inside the combustion chambers. The higher temperatures and pressure generate a larger thermodynamical efficiency, but also induce larger wall heat fluxes which can be problematic. These heat fluxes must be estimated in order to correctly design the cooling and thermal protection of the chamber to better protect the wall hot spots.

1.2 Oxycombustion

1.2.1 CO_2 capture

A mean of reducing the CO_2 emissions is capturing the gas after it is produced in industrial plants and then storing it in underground gas reservoirs. An example of such a facility is the Lacq industrial complex developed by Total (2015), visible in Fig. 1.5. For current plants, because of the highly diluted burnt gases (70% of nitrogen), the CO_2 extraction from the smoke and fumes represents about two thirds of the overall cost of the capture process (Total (2015)).

The CO_2 capture is also important from an industrial point of view since it is used in Enhanced Oil Recovery (EOR) techniques. The CO_2 which is recovered from industrial plants is afterwards used in oil and gas wells where it is injected while the crude oil is pumped in order to maintain the pressure level inside the shaft. Doing so increase the quantity of crude oil or gas which can then be extracted.

An easier approach to separate the CO_2 from the smoke and fumes is to increase its concentration in the exhaust gases. For the moment 3 approaches are considered: Pre-combustion, Post-combustion and Oxy-combustion (Fig. 1.6).

Post-combustion

The fumes are mixed with a chemical solvent, monoetanolamine (MEA), which reacts only with the CO_2 molecules. The CO_2 is then extracted by heating the solvent mixture. The advantages of this process is that it can be adapted to nearly every industrial plant producing CO_2. Indeed, it is only needed to transport the flue gases to the separation unit, which requires few modifications to existing plants.
On the other hand, this technology is hardly optimizable and is quite

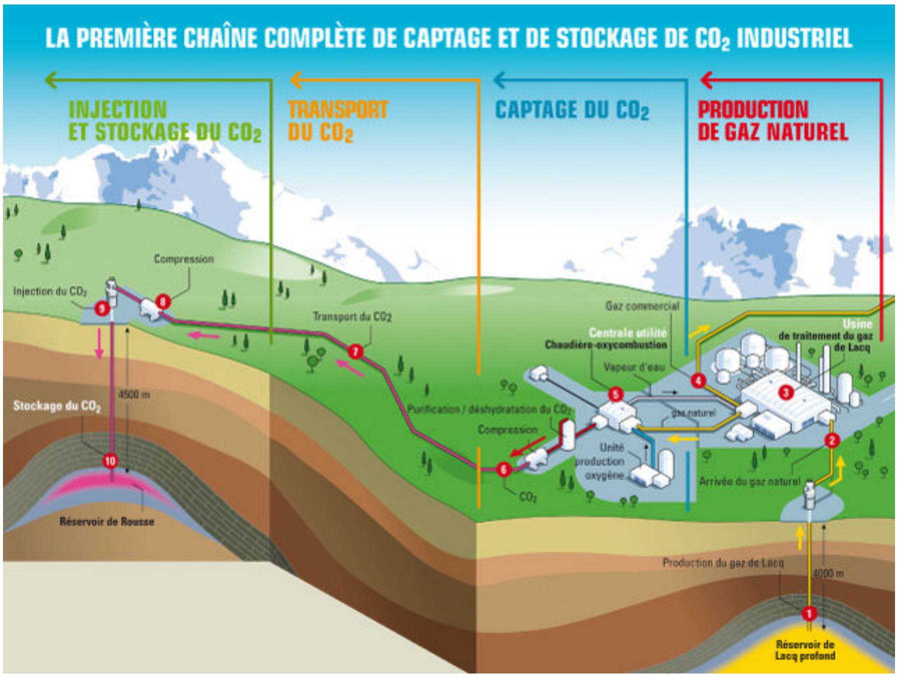
LA PREMIÈRE CHAÎNE COMPLÈTE DE CAPTAGE ET DE STOCKAGE DE CO2 INDUSTRIEL
INJECTION ET STOCKAGE DU CO2
TRANSPORT DU CO2
CAPTAGE DU CO2
PRODUCTION DE GAZ NATUREL
Compression
Injection du CO2
9
8
Transport du CO2
7
4500 m
Stockage du CO2
10
Réservoir de Rousse
Gaz commercial
Centrale utilité
Chaudière-oxycombustion
Usine de traitement du gaz de Lacq
Vapeur d'eau
4
5
3
Purification / déshydratation du CO2
gaz naturel
Compression
Unité production oxygène
2
6
CO2
Arrivée du gaz naturel
Production du gaz de Lacq
4000 m
1
Réservoir de Lacq profond

Figure 1.5: *Lacq CO2 capturing facility. Extracted from Total (2015)*

expensive and very energy-intensive. If the main goal is CO_2 sequestration, and not simply separation, it can be more interesting to apply more recent technologies when designing new plants.

Pre-combustion

The precombustion approach is in fact a gasification process. The fossil fuel is not burned directly but is instead transformed into a synthetic gas mixture (SynGas) which mainly comprises CO, $CO2$ and H_2. Water vapor is then used in reaction with the syngas, which leads to CO_2 molecules being the only carbon based byproducts. Following the process, the CO_2 can be easily separated using a similar solvent-based technique as for the post-combustion process. The resulting H_2 can then be used as a decarbonated fuel for combustion applications. An extensive overview of the different gasification technologies was done by Ulber (2015).

Oxy-combustion

By removing the nitrogen present in the air-combustion systems, the burnt gases created by oxycombustion are mostly comprised of CO_2 and H_2O. Since the CO_2 concentration is high after condensation of the water

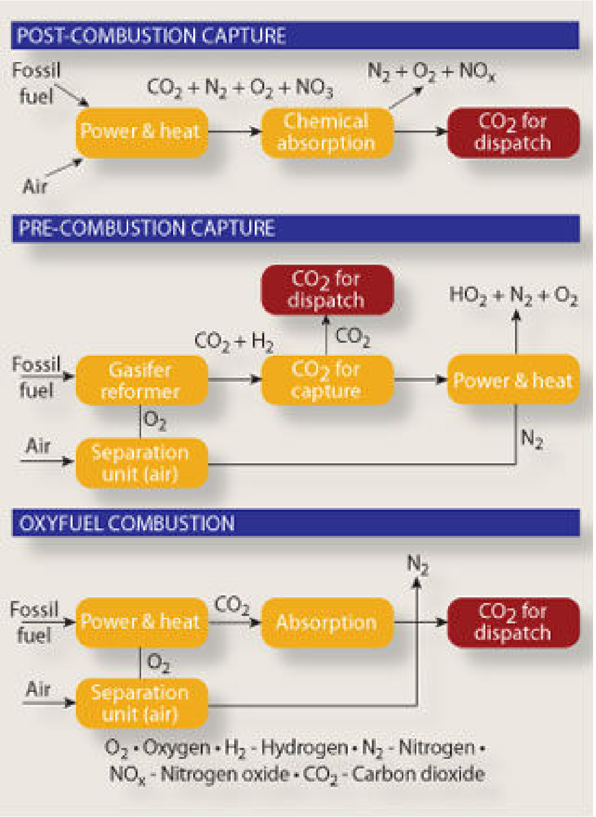
POST-COMBUSTION CAPTURE
Fossil fuel
Air
Power & heat
$CO_2 + N_2 + O_2 + NO_3$
Chemical absorption
$N_2 + O_2 + NO_x$
CO_2 for dispatch
PRE-COMBUSTION CAPTURE
Fossil fuel
Gasifer reformer
O_2
Air
Separation unit (air)
$CO_2 + H_2$
CO_2 for capture
CO_2
CO_2 for dispatch
Power & heat
$HO_2 + N_2 + O_2$
N_2
OXYFUEL COMBUSTION
Fossil fuel
Power & heat
CO_2
Absorption
N_2
CO_2 for dispatch
O_2
Air
Separation unit (air)
O_2 • Oxygen • H_2 - Hydrogen • N_2 - Nitrogen •
NO_x - Nitrogen oxide • CO_2 - Carbon dioxide

Figure 1.6: *Comparison of the 3 different approaches for* CO_2 *capturing: Post-combustion, Pre-combustion and Oxyfuel combustion. Source: Royal Society of Chemistry, United Kingdom.*

vapor, 90 to 95 %, it is much easier to extract and store. Oxycombustion plants are currently envisioned but are yet to be considered as a mainstream application.

1.2.2 NO_x reduction

The different nitrogen oxides are among the greenhouse gases group, and represent mainly N_2O, NO and NO_2. The first is responsible for greenhouse effect with a greenhouse power of nearly 10 times that of methane. The NO and NO_2 on the other hand are noxious gases and are responsible for ozone production in the lower layers of the atmosphere and for acid rains.

As stated earlier, one of the goals of European Commission is to attain an increase in energy systems efficiency of 27% by 2030. The improvement of combustion efficiency leads to higher temperature and pressure operating conditions. The increase in the operating temperature of combustion chambers leads to an increase in the quantity of produced NO_x through the Zel'Dovich thermal mechanism (Zel'Dovich (1946)). A similar effect exists for the pressure (Biagioli and Güthe (2007)).

The oxycombustion technology solves the NO_x emissions issue by eliminating the nitrogen in the combustive. Since no nitrogen is present to begin with, the nitrogen dioxides cannot be produced in the post flame region. The absence of N_2 in the initial gas mixture simplifies the determination of the optimal operating conditions, since the issue of finding the optimal operating point which minimizes the CO_2 and NO_x emissions is simpler. Indeed, as seen in Fig. 1.7, when increasing the operating temperature in combustion chambers as it is currently done in order to improve the efficiency, the CO_2 emissions are reduced, but the NO_x emissions increase at the same time. Hence, an optimal compromise must be found.

1.2.3 Oxytec Chair

In the scope of improving the existing technologies and developing the future ones, Air Liquide joined forces with the french CNRS, ANR and the engineering school CentraleSuplelec through the OxyTec chair with the goal of better understanding the different phenomena and their interactions inside oxygen-enriched combustion or gasifications configurations. These processes are a part of the strategic program of Air Liquide $R\&D$.

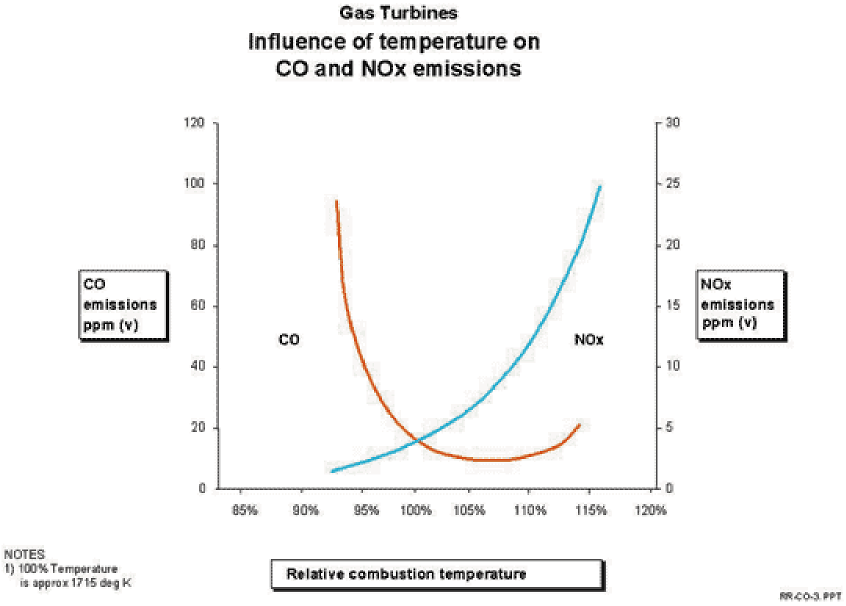

Figure 1.7: *CO_2 vs NO_x emissions as a function of the operating temperature. Extracted from www.topac.com ().*

It is considered as promising technology for the production of steam and carbon-free electricity.

The Oxytec chair is designed to improve the knowledge of these technologies for gaseous (natural gas, synthesis gas), liquid (heavy fuel oil, waste oil distillation) and future solid (coal, biomass) fuels for systems operating under pressure. The adopted approach combines experimentation with modeling and numerical simulations (Fig. 1.8). The experimental rig developed with the help of the Oxytec chair is equipped for an instrumented detailed analysis of the flow and heat transfer in flames stabilized on swirling flows. The combustion chamber operates at high pressure and the oxidizer used is enriched with oxygen while the gases are diluted by CO_2 and water vapor.

1.2.4 Positioning inside the Oxytec chair

Inside the Oxytec Chair, this thesis represents the first numerical study inside the task "*Simulating the multi physics interactions*" (task n°3). The initial goal was to determine a method for conducting unsteady, high-fidelity, coupled simulations accounting for turbulent reactive flows, heat transfer inside walls and hot gases radiation. The aimed goal in-

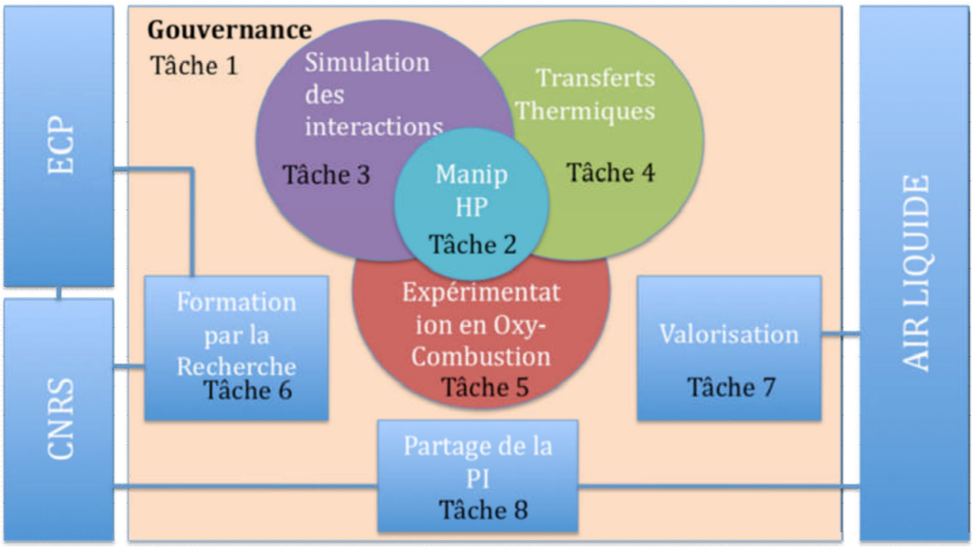
ECP
CNRS
Gouvernance
Tâche 1
Simulation des interactions
Tâche 3
Transferts Thermiques
Tâche 4
Manip HP
Tâche 2
Expérimentation en Oxy-Combustion
Tâche 5
Formation par la Recherche
Tâche 6
Valorisation
Tâche 7
Partage de la PI
Tâche 8
AIR LIQUIDE

Figure 1.8: *Oxytec industrial chair tasks and partners. (French)*

side the Oxytec chair is to have a numerical tool allowing multi physics simulations, in order to predict the oxycombustion chamber physics, and more precisely the heat fluxes in the most fragile areas of the chambers. To do so, different studies were needed. First of all, numerical tools for each phenomenon are needed. Once each phenomenon can be simulated in a stand-alone configuration, the pair by pair coupling must be tested for flow-wall and flow-radiation. Then, the final coupled tool can be used.

The work conducted in this thesis was mostly aimed toward a better understanding of conjugate heat transfer, and the development of a new coupling technique for flow and wall heat transfer solvers. Efforts were mostly made in order to improve the existing methods, and finally proposing a new method.

1.2.5 Conjugate Heat transfer

In the previous subsection it was mentioned that the operating conditions of combustion chambers are currently being increased which leads to higher pressure and temperature levels. This modification of operating conditions leads to larger wall heat flux levels, and the increase in power enlarge the difference between the real levels and the ones estimated using empirical models. It is therefore compulsory to achieve a better understanding of the physics inside the chambers in order to correctly lead the design process. Because of the high cost of conducting experimental studies, numerical investigations are done beforehand so as to reduce the final the number of configurations which need to be studied experimentally.

To estimate the levels of wall heat flux, the different heat transfer mechanisms need to be studied inside the combustion chamber. One in particular is the thermal interaction between a flow (reactive or non-reactive) with a solid wall: *Conjugate Heat Transfer*. Such a multi physics configuration is in fact a coupled problem. The fluid and solid temperature fields depend in each domain on the different thermo-physical parameters (density, heat capacity and thermal conductivity), but are linked at the interface where both temperature and wall heat flux must be continuous through the fluid/solid interface. Such a constraint leads to the following relation of boundary conditions at the interface for both domains:

$$\forall t,\, T_{bnd,f} = T_{bnd,s} \tag{1.1}$$

$$\forall t,\, \boldsymbol{\phi}_{bnd,f} \cdot -\mathbf{n}_{ext,f} = \boldsymbol{\phi}_{bnd,s} \cdot \mathbf{n}_{ext,s} \tag{1.2}$$

Several analytical studies exist concerning conjugate heat transfer. For laminar flows, comparisons of analytical and numerical solutions exist:

- *Flat plate*: Steady configurations, where a flat plate has one side with a prescribed boundary condition while the other end is connected to a flow. Examples exist for a finite plate with natural convection Pozzi and Lupo (1988), or forced convection Pozzi and Lupo (1989b).
- *Plane duct*: Channel flow configurations with heat conduction in the walls. Both steady Pozzi and Lupo (1989a) and unsteady Fourcher and Mansouri (1997) are available.

While enriching and providing with analytical test cases, these examples are limited by their analytical nature. Industial applications are often unsteady configurations with turbulent flows which cannot be solved analytically, thus meaning that for a better understanding of the undergoing multi phenomena interaction, fully unsteady numerical simulations are needed.

A first step towards a better understanding of the conjugate heat transfer phenomenon is the study of turbulent flows alone with different prescribed boundary conditions. The flow-wall interface is replaced with a boundary condition for the flow, though it may vary over time as in the studies conducted by Kawamura et al. (1998), Kawamura et al. (1999) and Abe et al. (2004). The three studies were based on turbulent channel flows with duct sections with low to high reynolds numbers as well as for different Prandtl numbers.

It was also shown in these works that while an isothermal boundary condition is used for a flow, the heat flux fluctuations for $Pr \approx 0.71$ attain about 40% of the mean heat flux (Fig. 1.9) for a large spectrum of Reynolds numbers. Such high fluctuations are high enough that they can have an influence on the fatigue of the walls considered. Thus, for a better prediction of the time evolution of the materials used, fully unsteady studies of conjugate heat transfer are needed. First of all to better estimate the wall heat flux and temperature. This feat is achieved through the higher obtained accuracy of the numerical results. Secondly, by studying the unsteady time evolution of the temperature inside the walls.

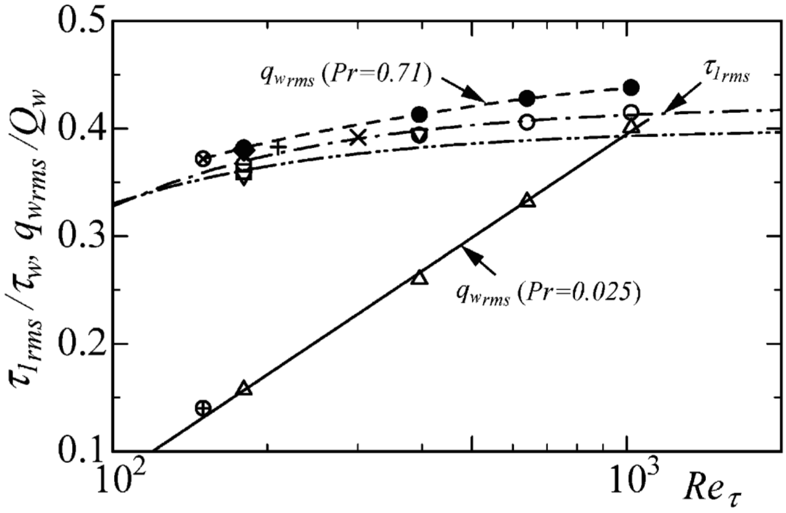

Figure 1.9: *Heat flux fluctuations over mean heat flux as a function of the Reynolds number. Extracted from Abe et al. (2004).*

Turbulent configurations are studied since the early 2000's with the help of numerical tools where both media are solved. The techniques used cover the full scope of flow solver: RANS (Noh-Pat et al. (2015), Mensch and Thole (2015)), LES (Amaya (2010), Jauré (2012)) and DNS Tiselj et al. (2001).

Those studies showed that taking into account the wall's physics can have a non-negligible effect on the flow characteristics, and also lead to a better prediction of the wall temperature. Hence, for high-fidelity predictive simulations, such as those envisioned in this thesis' work, such effects need to be taken into account. The work presented hereafter will tackle the question of accounting for this interaction in reactive flows-wall coupling.

1.3 Thesis work

1.3.1 Goal of the thesis

Considering the different topics discussed previously in this chapter, the goal of this thesis was defined as follows:

Providing a methodology for conducting ***unsteady high-fidelity*** *simulations of* ***turbulent reactive flows*** *while accounting for different mechanisms of heat transfer such as* ***conjugate heat transfer*** *and* ***gases radiations****.*

With the aim of answering the problem defined here-above, work was done with a focus on the conjugate heat transfer methodology. The results obtained are detailed in this manuscript following the outline described in the next section.

1.3.2 Manuscript structure

- **Chapter 2:** *Presentation of the different numerical tools used in this work*

  In order to conduct coupled simulations, a good understanding of each phenomenon is needed before attempting to conduct coupled studies. In this chapter the different numerical resolution codes used in this thesis are presented and then validated on test configurations.

- **Chapter 3:** *Coupling procedures*

  High fidelity studies of conjugate heat transfer are both rare and relatively new. Few methodologies exist for coupled simulations accounting for the heat transfer inside the walls for combustion applications. Chapter 3 presents the different existing approaches accounting for conjugate heat transfer in numerical resolution codes. The methods are compared and a methodology for coupled simulations is chosen with the help of this comparison.

- **Chapter 4:** *Coupling time step size determination*

  In this chapter, the challenge of determining the coupling time step is dealt with. In existing works, the frequency is either chosen *a priori* or is determined *a posteriori* after several computations are made. The value obtained is case sensitive. The approach presented here allows for an automatic determination of the coupling step over time while the only input used is the numerical precision required by the user.

- **Chapter 5:** *Permanent regime convergence acceleration*

  The time scales inside walls for heat transfer are several orders of magnitude higher than the ones inside turbulent flows. Such a discrepancy leads to huge physical times which need to be computed in order to achieve the permanent state for the flow-wall configuration. That is why when only the permanent state is sought, a method for computing that state is needed. To do so, the thermal solid state is accelerated towards its permanent regime thus allowing for a prediction of the mean and root-mean-square values in the permanent regime. Such a method is presented in chapter 5.

- **Chapter 6:** *Coupled simulations of a configuration of Flame-Wall interaction*

  The coupling methodology developed in chapters 3, 4 and 5 is applied here on a configuration of flame-wall interaction experimentally studied by Singh et al. (2013). The experimental configurations consists of a jet flame impinging on a cooled wall made of quartz. The results obtained with the coupling method are both compared to the experimental results and to another method available in the literature.

- **Chapter 7:** *Application of the Conjugate Heat Transfer methodology to a laboratory-scale combustor*

  The coupling methodology developed in chapters 3, 4 and 5 is applied to an experimental configuration studied by Guiberti et al. (2015). The configuration consists of a premixed flame inside a duct chamber. The fuel is a H_2-CH_4 mixture. Heat losses were shown to have an influence on the flame shape in this configuration Mercier (2015). The results obtained showed a good capability of the coupling methodology to correctly solve the multi-physics, and the gases radiation was shown to have a significant effect on the wall temperature.

1.3.3 Major contributions

The major contributions of this thesis' work are the following:

- An original interface model for conjugate heat transfer coupled simulations was developed. The usage of this model allows an automatic control of the coupling time step size based on variable step integrators. The coupling step size control requires only a wished numerical accuracy, and step size is determined on the fly according to the physics taking places in the simulation.

- An acceleration method which is coherent with the step size control approach was developed. Using this approach, the exact permanent state can be attained directly when the transient heating is not of interest.

- The coupling methodology for conjugate heat transfer developed in this work was validated on two different cases of reactive flows (one turbulent and one non-turbulent). The results shows a quantitative comparison of the experimentally measured and numerically computed wall temperatures which is an important result and is hard to come by in the existing literature.

1.3.4 Communications

1.3.4.1 International journals

- C. Koren, R. Vicquelin, O. Gicquel. *Coupling frequency determination and acceleration to steady state in unsteady conjugate heat transfer.* *Submitted* to International Journal of Heat and Mass Transfer

1.3.4.2 Conferences

International conferences

- C. Koren, R. Vicquelin, O. Gicquel. *Automatic determination of the coupling period in unsteady conjugate heat transfer. Application to large eddy simulation of flame-wall interaction.* 15th International Conference on Numerical Combustion. Avignon, France. 2015.

National conferences

- C. Koren, R. Vicquelin, O. Gicquel. *Détermination automatique de la période de couplage entre un code de simulation aux grandes échelles et un code de conduction thermique.* Congrès annuel de la Société Française de Thermique. La Rochelle, France. 2015.

Chapter 2

Numerical codes used for multi physics simulations

2.1 Turbulent reactive flows 20

2.1.1 Low Mach number approximation 20

2.1.2 Filtered equations 23

2.1.3 Test cases 24

2.2 Heat transfer in solids 32

2.2.1 1D diffusion code 32

2.2.2 3-dimensional unsteady heat transfer in solids solver 36

2.2.3 3-dimensional steady heat transfer in solids solver 37

2.3 Radiation in semi-transparent gases 38

2.3.1 Radiative Transfer Equation 38

2.3.2 Numerical methods 40

2.3.3 1D validation 40

2.4 Coupling: OpenPALM coupler 41

2.5 Conclusion 43

To conduct multi-physics simulations, it is first necessary to describe each different phenomenon accurately. In this chapter, each numerical resolution code used during this thesis work is presented before being validated using either an analytical solution or experimental measurements.

2.1 Turbulent reactive flows

The code used for turbulent reactive flows simulation is the YALES2 code (www.coria cfd.fr (2015)). It is based on the low-Mach number flow assumption. The numerics of the code include fourth order space discretization and fourth order time integration schemes. (Moureau et al. (2011), Malandain (2012)) The following subsections present the set of equations solved by the code, as well as three test cases: A non-reactive channel flow with variable density, a 1D DNS (Direct Numerical Simulation) flame computation using detailed chemistry and a 1D thickened flame.

2.1.1 Low Mach number approximation

When studying the Navier-Stokes equations, if the considered gas velocity is small compared to the sound speed c (Mach number $Ma \leq 0.2$) then the Low Mach number approximation can be applied: Compressibility effects are neglected while taking into account the dilatation of density with the temperature. This approach decouples density and pressure in the flow equations to filter acoustics out.

The starting point is the definition of the system of balance equations describing the behavior of a turbulent reactive flow for density ρ, velocity $\mathbf{u}$, and enthalpy h:

$$
\begin{aligned}
\frac{\partial \rho}{\partial t} + \frac{\partial \rho u_i}{\partial x_i} &= 0 && (2.1)\\
\frac{\partial \rho u_j}{\partial t} + \frac{\partial \rho u_i u_j}{\partial x_i} &= -\frac{\partial p}{\partial x_i} + \frac{\partial \tau_{ij}}{\partial x_i} + S_j && (2.2)\\
\frac{\partial \rho Y_k}{\partial t} + \frac{\partial \rho u_i Y_k}{\partial x_i} &= -\frac{\partial \rho Y_k V_{k,i}}{\partial x_i} + \rho \dot{\omega}_k && (2.3)\\
\frac{\partial \rho h}{\partial t} + \frac{\partial \rho u_i h}{\partial x_i} &= \frac{dp}{dt} + \tau_{ij}\frac{\partial u_i}{\partial x_i} - \frac{\partial q_i}{\partial x_i} && (2.4)\\
q_i &= -\lambda \frac{\partial T}{\partial x_i} + \rho \sum_{k=1}^{Nsp} h_k Y_k V_{k,i} && (2.5)\\
p &= \rho r T && (2.6)
\end{aligned}
$$

Where S_j is a momentum source term, Y_k is the mass fraction of the k^{th} species, $\dot{\omega}_k$ is its source term, Nsp the number of species and the enthalpy h is defined as:

$$h = \int_{T_0}^{T} c_p dT + \sum_{k=1}^{Nsp} \Delta h_{f,k}^0 Y_k \tag{2.7}$$

and $\Delta h_{f,k}^0$ is the formation enthalpy of the k^{th} species.

To use the low-Mach number assumption, the previous system is recast in dimensionless form (Majda and Sethian (1985)). A Taylor series expansion of the different thermochemical variables Φ^* is then done in the dimensionless form in terms of the Mach number Ma:

$$\Phi^* = \Phi_0^* + Ma\Phi_1^* + Ma^2\Phi_2^* + \mathcal{O}(Ma^3) \tag{2.8}$$

Injecting these expansions inside the set of equations for turbulent reactive flows leads to the following set of equations (The full derivation process was done by Benteboula (2006)):

$$\begin{aligned}
\frac{\partial \rho_0}{\partial t} + \frac{\rho_0 u_{0,i}}{\partial x_i} &= 0 && (2.9)\\
\frac{\partial p_0}{\partial x_j} &= 0 && (2.10)\\
\frac{\partial p_1}{\partial x_j} &= 0 && (2.11)\\
\frac{\partial \rho_0 u_{0,j}}{\partial t} + \frac{\partial \rho_0 u_{0,i} u_{0,j}}{\partial x_i} &= -\frac{\partial p_2}{\partial x_i} + \frac{\partial \tau_{0,ij}}{\partial x_i} + S_{0,j} && (2.12)\\
\frac{\partial \rho_0 Y_{0,k}}{\partial t} + \frac{\partial \rho_0 Y_{0,k} u_{0,i}}{\partial x_i} &= -\frac{\partial \rho_0 Y_{0,k} V_{0,(k,i)}}{\partial x_i} + \rho_0 \dot{\omega}_{0,k} && (2.13)\\
\frac{\partial \rho_0 h_0}{\partial t} + \frac{\partial \rho_0 u_{0,i} h_0}{\partial x_i} &= \frac{\partial p_0}{\partial t} - \frac{\partial q_i}{\partial x_i} + \rho \dot{\omega}_0 && (2.14)\\
q_i &= -\lambda \frac{\partial T_0}{\partial x_i} + \rho_0 \sum_{k=1}^{Nsp} Y_{0,k} h_{0,k} V_{0,(k,i)} && (2.15)\\
p_0 &= \rho_0 r_0 T_0 && (2.16)
\end{aligned}$$

In incompressible low Mach flows, the velocity is separated into an irrotational and solenoidal components (Chorin (1986)). This method can be generalized to the variable density equations under the low Mach number approximation by using the conservative form (Kraushaar (2011), Malandain (2012)). In YALES2, the density is determined with the help of the equation of state (Eq. 2.16), but to advance the velocity, the pressure gradient is needed, and a prediction-correction algorithm is used. By neglecting the 0 subscript for first order Mach number terms for the sake of simplicity, the following equations can be written for the velocity prediction using a first order time integration scheme:

$$\frac{\rho \mathbf{u}^* - \rho \mathbf{u}^n}{\Delta t} + \nabla \cdot (\rho \mathbf{u}^{n+\frac{1}{2}} \mathbf{u}^{n+\frac{1}{2}}) = -\nabla \cdot (p_2^{n-\frac{1}{2}}) + \nabla \cdot (\tau^n) + \mathbf{S}^n \quad (2.17)$$

In YALES2, the prediction step is implemented using a fourth order explicit scheme named TFV4A. This scheme is a combination of both the Runge-Kutta 4 ($\mathcal{RK}$) and Lax-Wendroff ($\mathcal{LW}$) schemes (Kraushaar (2011)). Typically, the obtained time integration is of the following form for a scalar Φ:

$$\Phi^{n+1} = \Phi^n + \alpha \Delta t \mathcal{LW}(\Phi) + (1-\alpha) \Delta t \mathcal{RK}(\Phi) \quad (2.18)$$

Where $\alpha = 0$ corresponds to a RK4 integration scheme and $\alpha = 1$ to the Lax-Wendroff integration scheme.

A correction step is applied afterwards to the velocity using the mid-step pressure gradient with the following formula:

$$\frac{\rho \mathbf{u}^{n+1} - \rho \mathbf{u}^{*}}{\Delta t} = -\nabla p_2^{n+\frac{1}{2}} \tag{2.19}$$

The correction step needs the value of the pressure gradient. It is obtained by applying the divergence operator to the previous equation:

$$\nabla^2 p_2^{n+\frac{1}{2}} = \frac{\nabla \cdot (\rho \mathbf{u}^{*})}{\Delta t} - \frac{\nabla \cdot (\rho \mathbf{u}^{n+1})}{\Delta t} \tag{2.20}$$

and considering that $\nabla \cdot (\rho \mathbf{u}^{n+1})$ is the mid step gradient used to advance the density from $t = t_{n+\frac{1}{2}}$ to $t = t_{n+\frac{3}{2}}$, and using Eq. 2.9, the following Poisson equation is solved for the pressure in order to use it in the correction step:

$$\nabla^2 p_2^{n+\frac{1}{2}} = \frac{\nabla \cdot (\rho \mathbf{u}^{*})}{\Delta t} + \frac{\rho^{n+\frac{3}{2}} - \rho^{n+\frac{1}{2}}}{\Delta t^2} \tag{2.21}$$

2.1.2 Filtered equations

Filtering the previous set of equations, the following set of filtered equations is obtained for the Navier-Stokes low-Mach equations:

$$\frac{\partial \overline{\rho}}{\partial t} + \frac{\partial}{\partial x_i}(\overline{\rho}\widetilde{u}_i) = 0 \tag{2.22}$$

$$\frac{\partial \overline{\rho}\widetilde{u}_j}{\partial t} + \frac{\partial}{\partial x_i}(\overline{\rho}\widetilde{u}_i\widetilde{u}_j) = -\frac{\partial \overline{p}_2}{\partial x_j} + \frac{\partial(\overline{\tau}_{ij} + \overline{\tau}_{ij}^{sgs})}{\partial x_i} + \overline{S}_j \tag{2.23}$$

$$\begin{aligned} \frac{\partial \overline{\rho}\widetilde{Y}_k}{\partial t} + \frac{\partial}{\partial x_i}\left(\overline{\rho}\widetilde{u}_i\widetilde{Y}_k\right) = & -\frac{\partial}{\partial x_i}\left(\overline{\rho V_{k,i} Y_k}\right) - \frac{\partial}{\partial x_i}\left(\overline{\rho}\widetilde{u_i Y_k} - \overline{\rho}\widetilde{u}_i\widetilde{Y}_k\right) \\ & + \overline{\rho\dot{\omega}_k} \end{aligned} \tag{2.24}$$

$$\frac{\partial \overline{\rho}\widetilde{h}}{\partial t} + \frac{\partial}{\partial x_i}(\overline{\rho}\widetilde{u}_i\widetilde{h}) = -\frac{\partial \overline{q}_i}{\partial x_i} - \frac{\partial}{\partial x_i}\left(\overline{\rho}\widetilde{u_i h} - \overline{\rho}\widetilde{u}_i\widetilde{h}\right) + \overline{\rho\dot{\omega}} \tag{2.25}$$

$$p_0 = \overline{\rho} r\widetilde{T} \tag{2.26}$$

Due to the filtering of the equations, some terms are unknown and require modeling. These terms are the unresolved sub-grid turbulent fluxes and correspond for a variable Φ to:

$$\mathcal{J}_{\Phi}^{SGS} = \overline{\rho}\widetilde{u_i\Phi} - \overline{\rho}\widetilde{u}_i\widetilde{\Phi} \tag{2.27}$$

Several turbulent sub-grid scale models exist for $\overline{\tau}_{ij}^{sgs}$ in the literature. The ones available in YALES2 are: The Smagorinsky model (Smagorinsky (1963)), the dynamic Smagorinsky model (Germano (1992)), WALE model (Nicoud and Ducros (1999)) and sigma model (Nicoud et al. (2011)). The unresolved sub-grid scale turbulent fluxes for the species mass fractions Y_k, $\mathcal{J}_{Y_k}^{sys}$, and enthalpy h, $\mathcal{J}_h^{sgs}$, are obtained respectively by scaling $\overline{\tau}^{sgs}$ with the turbulent Schmidt number S_{ct} and turbulent Prandtl number P_{rt}.

2.1.3 Test cases

2.1.3.1 Non reactive case: Turbulent channel flow

The non-reactive flow test case is a turbulent channel flow visible in Fig. 2.1. The gas composition is fixed, no species are transported, and the temperature T is treated as a passive scalar. The number of point used are: 256 in the streamwise direction (X), 192 in the spanwise direction (Y) and 255 in the wall normal direction (Z). The time integration scheme used for both velocity and scalars is an explicit fourth order Runge-Kutta scheme.

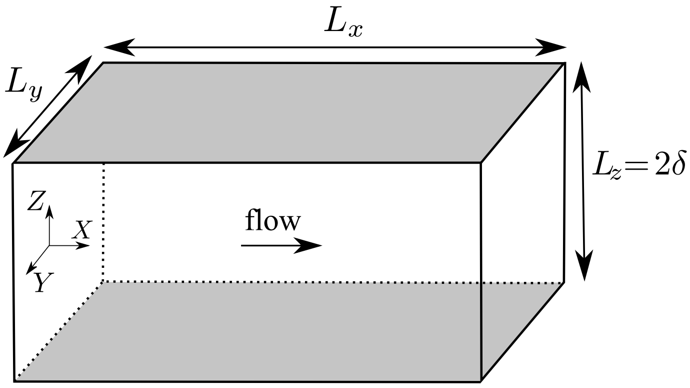

Figure 2.1: *Computational domain of the channel flow configuration where δ =0.1 m. The streamwise and spanwise lengths verify $L_x = 4\pi L_z$ and $L_y = 2\pi L_z$ respectively.*

The flow is characterized by the bulk (Re_b), practical (Re_{D_h}) and friction Reynolds (Re_τ) numbers:

$$Re_b = \frac{\rho_b u_b \delta}{\mu_b} \quad (2.28)$$

$$Re_{D_h} = 4Re_b \quad (2.29)$$

$$Re_\tau = \frac{\overline{\rho}_w u_\tau \delta}{\overline{\mu}_w} \quad (2.30)$$

where:

$$\rho_b = \frac{\int_0^{2\delta} \overline{\rho} dy}{2\delta} \text{ and } u_b = \frac{\int_0^{2\delta} \overline{\rho u} dy}{\int_0^{2\delta} \overline{\rho} dy} \tag{2.31}$$

The friction velocity u_τ is based on the wall mean viscous stress $\overline{\tau}_w$ as:

$$u_\tau = \sqrt{\frac{\overline{\tau}_w}{\overline{\rho}_w}} \tag{2.32}$$

The configuration studied here is a configuration with a constant density, where the temperature at the walls is set to $950K$ and the friction Reynolds number is set to $Re_\tau = 395$. Periodical boundary conditions are applied in the X and Y directions for the flow, while an atmopheric pressure is considered. The reference results are extracted from Moser et al. (1999) for the velocity fields and from Kasagi et al. (1992) for the temperature. A uniform heating source term is added in the energy equation using the same approach as Kim and Moin (1989):

$$\mathcal{Q} = \frac{2}{Re_\tau Pr} \tag{2.33}$$

where Pr is the Prandtl number. The different results for velocity and temperature fields are plotted under their non-dimensional forms defined as follows for wall distance y^+, streamwise velocity u^+ and temperature T^+:

$$y^+ = \frac{\overline{\rho}_w |y - y_w| u_\tau}{\overline{\mu}_w} \text{ and } u^+ = \frac{u}{u_\tau} \tag{2.34}$$

and

$$T^+ = \frac{|T - T_w|}{T_r} \text{ and } T_r = \frac{|\overline{\phi}_w|}{\overline{\rho}_w \overline{c_p}_w u_\tau} \tag{2.35}$$

The results for the mean and root-mean-square fluctuations for the non-dimensional velocity and temperature are given in figures 2.2, 2.3, 2.4, 2.5. Figure 2.2 shows the mean value of the streamwise velocity while Fig. 2.3 shows the root-mean-square fluctuations for all three velocity components. Similarly, figures 2.4 and 2.5 show the mean and root-mean-square fluctuations of the temperature respectively. As it can be seen, for both temperature and velocity the agreement is very good both in terms of mean values and of root-mean-square fluctuations.

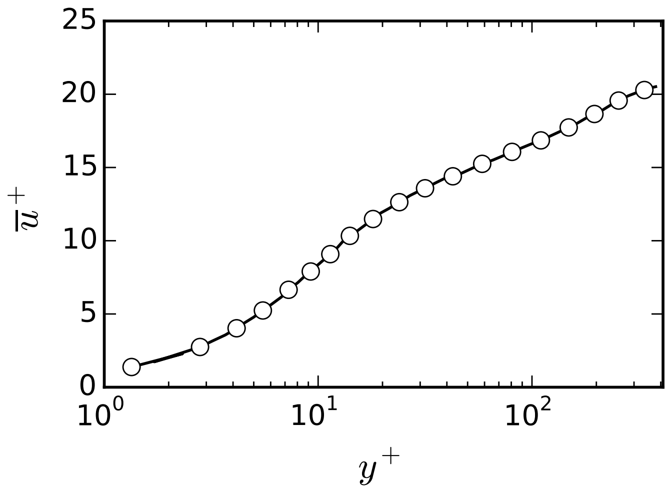

Figure 2.2: *Mean velocity profile along the wall normal direction scaled by* u_τ. *Circles: Moser et al. (1999). Black plain line: Numerical results*

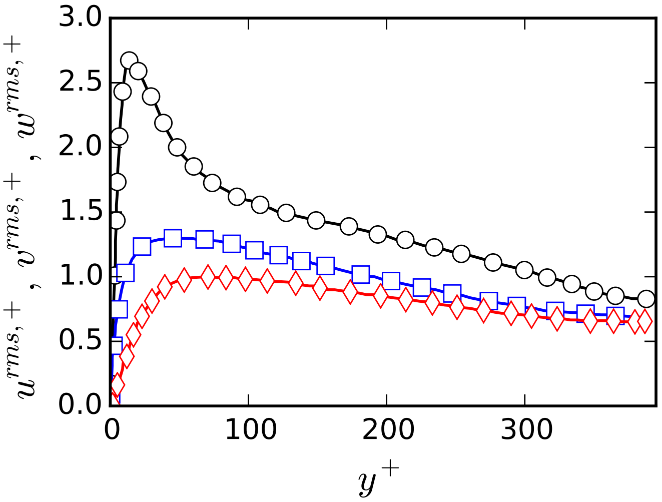

Figure 2.3: *Root-mean-square velocity fluctuations scaled by* u_τ *profile along the wall normal direction. Circles:* u^{rms} *from Moser et al. (1999). Black plain line:* u^{rms} *numerical results. Blue squares:* v^{rms} *from Moser et al. (1999). Blue plain line:* v^{rms} *numerical results. Red diamonds:* w^{rms} *from Moser et al. (1999). Red plain line:* w^{rms} *numerical results.*

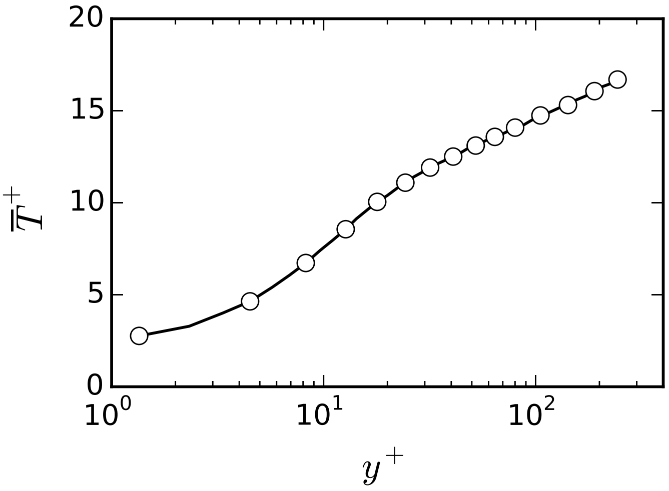

Figure 2.4: *Mean temperature profile along the wall normal direction. Circles: Kasagi et al. (1992). Black plain line: Numerical results*

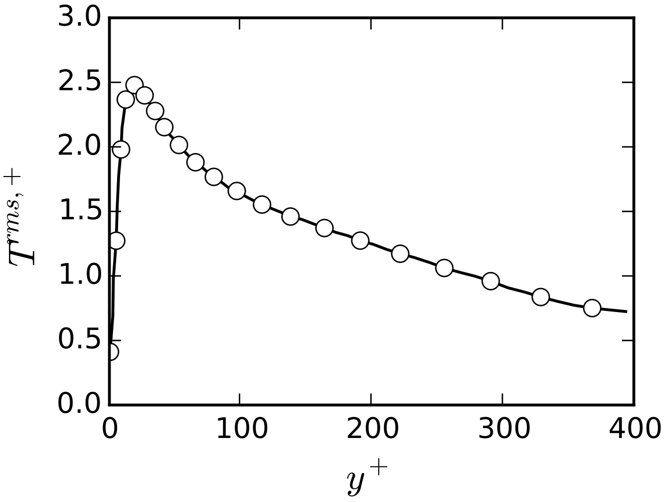

Figure 2.5: *Root-mean-square temperature profile along the wall normal direction. Circles: Kasagi et al. (1992). Black plain line: Numerical results*

2.1.3.2 Reactive: 1D flames with detailed chemistry

In this section, the fully reactive low Mach equations are considered with transported species mass fractions. The flames studied here are 1D premixed flames of methane with an equivalence ratio of 0.83. The set of solved equations is the one presented in section 2.1.2. The kinetic scheme used for this test is the one proposed by Coffee (1986). The cells size is taken equal to 0.01 mm to ensure a correct resolution of the flame front. The entire domain is 1 cm thick, leading to a number of 1 000 cells.

The computations is initialized with unburnt gases on the left side ($x \leq 0$) and burnt gases on the right side ($x \geq 0$). The junction between the two section is done by imposing an hyperbolic tangent function profile, centered at $x = 0$ and with a thickness of 0.4 mm. The initial unburnt gases velocity is set to 0.3 and is later on modified inside the computation until a convergence is achieved, leading to a steady flame. The final results are given in Fig. 2.6 which shows the temperature, density and velocity profiles, as well as some species mass fractions scaled by their maximum value.

In order to validate the final computed flame configuration, the laminar flame speed is computed and compared to the experimental results published by Egolfopoulos et al. (1989). The computation method is based on the mass conservation in the framework attached to the moving flame and is the following:

$$s_l = \frac{\rho_b(u_b - u_f)}{\rho_f - \rho_b} \tag{2.36}$$

where the f subscript denotes the fresh gases and the b subscript is used for the burnt gases. The results for the flame speed are given in Tab. 2.1. The numerically obtained laminar flame speed is larger than the experimentally measured value but the difference is smaller than the measurement's uncertainty ($\approx 2\,cm/s$).

Experimental	30.95 cm/s
Computation	32.1 cm/s

Table 2.1: *Experimental and numerical values for the laminar flame speed of premixed air/methane flame with an equivalence ratio of 0.83. Experimental values extracted from Egolfopoulos et al. (1989).*

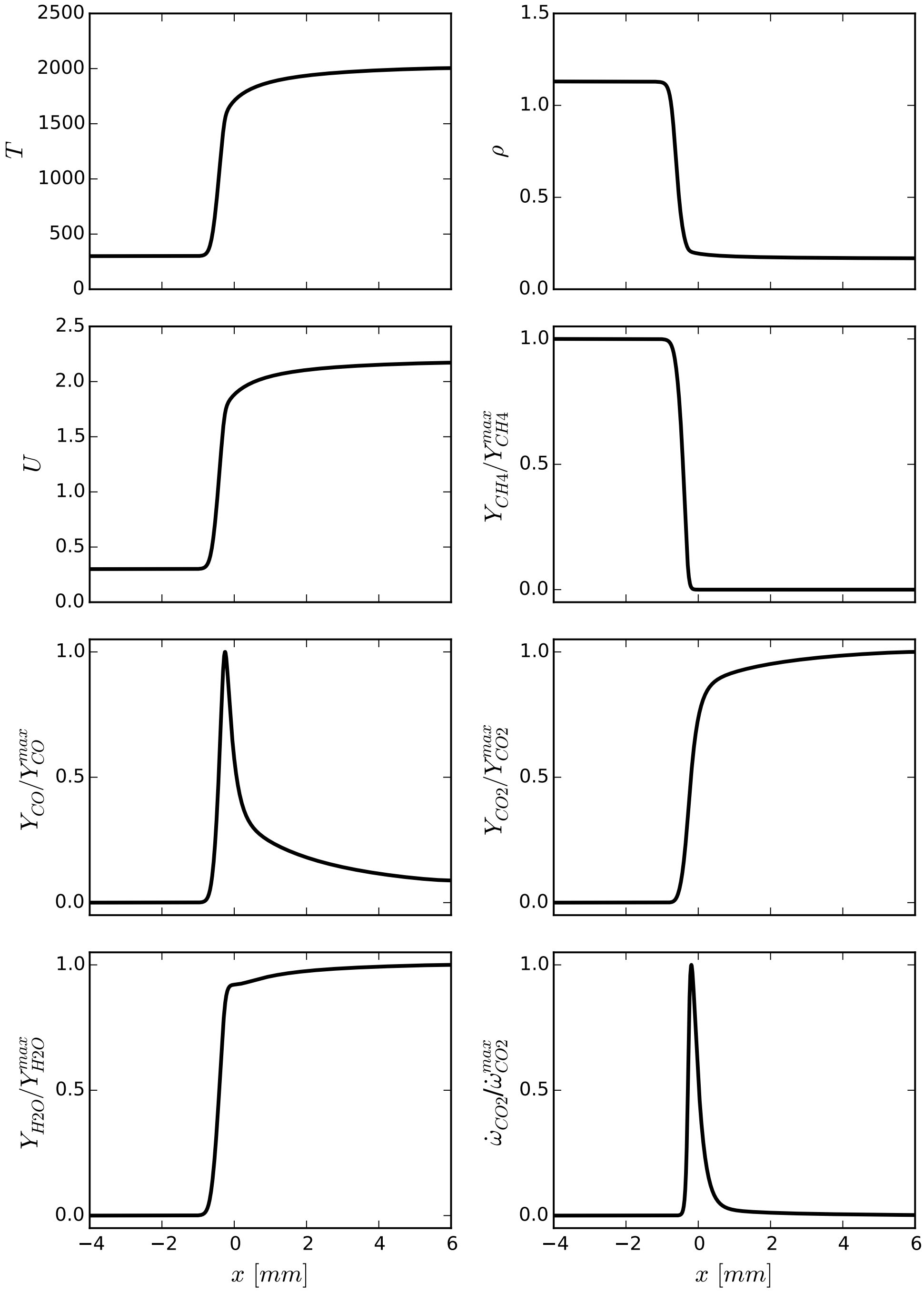

Figure 2.6: *1D profiles of temperature, density, gas velocity, Y_{CH_4}, Y_{CO}, Y_{CO_2}, Y_{H_2O} and $\dot{\omega}_{CO_2}$ for a 1D DNS premixed flame of air/methane with an equivalence ratio of 0.83. The mass fractions and source term are scaled by their maximum value.*

2.1.3.3 Reactive: 1D flames with dynamic thickening

When using LES to compute experimental configurations, the computational cost might impose a mesh cell size too large for a correct resolution of the flame front. In such cases a possible solution is to use a technique called flame thickening. For LES, such a technique is named TFLES (Thickened Flame for LES), and was developed by Butler and O'Rourke (1977) and extended by Colin et al. (2000). By artificially modifying the diffusive fluxes $\mathcal{J}_k$ and the reaction rates $\dot{\omega}_k$ with a thickening factor $\mathcal{F}$ such as:

$$\begin{aligned} \mathcal{J}_k &\rightarrow \mathcal{F}\mathcal{J}_k && (2.37) \\ \dot{\omega}_k &\rightarrow \frac{\dot{\omega}_k}{\mathcal{F}}, && (2.38) \end{aligned}$$

The fluxes are thickened by applying the thickening factor $\mathcal{F}$ to the corresponding diffusivity D_k. Doing so allows for a conservation of the laminar flame speed since:

$$s_l \propto \sqrt{D_k \dot{\omega}_k} \tag{2.39}$$

thus the laminar flame speed s_l is unchanged, while the flame thickness δ_0 is multiplied by $\mathcal{F}$ since:

$$\delta_0 \propto \frac{D_{th}}{s_l} \tag{2.40}$$

The thickening is applied to the mass fractions Y_k of the different transported species and for the Enthalpy. The modified filtered equations are the following for a given species k and for the enthalpy:

$$\begin{aligned} \frac{\partial \bar{\rho}\widetilde{Y}_k}{\partial t} + \frac{\partial}{\partial x_i}\left(\bar{\rho}\widetilde{u}_i\widetilde{Y}_k\right) &= -\frac{\partial}{\partial x_i}\left(\mathcal{F}\overline{\rho V_{k,i} Y_k}\right) - \frac{\partial}{\partial x_i}\left(\bar{\rho}\widetilde{u_i Y_k} - \bar{\rho}\widetilde{u}_i\widetilde{Y}_k\right) \\ &\quad + \frac{\overline{\rho\dot{\omega}_k}}{\mathcal{F}} && (2.41) \\ \frac{\partial \bar{\rho}\widetilde{h}}{\partial t} + \frac{\partial}{\partial x_i}(\bar{\rho}\widetilde{u}_i\widetilde{h}) &= \frac{\partial}{\partial x_i}\left(\mathcal{F}\lambda\frac{\partial \overline{T}}{\partial x_i} - \mathcal{F}\rho_0\overline{\sum_{k=1}^{Nsp} Y_k h_k V_{k,i}}\right) \\ &\quad -\frac{\partial}{\partial x_i}\left(\bar{\rho}\widetilde{u_i h} - \bar{\rho}\widetilde{u}_i\widetilde{h}\right) + \frac{\overline{\rho\dot{\omega}}}{\mathcal{F}} && (2.42) \end{aligned}$$

The thickening factor $\mathcal{F}$ can be either constant over the entire domain, or it can vary locally and depend on a flame sensor S_f. The constant thickening has the drawback of modifying the flow physics everywhere, including where no thickening is needed. Moreover, if used, it will alter the value of the wall heat fluxes computed inside the flow solver, which is problematic for coupled conjugate heat transfer simulations. This aspect can be corrected by using a local thickening based on a flame sensor. This approach was first proposed by Légier et al. (2000). It consists of computing a flame sensor S_f which indicates where the flame front is present. It is a scalar between 0 and 1, where 1 indicates the flame front and 0 is a non-reactive zone where no thickening is used. The thickening factor depends on the flame sensor in the following way:

$$\mathcal{F} = 1 + (A_F - 1)S_f \tag{2.43}$$

Where A_F is the thickening amplitude. The work done by Légier et al. (2000) used a constant value for A_F. Yet, considering that the mesh cells size might not be the same everywhere, a dynamical thickening, with space dependent thickening amplitude can be used (Kuenne et al. (2011)). When the second option is used, the user must provide with the laminar flame thickness, δ_0, and the number of points needed to correctly resolve the flame front, N_p. A_F is then given as follows for a cell of length Δx:

$$A_F = max\left(1, N_p \frac{\Delta x}{\delta_0}\right) \tag{2.44}$$

For this case, a progress variable Y_c is defined as:

$$Y_c = Y_{CO} + Y_{CO_2} + Y_{H_2O} \tag{2.45}$$

and the flame sensor is based on its source term $\dot{\omega}_{Y_c}$ and is defined as:

$$S_f = min\left(1, \frac{\dot{\omega}_{Y_c}}{\dot{\omega}_{thres}} A_F\right) \tag{2.46}$$

Where $\dot{\omega}_{thres}$ is a threshold value provided by the user. In order to avoid numerical instabilities due to stiff variations, when the sensor goes from 1 to 0, the sensor is smoothed on a few neighboring points of the reactive zone.

For this case the kinetic scheme published by Coffee (1986) is used, which takes into account 14 species and 38 reactions. Computations were run on the same domain as for the previous section (length of 1 cm). The mesh cells size is set to 0.25 mm, thus leading to a thickening amplitude of about 6.7 throughout the domain. The spatial temperature field of the

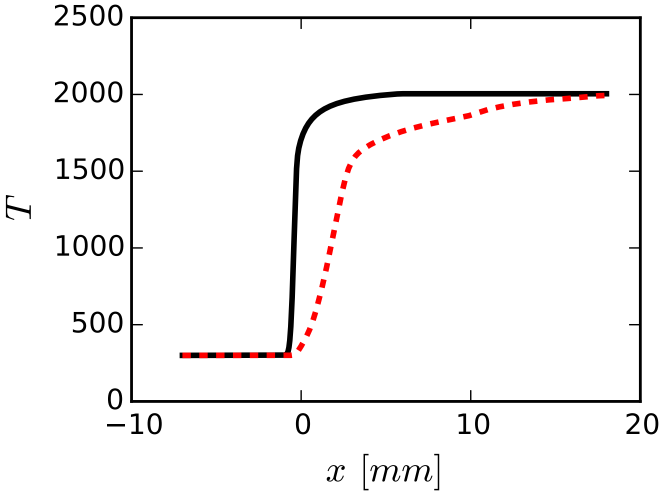

Figure 2.7: *Spatial 1D profiles of the temperature for the DNS flame (black plain line) and thickened flame (red dashed line).*

thickened flame is plotted in Fig. 2.7 with the DNS flame. As it can be seen, the flame is effectively thickened. Results are plotted in Fig. 2.8 for the temperature and several species as a function of the progress variable Y_c. As it can be seen, on this 1D case the dynamical flame sensor is capable of capturing the evolution of the different species, thus conserving the chemical structure of the flame. This methodology is then considered suitable for the Large Eddy Simulations which will be conducted in chapter 6.

2.2 Heat transfer in solids

2.2.1 1D diffusion code

During this thesis work, a number of studies was conducted with the help of a 1D diffusion code. The approach chosen was that of a code using finite-volume schemes in 1D in order to have a similar behavior to that of an LES solver. The equation solved by the code is the heat equation in solids, which is:

$$\rho c_p \frac{\partial T}{\partial t} = -\frac{\partial}{\partial x}(\phi) + \mathcal{P} \tag{2.47}$$

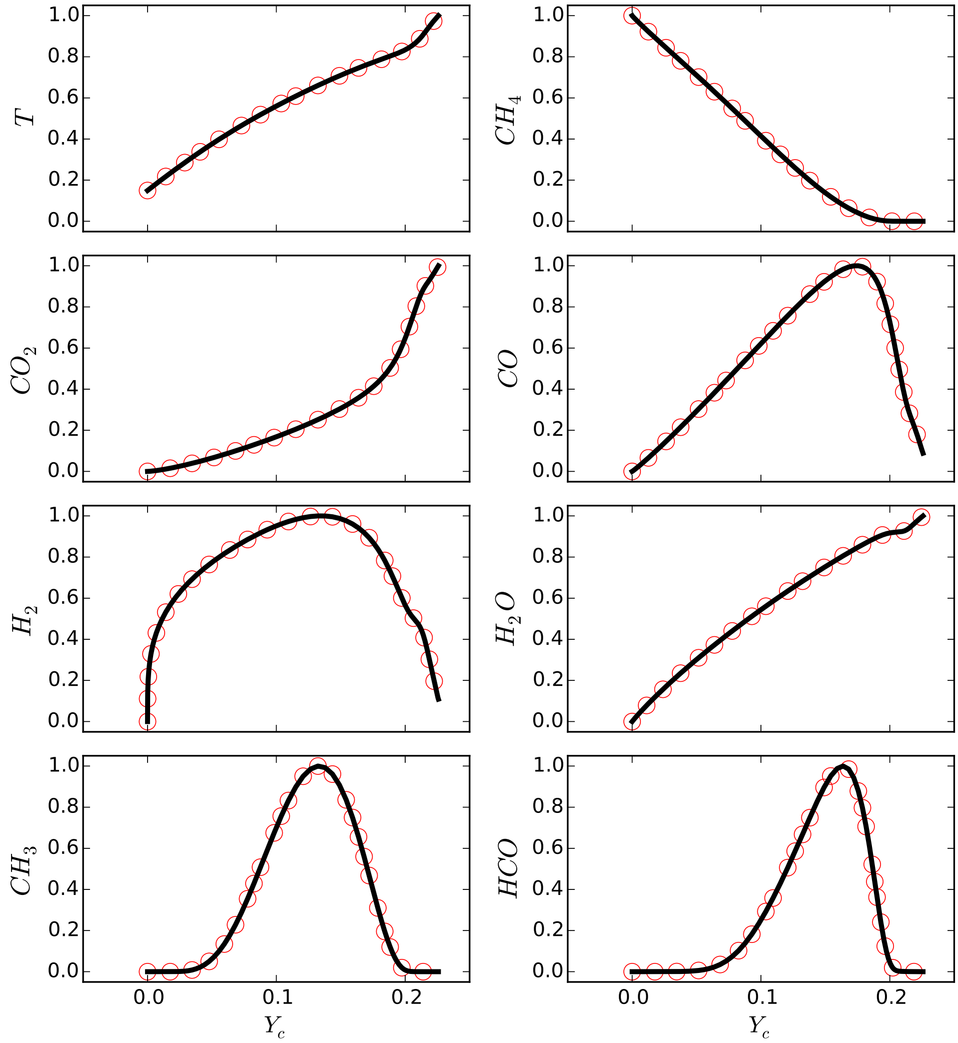

Figure 2.8: *1D profiles of temperature, CH_4, CO_2, H_2, CO, H_2O, CH_3 and HCO scaled by the maximum value of the DNS flame as a function of the progress variable Y_c. red circles: DNS flame, black plain line: thickened flame.*

The 1D configuration is shown in Fig. 2.9, which leads to the spatially discretized form:

$$\frac{\partial T_i}{\partial t} = -\frac{\phi_{i+\frac{1}{2}} - \phi_{i-\frac{1}{2}}}{\Delta x} + \mathcal{P}_i \tag{2.48}$$

The fluxes are computed using the Fourier law:

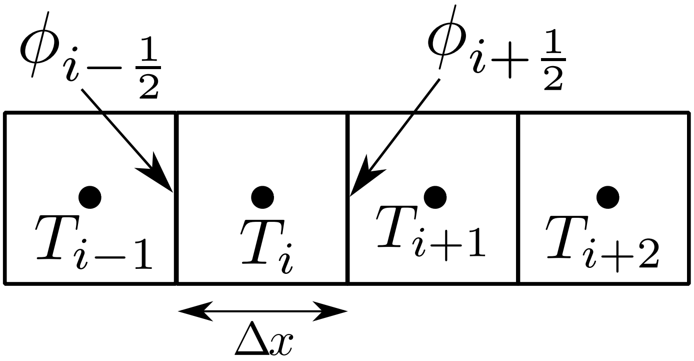

Figure 2.9: *Discretization of the 1D domain. Cells are all of the same length Δx. Finite volume balances are done over the i^{th} cell using the $(i+\frac{1}{2})^{th}$ and $(i-\frac{1}{2})^{th}$ fluxes.*

$$\phi = -\lambda_s \frac{\partial T}{\partial x} \tag{2.49}$$

The code uses fourth order spatial discretizations in space for the temperature gradients:

$$\frac{\partial T_{i+\frac{1}{2}}}{\partial x} = \frac{T_{i-1} - 15T_i + 15T_{i+1} - T_{i+2}}{12\Delta x} \tag{2.50}$$

Explicit time integration schemes are used. Both the forward Euler and second order mid-point integration scheme (Runge-Kutta 2) are available. The validation of the 1D diffusion code is done with the help of the Method of Manufactured Solutions (MMS). The method of manufactured solutions is a method for testing numerical solvers. The results explain whether or not the solver solves correctly the equation meant to be solved (Salari and Knupp (2000), Roache (2002)). The name comes from the fact that instead of searching the analytical solution of a given initial problem, an artificial solution is created, and the corresponding initial problem is sought. For example: The wished solution for the heat equation is $T(t,x) = f(t,x)$, where f is not a real solution of the heat equation, thus leading to:

$$\rho c_p \frac{\partial f}{\partial t} \neq \frac{\partial}{\partial x}(\lambda \frac{\partial f}{\partial x}) \tag{2.51}$$

To fix this issue, a source term is introduced into Eq. 2.51. This source term, $S_f(t,x)$ is obtained **analytically** as follows for the heat equation:

$$S_f(t,x) = \rho c_p \frac{\partial f}{\partial t} - \frac{\partial}{\partial x}(\lambda \frac{\partial f}{\partial x}) \tag{2.52}$$

The source term is then injected inside the numerical solver. Comparing the numerical solution to the analytical one will then tell if the code is solving correctly the given equation.

The artificial solution chosen for this test case is the following:

$$T_{MMS}(t,x) = T_0 + (L_0^2 - x^2)t \tag{2.53}$$

For an homogeneous media, the obtained source term is:

$$S_f(t,x) = \rho c_p (L_0^2 - x^2) + 2\lambda t \tag{2.54}$$

The test was done for aluminium, and the results for the temperature field are given in Fig. 2.10 for $t = 10$ s and $t = 25$ s. The initial temperature was set to $T_0 = 300K$. L_0 was taken as equal to 0.5 cm and 100 points were used. The Fourier number based on one cell length Δx is equal to 0.1.

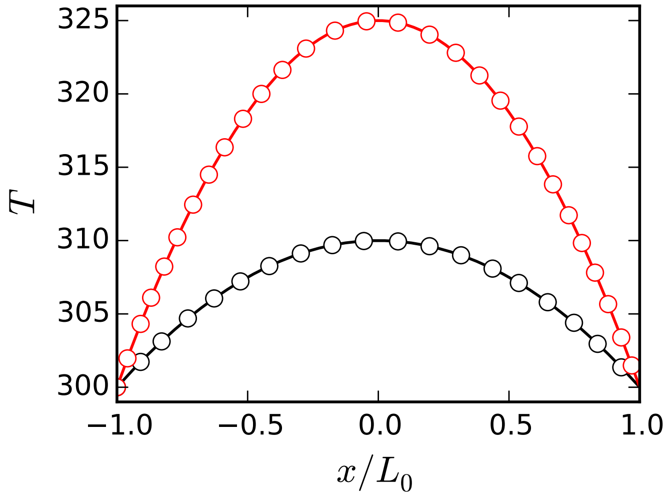

Figure 2.10: *Temperature fields for aluminium ($\lambda = 236$, $\rho = 2\,708$ and $c_p = 896$ in SI units). Black circles: Analytical solution a $t = 10$ s. Black plain line: Numerical solution a $t = 10$ s. Red circles: Analytical solution a $t = 25$ s. Red plain line: Numerical solution a $t = 25$ s.*

As seen in Fig. 2.10 the agreement between analytical and numerical solutions is very satisfying. This shows that the 1D code resolves correctly the heat equation. Moreover, the order of the two time integration schemes was tested using the same test case by changing the Fourier number used. The results are available in Fig. 2.11. The latter shows that for both integration methods theoretical order is numerically retrieved.

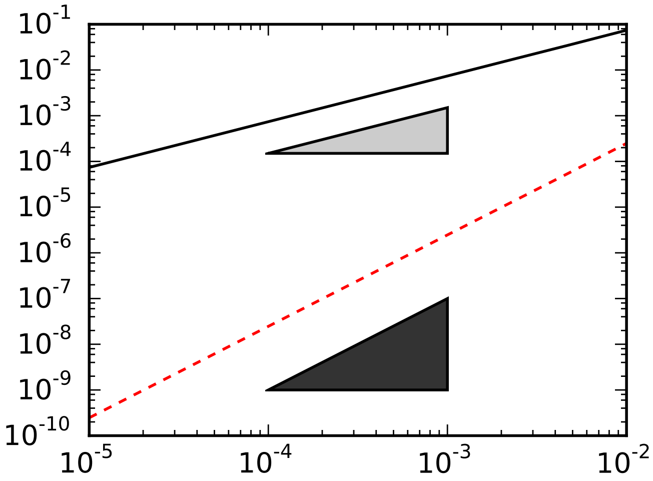

Figure 2.11: *Numerical L^2 integration error as a function of the time step size. Black plain line: Explicit forward Euler method. Red dashed line: Explicit mid-point method. Gray faced triangle: First order slope. Black faces triangle: Second order slope.*

2.2.2 3-dimensional unsteady heat transfer in solids solver

An unsteady heat transfer solver in solids is available in the YALES2 library. The version available at the beginning of this work provided only a second order Crank-Nicholson implicit time integration scheme and was lacking a Neumann boundary condition. In order to use this solver for coupled 3D simulations, several modifications were done. A fourth order Runge-Kutta time integration scheme was added as well as the Neumann boundary condition (prescribed heat flux) and a convective heat flux boundary condition (prescribed T_{ext} and h_{ext}).

The validation of these additions, RK4 integration scheme and Neumann boundary condition, was done by computing the temperature field for

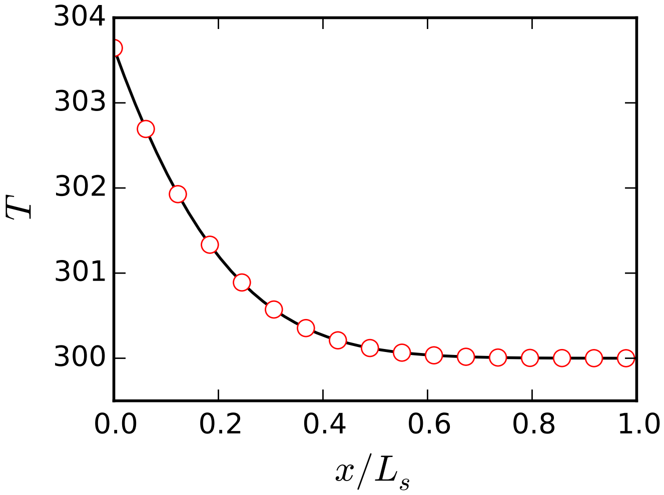

Figure 2.12: *Temperature fields inside an aluminium layer of thickness* $L_s = 0.5$ *cm, computed by the 3D HTS YALES2 solver and 1D diffusion code. Red circles: 1D diffusion code. Black plain line: 3D HTS solver of the YALES2 library.*

aluminium on a pseudo-1D case and comparing the results to those of the 1D diffusion code. The pseudo-1D configuration was obtained by simulation of a 3D slab and using periodical boundary conditions in the y and z directions. Thermo-physical parameters for the aluminium are the same as those used in the previous subsection. The prescribed heat flux was $\phi_0 = 10\ kW/m^2$ and the time simulated is $\tau = 0.5$ s. The results plotted in Fig. 2.12 show a very good agreement between the two temperature fields.

2.2.3 3-dimensional steady heat transfer in solids solver

During the development of the accelerated hybrid cell coupling method (chapter 5), the need for a steady heat transfer solver arose. This steady solver was written by using the data structure from the unsteady heat transfer solver of the YALES2 library. Since for the steady solver the resolved equation is:

$$-\nabla(\boldsymbol{\phi}) + \mathcal{P} = 0 \tag{2.55}$$

the explicit integration scheme was replaced with a Poisson solver available in the YALES2 library (Malandain et al. (2013)). The validation of this steady solver was done using a pseudo-1D configuration by computing a 3D slab with periodical boundary conditions in the y and z directions. The media used is quartz, with a thermal conductivity $\lambda = 1.5\ W/K/m$ and a thickness $L_s = 12$ mm. The prescribed heat flux on the left side (x=0) is $\phi_0 = 4500\ W/m^2$ and on the right side ($x = L_s$) the set boundary condition is a convective heat flux with an exterior temperature $T_{ext} = 293$ K and a convection coefficient $h_{ext} = 10\ W/K/m^2$. The obtained temperature field is plotted in Fig. 2.13 where it is compared to theoretical 1D temperature field. Both curves show an excellent agreement, thus validating the steady heat transfer solver.

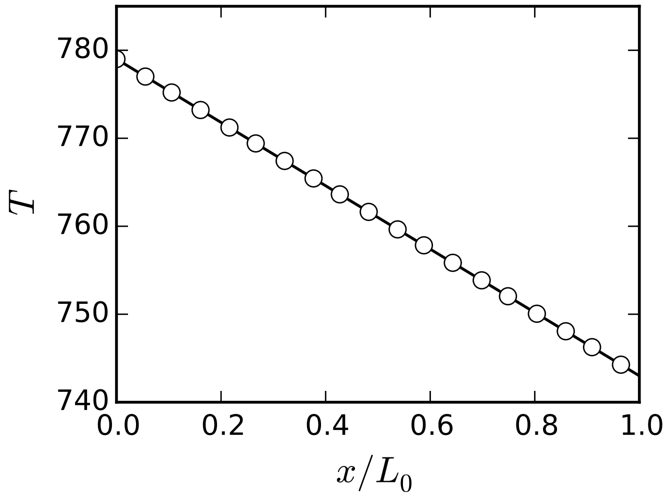

Figure 2.13: *Temperature fields inside a quartz layer of thickness $L_s = 12$ mm, computed by the 3D steady HTS YALES2 solver. Black circles: Theoretical solution. Black plain line: 3D steady HTS solver.*

2.3 Radiation in semi-transparent gases

2.3.1 Radiative Transfer Equation

Thermal radiative transfer is caused by electromagnetic waves and differs from the two other heat transfer modes, convection and conduction: The latter can both be described with partial differential equations obtained with the help of energy balance equations over infinitesimal volumes since these are short-range phenomena. Radiative heat transfer on the other hand, is a long-range phenomenon and the corresponding equations must be solved over the entire considered domain. The different variables used are: three spatial coordinates, two angle coordinates (for the direction of the ray of energy), one spectral variable (frequency) and time.

When considering an energy beam (or ray) of frequency ν with a corresponding radiative intensity I_ν which travels over a distance ds in the direction $\mathbf{s}$, its energy can be modified through three mechanisms, as seen in Fig. 2.14 where such a schematic example is plotted. First of all, energy can be absorbed by the crossed media with an absorption coefficient κ_ν. Second of all, the media can emit energy with the same probability, hence an emission coefficient κ_ν, which can add to the initial radiative intensity. Finally, a part of the initial intensity can be scattered in another direction with a scattering coefficient σ_ν. The obtained Radiative Transfer Equation (RTE) for a media of refractive index n can be written as:

$$\begin{aligned}\frac{d}{ds}(\frac{I_\nu}{n^2}) \quad = \quad & \underbrace{-\kappa_\nu\frac{I_\nu}{n^2} - \sigma_\nu\frac{I_\nu}{n^2}}_{\text{Energy lost by absorption and scattering}} \\ & \underbrace{+\kappa_\nu I_\nu^\circ}_{\text{Energy emitted by the media}} \\ & \underbrace{+\frac{\sigma_\nu}{4\pi n^2}\int_{4\pi} I_\nu(\mathbf{s}_i)\mathbf{\Phi}_\nu(\mathbf{s},\mathbf{s}_i)d\Omega_i}_{\text{Energy received by scattering}} \end{aligned} \tag{2.56}$$

Where $I_\nu(\mathbf{s}_i)$ is the intensity traveling in the direction $\mathbf{s}_i$ and $\mathbf{\Phi}_\nu(\mathbf{s},\mathbf{s}_i)$ is the probability that a ray traveling in the direction $\mathbf{s}_i$ will be scattered to the direction $\mathbf{s}$ inside the considered volume to go in the direction $\mathbf{s}$. A global extinction coefficient β_ν can also be defined in order to simplify the RTE:

$$\beta_\nu = \kappa_\nu + \sigma_\nu \tag{2.57}$$

Once the radiative intensity is known throughout the entire domain, both radiative heat flux, $\mathbf{q}^R$ and radiative volumetric power P^R can be computed. The radiative heat flux first off all, is computed as:

$$\begin{aligned}\mathbf{q}^R &= \int_{\nu=0}^{+\infty} \mathbf{q}_\nu^R d\nu \\ &= \int_{\nu=0}^{+\infty}\int_{4\pi} I_\nu \mathbf{s} d\Omega d\nu \end{aligned} \tag{2.58}$$

and for the volumetric radiative power:

$$P^R = -\nabla\cdot\mathbf{q}^R \tag{2.59}$$

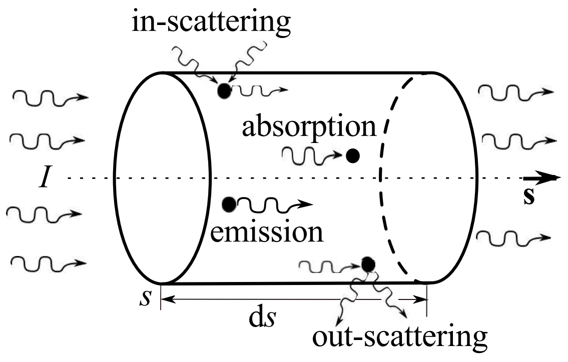

Figure 2.14: *A schematic description of radiation energy evolution over a distance ds. Extracted from Zhang (2013).*

2.3.2 Numerical methods

The numerical code used in this work, Rainier, which is an in-house code of the EM2C laboratory (Refahi (2013), Zhang (2013)) uses the Monte-Carlo statistical method to solve the radiative transfer equation. The approach of using the Monte-Carlo method for the study of radiative transfer was first done by Fleck (1961) and Howell and Perlmutter (1964) who studied radiation heat transfer in participative media. In this approach, large bundles of photons are emitted inside the considered system ($\approx$ 100 000). Each photon progression is tracked until it has no more energy or it leaves the system. The issue with the Monte-Carlo method is that convergence speed of the system follows a $1/\sqrt{N}$-law where N is the number of photon bundles. In Rainier, an emission based reciprocal Monte-Carlo method is used in order to accelerate the convergence of the statistical computation (Zhang (2013)).

2.3.3 1D validation

The one dimensional test case used to validate the Rainier code is that of a parabolic temperature profile such as:

$$T(x) = T_0 + T_1(1 - (x/L)^2) \tag{2.60}$$

where $T_0 = 500K$ and $T_1 = 2000K$. The wall's temperature is set to $T_{wall} = T_0$ and the considered domain is the one for $x \in [-L, L]$ with $L = 5cm$. The walls are considered as black bodies, emissivity $\epsilon_{wall} = 1$. The water vapor mole fraction is $X_{H_2O} = 0.155$ and the CO_2 mole fraction is taken as $X_{CO_2} = 0.116$. The scattering coefficient σ_ν and absorption coefficient κ_ν are tabulated as a function of pressure and temperature (Zhang (2013)).

The radiative power is computed over the entire domain and is plotted in Fig. 2.15 alongside the analytical solution for the radiative power for comparison, and the temperature field in the 1D domain. The numerical results show a very satisfying agreement between the analytical and numerical radiative power fields while using 1000 rays per cell which is sufficient for 1D cases. Hence, the statistical Monte-Carlo based solver is considered validated and capable of correctly resolving the radiative transfer equation.

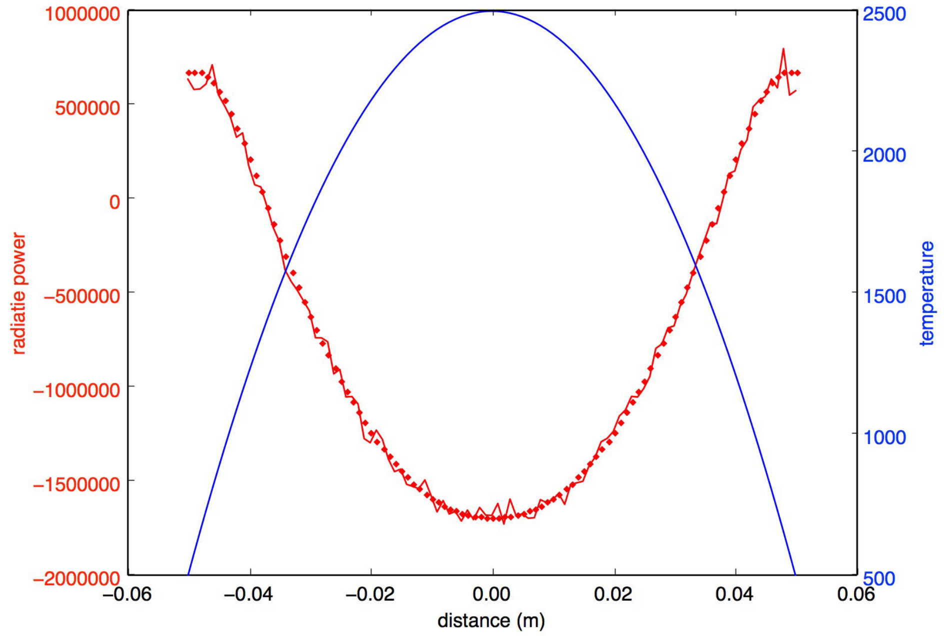

Figure 2.15: *One dimensional fields for the 1D test case. Blue line: Imposed temperature profile. Red diamonds: Analytical radiative power field. Red line: Numerical solution obtained with the Monte-Carlo solver Rainier.*

2.4 Coupling: OpenPALM coupler

The coupling between codes done during this work has been achieved through the use of the OpenPALM coupler (Duchaine et al. (2015)). The coupler is codeveloped by the CERFACS and ONERA organisations. It combines three elements: PALM, CWIPI and PrePALM.

The PALM library is the one in charge of the parallel communications and launching of the different applications. It serves as the interface between the coupled codes: each code sends its data to the palm application which then dispatches the information (Buis et al. (2006)).

The CWIPI library is a parallel communication and interpolation tool. It allows for mesh interpolation when the meshes used by the different codes are not conforming (Refloch et al. (2011)). The communication graph created by CWIPI is optimized for High Performance Computing application by minimizing the global cost of the parallel communications. Very high scalability was found by using these tools with up to 10 000 cores (Duchaine et al. (2015)).

The last piece of the puzzle is the PrePALM Graphical User Interface (GUI). It allows for an easy creation of the communications and links between the different codes. An example of a coupling done with the PrePALM GUI is given in Fig. 2.16 for a multi physical configuration involving reacting flows, gases radiation and heat transfer in solids.

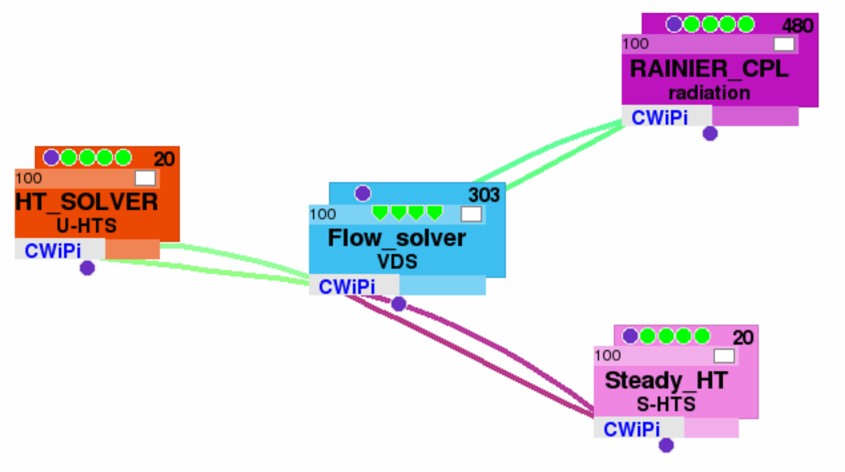

Figure 2.16: *An example of an OpenPALM canvas extracted from the GUI for a multiphyiscal simulation accounting for turbulent reactive flows, radiation and heat transfer inside the walls. The lines represent the communications between the different solvers: Orange: Unsteady heat transfer solver. Blue: Reactive flow solver. Pink: Steady heat transfer solver. Purple: Radiation solver.*

OpenPALM also has the advantage of allowing for generic communications. Since the information is sent to the palm application and not to a specific code, the modifications introduced to the different codes source files are minimal and are only done once. These changes do not depend on the partnering code(s), only the data to send/receive is different. All of these different reasons are what motivated the choice of OpenPALM as the coupling tool.

2.5 Conclusion

In this chapter, the different numerical tools used during this thesis work have been presented. The different elements were validated using analytical or experimental data: Reactive flow solver, flame thickening, steady and unsteady heat transfer in solids solvers as well as the gas radiation solver. This validation served a double purpose: first of all, to understand each numerical tool, and secondly to ensure that each tool alone is efficient and accurate before combining several, or all, of them for multi-physics simulations.

Chapter 3

Coupling procedures for conjugate heat transfer

3.1 State of the art: Numerical methods for multi physics simulations 46
3.1.1 One code to solve them all or divide and conquer? 46
3.1.2 Existing coupling methods for CHT 48
3.1.3 Goals: What is left to improve 54
3.2 Considered coupling boundary conditions . . 54
3.2.1 Coupling boundary conditions 54
3.2.2 Neumann - Dirichlet 55
3.2.3 Neumann - Neumann 60
3.2.4 Dirichlet - Dirichlet 63
3.3 Hybrid cell interface model for updating the boundary temperature 64
3.3.1 Updating procedure for the boundary temperature 66
3.3.2 Adequacy of the model 66
3.3.3 1D test of the hybrid cell: Method of Manufactured Solutions 71
3.4 Conclusion 74

In this chapter, a state of the art for coupling methods for Conjugate Heat Transfer is presented. The different approaches strengths and weaknesses are discussed before choosing a coupling method.

3.1 State of the art: Numerical methods for multi physics simulations

3.1.1 One code to solve them all or divide and conquer?

When one wishes to deal with several physical phenomena at the same time, the complexity of the necessary numerical tools increases. The reason is that each phenomenon requires at least one mathematical equation and that these equations have different mathematical properties. The heat equation for example is a parabolic equation. It is also linear if λ, ρ and c_p dependance on the temperature can be neglected:

$$\rho c_p \frac{\partial T}{\partial t} = -\nabla \cdot (-\lambda \nabla T) + S_T \tag{3.1}$$

The Navier-Stokes equations are of parabolic and hyperbolic nature, and present a large range of temporal and spatial scales in turbulent flows:

$$\frac{\partial \rho \mathbf{u}}{\partial t} + \nabla \cdot (\rho \mathbf{u} \otimes \mathbf{u}) = \nabla p + \nabla \cdot \tau + \rho \mathbf{g} \tag{3.2}$$

While the Radiative Transfer Equation is an Integro-Differential equation which has to be resolved implicitly:

$$\frac{d}{ds}\left(\frac{L'_\nu}{n^2}\right) + \beta_\nu \frac{L'_\nu}{n^2} = \kappa_\nu L^\circ_\nu(T) + \frac{\sigma_\nu}{4\pi n^2}\int_0^{4\pi} \mathbf{\Phi}_\nu L'_\nu d\Omega \tag{3.3}$$

These differences are the reason why the numerical methods used for the resolution of these different equations are not the same. The heat equation is a transport equation without any coupling with another field like the velocity in fluids. Thanks to its parabolic nature it can be solved either explicitly or implicitly (Hairer et al. (2008)).

On the other hand, the Navier-Stokes set of equations is more complexe since it involves the coupling between several equations and variables: energy, velocity and pressure. This coupling, which is non-linear, makes implicit solvers difficult to create while enforcing the conservation laws, thus rendering explicit solvers more suitable. The Radiative Transfer Equation which is an implicit equation by nature require specific methods for its resolution like Discrete Ordinate Method, Ray-tracing method or a statistical Monte-Carlo method.

Therefore, one of the first questions to answer is what is the best solution: to solve all the different equations at once while ensuring the coupling between the different physical equations, or, to use different solvers for each equation, which are then coupled afterwards in order to ensure the physics' coherence.

The first approach ensures the continuity of all variables and is usually used for DNS computations such as those done by Tiselj et al. (2001), Tiselj and Cizelj (2012),Tiselj et al. (2013), Flageul et al. (2015) and Nordstrom and Berg (2013). These examples are valid for conjugate heat transfer. Yet, using one code has a few drawbacks. First of all, as mentioned just above, different equations may require different numerical methods. It can become quite difficult to implement all of these methods in one code and to solve all of them together in an efficient way.

Secondly, the configurations to be studied are unsteady, adding to the global complexity. The unsteady nature leads to another issue: the different phenomena have different time scales. When comparing the heat conduction in a wall with a reactive flow, the former's time scale is easily two to three orders of magnitude higher than the latter's. Hence, solving both equations at once, implies using the same integration time step which is limited by the fastest physics. Doing so in the flow-wall interaction means using integration time steps much smaller than needed for the wall and thus leading to a waste of computational resources by the solid wall solver.

Because of that, the usually most efficient approach is to use code coupling. Each phenomenon is dealt with a specific numerical code, in which optimized numerical methods are implemented. The different integration time steps are independent and can be different in each code. Conjugate heat transfer coupled simulations were done by Chemin (2006), Radenac (2006), He and Oldfield (2011) where a flow solver is coupled to a wall heat transfer solver. The coupling between gases radiation and turbulent flows was done by Tessé et al. (2004), Wu et al. (2005), Santos et al. (2008), Dorey et al. (2011), Zhang et al. (2013) and a full coupling also including the heat transfer inside the wall was done by Amaya (2010), Berger et al. (2015). An advantage of doing so, is that if at some point a better tool is available for a certain phenomenon, it can replace the existing one in the coupling loop without having to modify the other numerical codes.

To ensure the coherence of the physical problem, the different codes are coupled on a regular basis. Every coupling time step, Δt_{cpl}, the codes exchange information needed for the closure of the inner physics problems: Flow equations, heat transfer, gases radiation, etc...

The difficulty resides in determining the optimal frequency of exchange. This optimal exchange frequency, is a compromise between computational cost since the more often data is sent, the more expensive the whole simulation is, and the need for precision, since the more often exchanges happen the more precise the simulation. Other difficulties reside in choosing correctly the data to send, or in other words, the coupling between the different codes. In some cases, depending on the order of the exchange, the coupling can be unstable (Giles (1997)).

Therefore the possible gain of a code coupling approach is higher than that of a single code, but different challenges are to be tackled. That is why it was chosen for the work done in this thesis.

3.1.2 Existing coupling methods for CHT

Conjugate Heat Transfer is the study of heat transfer between a flow and a wall. The interface causes a jump in thermo-physical properties, but the temperature remains a continuous function through it. Similarly, the principle of energy conservation implies that the heat flux is also continuous. Two constraints exist then, and at each moment, the following equalities must be true:

$$T_{f,bnd} = T_{s,bnd} \tag{3.4}$$

where $T_{f,bnd}$ (respectively $T_{s,bnd}$) represents the fluid (respectively solid) boundary temperature. And:

$$-\lambda_f \frac{\partial T_f}{\partial n} \cdot \mathbf{n}_{ext,f} = -\lambda_s \frac{\partial T_s}{\partial n} \cdot \mathbf{n}_{ext,s} \tag{3.5}$$

where $\dfrac{\partial T_f}{\partial n}$ (respectively $\dfrac{\partial T_s}{\partial n}$) represents the fluid (respectively solid) boundary temperature normal gradient. In the following subsections the different parameters defining a coupling method are discussed.

3.1.2.1 Weak or strong coupling

A multi-physics coupling between two codes can be defined as weak or strong. The definition depends on the way the continuity relations are imposed at the fluid-solid interface.

- *Strong coupling*: Strong coupling corresponds to a strict numerical coupling: During a coupling iteration each code advances and then the boundary temperature and heat flux are exchanged. The values of both are compared at the end of the iteration, and the solution is considered as converged if both temperature and heat flux values obtained by the two codes at the end of the iteration are the same. If this convergence is not attained a new iteration is computed with the same initial temperature fields but with different boundary conditions on the fluid-solid interface and that until convergence is achieved. This process is done with the help of a fixed-point type algorithm. This approach leads to a continuity of the boundary temperature and a strict energy conservation through the fluid-solid interface. Nevertheless, the overhead in numerical cost is important, since coupling steps are rejected until the boundary conditions converge, rendering the method uninteresting for 3D unsteady reactive computations. The main examples for this approach are mostly available in 1D and 2D: Birken et al. (2010), Geiser and Güttel (2012) and Lindstrom and Nordstrom (2010)

- *Weak coupling*: The weak coupling approach operates just like the strong coupling approach in terms of boundary conditions used for the coupling. The difference lies in the fact that once the coupling iteration is over, no convergence criteria is computed, and the obtained temperature fields are kept. The interface coupling boundary conditions are then updated using the output of the other code, and a new coupling iteration is started. For example, the temperature used by the flow solver during an entire coupling iteration is equal to the wall's temperature at the end of the former coupling iteration. Example of such weak couplings are available in the conjugate heat transfer studies done by Chemin (2006), Radenac (2006), He and Oldfield (2011) and Berger et al. (2015)

Weak coupling appears to be the most adequate of the two for 3D reactive simulations accounting for combustion. Thus the algorithms discussed hereafter will only be weak couplings.

3.1.2.2 Steady and Unsteady coupling

A question which arises when studying an unsteady conjugate heat transfer problem, is what information is sought: Mean values ? Root-mean-square values ? Instantaneous fields ? According to the answer, the tools used might be different.

When the only information sought is the steady state fields in the fluid and wall, an unsteady flow solver can be coupled to a steady wall heat transfer solver. Such an approximation is possible if the flow's boundary conditions do not change over time. In that case, the resulting temperature field will be equal to the mean steady field: Chemin (2006), Errera and Chemin (2013).
The limitation of such an approach is that it is only suitable for laminar flows with an unsteady flow solver, or with a RANS solver which solves the Reynolds averaged Navier-Stokes equations, thus granting access to the mean fields only. In more complex configurations such as combustion chambers, this approach is not applicable: a reactive flow inside a combustion chamber is often a turbulent unsteady flow which induces an unsteady behavior inside the walls and hence requiring unsteady tools to be studied.

An opposite approach also exists, where an unsteady wall heat transfer solver is coupled with steady flow states. The steady flow solver is first converged and then sends a heat flux to the solid solver. The unsteady evolution of the wall is then computed between times $t = t_n$ and $t = t_{n+1}$. Together, theses steps represent a coupling step. The resulting algorithm allows for a transient computation of the wall temperature field over time Errera and Baque (2013), Baque et al. (2013), Baqué (2012).

In other cases, the full transient evolution of the fluid-solid configuration is to be studied. To do so, both the fluid and solid are simulated using unsteady solvers. By coupling two unsteady solvers the fully unsteady characteristics of the flow and/or wall can be captured. Mean and fluctuating components can be computed and the minimal and maximal values can be retrieved. Examples of such works is available in: Duchaine et al. (2009), Duchaine et al. (2013), He (2013), Radenac et al. (2014), Kazemi-Kamyab et al. (2013), Roe et al. (2008) who studied the conjugate heat transfer using unsteady solvers for aeronautical applications. Amaya et al. (2010) and Berger et al. (2015) added the gas radiation phenomenon to the multi-physics configuration in a helicopter engine using LES and Discrete Ordinate Method for the radiation.
As knowing the level of fluctuations is important in order to conduct fatigue studies on the materials, full unsteady coupling are best suited for combustion applications.

3.1.2.3 Synchronization of the solvers

If a fully unsteady coupling is used, an issue which arises is how to best synchronize the different solvers. In which order should they advance? What is the optimal coupling in terms of time "lost" by coupling instead of computing? To answer these questions, it is necessary to study the different existing coupling schemes.

To fully define a coupling procedure, one should choose between a staggered (or sequential) coupling and a parallel coupling. Both coupling schemes are explained in the following paragraphs with the help of a Neumann-Dirichlet coupling, and unsteady solvers. A coupling step, of size Δt_{cpl}, is computed by each numerical resolution code. Yet, each code also has its own time step, linked to thermo-physical properties of the medium considered and the numerical methods and discretization used. The flow solver computes N_f steps while the wall solver computes N_s steps. Thus leading to the following relation:

$$\Delta t_{cpl} = N_f \Delta t_f = N_s \Delta t_s \tag{3.6}$$

Staggered scheme

The staggered scheme is so called because the two codes are not running at the same time (Fig. 3.1). At every instant, only one code is advancing. If code A is advancing, once it has finished, it computes the boundary condition needed for its partner, code B, and then sends it. Once the information is sent, code A goes into a standby mode where it waits that code B advances on its turn and sends a new boundary condition.

For unsteady simulations such a scheme is too inefficient. As explained above, while one code advances, the other one is in standby mode. The created situations is such that at every instant the cores used by one code are not doing anything, thus leading to a great waste of computational ressources, and hence a parallel coupling scheme is needed in order a achieve optimal performances.

Parallel coupling

To answer the need expressed in the previous paragraph, a parallel scheme is used. This time, both codes advance at the same time (Fig. 3.2). Two coupling points are separated by a time defined as Δt_{cpl}, the coupling time step. Each code advances over that same period. Once each code

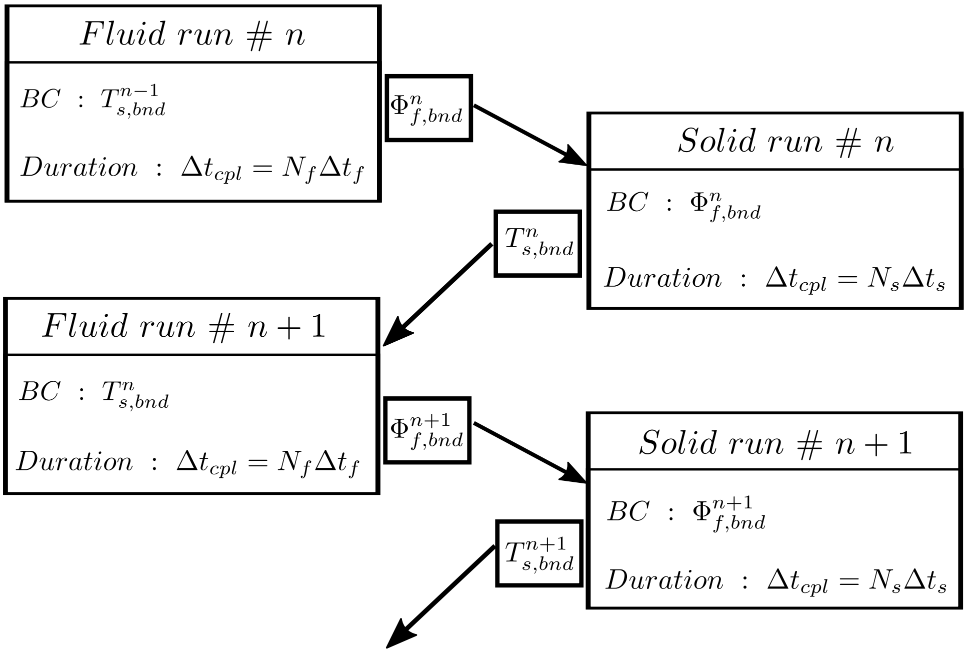
Fluid run # n
BC : $T^{n-1}_{s,bnd}$
Duration : $\Delta t_{cpl} = N_f \Delta t_f$
$\Phi^n_{f,bnd}$
Solid run # n
BC : $\Phi^n_{f,bnd}$
Duration : $\Delta t_{cpl} = N_s \Delta t_s$
$T^n_{s,bnd}$
Fluid run # n + 1
BC : $T^n_{s,bnd}$
Duration : $\Delta t_{cpl} = N_f \Delta t_f$
$\Phi^{n+1}_{f,bnd}$
Solid run # n + 1
BC : $\Phi^{n+1}_{f,bnd}$
Duration : $\Delta t_{cpl} = N_s \Delta t_s$
$T^{n+1}_{s,bnd}$

Figure 3.1: *Sequential coupling procedure for conjugate heat transfer. Adapted from Duchaine et al. (2009)*

has computed a time equal to Δt_{cpl}, both codes exchange the needed data on the shared boundary.
The parallel scheme requires for optimal performances, to synchronize the solvers in computational time in order to reduce as much as possible the time wasted by a code waiting for the other. This means dividing the available cores in a fashion that the computational time needed to simulate a coupling time step is the same for both codes.

An estimation can be made, if perfect scaling is assumed. Noting C_N^P the computational time of N steps using P cores:

$$C_N^P = \frac{C_N^{ref}}{P} \tag{3.7}$$

By estimating the value of the reference computational time C_N^{ref} of each code, and knowing that perfect synchronizing leads to:

$$C_{N_f,f}^{P_f} = C_{N_s,s}^{P_s} \tag{3.8}$$

The ratio between the number of CPU-cores allocated to the flow solver

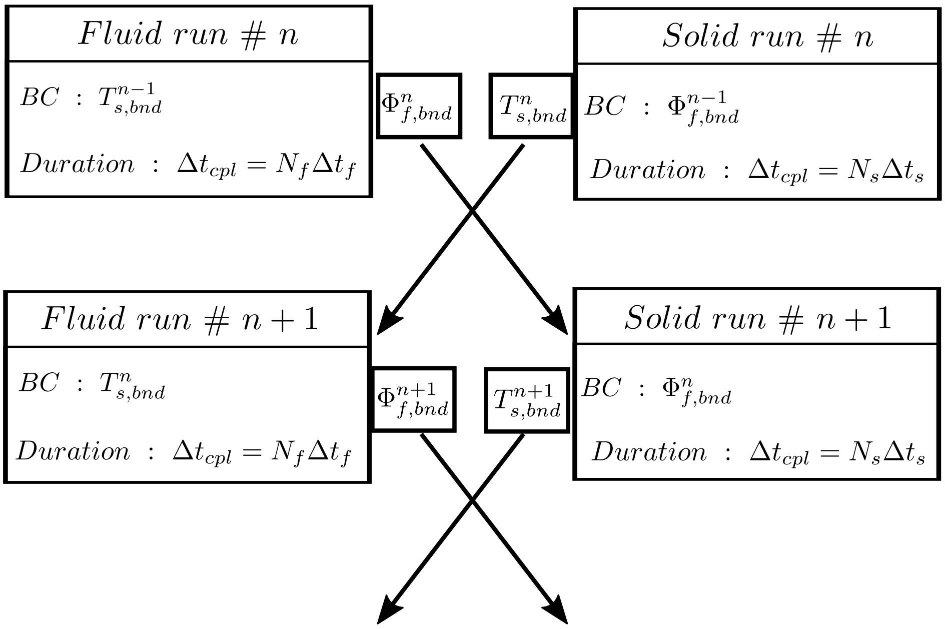
$Fluid\ run\ \#\ n$
$BC\ :\ T^{n-1}_{s,bnd}$
$Duration\ :\ \Delta t_{cpl} = N_f \Delta t_f$
$\Phi^{n}_{f,bnd}$
$T^{n}_{s,bnd}$
$Solid\ run\ \#\ n$
$BC\ :\ \Phi^{n-1}_{f,bnd}$
$Duration\ :\ \Delta t_{cpl} = N_s \Delta t_s$
$Fluid\ run\ \#\ n+1$
$BC\ :\ T^{n}_{s,bnd}$
$Duration\ :\ \Delta t_{cpl} = N_f \Delta t_f$
$\Phi^{n+1}_{f,bnd}$
$T^{n+1}_{s,bnd}$
$Solid\ run\ \#\ n+1$
$BC\ :\ \Phi^{n}_{f,bnd}$
$Duration\ :\ \Delta t_{cpl} = N_s \Delta t_s$

Figure 3.2: *Parallel coupling procedure for conjugate heat transfer. Adapted from Duchaine et al. (2009)*

P_f and the number allocated to the wall solver P_s can be computed:

$$\frac{P_f}{P_s} = \frac{C^{ref}_{N_f,f}}{C^{ref}_{N_s,s}} \tag{3.9}$$

Since it is the flow solver which represents the largest share of the computational cost, it is wise to make sure that it never has to wait for the solid solver. Hence, the value for the ratio given just-above is taken as slightly larger than the optimal value so that it is always the solid solver which finishes first to compute the coupling step.

Using parallel coupling also requires special attention on the boundary conditions exchanged, in order to ensure the conservation of energy and the continuity of the temperature field through the interface. Radenac (2006) showed that the parallel algorithm creates an energy deficit at the interface due to the wall heat flux mismatch of the two solvers during a coupling iteration. Similarly Δt_{cpl} is an important parameter, since it has a direct influence both on the stability of the coupled configuration and on the precision of the computation. In the available studies, its value is chosen in an arbitrary way, and when the validity is verified, it is done *a posteriori* such as in the work by Jauré (2012).

3.1.3 Goals: What is left to improve

The study conducted here above showed that when combining all the different possibilities, a number of coupling procedures exist. Since the goal of this thesis is to study unsteady turbulent reactive flows, the number of options is reduced. For all of the reasons mentioned previously, from here on, only the **weak** coupling of two (or more) **unsteady** solvers will be considered with **parallel** coupling. A degree of freedom still exists concerning the coupling boundary conditions. It will be the subject of the next section.

The goal of this work concerning coupled simulations of conjugate heat transfer, is to develop a coupling methodology where:

- The coupling methodology is of a parallel nature, in order to optimize the computational efficiency of the numerical tool and to reduce the cost of the coupling between the different numerical resolution solvers.
- The continuity of temperature and heat flux between the two media is to be ensured at every step in order to respect the physical condition of temperature continuity through the fluid-solid interface
- Similarly, the conservation of energy over a coupling step is to be ensured by the methodology
- The methodology should provide a way of determining the value of the coupling time step Δt_{cpl}

The development of this methodology will be the heart of the rest of this chapter, as well as for chapters 4 and 5.

3.2 Considered coupling boundary conditions

3.2.1 Coupling boundary conditions

Since temperature and heat flux are not to have jump conditions through the boundary in order to respect the physics of the conjugate heat transfer configuration, two "natural" boundary conditions emerge. These two conditions are the Neumann and Dirichlet conditions, which leads to 3 different possible couplings:

- Neumann - Dirichlet coupling: One code uses a prescribed heat flux while the seconds is using a prescribed temperature boundary condition
- Dirichlet - Dirichlet coupling: Both codes use a prescribed temperature boundary condition
- Neumann - Neumann coupling: Both codes use a prescribed heat flux boundary condition

A third boundary condition exists, it is the Robin boundary condition. It is a mix of the two other boundary conditions:

$$\text{Robin's BC: } a \cdot \boldsymbol{\phi}_{bnd} \cdot \mathbf{n}_{ext} + hT_{bnd} \tag{3.10}$$

In some cases it is used instead of the Neumann boundary condition in order to improve the stability and/or speed of convergence of certains numerical schemes Chemin (2006), Duchaine et al. (2009).
The three couplings, Neumann-Dirichlet, Dirichlet-Dirichlet and Neumann-Neumann are presented more thoroughly in the following subsections. In this section, the best choice of the coupling boundary conditions is discussed. The three coupling options, Neumann-Dirichlet, Neumann-Neumann and Dirichlet-Dirichlet are all considered, and their adequacy with the goals set in the previous section is tested.

3.2.2 Neumann - Dirichlet

The Neumann-Dirichlet coupling is what may seem as the most natural combination, since both temperature and heat flux need to be continuous through the fluid/wall interface. In this configuration one code uses a prescribed temperature while the other uses a prescribed heat flux (As in Fig. 3.1). Giles (1997) showed that for such a coupling to be numerically stable, it is the flow which needs to send the heat flux to the wall, while using the wall's boundary temperature as a boundary condition. Otherwise, numerical instabilities will be amplified leading to an overshoot of the temperature

$$T_{f,bnd}(t) = T_{s,bnd}(t_n),\ \forall t \in [t_n, t_{n+1}] \tag{3.11}$$

$$\phi_{s,bnd}(t) = \phi_{f,bnd}(t_n),\ \forall t \in [t_n, t_{n+1}] \tag{3.12}$$

Extensive work conducted on this kind of coupling, which is currently the most widely used, is available: Duchaine et al. (2009), Amaya et al. (2010), Jaure et al. (2013) used it for the simulation of aeronautical applications, Errera and Chemin (2013) studied the optimal value of the Robin boundary condition coefficients when coupled with a Dirichlet boundary condition in terms of stability, and Radenac et al. (2014) studied the energy conservation of such a problem and proposed an energy correction methodology.

The first studies tried several values of coupling time steps, and selected the largest which showed similar results to the lowest value. The current trend is to increase the coupling frequency in order to increase the accuracy and to alleviate the problem of the coupling frequency as in the work of Jaure et al. (2013), Jauré (2012) concerning the conjugate heat transfer inside aeronautical combustion chambers.

During this thesis work, an attempt was made in trying to evaluate the optimal coupling time step using the operator splitting theory. Examples of use of this framework are available in Marchuk (1968), Oran and Boris (2001), Schwer et al. (2003) and Duarte (2011). Considering Eq. 3.1, it can be written under the following formulation, when considering constant values for ρ and c_p, and in one dimension:

$$\frac{\partial T}{\partial t} = D_x(T) \tag{3.13}$$

Where D_x is the discrete diffusion operator.

General splitting framework

Considering that same problem in the semi-discrete space, for spatial distcretization, leads to a time evolutionary problem for the domain temperature:

$$\frac{dT}{dt} = D_x(T) \tag{3.14}$$

Considering D_x matrix operator form, $\mathcal{D}_x$, the latter can be separated into two independent discrete diffusion operators, $\mathcal{F}_x$ for the fluid domain and $\mathcal{S}_x$ for the solid domain such as:

$$\mathcal{D}_x = \mathcal{F}_x + \mathcal{S}_x \tag{3.15}$$

Equation 3.1 can then be considered under its split formulation with the matrice representations of the different space operators, where $\mathcal{T}$ represents the temperature vector over all space:

$$\frac{d}{dt}\mathcal{T} = \mathcal{F}_x\mathcal{T} + \mathcal{S}_x\mathcal{T} \tag{3.16}$$

Equation 3.16 can be solved analytically, leading to the following solution:

$$\mathcal{T}(t) = e^{t(\mathcal{F}_x+\mathcal{S}_x)}\mathcal{T}_0 \tag{3.17}$$

Where T_0 is the initial value of T at $t = 0$. In order to reduce the computational cost when numerical methods are used, it is possible to solve the full system by considering a succession of different sub-problems. If the full equation is to be advanced by Δt, then the two following equations are to be solved for a first order Lie splitting. First the contribution of the $\mathcal{F}_x$ operator is accounted for, by solving the following equation:

$$\begin{cases} \dfrac{d}{dt}\mathcal{T}^* & = & \mathcal{F}_x\mathcal{T}^* \\ \mathcal{T}^*(t = t_n) & = & \mathcal{T}(t_n) \end{cases} \tag{3.18}$$

Then, the contribution of the second operator, $\mathcal{S}_x$, is accounted for:

$$\begin{cases} \dfrac{d}{dt}\mathcal{T} & = & \mathcal{S}_x\mathcal{T} \\ \mathcal{T}(t = t_n) & = & \mathcal{T}^*(t_n + \Delta t) \end{cases} \tag{3.19}$$

Where $\mathcal{T}^*$ is an intermediate solution used as a mid step prediction. Thus leading to the following analytical solution:

$$\mathcal{T}(t_n + \Delta t) = e^{\Delta t\mathcal{S}_x}e^{\Delta t\mathcal{F}_x}\mathcal{T}(t_n) \tag{3.20}$$

Numerical analysis of split integration scheme of order 1 and 2, leads to knowing that the error expansion depends on the commutator of $\mathcal{F}_x$ and $\mathcal{S}_x$, $[\mathcal{F}_x, \mathcal{S}_x]$, defined as:

$$[\mathcal{F}_x, \mathcal{S}_x] = \mathcal{F}_x\mathcal{S}_x - \mathcal{S}_x\mathcal{F}_x \tag{3.21}$$

Hence, if the two operators $\mathcal{F}_x$ and $\mathcal{S}_x$ commute, there is no splitting error, and otherwise, if $[\mathcal{F}_x, \mathcal{S}_x]$ is known, the splitting error can be computed.

Applying the splitting framework to a Neumann-Dirichlet coupling

To be applied to the conjugate heat transfer, the coupled problem need to be rewritten. By considering a space-splitting, and considering the temperature field over the entire domain:

$$\mathcal{T}_{tot} = \begin{pmatrix} \mathcal{T}_f \\ \mathcal{T}_s \end{pmatrix} \tag{3.22}$$

Considering that the $\mathcal{T}_{tot}$ verifies the following diffusion equation where $\mathcal{D}_{th}$ is the diffusion operator:

$$\frac{d}{dt}\mathcal{T}_{tot} = \mathcal{D}_{th}\mathcal{T}_{tot} \tag{3.23}$$

Where:

$$\mathcal{D}_{th} = \mathcal{D}_f + \mathcal{D}_s + \mathcal{D}_{cpl} \tag{3.24}$$

$$\mathcal{D}_f = \begin{pmatrix} a_f\Delta_x^{num} & 0 \\ 0 & 0 \end{pmatrix} \tag{3.25}$$

$$\mathcal{D}_s = \begin{pmatrix} 0 & 0 \\ 0 & a_s\Delta_x^{num} \end{pmatrix} \tag{3.26}$$

$\mathcal{D}_f$ and $\mathcal{D}_s$ are the inner diffusion operators, which update only the interior points of each domain. Δ_x^{num} is the second order space derivative operator. As it can be seen $\mathcal{D}_f$ and $\mathcal{D}_s$ commute. But these are not the full operators needed for the temperature's evolution. The $\mathcal{D}_{cpl}$ operator is the one which allows the coupling, and holds the overlapping terms:

$$\mathcal{D}_{cpl} = \begin{pmatrix} 0 & \mathcal{T}_{f,bnd}^{update} \\ -\lambda_f\nabla_{x,bnd}^{num} & 0 \end{pmatrix} \tag{3.27}$$

where $-\lambda_f\nabla_{x,bnd}^{num}$ is the operator which provides the fluid heat flux necessary for the solid energy balance equation at the interface (∇_x^{num} is the first order space derivative operator). $\mathcal{T}_{f,bnd}^{update}$ is fluid update operator which at every coupling updates the fluid boundary temperature, such a $T_{f,bnd}(t) = T_{s,bnd}(t_n)$, $\forall t \in [t_n, t_{n+1}]$. Hence, the full coupled diffusion operators can be written as:

$$\mathcal{D}_s^{cpl} = \begin{pmatrix} 0 & 0 \\ \\ -\lambda_f \nabla_{x,bnd}^{num} & a_s \Delta_x^{num} \end{pmatrix} \tag{3.28}$$

and:

$$\mathcal{D}_f^{cpl} = \begin{pmatrix} a_f \Delta_x^{num} & \mathcal{T}_{f,bnd}^{update} \\ \\ 0 & 0 \end{pmatrix} \tag{3.29}$$

Thus leading to the following expression of the coupled problem as a splitting problem, when integrating between t_n and $t_{n+1} = t_n \Delta t_{cpl}$:

$$\frac{d}{dt}\mathcal{T}_{tot} = (\mathcal{D}_f^{cpl} + \mathcal{D}_s^{cpl})\mathcal{T}_{tot} \tag{3.30}$$

leading to the following comutator:

$$[\mathcal{D}_f^{cpl}, \mathcal{D}_s^{cpl}] = \begin{pmatrix} -\mathcal{T}_{f,bnd}^{update} \lambda_f \nabla_x^{num} & \mathcal{T}_{f,bnd}^{update} a_s \Delta_x^{num} \\ \\ -\lambda_f \nabla_{x,bnd}^{num} a_f \Delta_x^{num} & -\lambda_f \nabla_{x,bnd}^{num} \mathcal{T}_{f,bnd}^{update} \end{pmatrix} \tag{3.31}$$

The commutator is nearly never equal to zero which leads to a non zero splitting error of order 1 (Duarte (2011)). It is also important to note that the operators $\mathcal{T}_{f,bnd}^{update}$ and $\lambda_f \nabla_{x,bnd}^{num}$ only use the boundary temperature by the former and the boundary temperature and its nearest neighbour(s) by the latter.

Computing the splitting error can be used as a way of estimating the optimal coupling time step to use (Duarte (2011)). This approach is limited by the fact that the splitting formalism corresponds to a sequential coupling and not a parallel one, since in the splitting scheme, the operators are solved one after another. For the sake of optimizing the computational efficiency, parallel coupling should be used, rendering the above results unsuitable.

For a parallel coupling scheme, both operators are solved independently at the same time, which means that the numerical solution obtained is a sum of both diffusive contributions and not a succession of the two operators. This formula cannot use the splitting results, since it is no longer a multiplication of operators. Therefore, a simple approximation of the coupling error through the use of the operator-splitting framework is not possible, and a roadblock is reached. Because of the need of parallel coupling, it was decided to give up on the Neumann-Dirichlet coupling in favor of trying to attain the goals of section 3.1.3 by using other coupling boundary conditions.

3.2.3 Neumann - Neumann

A Neumann-Neumann coupling signifies that each codes is using a prescribed heat flux as a boundary condition on the interface. The main advantage of such a coupling is that the conservation of energy is forced no matter what, since:

$$\phi_{bnd,f} = \phi_{bnd,s}, \ \forall t \tag{3.32}$$

The value of the boundary flux is computed with the help of the temperatures of fluid and solid near the interface. In a numerical case, the values used are taken from the two cells neighboring the boundary (Fig. 3.3). By noting T_{bnd} and ϕ_{bnd} the boundary temperature and heat flux, the continuity of the temperature ensures that T_{bnd} is the same on both side of the interface.

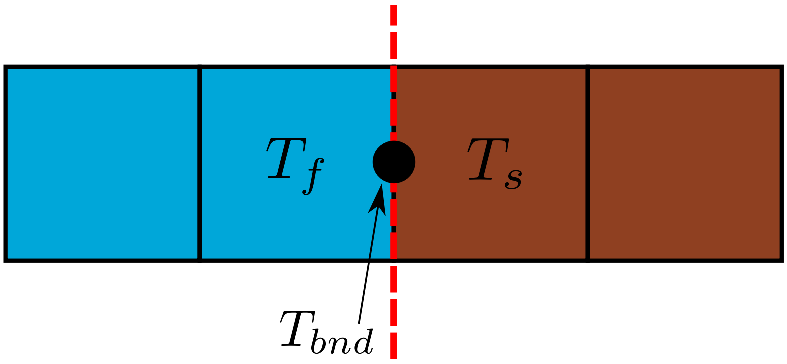

Figure 3.3: *1D configuration of flow-wall boundary. Blue cells on the left: Flow domain. Brown cells on the right: Wall domain.*

When considering a first order approximation of the heat flux in one dimension, the continuity of the heat flux leads to the following equation:

$$\frac{\lambda_f}{\Delta x_f}(T_{bnd} - T_f) = \frac{\lambda_s}{\Delta x_s}(T_s - T_{bnd}) \tag{3.33}$$

for the sake of simplicity only the first order formula is used in this example. Higher order approximation of the temperature gradient can be used in order to increase the spatial accuracy if needed. The value of the boundary temperature can then be retrieved:

$$T_{bnd} = \frac{\dfrac{\lambda_f}{\Delta x_f} T_f + \dfrac{\lambda_s}{\Delta x_s} T_s}{\dfrac{\lambda_f}{\Delta x_f} + \dfrac{\lambda_s}{\Delta x_s}} \tag{3.34}$$

Injecting this expression of T_{bnd} into one of the expressions of the heat flux in Eq. 3.33, then leads to:

$$\phi_{bnd} = -\left(\frac{\lambda_f}{\Delta x_f} \frac{\lambda_s}{\Delta x_s} \right) \frac{T_s - T_f}{\dfrac{\lambda_f}{\Delta x_f} + \dfrac{\lambda_s}{\Delta x_s}} \tag{3.35}$$

Which can be simplified into:

$$\phi_{bnd} = -\frac{T_s - T_f}{\dfrac{\Delta x_s}{\lambda_s} + \dfrac{\Delta x_f}{\lambda_f}} \tag{3.36}$$

Using the expression from Eq. 3.36, the value of the interface heat flux can be computed at every instant if thermal conductivities and temperature are known inside each of the interface's neighboring cells. The boundary flux thus evolves naturally during a coupling iteration.

A danger exists when using such coupling. If the size of the coupling time step taken is too large, the temperature fields in both media might evolve in an unnatural fashion. Studying the case of Fig. 3.4, also studied in Radenac (2006), where each domain has a different temperature is an interesting example.

Each domain has an initial temperature which is different, thus leading to a near infinite initial heat flux. Figure 3.5 shows the temperature field over the entire domain after one coupling step which is too large. It is possible to see that when Δt_{cpl} is too large, the predicted boundary temperatures are too far away from each other. This results in an overshot estimation of the interface wall heat flux which will then end in an instability. The coupled computation will then enter an oscillatory state which will never converge towards the correct state.

It can be explained by the fact that on an extreme case such as this, the boundary flux changes quite fast, as can be seen in Fig. 3.6. Therefore

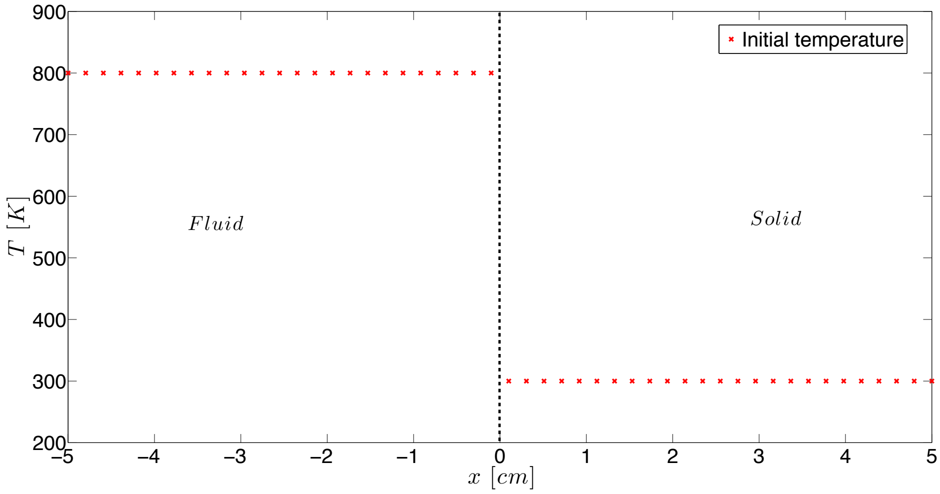

Figure 3.4: *Initial temperature field over a fluid-solid domain. Dashed line stands for the boundary. Left side is the fluid's side and the wall is on the right.*

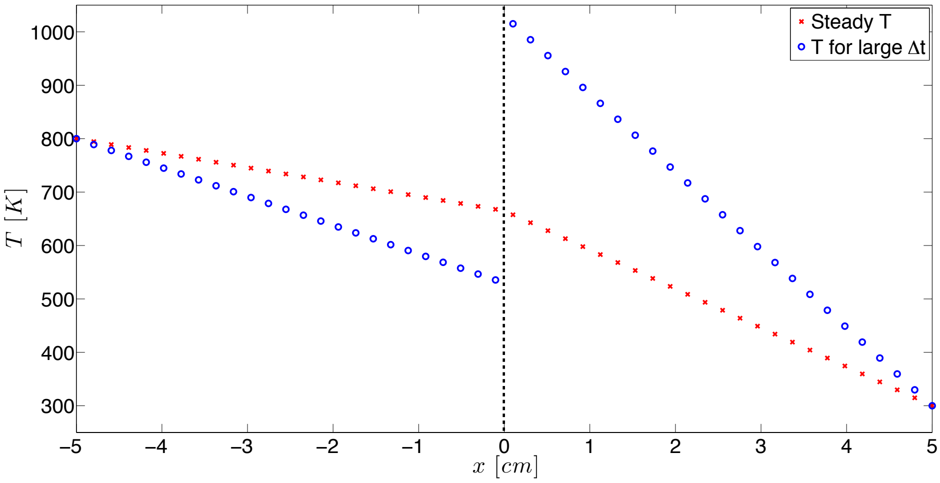

Figure 3.5: *Red cross: steady state temperature which should be obtained. Blue circles: Temperature field after several coupling steps for a large coupling step. Dashed line stands for the boundary. Left side is the fluid's side and the wall is on the right.*

the coupling time step must be small enough in order to correctly resolve the stiff problem. The issue, is that in a given configuration, the stiffness cannot be estimated beforehand, which leads to the use of small coupling time steps. The Neumann-Neumann coupling provides an energy conserving methodology, but also one that does not ensure the continuity of the temperature, and which precision is highly dependent on the value of the coupling step size chosen. This conclusion, similar to those found for the Neumann-Dirichlet coupling, yields the same result: Since this coupling does not provide a mean to determine the coupling time step size, it will not be considered as a suitable candidate for the rest of this work.

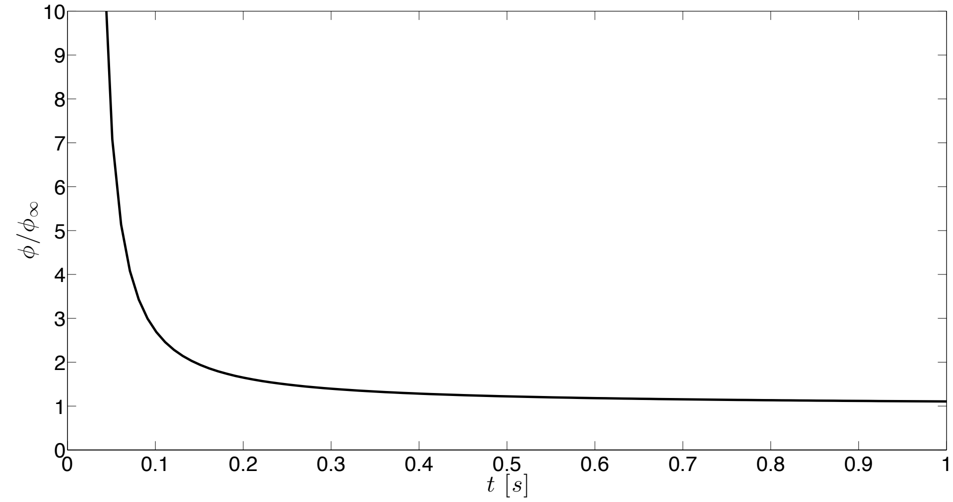

Figure 3.6: *Evolution of the boundary heat flux over time, normalized by the steady state heat flux.*

3.2.4 Dirichlet - Dirichlet

A Dirichlet-Dirichlet coupling means that both codes use a common prescribed temperature boundary condition. Determining the boundary temperature value when knowing the temperature value on each side of the interface can be done in the same way as in the previous section, with the example of first order approximations of the spatial derivatives:

$$T_{bnd} = \frac{\dfrac{\lambda_f}{\Delta x_f} T_f + \dfrac{\lambda_s}{\Delta x_s} T_s}{\dfrac{\lambda_f}{\Delta x_f} + \dfrac{\lambda_s}{\Delta x_s}} \tag{3.37}$$

In a similar way to the Neumann-Neumann coupling, the fixed state of the common boundary condition may raise some issues. The first, is that since it is the boundary temperature which is set, the boundary heat flux is different on each side, and thus leading to an energy loss, ΔE, during the coupling iteration (Radenac (2006)):

$$\Delta E = | \int_{t_n}^{t_n+\Delta t_{cpl}} (\phi_{f,bnd} - \phi_{s,bnd}) dt | \tag{3.38}$$

The longer the iteration, and the larger is Δt_{cpl}, the higher is the difference between the time integrated heat flux which leaves each side of the interface. Such an issue must be dealt with for this approach to be useful.

The second issue, is the updating of the boundary temperature. Indeed, it can be done with the help of Eq. 3.37 after each coupling step in order to regain the continuity of the heat flux, just as for the Neumann-Neumann coupling. But the energy loss is still present, which then requires an energy correction on each domain (Radenac (2006)). Another approach may be based on a balance equation applied to the interface temperature, taking into account the heat flux on each side (See next section).

3.2.4.1 Conclusion

Based on the existing works on coupled conjugate heat transfer, three coupling boundary conditions were considered. Each couple was studied and the possibility of attaining the goals set in section 3.1.3 was investigated. According to the results of this study, the most suitable coupling appears to be a Dirichlet-Dirichlet coupling. It is the coupling retained for the rest of the manuscript.

3.3 Hybrid cell interface model for updating the boundary temperature

The new interface model relies on an hybrid cell at the boundary of the fluid and solid domains (see Fig. 3.7). Once the control volume is created, an energy balance equation for the enthalpy, H_{hyb} is written:

$$\frac{dH_{hyb}}{dt} = \sum_{j=1,n_{face}} A_j \boldsymbol{\phi}_j \cdot \mathbf{n}_{ext,j} \tag{3.39}$$

Where n_{face} is the number of internal faces of the hybrid cell, A_j the surface of the $j-th$ face and $\mathbf{n_{ext,j}}$ the outgoing normal of that same

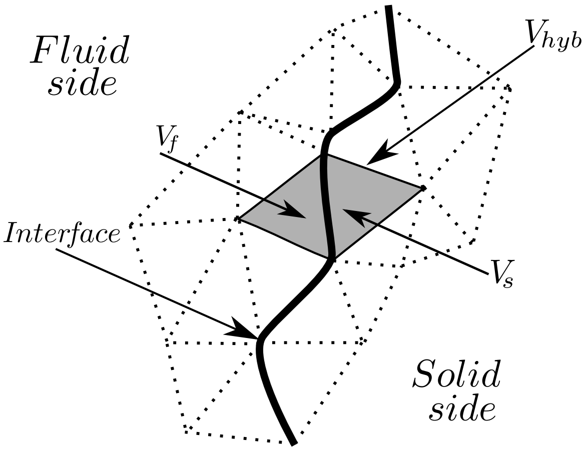

Figure 3.7: *Fluid and solid domains used for a coupled simulation. Dashed triangles represent the mesh and both grey triangles represent the two cells which make the hybrid cell around the interface.*

face. The faces' fluxes, $\boldsymbol{\phi}_j$ describe the total heat flux at the face. Thus, it can contain conductive, convective and radiative contributions. For greater clarity, the sum in Eq. 3.39 is replaced with:

$$\sum_{j=1,n_{face}} A_j \boldsymbol{\phi}_j \cdot \mathbf{n}_{ext,j} = -\Phi_f - \Phi_s \tag{3.40}$$

Where Φ_f and Φ_s are respectively the fluxes integrated over all internal faces of the fluid, and solid faces of the hybrid cell. The enthalpy is an extensive variable, which means that the total enthalpy of the hybrid cell can be written as the sum of the enthalpies of each subcell:

$$\frac{dH_{hyb}}{dt} = \int_{V_f} \rho_f c_{p,f} \frac{dT_{bnd}}{dt} dV + \int_{V_s} \rho_s c_{p,s} \frac{dT_{bnd}}{dt} dV \tag{3.41}$$

By neglecting the variations of thermo-physical properties in each subcell during the lapse of time considered, leads to:

$$\frac{dH_{hyb}}{dt} = (\rho_f c_{p,f} V_f + \rho_s c_{p,s} V_s) \frac{dT_{bnd}}{dt} \tag{3.42}$$

Combining these different relations, leads to the following equation for the boundary temperature:

$$\frac{dT_{bnd}}{dt} = -\frac{\Phi_f + \Phi_s}{\rho_f c_{p,f} V_f + \rho_s c_{p,s} V_s} \tag{3.43}$$

Thanks to this interface model, the energy conservation is ensured, since the difference between the integrated heat fluxes is used to update the boundary temperature. Equation 3.43 is an Ordinary Differential Equation. Solving an ODE can be done by using an adaptive time step, which will be used in the next chapter for the coupling time step determination.

3.3.1 Updating procedure for the boundary temperature

The boundary temperature is updated every coupling time step. The procedure is as follows:

1. Both codes are at time t_n and have the same Dirichlet boundary condition $T_{bnd} = T_{bnd}^n$

2. Each code advances independently to time $t_{n+1} = t_n + \Delta t_{cpl}$, while the boundary temperature is set to T_{bnd}^n during the entire time. The fluid code carries out N_f iterations while the solid's completes N_s iterations.

3. The heat fluxes are computed in both code in order to close the divergence on the hybrid cell

4. Equation 3.43 is solved and yields the boundary temperature for time $t = t_{n+1}$, T_{bnd}^{n+1}

The interface model works like domain decomposition, where each piece is advanced separately and the common points are updated in the end of the iteration. The estimation of the boundary temperature is done by a third independent numerical code, which interacts with the two others. The advantage of this approach is that there is no energy loss, since all fluxes leaving the two domains are then used to solve the energy balance of the thin boundary layer.

3.3.2 Adequacy of the model

3.3.2.1 Asymptotic case: Conjugate Heat Transfer between Gas and Metal

The most commonly used coupling method found in the literature is the Neumann-Dirichlet coupling which is based on the work of Giles (1997).

This coupling method relies on applying a Dirichlet boundary condition in the flow solver and a Neumann boundary condition in the solid heat transfer solver at the interface between both media. The corresponding energy budget of the separate fluid and solid cells at the interface is represented in Fig. 3.8 (right). On the fluid side, the Dirichlet condition on the wall temperature yields an instantaneous equilibrated sum of fluxes on the fluid cell. Therefore, the face-integrated flux, Φ_w, sent to the solid heat transfer solver as a Neumann condition is identical to the previously defined quantity $\Phi_{f,bnd}$:

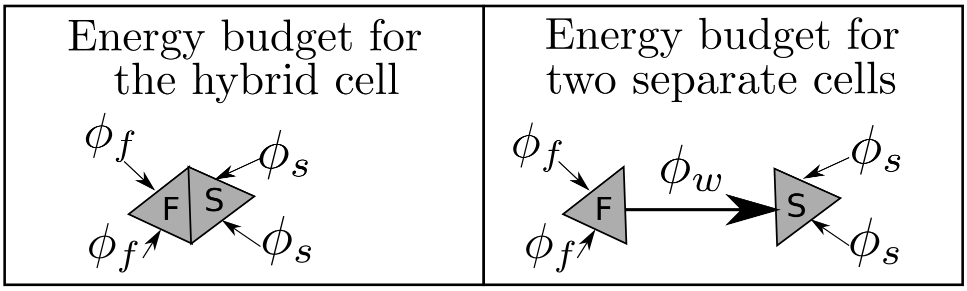

Figure 3.8: *Left: Energy budget over the entire hybrid cell. Right: Energy budget over a fluid cell with a Dirichlet BC yielding a boundary flux, Φ_w, used by the solid cell as a Neumann BC.*

$$\Phi_w = \sum_{i \neq wall} \left(\boldsymbol{\phi}_{f,i} \cdot \mathbf{n}_i^{ext} \right) A_i = \Phi_{f,bnd}. \tag{3.44}$$

In the Neumann-Dirichlet approach, the wall temperature is then determined by the solid heat transfer solver as

$$\frac{dT_{bnd}}{dt} = -\frac{\Phi_w + \Phi_{s,bnd}}{V_s \rho_s c_{ps}} = -\frac{\Phi_{f,bnd} + \Phi_{s,bnd}}{V_s \rho_s c_{ps}} \tag{3.45}$$

When considering the conjugate heat transfer between a gas and a metal, in most cases, $\rho_s c_{ps} V_s$ is several orders of magnitude higher than $\rho_f c_{pf} V_f$, which changes Eq. (3.43) solved for the hybrid cell interface model into Eq. (3.46):

$$\frac{dT_{bnd}}{dt} \approx -\frac{\Phi_{f,bnd} + \Phi_{s,bnd}}{V_s \rho_s c_{ps}} \tag{3.46}$$

Hence, Eq. (3.46) yields an equation for the boundary temperature which is the same as the one solved for the boundary temperature in the Neumann-Dirichlet coupling method. As long as Eq. (3.46) is valid, both the

Neumann-Dirichlet coupling and Dirichlet-Dirichlet based interface model provide the same evolution for the boundary temperature. This analysis shows that the hybrid cell interface model is a generic coupling, which for applications such as Gas Turbines or combustion chambers, simplifies into a Neumann-Dirichlet coupling first studied by Giles (1997).

3.3.2.2 Physical analysis of boundary layer fluctuations

Work done by Tiselj et al. (2001) and Tiselj et al. (2013) used a fully explicit flow solver to conduct DNS simulations of conjugate heat transfer in channel flow configurations. The flow considered is incompressible and the temperature was considered as a passive-scalar, without influence on the velocity or density field. The conjugate heat transfer was taken into account by solving the diffusion equation of the temperature over the flow and walls at the same time inside the same numerical solver. The walls were defined as zones with a velocity imposed as zero.

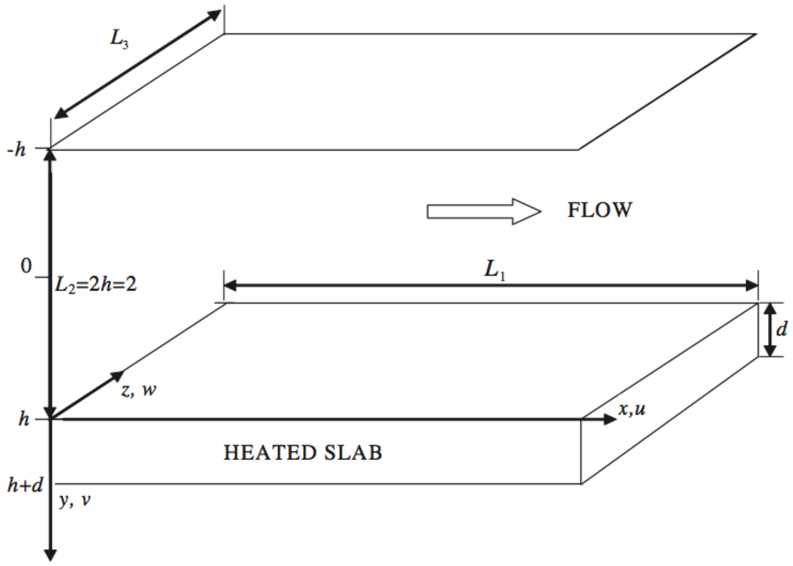

Figure 3.9: *Channel flow configuration studied by Tiselj et al. (2013). Periodical boundary conditions are used in the x and z directions. In the y direction periodical boundary conditions are imposed to the solid slab: the face situated in $y = h + d$ is linked to the one in $y = -h$.*

It was shown in these studies that K (thermal activity ratio, b_f/b_s, $b_i = \sqrt{\lambda_i \rho_i c_{p,i}}$), G (ratio of thermal diffusivities a_f/a_s) and the thickness of the wall and G have an influence on the length of penetration, but also on the level of fluctuations at the boundary. The influence of K for different values of G can be seen in Fig. 3.10 which is extracted from Tiselj et al. (2013).

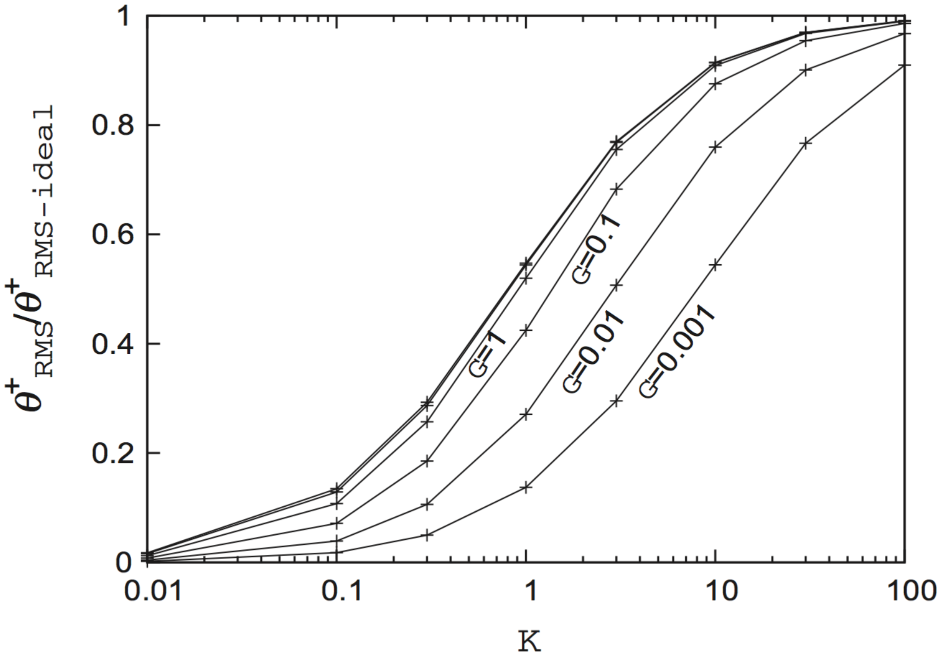

Figure 3.10: *Normalized temperature fluctuations at the fluid-solid interface scaled by the value of the normalized thermal fluctuations for standalone flow simulations with Neumann boundary conditions. Abscissa is thermal activity ratio K. Curves are given for several values of G. Channel flow configuration with* $Re_\tau = 180$ *and* $Pr = 1$*. Figure extracted from: Tiselj et al. (2013).*

The influence of K can be explained with the help of its definition. K is thermal activity ratio, which compares the effusivities of both media. When comparing two materials, the one having a larger value of b is the one which will have the more preponderant role in imposing of the contact temperature.
This is why when K is near 0, the fluctuations are null, since the boundary temperature is imposed by the wall which is at a constant temperature. On the other hand, when K is large, it is the flow which impose the boundary temperature, and thus the fluctuations can attain the boundary with little to no attenuation due to the wall. For $K \approx \infty$, the wall's effusivity is so small that it has no influence whatsoever on the boundary temperature value, which is equivalent to an iso-flux boundary condition for the fluid.

The influence of G is different (Fig. 3.10). It compares thermal diffusiv-

ities, and thus the length of penetration of thermal waves. When G is large, the fluid thermal diffusivity is larger than the solid's, and at some point the amplitude of the fluctuations arriving at the wall are not limited by the damping effect of the fluid layer (due to the skin effect) but by the ratio of effusivities: K.
On the other hand, when G becomes small, thermal diffusivity of the solid layer is much larger than the fluid diffusivity, meaning that thermal perturbations are capable of crossing the slab without being totally damped. The crossing of the slab leads to a phase lag ω_0 which for a semi-infinite slab can be written analytically: $\omega_0(x) = -\pi/4 - x/L_p$, where $L_p = \sqrt{2a/\omega}$ is the depth of penetration of thermal wave for low values of G, and x the distance crossed by the perturbation inside the wall. This phase lag generates a destructive interference between thermal waves arriving from both sides of the slab, thus reducing the final boundary temperature fluctuations. (Tiselj et al. (2013), Tiselj and Cizelj (2012), Tiselj et al. (2001)).

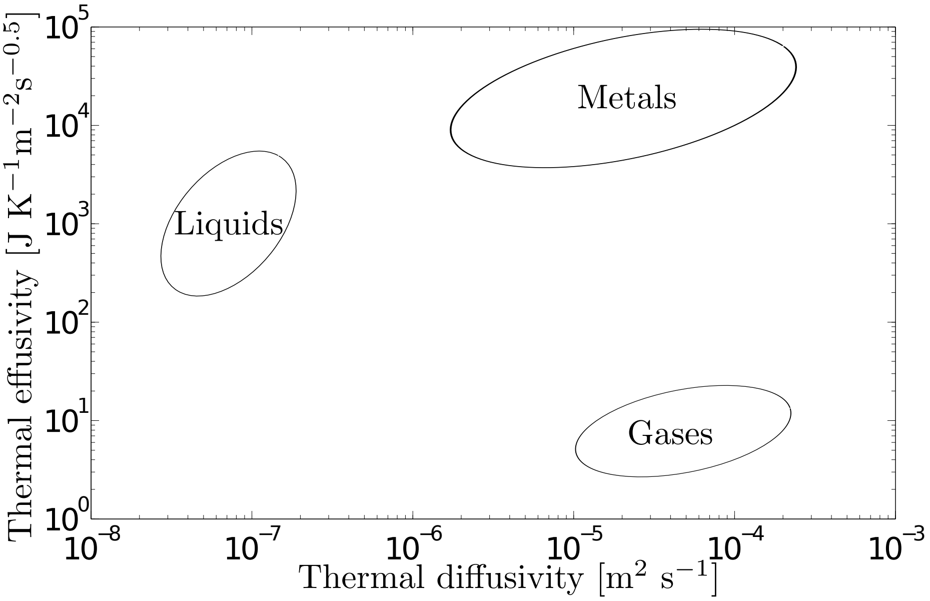

Figure 3.11: *Effusivity Vs. Diffusivity map for three groups: Gas, Liquids and Metals.*

Studying Fig. 3.11 shows that for conjugate heat transfer configurations where combustion is considered, and hence, gas-wall interaction, the value of G is usually above 1, while $K \approx 10^{-3}$. Such conditions show that the boundary temperature when seen by the flow is quasi-constant during short time periods compared to the solid time scale. For the wall heat transfer solver, the use of the Dirichlet boundary condition is correct while the coupling time step is small compared to the diffusive time scale in the wall.

From this analysis, it comes out that the interface model is adequate for Conjugate Heat Transfer computations. It has the advantage of begin a generic coupling which has a similar behavior as the currently used Neumann-Dirichlet coupling for gas-wall applications, while being coherent with the physics in each medium.

3.3.3 1D test of the hybrid cell: Method of Manufactured Solutions

Deriving an analytical solution for conjugate heat transfer is difficult because of the interface continuity and jump relations. To overcome this issue, the Method of Manufactured Solutions presented in chapter 2 is used here for the validation of the interface model. The MMS method is applied here to a two layer 1D configuration in order to verify that the hybrid cell is able to correctly solve the physics at the boundary. Each layer is governed by a 1D heat equation. The method of manufactured solutions was presented in section 2.2.1. The difficulty in applying it in this case is due to the fact that the approach is supposed to be applied to continuous functions of class C^1: the function is derivable and its derivate is a continuous function as well (Salari and Knupp (2000)). Because of the jump of thermal properties through the boundary, the temperature gradient is not continuous. That is why the studied function is the heat flux and not the temperature. The imposed profile is a spatial cosine with an exponential time decrease:

$$\phi(t,x) = -cos(\omega_0 x)e^{-kt} \tag{3.47}$$

Using the Fourier's law, leads in 1D to:

$$\frac{\partial T}{\partial x}(t,x) = \frac{cos(\omega_0 x)e^{-kt}}{\lambda(x)} \tag{3.48}$$

With:

$$\lambda(x) = H(-x)\lambda_1 + H(x)\lambda_2 \tag{3.49}$$

Where H is the Heaviside function. To obtain the temperature field over space, Eq. 3.48 need to be integrated:

$$T(t,x) = e^{-kt} \int_{-L_1}^{x} \frac{cos(\omega_0 y)}{\lambda(y)} dy \tag{3.50}$$

Thus leading to:

$$T(t,x) = \frac{e^{-kt}}{\omega_0} \left(\frac{sin(\omega_0 x)}{\lambda(x)} + \frac{sin(\omega_0 L_1)}{\lambda_1} \right) \tag{3.51}$$

Injecting the analytical functions of ϕ and T inside the heat equation, yields the following source term $S(t,x)$:

$$S(t,x) = e^{-kt} \left(\omega_0 sin(\omega_0 x) - \frac{k\rho c_p}{\omega_0} \left[\frac{sin(\omega_0 x)}{\lambda(x)} + \frac{sin(\omega_0 L_1)}{\lambda_1} \right] \right) \tag{3.52}$$

Results

The MMS method is applied to the hybrid cell, where the two media are defined in Tab. 3.1. Each domain is computed by a 1D diffusion code. Both codes use the same time step, determined so that the numerical Fourier number, $F = (\lambda \Delta t)/(\rho c_p \Delta x_1^2)$, is equal to 0.1 for medium 1. The two codes use the same integration time step, and are coupled every time step since the only goal here is to test the hybrid cell formalism.

	Medium 1	Medium 2
ρ	10	200
λ	263	2000
C	50	200
N_{points}	300	300
Length [m]	0.005	0.02
ω_0	$4\pi/L_1$	-

Table 3.1: *Parameters used for the MMS test case*

Figure 3.12 shows the initial temperature field (plot a) over the entire domain, the temperature field after 25 ms over the entire domain (plot b), and the temperature field in the near interface zone after 25 ms (plot c). Plot b) shows that the time evolution of the temperature is well captured by the 1D code. In the same way, plot c) shows that the boundary evolution and the gradient jump through the boundary are also well captured. Thanks to the MMS method, the hybrid cell is hence validated in 1D for the computation

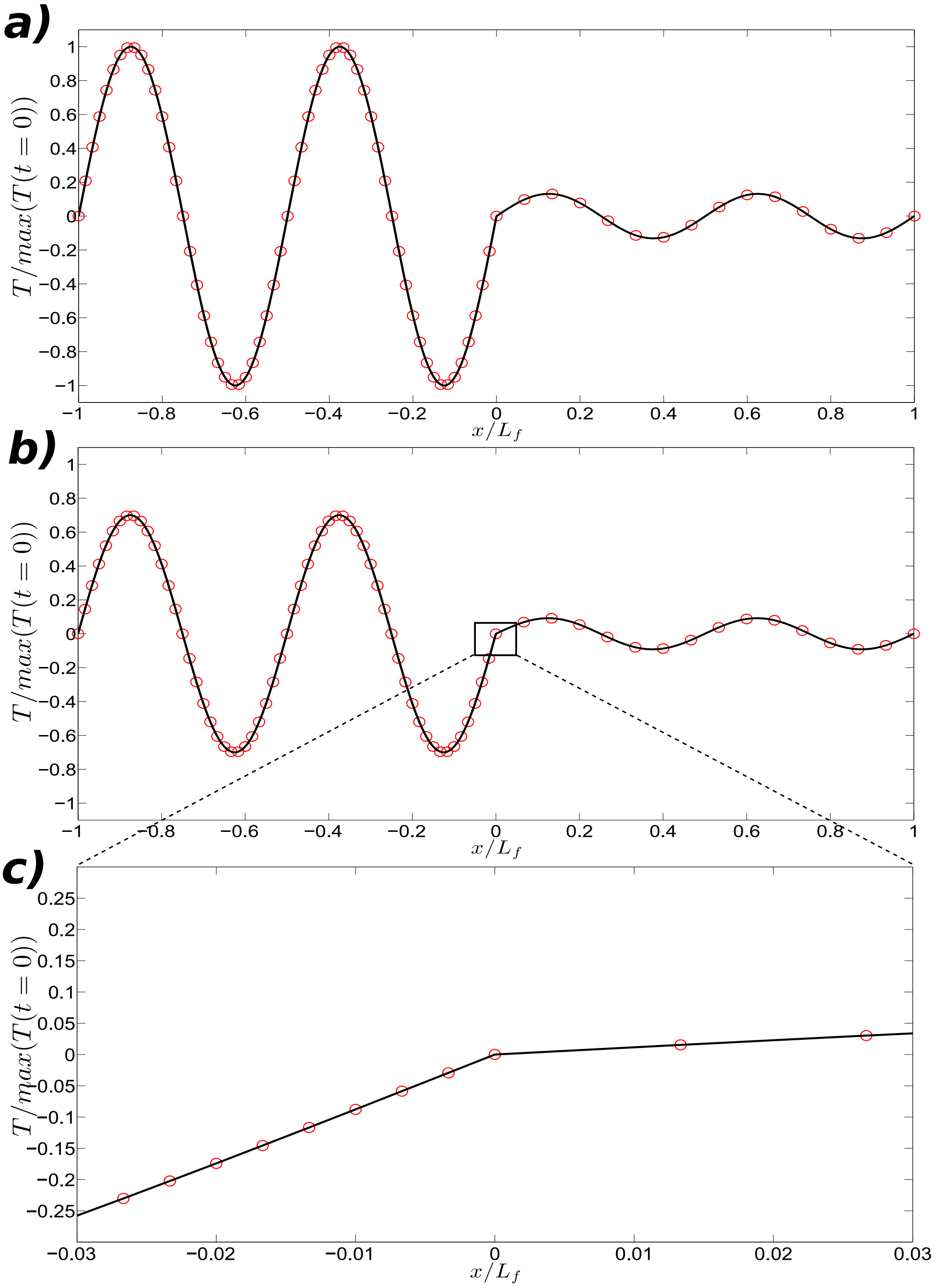

Figure 3.12: *Results for MMS test of the hybrid cell. Red circles: Analytical solution. Black line: Numerical solution. a) Solutions at time* $t = 0$. *b) Solutions at time* $t = 25ms$. *c) Zoom on the near boundary zone for* $t = 25ms$.

3.4 Conclusion

In this chapter, the state of the art of coupled conjugate heat transfer computations has been studied. The limitations of the currently used methods were first explained, and goals were set for the development of a novel methodology for coupled simulations.

Three different couplings were considered, and each was thoroughly studied with respect to the specifications set: An **unsteady parallel weak** coupling which verifies the constraints of the temperature continuity through the fluid-solid interface and the conservation of energy over a coupling step. The Neumann-Dirichlet and Neumann-Neumann approaches were both unable to provide a solution for all of the specified specifications. The Dirichlet-Dirichlet coupling then appeared as a promising approach with the help of an interface model which is used for the update of the interface boundary condition. The interface model also yielded an ordinary differential equation for the interface boundary temperature. Thanks to this ODE higher orders of accuracy for the boundary temperature can be achieved, since it can be solved using high-order integration schemes, while the Neumann-Dirichlet and Neumann-Neumann only yield first order accuracy.

Chapter 4

Coupling step size determination

4.1 Deriving a method to determine the size of the coupling time step 76

4.1.1 General setting 76

4.1.2 Numerical integration methods 77

4.1.3 Integration time step size determination for Ordinary Differential Equations 78

4.1.4 PID Control framework 80

4.1.5 Automatic determination of the coupling time step for conjugate heat transfer 83

4.2 1D validation of the coupling step size determination 85

4.2.1 1D test setup 85

4.2.2 Control loop with time step rejection 86

4.2.3 Control loop without time step rejection 88

4.2.4 PID controllers behavior study 89

4.3 Conclusion 96

One of the main issues with coupled conjugate heat transfer simulations is choosing the optimal coupling time step. Such a compromise has to take into account several input parameters: Accuracy, numerical stability, computational efficiency. The numerical stability is mandatory, if not achieved the computation is not doable. Concerning the two other parameters, the optimal time step value depends on which one is the most important. Finding the best time step then becomes an optimisation problem. This chapter shows a method offering a way to solve such an optimisation problem, and how to apply it to the coupled simulations of conjugate heat transfer.

4.1 Deriving a method to determine the size of the coupling time step

This section will present the available mathematical frameworks available for step size control: ODE integration and PID controllers. Results from both of these frameworks will then be applied to the integration of the balance equation delivered by the interface model of the hybrid cell (section 3.3). Doing so yields an automatic control of the coupling time step between a wall's heat transfer solver and a flow solver for conjugate heat transfer applications.

4.1.1 General setting

The starting point is the need to solve an Ordinary Differential Equation (ODE), defined as:

$$\begin{cases} \dfrac{df}{dt}(t) = g_{rhs}(t, f), t \geq t_0 \\ \\ f(t = t_0) = f_0 \end{cases} \tag{4.1}$$

For the sake of simplicity, the right hand side term of Eq. 4.1 is summarized by the function g_{rhs} which may depend both on time and on f. Hence, knowing the initial value of f, at time $t = t_0$, Eq. 4.1 can be solved by integrating the function g_{rhs}, and the value of f is obtained for any time t:

$$f(t) = f(t_0) + \int_{t_0}^{t} g_{rhs}(t, f)dt \tag{4.2}$$

For real applications, it is often impossible to compute analytically the integral of g, which leads to the need of a numerical integration. When numerical integration is used, the values of f are obtained for a list of discrete values $(t_n)_{0 \leq n \leq N_t}$. For the sake of simplicity, the numerical values of f, computed numerically at the discrete values of time t_n are noted f^n, such as : $f^n = f(t = t_n)$. Solving Eq. 4.1 then requires the computation of N_t integrals, such as:

$$f^{n+1} = f^n + \int_{t_n}^{t_{n+1}} g_{rhs}(t, f) dt \tag{4.3}$$

The numerical integration time step Δt^n is defined as follows: $\Delta t^n = t_{n+1} - t_n$. One of the main issues for numerical integration is choosing the best time step used for the integration. When explicit integration is used, the step size is naturally limited by the stability of the integration scheme (Hairer et al. (2008), Hairer et al. (2010)). For implicit integration, which is unconditionally stable, the difficulties which arise are the complexity of the system to solve, and hence the potentially high computational cost of an integration step. The high computational cost of one integration step for an implicit step is offset by the possibility to use a time step of any size. The only limitation for the used integration time step then becomes the accuracy of the numerical solution (Hairer et al. (2008), Hairer et al. (2010)). According to the numerical integration scheme used, it is needed to choose an integration time step which guarantees both stability and sufficient precision.

For explicit methods, the stability can be ensured indirectly by imposing a certain accuracy for the integration step. Indeed, an unstable method will lead to a poor accuracy before a possible divergence of the computation. Hence, having a method which automatically adapts the size of the integration time step according to the achieved accuracy will ensure the stability of the explicit integration method by reducing the size of the time step (As seen in appendix A).

4.1.2 Numerical integration methods

The computation of the integral in Eq. 4.3 is done numerically with a numerical integration method which has a global order k. A numerical integration is said of global order k, if the numerical estimate of the integral in Eq. 4.3, noted as $I_{[k]}(f, g_{rhs}, t_n, t_{n+1})$, verifies locally (for one integration step):

$$I_{[k]}(f, g_{rhs}, t_n, t_{n+1}) = \int_{t_n}^{t_{n+1}} g_{rhs}(t, f) dt + \alpha \cdot (\Delta t^n)^{k+1} + o\left((\Delta t^n)^{k+1}\right) \tag{4.4}$$

and for a fixed integration step Δt, such as $\forall n, \Delta t^n = \Delta t$, verifies for N steps:

$$\begin{aligned} f^N &= f(t = t_0) + \sum_{n=0}^{N-1} I_{[k]}(f, g_{rhs}, t_n, t_{n+1}) \\ &= f(t = t_N) + \beta \cdot (\Delta t)^k + o\left((\Delta t)^k\right) \end{aligned} \tag{4.5}$$

From here on, the numerical estimate of the function f at time $t = t_n$, computed with a method of order k, will be noted as $f^n_{[k]}$.

4.1.3 Integration time step size determination for Ordinary Differential Equations

In order to compute the value of $f(t)$ within a prescribed accuracy, η, the value of the integration time steps should not be too large. The challenge is that by not having access to the analytical form of the function f, it is not possible to predict *a priori* the value of the integration time step which will suffice. When facing such functions, the largest time step which allows for a given accuracy may also depend on the local stiffness of the equation. Thus, it is needed to control on the fly the value of the integration time step (Hairer et al. (2008), Hairer et al. (2010), Duarte (2011), Estep et al. (2009)). The basis for such a control is presented hereafter.

Solving Eq. 4.2 requires a computation of the integral in the right hand side. In a numerical resolution code, the integration is done numerically, and therefore the computed value is not exact. Thus, a control loop is needed in order to attain the wished accuracy. As shown in Fig. 4.1, the integration step size control is achieved through a number of inner itera-

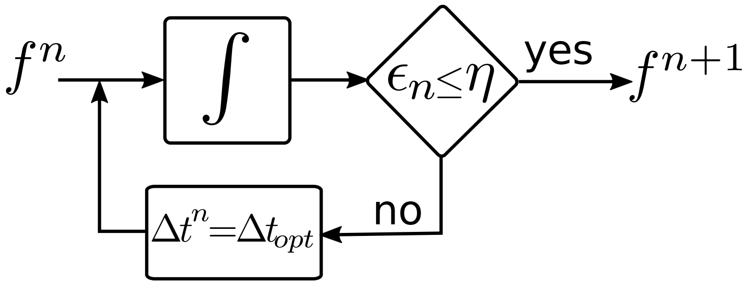

Figure 4.1: *Generic control loop to advance thefunction f^n to its value f^{n+1} with a numerical integration error ϵ_n below a given tolerance η by adapting the integration time step Δt^n.*

tions. First of all, a numerical value of the integral is computed. Then, the numerical integration error ϵ_n is computed and compared to a prescribed error tolerance η. **If** the numerical error is below that tolerance, then the numerical solution is **accepted** and the next step is computed. On the other hand, when the numerical error is above the tolerance, the time step is **rejected** since the numerical error is too large and it has to be recomputed using a **new** and **smaller** time step. This new time step is estimated using the computed numerical integration error and integration step is recomputed. The process is repeated until the error is small enough.

The issue when using numerical integration, is that most often, the exact solution is unknown. Hence, the value of the numerical error ϵ_n is not known. To use the control loop effectively, an estimation of the error is used instead of the exact value. The estimation is based on the mathematical properties of the integration schemes.
First of all, the integration scheme has an order, k, such as when integrating the function between $t = t_n$ and $t = t_{n+1}$, the following relationship is verified for an integration step Δt^n (4.1.2):

$$f_{[k]}^{n+1} = f(t_{n+1}) + o\left((\Delta t^n)^{k+1}\right) \tag{4.6}$$

For the time step Δt^n, the k^{th} order method error is defined as :

$$\epsilon_n = |f_{[k]}^{n+1} - f(t_{n+1})| \tag{4.7}$$

One of the most straightforward methods to estimate the error of an integration method of order k, is to compute the integral with a method of order k+1 as well. By doing so, it is possible to estimate the error of the method of order k through the comparison of both solutions:

$$\begin{aligned} \epsilon_n &= |f_{[k]}^{n+1} - f(t_{n+1})| \\ &= |f_{[k]}^{n+1} - f_{[k+1]}^{n+1} + f_{[k+1]}^{n+1} - f(t_{n+1})| \\ &\leq \underbrace{|f_{[k]}^{n+1} - f_{[k+1]}^{n+1}|}_{O(\Delta t^{k+1})} + \underbrace{|f_{[k+1]}^{n+1} - f(t_{n+1})|}_{O(\Delta t^{k+2}) \ll O(\Delta t^{k+1})} \end{aligned} \tag{4.8}$$

Therefore, ϵ_n is estimated as:

$$\epsilon_n = |f_{[k+1]}^{n+1} - f_{[k]}^{n+1}| \tag{4.9}$$

Once the error is computed, the optimal time step, Δt_{opt}, has to be computed if the error is too large. Using Eq. 4.4, and by neglecting the high order terms grouped inside $o\left((\Delta t^n)^{k+1}\right)$, the following relation can be written for the numerical integration error ϵ_n and integration time step Δt^n:

$$\epsilon_n \approx \alpha(\Delta t^n)^{k+1} \tag{4.10}$$

Based on Eq. 4.10, it can be also deduced that the error tolerance η may be linked to an optimal time step. This time step is the largest one which could have been used in order to achieve exactly η for the error.

$$\eta = \alpha(\Delta t_{opt})^{k+1} \tag{4.11}$$

By combining equations 4.10 and 4.11, the optimal time step can then be computed with the help of the time step which was used for the initial computation :

$$\Delta t_{opt} = \Delta t^n \left(\frac{\eta}{\epsilon_n}\right)^{1/(k+1)} \tag{4.12}$$

Equation 4.12 is the most basic formula available for the estimation of an optimal integration time step. It is clear from this formula that when the error is larger than the tolerance, the returned optimal step size is indeed smaller than the one used. Hence, the step size is effectively controlled by this method.

The order of the method, k, also has an effect on the time step control. As it can be seen, the larger k is, the closer is the ratio $(\eta/\epsilon_n)^{1/(k+1)}$ to 1 thus leading to a smoother evolution of the integration time step: smaller modifications of the time step are needed for a method of order 2 than for a method of order 1 in order to reduce in half the error (Fig. 4.2). Hence, normally the highest possible order should be used since it will allow for the largest time step.

In the 1980's, control theory specialists began studying the question of integration step size control and noted that it was a control problem, and hence, could be tackled through that angle (Gustafsson et al. (1988)). This is the subject of the next section.

4.1.4 PID Control framework

The first work to link control theory with step size control was done by Gustafsson et al. (1988), Gustafsson (1991). Their work is based on the resolution of a control problem. A control problem is defined with

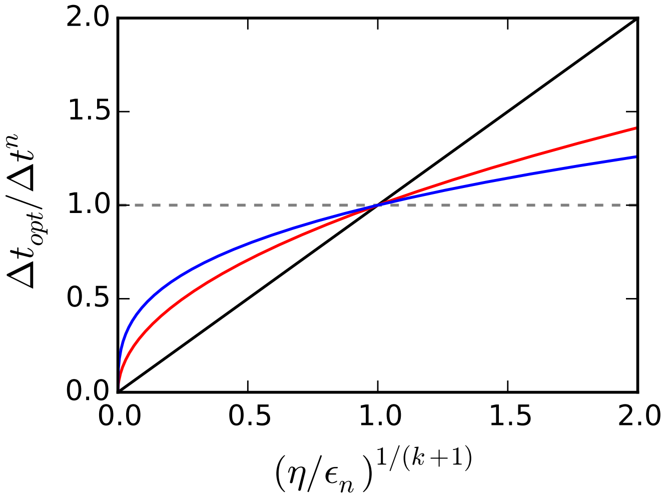

Figure 4.2: *Evolution of the optimal integration time step scaled by used integration time step as a function of the numerical integration error for different orders. Gray dashed line: k+1 =0. Black plain line: k=0. Red plain line: k=1. Blue plain line: k=2*

the help of two variables : C and θ. θ is a goal variable, which is wished to be as close as possible to a given target value θ_0. C is the feedback control variable, and depends on θ. The mathematical problem to solve is an optimization problem, where the optimal value of C is sought in order for θ to attain θ_0.

A possible angle of attack, is the usage of PID controllers, where PID stands for Proportional, Integral and Derivative. These controllers are called so since the link between the control variable can be linked to the goal variable either proportionally, integrally or derivatively. This link is shown in Eq. 4.13 which is the general PID control equation (Hairer et al. (2010)). K_P, K_I and K_D are respectively the proportional, integrator and derivative control gains.

$$-\dot{C}(t) = K_P\dot{\theta}(t) + K_I\theta(t) + K_D\ddot{\theta}(t) \tag{4.13}$$

Equation 4.13 is the ideal control equation. Yet, in real applications, there is a lag effect: The feedback is not sent instantly to the control variable, which leads to a time corrected equation, where τ is the time delay (or lag) of the feedback:

$$-\dot{C}(t) = K_P\dot{\theta}(t-\tau) + K_I\theta(t-\tau) + K_D\ddot{\theta}(t-\tau) \tag{4.14}$$

Using basic PID framework results, such as those available in Hairer et al. (2008), Gustafsson (1991), Söderlind (2002), it is possible to write Eq. 4.15, where θ and C are defined for the specific case of integration step size control.

$$\begin{cases} C = log(\Delta t) \\ \theta = log(\epsilon) - log(\eta) \end{cases} \tag{4.15}$$

For the step size control the goal is to have an error as closed as possible to the prescribed tolerance η, and hence have the largest value of C in order to achieve that goal. Equation 4.14 is solved with the help of differences formulae hereafter, by considering that the feedback lag is equal to the time step used,$\tau = \Delta t^n$, and $t = t_{n+1}$:

$$\begin{aligned} \dot{C}(t_{n+1}) &= log(\Delta t^{n+1}) - log(\Delta t^n) \\ \theta(t_n) &= log(\epsilon^n) - log(\eta) \\ \dot{\theta}(t_n) &= \theta(t_n) - \theta(t_{n-1}) \\ \ddot{\theta}(t_n) &= \dot{\theta}(t_n) - \dot{\theta}(t_{n-1}) \\ &= \theta(t_n) - 2\theta(t_{n-1}) + \theta(t_{n-2}) \end{aligned} \tag{4.16}$$

The solving of Eq. 4.14 leads to Eq. 4.17. The latter gives access to the optimal integration time step as a function of the integration error of the function f, for the n^{th} integration step.

$$\begin{aligned} \Delta t^n_{opt} &= \Delta t^n f_P f_I f_D \\ f_P &= \left(\frac{\eta}{\epsilon^{[k]}_{n-1}}\right)^{-(K_P+2K_D)} \\ f_I &= \left(\frac{\eta}{\epsilon^{[k]}_{n}}\right)^{K_P+K_I+K_D} \\ f_D &= \left(\frac{\eta}{\epsilon^{[k]}_{n-2}}\right)^{K_D} \end{aligned} \tag{4.17}$$

The values of K_P, K_I and K_D are the key factors for the behavior of the PID controller. Depending on the values chosen, the controller will filter different frequencies and will present different performances in terms of robustness (Gustafsson et al. (1988), Gustafsson (1991), Söderlind (2002), Söderlind (2003)). Entire studies are dedicated to the optimisation process of the three gains.

It can be noted, that when K_P and K_D are taken equal to zero, and K_I equal to $1/(k+1)$, the controller is the same as the formula developed in the previous section with the help of the Taylor expansion.

This work concentrates on the use of an I, PI and a PID controllers. The values for different gains for each controllers were chosen from those available in the litterature: PI controller from Gustafsson (1991), and the PID H312 controller by Söderlind (2003) The values used are summarized in Tab. 4.1, where: $\beta = K_P + K_I + K_D$, $\alpha = K_P + 2K_D$ and $\gamma = K_D$.

Controller	$\alpha(k+1)$	$\beta(k+1)$	$\gamma(k+1)$
I	0	1	0
PI	0.4	0.7	0
PID	1/9	1/18	1/18

Table 4.1: *Values used for the different gains, available in Gustafsson (1991), Söderlind (2003), for an integration scheme of order k.* $\alpha = K_P + 2K_D$, $\beta = K_P + K_I + K_D$ *and* $\gamma = K_D$.

4.1.5 Automatic determination of the coupling time step for conjugate heat transfer

Equation 4.18 was developed in the previous chapter. By definition, the time step used to solve Eq. 4.18 is the coupling time step. This means that by using the results of the step size control for ODE's presented in the previous sections, applied to Eq. 4.18, a control of the coupling time step may be achieved.

$$\frac{dT_{bnd}}{dt} = -\frac{\Phi_f + \Phi_s}{\rho_f c_{p,f} V_f + \rho_s c_{p,s} V_s} \tag{4.18}$$

Meaning that for the rest of the chapter:

$$g_{rhs} = -\frac{\Phi_f + \Phi_s}{\rho_f c_{p,f} V_f + \rho_s c_{p,s} V_s} \tag{4.19}$$

Using the step size control framework requires two integration schemes with different orders. Yet, the wall heat flux values used for the right hand side term are only known at the coupling instances. Hence, in order to increase the order of the integration method, only previous values of the right hand side function can be used. This leads to explicit multi-step integration schemes, also known as Adams-Bashforth schemes (Hairer et al. (2008)).

These schemes are derived from approximating the function to integrate with interpolation polynomials. This implies, that for the method of order k, k points are used. The right hand side function is approximated as follows:

$$g_{rhs}(t) \approx \sum_{i=0}^{k-1} g_{rhs}(t_{n-i}) P^k_{n-i}(t) \tag{4.20}$$

Where $P^k_n(t)$ is the Lagrange interpolation polynomial defined as:

$$P^k_{n-j}(t) = \prod_{i=0,\ i\neq j}^{k-1} \frac{t - t_{n-i}}{t_{n-j} - t_{n-i}} \tag{4.21}$$

Integrating an approximation with k points is of order k (Hairer et al. (2008)), and leads to following integration scheme:

$$f^{n+1}_{[k]} = f^n + \sum_{i=0}^{k-1} g_{rhs}(t_{n-i}) \int_{t_n}^{t_{n+1}} P^k_{n-i}(t) dt \tag{4.22}$$

The results found in appendix A showed that for the Adams-Bashforth methods, the optimal couple of integration methods, in terms of computational cost, is the one of orders 1 and 2. To ensure the energy conservation, the first order scheme used here is a conservative scheme defined as:

$$f^{n+1}_{[1]} = f^n + \Delta t^n \overline{g^n_{rhs}} \tag{4.23}$$

Where $\overline{g^n_{rhs}}$ is computed as the exact numerical right hand side term, by time integrating on both sides of the fluid-solid interface the wall heat fluxes:

$$\overline{g^n_{rhs}} = \frac{1}{\Delta t^n} \int_{t=t_n}^{t_n+\Delta t^n} g_{rhs}(t) dt \tag{4.24}$$

While the second order scheme is the following Adams-Bashforth scheme:

$$f^{n+1}_{[2]} = f^n + \Delta t^n g_{rhs}(t_n) + \frac{(\Delta t^n)^2}{2(\Delta t^{n-1})} (g_{rhs}(t_n) - g_{rhs}(t_{n-1})) \tag{4.25}$$

From here on, these results will be applied to the hybrid cell temperature. This means that the function f will be replaced by the boundary temperature T_{bnd}. The time step used is the coupling time step, hence: $\Delta t^n = \Delta t^n_{cpl}$. In the next section, this framework will be applied on a one dimensional test case.

4.2 1D validation of the coupling step size determination

The automatic time step determination is tested with the help of a 1D heat-diffusion code presented in section 2.2.1. Reference results for the two-media configuration were obtained through highly resolved computations (in time and space).

4.2.1 1D test setup

The fluid medium has the same physical properties as the burnt gases mixture issued from the oxycombustion of methane at a pressure of 20 bars. The wall is made from inconnel steel, which is a stainless alloy commonly used for high pressure combustion chambers. The one-dimensional configuration is presented in Fig. 4.3 and the values of the different thermal properties of both media are given in Tab. 4.2.

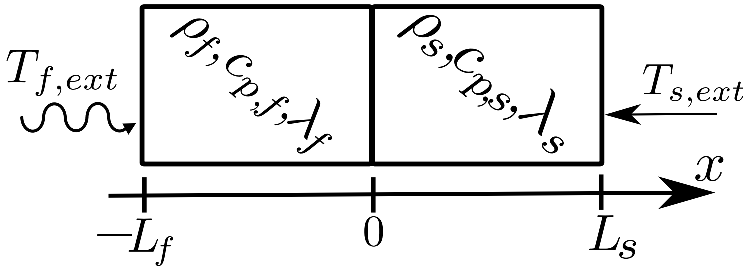

Figure 4.3: *One-dimensional test case configuration. The length L_f of the fluid part is 1 mm while the length L_s of the solid part is 1 cm.*

The numerical test case consists of two 1D codes coupled with each other. For the sake of simplicity the boundary between the two media is located at $x = 0$. The fluid part is located on the left, in the negative x values domain, while the wall is on the right in the positive x values zone.
The outer boundary conditions used are a constant temperature for the wall. A fluctuating temperature is prescribed at the fluid's outer end,

Inconnel steel		Burnt gases	
λ_s	11.7	λ_f	0.15774
ρ_s	8510.0	ρ_f	3.6504
$c_{p,s}$	439.0	$c_{p,f}$	1737.9

Table 4.2: *Properties of both media considered in 1D test cases in SI units: Thermal conductivity, density, thermal capacity at constant pressure.*

such as:

$$\begin{aligned} T_{f,ext} &= T(t, x = -L_f) \\ &= T_0(1 + 0.1 sin(2\pi f_{ext} t)) \end{aligned} \tag{4.26}$$

where T_0 =1 000 K and $T_{s,ext} = 293K$.

4.2.2 Control loop with time step rejection

The three controllers presented in the previous section, Tab. 4.1, are compared. Figure 4.4 shows that when a control loop with time step rejection is used, all three controllers provide similar results in terms of error and step size. The difference resides in the number of rejected time steps. A comparison of the number of rejected time steps for the same simulation is available in Tab. 4.3.

Controller	I	PI	PID
Total number of steps	478	739	721
Number of rejected steps	113	38	31

Table 4.3: *Comparison of the total number of coupling steps with the number of rejected steps for $\eta = 1\%$, $f_{ext} = 100$ Hz and a simulated time of 60 periods.*

Results show that for the three controllers, the numerical error remains below the prescribed tolerance. The error and coupling time step are seen to evolve according to a frequency which is twice the one of the exterior perturbation. This is due to the absolute value used to compute the numerical integration error which doubles the observed frequency. The evolution of the accepted step size is similar for the PI and PID controllers while the I controller presents much larger variations. The result of these larger variations is that the number of rejected steps is 4 times higher for the I controller than for the PI or PID controllers, which is a known characteristic of the I controller (Gustafsson (1991), Söderlind (2003)).

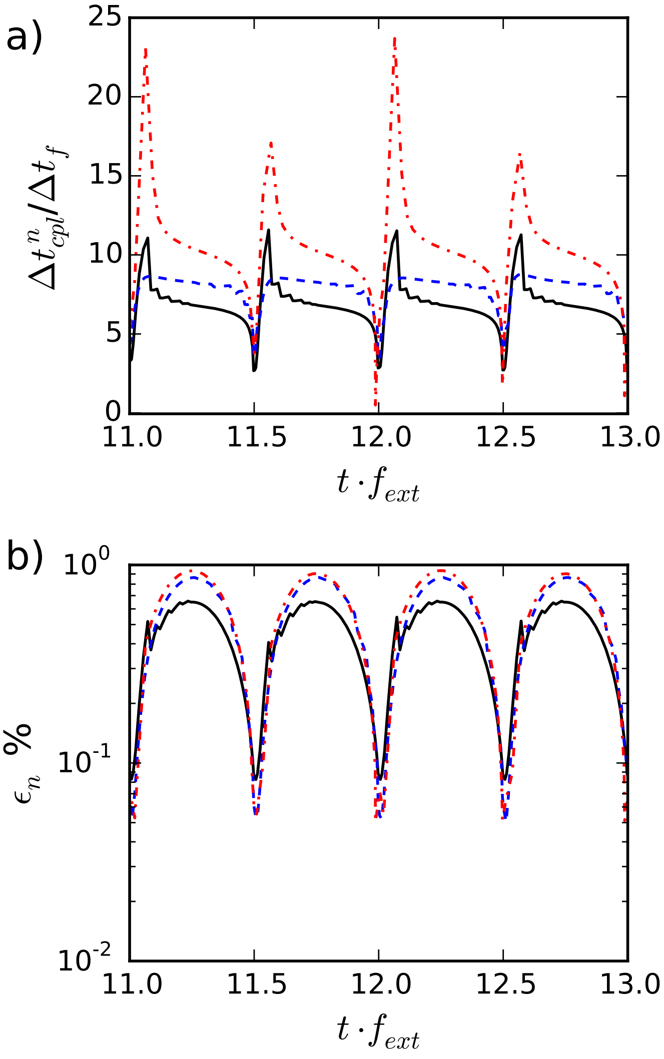

Figure 4.4: *Evolution of the accepted time step scaled by the fluid solver's time step (a) and corresponding numerical error (b) for the I (red dashed-dotted line), PI (blue dashed line) and PID (black plain line) controllers for* $\eta = 1\%$ *and* $f_{ext} = 100$ *Hz.*

Nevertheless, for this case the I controller is more efficient in terms of computational time since it is 1.5 times faster than the PI and PID controllers. These results would indicate that the I controller is the best-suited controller for the considered application. The issue with such an approach is that rejecting time steps means recomputing the integral with a smaller time step. Doing so for coupled simulations is problematic since both media then need to recompute their temporal evolution between the initial time t_n and the new final time $t = t_n + \Delta t_{opt}$. Computing multiple times LES or DNS iterations of a flow solver will generate an additional computational cost which is not affordable.

For the sake of optimal computational cost, it is proposed to use the step size control loop without rejection. The reason is that conjugate heat transfer problems are not highly stiff problems, and hence the error's overhead is not huge and hence should be fixed by reducing the next coupling step size value. For this reason, instead of using the control loop, the optimal value for n-th coupling step size is used for the (n+1)-th coupling step size:

$$\Delta t_{cpl}^{n+1} = \Delta t_{cpl,opt}^{n} \tag{4.27}$$

Tests of this approach are conducted in the next section.

4.2.3 Control loop without time step rejection

As mentioned before, for complete reactive flows numerical simulations, the additional computational cost created by the rejection of time steps is not affordable up to now. For that reason, tests are conducted without rejection in order to compare all three controllers in terms of stability and efficiency. Fig. 4.5 shows the temperature's fluctuation field over time for a signal of 5 Hz. It shows an instability which occurs for the I controller which is due to a faulty time step control when non-optimal steps are not rejected. This issue was only encountered for the I-controller for some frequencies, since the other controllers are able to filter more efficiently instabilities (Gustafsson et al. (1988), Söderlind (2003)). For this reason the I controller is considered not stable enough and hence unsuitable for this usage.

Figure 4.6 shows the instant error of the boundary temperature computed using the interface model, as well as the ratio between coupling time step and fluid time step for $f_{ext} = 100$ Hz and $\eta = 0.1$. The error stays

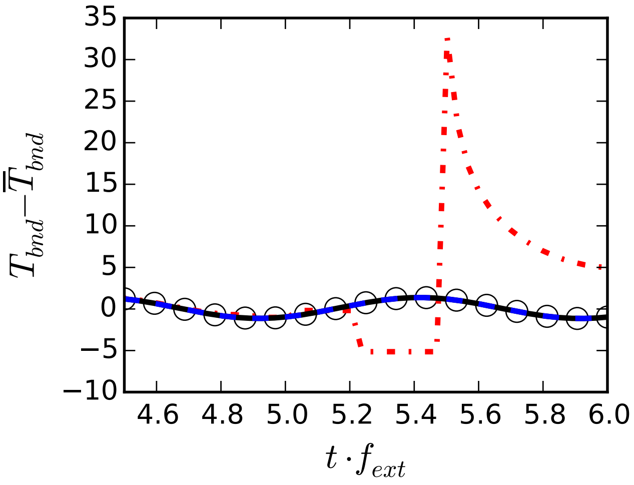

Figure 4.5: *Example of temporal evolution of the difference of the boundary temperature* T_{bnd} *with its mean value,* $\overline{T}_{bnd}$ *for the reference solution (black squares) and the I (red dashed-dotted line), PI (blue dashed line) and PID (black plain line) controllers.* $\eta = 5$ *% and* $f_{ext} = 5$ *Hz.*

close to the prescribed tolerance with some overhead because of the non-rejection. The difference lies in the mean value of the coupling time step, which evolves inversely to the frequency of the fluctuations. As it is seen, the time step adjusts itself accordingly to the integration error on the fly.

To differentiate the PI and PID controllers, it is interesting to study the ratio of coupling time step over fluid time step. The higher this ratio, the lower the coupling cost is, since it indicates a lower number of communications. Hence, the controller with highest ratio should be the most cost efficient. A study of this ratio as a function of the prescribed tolerance and signal frequency is done in the following section.

4.2.4 PID controllers behavior study

These first results show that automatic control of the coupling step size works. Nevertheless, it is interesting to study the influence of both frequency and error tolerance values on the coupling time step.

4.2.4.1 Prescribed error tolerance dependance

Studying the mean coupling time step size is interesting because it allows a view of the influence of the different parameters on an approximation

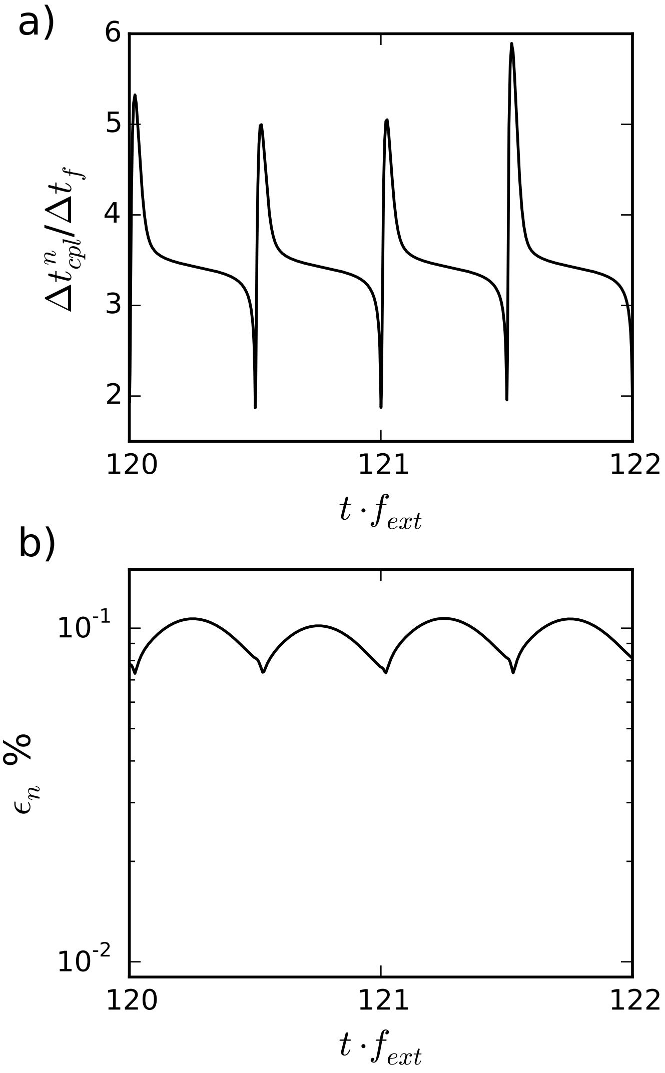

Figure 4.6: *Evolution of the coupling time step scaled by the fluid time step (a) and the corresponding numerical integration error (b) computed by the PID controller without considering step rejection. Case conditions:* $\eta = 0.1\%$ *and* $f_{ext} = 100$ *Hz.*

of the mean computational cost due to the coupling. The higher the coupling time step, the lower is the computational cost.

The first influence studied is that of the error tolerance used with a constant frequency. The test case is the same as before, with a frequency of 100 Hz. Results are available in Fig. 4.7. The results plotted in Fig. 4.7 show that the mean value of the coupling step size increases with the prescribed error tolerance, which is something to expect. Moreover, it appears that the relation linking both quantities is a power-law:

$$\Delta t^n_{cpl} = a\eta^b \tag{4.28}$$

This can be explained by reminding that the numerical integration error is linked to the coupling time step as follows:

$$\epsilon_n = \alpha(\Delta t^n_{cpl})^{k+1} \tag{4.29}$$

for an integration method of order k and where α is independent of η. If the PI/PID controller is efficient, then the numerical integration error is close the prescribed tolerance, $\epsilon_n \approx \eta$, meaning that:

$$\Delta t^n_{cpl} = (\eta/\alpha)^{1/(k+1)} \tag{4.30}$$

thus explaining the slope seen in figures 4.7 and 4.8 for $k = 1$, which is consistent with the first order scheme used for the integration error estimation. The mean values computed are slightly larger for the PI controller than for the PID controller which indicates that the former is more cost-efficient than the latter. On the other hand, the fluctuations of the coupling time step size, plotted in Fig. 4.8, of the PI controller are one order of magnitude higher than those of the PID controller. Thus leading to the following results:

- The temporal evolution of the coupling time step size is smoother for the PID controller than for the PI controller. Hence, it allows for a better load balancing between the two codes.
- The higher smoothness of the PID coupling step size leads to a smaller global number of coupling steps than for the PI controller.

Taking these results into account leads to the conclusion that the PID H312 controller is the best suited for the coupling time step size determination. The rest of the study will only use this controller.

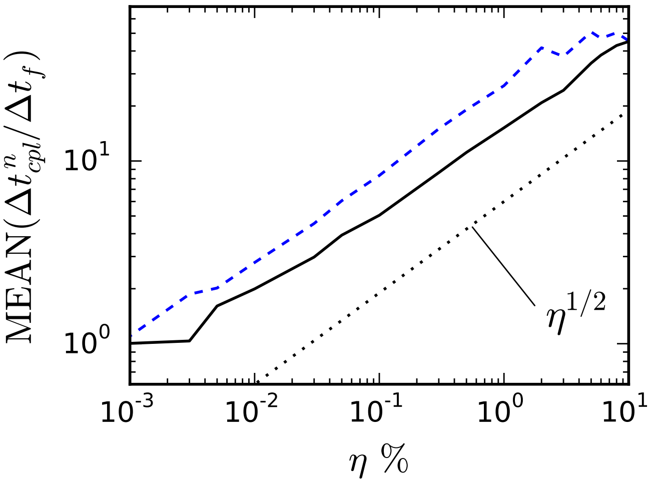

Figure 4.7: *The mean coupling time step scaled by the fluid time step as a function of the prescribed tolerance* η *for* $f_{ext} = 100$ *Hz. Black plain line : PID controller. Blue dashed line : PI Controller. Black dotted line :* $\alpha\eta^{1/(k+1)}$.

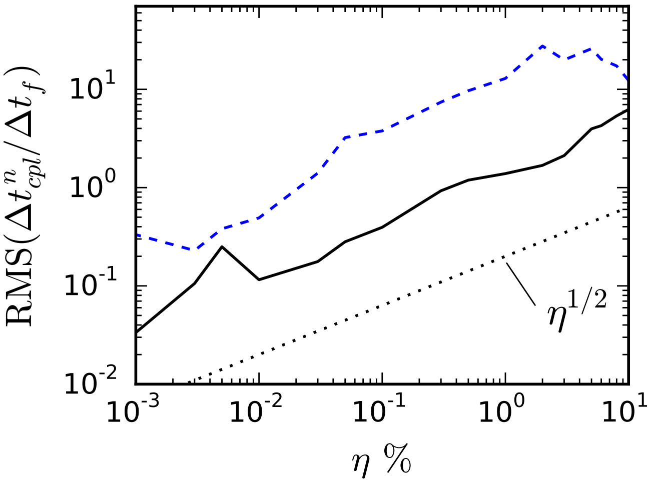

Figure 4.8: *The root-mean-square (RMS) of the coupling time step scaled by the fluid time step as a function of the prescribed tolerance* η *for* $f_{ext} = 100$ *Hz. Black plain line : PID controller. Blue dashed line : PI Controller. Black dotted line :* $\alpha\eta^{1/(k+1)}$.

4.2.4.2 Temperature fluctuations frequency dependance

Another effect, is that of the frequency. The influence of the frequency f_{ext} is studied at a fixed tolerance η for three different values: $\eta = 0.05\%$, $\eta = 0.5\%$ and $\eta = 5\%$. The results plotted in Fig. 4.9 and Fig. 4.10 show the influence of the frequency on the coupling step size for three different error tolerances.

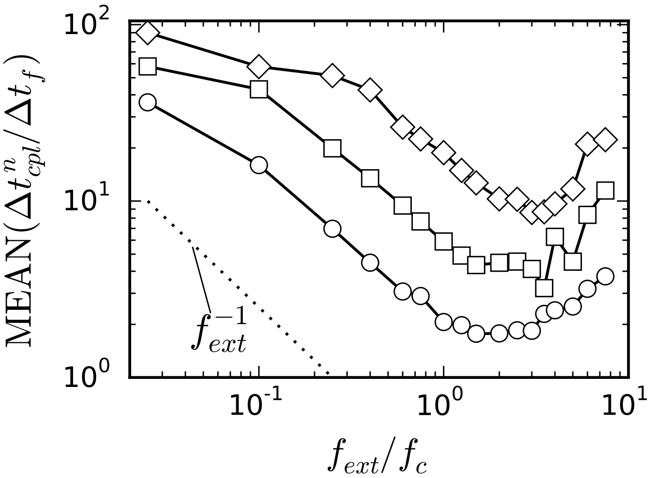

Figure 4.9: *The mean coupling time step scaled by the fluid time step computed by the PID controller as a function of the frequency f_{ext} for different values of the prescribed tolerance η: 0.05% (line and circles), 0.5% (line and squares) and 5% (line and diamonds). The frequency is scaled by the fluid domain cut-off frequency $f_c = 25a_f/(\pi L_f^2) = 200$ Hz*

The results plotted in Figures 4.9 and 4.10, with a frequency scaled by f_c which is the fluid cut-off frequency, defined as the frequency for which only 1% of the imposed fluctuations amplitude at the fluid outer boundary would reach the distance L_f in a semi-infinite domain. This cut-off frequency is estimated analytically with the help of the skin effect for semi-infinite domains: $f_c = 25a_f/(\pi L_f^2)$. For both figures, and for all three tolerance values, the same behavior is observed. A first zone defined for $f_{ext} \leq f_c$ where the coupling step decreases as f_{ext} increases, and then a second zone for $f_{ext} \geq f_c$ where the profiles of coupling step size flattens and then increases.

In the first zone, the slope indicates a f_{ext}^{-1}-law, which can be explained. For an integration method of order 1, a detailed Taylor expansion of

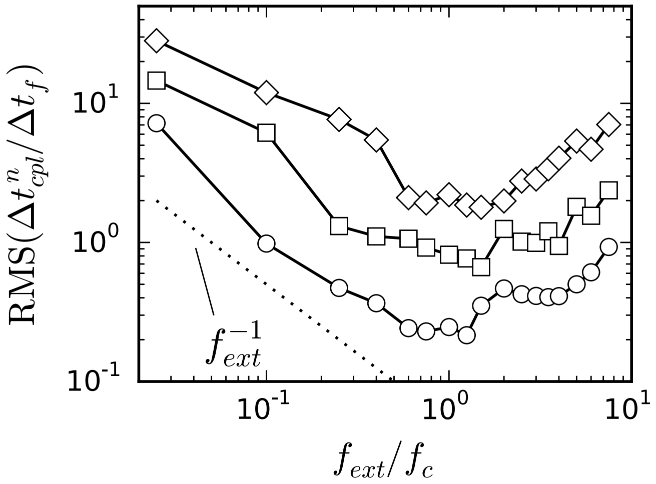

Figure 4.10: *The root-mean-square coupling time step scaled by the fluid time step computed by the PID controller as a function of the frequency f_{ext} for different values of the prescribed tolerance η: 0.05% (line and circles), 0.5% (line and squares) and 5% (line and diamonds). The frequency is scaled by the fluid domain cut-off frequency $f_c = 25 a_f/(\pi L_f^2) = 200\ Hz$*

the numerical integration error reveals that the proportionality factor in Eq. 4.29 is in fact linked to the second derivative of the boundary temperature :

$$\epsilon_n \propto \frac{\partial^2 T_{bnd}}{\partial t^2}(\Delta t^n_{cpl})^2 \tag{4.31}$$

When using the PID controller, the numerical integration error is close to the prescribed tolerance: $\epsilon_n \approx \eta$. Furthermore, the second order time derivative is proportional to f_{ext}^2. Therefore, the approximated coupling time step dependency on the f_{ext} is given by

$$\Delta t^n_{cpl} \propto \frac{\eta^{1/2}}{f_{ext}}, \tag{4.32}$$

which is the observed behavior for both mean and root-mean-square values.

The second zone, defined for $f_{ext} \geq f_c$, shows a different behavior. First, a small plateau is seen before the coupling time step size starts increasing. The reason for such a change is that the arriving fluctuations from the fluid outer boundary at the fluid-solid interface decrease with the frequency because of the damping effect of the fluid layer (Fig. 4.11).

As seen in Fig. 4.11, the larger the frequency, the smaller are the fluctuations which attain the fluid-solid interface. Figure 4.12 shows the contour map of the temperature root-mean-square fluctuations scaled by the fluid outer boundary conditions root-mean-square fluctuations, as a function of the position inside the fluid layer and of the frequency f_{ext}. As seen, the higher the frequency, the smaller are the fluctuations in the near wall region, which is in agreement with what was seen in Fig. 4.11. It is worth to note that the different iso-lines (black plain lines) computed for the coupled case are very close to those corresponding to a semi-infinite fluid (red dashed lines) except when in the near vicinity of the fluid-solid interface. The thermal inertia of the solid layer leads to an additional damping effect on the fluid-solid interface temperature. Hence, at some point the ratio between the mean and fluctuating components is so small that boundary temperature is nearly constant, leading to an increase in the coupling time step which at some point will attain the maximal stable time step.

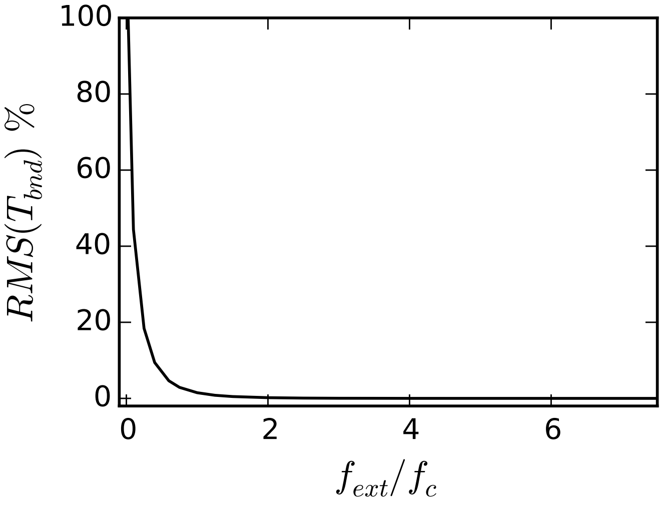

Figure 4.11: *Evolution of the boundary temperature root-mean-square, scaled by the maximal value measured for f_{ext} =5 Hz, fluctuations as a function of the exterior frequency f_{ext}.*

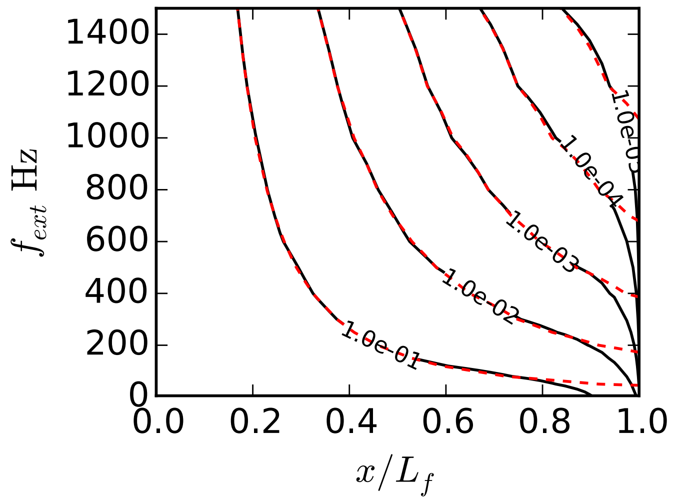

Figure 4.12: *Contours map of the temperature root-mean-square fluctuations scaled by the input fluctuations levels, as a function of the position in the fluid layer and exterior frequency* f_{ext}*. Black plain lines: Values for the coupled configuration. Red dashed lines: Values for a semi-infinite fluid.*

4.3 Conclusion

The mathematical framework of integration step size control and PID controllers was presented in this chapter. Relevant results were extracted and applied to the numerical solution of the boundary temperature balance equation. Thanks to these results, an automatic determination of the coupling time step for conjugate heat transfer has emerged for the hybrid cell based coupling method.

This methodology was first validated on a 1D test configuration. Then, a cost-optimized version was introduced where time steps too large are not rejected. The comparison of the three controllers showed that the PID controller was the best suited for such a task.

The influence of the error tolerance value and of the fluctuations frequency were also investigated. They showed that a reduction of the error tolerance leads to a reduction of the mean coupling step size. In the same way, increasing the perturbations' frequency has the same effect. Thus, a more accurate solution requires a smaller coupling time step.

Even though too large time steps are not rejected, the controller showed sufficient robustness by adjusting the next steps accordingly. This coupling methodology is applied to a case of flame-wall interaction in chapter 6 with the coupling of a LES solver and thermal solver, and for a confined flame in chapter 7.

Chapter 5

Attaining the permanent regime for the temperature in coupled conjugate heat transfer computations

5.1 Computing the permanent regime for flow configurations . . . 100

5.1.1 Steady flows . . . 100

5.1.2 Fourier space solvers . . . 102

5.1.3 Fully unsteady simulations in time domain . . . 102

5.2 Accurately describing the permanent regime using unsteady solvers . . . 106

5.2.1 Accelerating method with coupling step size control . . . 107

5.2.2 Non-linear extension of the model . . . 109

5.2.3 1D Validation of the acceleration method . . . 110

5.3 Conclusion . . . 112

Conjugate heat transfer is a temporal multi-scale phenomenon: The turbulent reactive flow has much smaller time scales than the solid walls. To gather statistics of the permanent regime it is necessary to compute the transient heating (or cooling) of the wall before attaining the permanent regime. The kind of physical time scales needed to be simulated then are far too large to be computed with existing numerical tools, highlighting the need to achieve the permanent regime more quickly. This chapter deals with challenge of artificially accelerating the numerical convergence towards the permanent regime in conjugate heat transfer configurations.

5.1 Computing the permanent regime for flow configurations

The large discrepancy between the flow and wall time scales leads to a technical challenge for coupled conjugate heat transfer simulations. Since several orders of magnitude separate the two scales, the time needed for the wall temperature field to attain its mean steady state is of the order of minutes or hours. Simulating such a large physical time with an unsteady flow solver (LES or DNS based) is not affordable with the currently available numerical tools and supercomputer clusters. Hence, for coupled conjugate heat transfer simulations to be a usable tool with high fidelity methods, a way to accelerate the wall's thermal transient is required.

This chapter deals first with the existing methods for coupled unsteady simulations, using LES or DNS for the fluid flow part. Then, a new acceleration method based on the linearity of the heat equation inside the wall is developed, before being combined with the coupling time step control method developed in chapter 4.

5.1.1 Steady flows

When considering a steady flow, the steady state solution of the coupled fluid-solid problem can be computed in a rather cost efficient way. A steady heat transfer solver is coupled with the flow solver. The equation solved for the temperature by the solid heat solver is the following:

$$\nabla \cdot (\lambda_s \nabla T) = 0 \tag{5.1}$$

Then, the flow equations are advanced using time marching techniques. An example of this approach is available in the works conducted by

Chemin (2006), where the chosen coupling algorithm is a staggered one (Fig. 5.1).

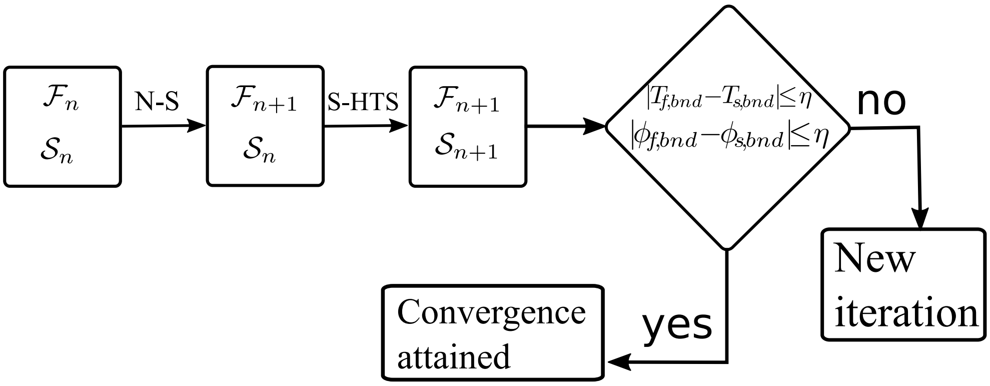

Figure 5.1: *Operating scheme of the steady coupling done by Chemin (2006). Initial fluid and solid states are denoted by $\mathcal{F}_n$ and $\mathcal{S}_n$ respectively. New iterations are computed as long as the convergence is not achieved for both boundary temperature and heat flux.*

A coupling iteration begins with the solid sending its boundary temperature to the flow solver so that it can use it as a boundary condition. The flow solver than advances in time and sends the resulting boundary wall heat flux to the solid heat transfer solver, which then uses the heat flux as a boundary condition while solving the steady heat equation. Once all of this is done, the boundary temperature and heat flux are compared on both sides of the fluid-solid interface to check their convergence, thus ending the iteration process. New coupling iterations are computed as long as needed for the boundary temperature and heat flux to converge. By doing so, the steady state mean fields are attained with a much smaller return time than with a fully unsteady computation. The work done by Chemin (2006) and Errera and Chemin (2013) also studied the convergence speed of the loop. It was also shown that in order to attain an optimal convergence speed and stability, a relaxation factor was to be used on the flux condition used by the wall's temperature solver, thus transforming it into a Robin boundary condition. This factor α depends only on the thermal properties of both media and on the spatial discretization used in the flow solver.

5.1.2 Fourier space solvers

Another method is that developped by He and Oldfield (2011) for Unsteady-RANS computations and which extension for LES is currently under study (He (2013)). Instead of solving the solid's unsteady heat equation in the time domain, it is solved in the frequency domain. The flow quantities can be decomposed using a Fourier series, meaning that for a quantity $G_f(t)$, the following can be written:

$$G_f(t) = G_0 + \sum_{n=1}^{+\infty} (A_n cos(n\omega t) + B_n sin(n\omega t)) \tag{5.2}$$

Where G_0 is the fundamental mode. For the application, only a finite number of modes N_m is used, taken between 20 and 30. It can then be written for the boundary heat flux computed by the flow solver:

$$\phi_{f,bnd}(t) = \sum_{n=0}^{N_m-1} G_n(t), \text{ and: } G_n(t) = A_n cos(n\omega t) + B_n sin(n\omega t) \tag{5.3}$$

Thanks to this decomposition, N_m solid heat equations are obtained inside the solid wall, one for each mode, which are then solved in the frequency domain for Fourier coefficients A_n and B_n. The boundary temperature is then obtained by applying a reverse Fourier transform.

The acceleration towards the permanent regime is achieved since the fundamental mode is solved apart and a steady solution is obtained for it. This approach allows for a rapid convergence of the mean field, and if enough harmonics are used to describe the flow, the statistics for the different fields can be obtained accurately and faster than with a classical transient heat transfer solver.

5.1.3 Fully unsteady simulations in time domain

The approach currently used for unsteady flows consists of computing the unsteady fields in both media, while desynchronizing the two solvers. It means that if both codes are desynchronized by a factor of 10, the fluid flow advances by a time of 1 s when the wall is advanced by 10 s. By doing so, the wall convergence towards its steady state is 10 times faster. This approach was developed in Duchaine et al. (2009) for the coupling of Large Eddy Simulations of aeronautical combustion chambers and unsteady heat transfer inside the wall, also applied by Duchaine et al.

(2013), Jauré (2012), Jaure et al. (2013) for similar applications, and deserves a thorough analysis.

This approach is here illustrated with the help of a fluid and solid media. The desynchronization factor will be noted as α. For the sake of simplicity, the period studied belongs to the interval $[0,\ t_1]$ in the fluid domain. Since a desynchronization is used, the time simulated inside both medium can be linked as follows:

$$t_s = \alpha t_f \tag{5.4}$$

This implies that when a signal U is sent from the fluid to the wall, it sees its frequency modified. It can be illustrated with the help of a sine function:

$$U_f = U_0 sin(\omega_f t_f) \tag{5.5}$$

Since the signal is equal at each coupling point, it means that:

$$U_f(t_f) = U_s(t_s) \tag{5.6}$$

This leads to:

$$U_0 sin(\omega_f t_f) = U_0 sin(\omega_s t_s) \tag{5.7}$$

And since the amplitudes of the sent and received signals are the same:

$$sin(\omega_f t_f) = sin(\omega_s t_s)\ ,\forall t_f \tag{5.8}$$

Using relation 5.4 leads to the following relation between the initial fluid signal frequency and the final frequency seen by the wall:

$$\omega_f = \alpha \omega_s \tag{5.9}$$

This means that the frequency seen by the wall is lower than the actual one seen by the flow. In practical applications, common values for α are of the order of 1000 to 10 000. Such a reduction of the frequencies seen by the wall may be problematic.

The effect of such a modification on the 1D skin effect is studied. When a domain sees a fluctuating boundary condition such as:

$$\phi_{bnd}(t) = \phi_0 sin(\omega t) \tag{5.10}$$

The resulting temperature field amplitude is the following:

$$T_s^{amp} = \frac{\phi_0}{\lambda_s}\sqrt{\frac{a_s}{\omega}} \tag{5.11}$$

Equation 5.11 shows that the amplitude of the temperature fluctuations scales with $\omega^{-\frac{1}{2}}$. The same can be shown for the depth of penetration of the thermal waves, which is defined as:

$$L_p = \sqrt{\frac{2a_s}{\omega}} \tag{5.12}$$

This means, that when a desynchronization is used, with a factor α, the desynchronized amplitude can be linked to the real amplitude:

$$(T_s^{amp})_{desync} = \sqrt{\alpha}(T_s^{amp})_0 \tag{5.13}$$

Hence, for a desynchronized coupled case, the temperature fluctuations level inside the wall are $\sqrt{\alpha}$ times higher than the reference case, and penetrate over a distance $\sqrt{\alpha}$ times higher.

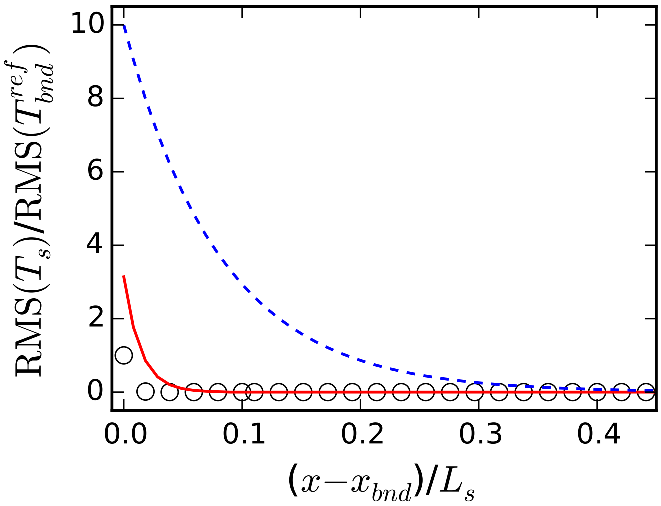

Figure 5.2: *Temperature RMS inside the wall, normalized by the reference case RMS amplitude at the fluid-wall interface. Circles: non-accelerated reference case. Red plain line: Neumann-Dirichlet coupling approach with a desynchronization factor* $\alpha = 10$*. Blue dashed line: Neumann-Dirichlet coupling approach with a desynchronization factor* $\alpha = 100$*. The* x *coordinate is normalized by the length of the solid domain and is centered at the interface position* x_{bnd}*. Case condition:* $f_{ext} = 100$ *Hz*

This approach has been tested on the configuration exposed in section 4.2. The results in Fig. 5.2 show that for a desynchronization factors of 10 and 100, the amplitude and depth of penetration of the fluctuations are effectively multiplied by $\sqrt{\alpha}$ for both values. These results are coherent with those found by Jaure et al. (2013), Amaya et al. (2010) and Amaya (2010), where one dimensional and three-dimensional studies were conducted.

Another issue that may arise, is that by artificially modifying the depth of penetration of the thermal waves, at some point the latter might reach the other side of the wall. To show such a case, a three-layer simulation is conducted (Fig. 5.3). The configuration exposed in Fig. 5.3 is similar to the one studied in chapter 4, while the right side of the wall is now in contact with another layer of gases with the same properties as the layer on the left, except that these gases are initially cold ($T = 293K$) and their outer boundary temperature is kept constant at $T_{f2,ext} = 293K$.

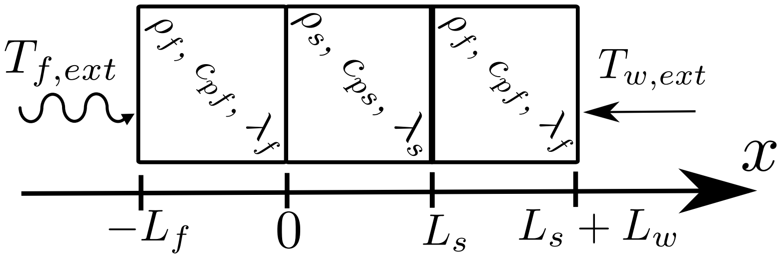
$T_{f,ext}$
$\rho_f, c_{pf}, \lambda_f$
$\rho_s, c_{ps}, \lambda_s$
$\rho_f, c_{pf}, \lambda_f$
$T_{w,ext}$
x
$-L_f$
0
L_s
$L_s + L_w$

Figure 5.3: *One-dimensional test case configuration with three layers of lengths:* L_f *=1 mm for the fluid part,* L_s *=1 mm for the solid part and* L_w *=3 cm for the second gas layer.*

The results in Fig. 5.4 show that for a solid layer, 1 mm thick, when $\alpha = 100$ and the frequency seen by the solid layer is $f_{s,bnd} = 1Hz$, about 10% of the fluctuations reach the cold side of the wall, while the temperature should stay constant. These results show that if it is wished to study a thin wall which is in contact with two different fluids, too large values of the desynchronization factor might turn the wall semi-transparent to the fluctuating perturbations sent by the fluids. The fluids then might interact in a way which does not exist in reality, and hence lead to false results. For example, when considering a combustion chamber where air cooling is used (such as in multi perforated configurations) and thin walls, as in Fig. 5.5, the hot gases interact with the cold gases which are used for cooling. This is problematic, since the cold gases which enter the chamber are then hotter than the reality, thus leading to larger temperatures at the walls.

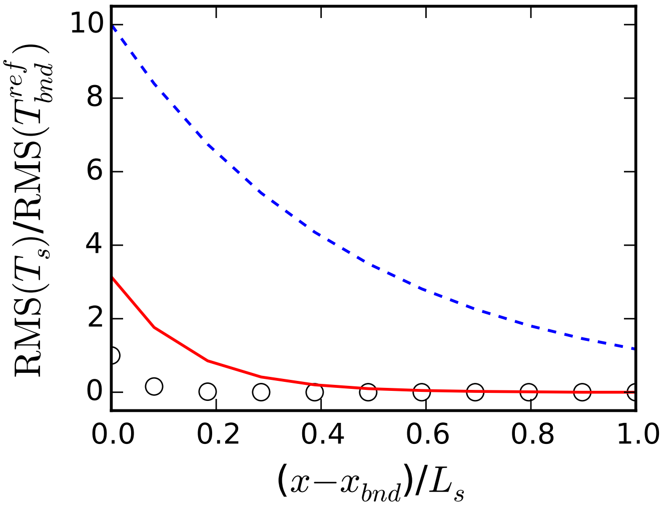

Figure 5.4: *Temperature RMS inside the wall, normalized by the reference case RMS amplitude at the fluid-wall interface. Circles: non-accelerated reference case. Red plain line: Neumann-Dirichlet coupling approach with a desynchronization factor* $\alpha = 10$*. Blue dashed line: Neumann-Dirichlet coupling approach with a desynchronization factor* $\alpha = 100$*. Case condition:* $f_{ext} = 100$ *Hz*

5.2 Accurately describing the permanent regime using unsteady solvers

Studying unsteady flows is necessary in order to obtain information on the fluctuations at the flow-wall boundary. Thus, the previous methods are not sufficient since there is no unsteady feedback from the wall to the flow. Yet, it arises new challenges, since unsteady quantities are to be measured.

As presented beforehand, the discrepancy between the fluid and solid time scales leads to a huge need in computing resources. Yet, the existing coupling methods have some limitations: One is only suited for steady

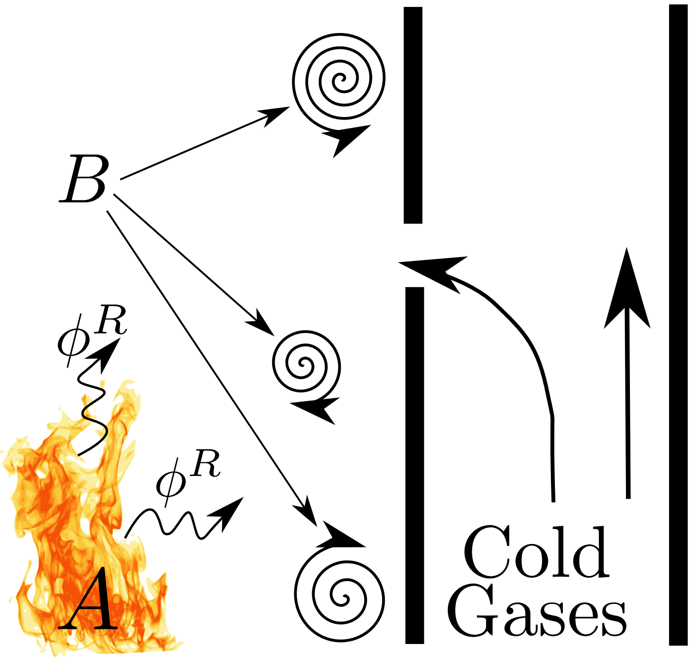

Figure 5.5: *Schematics of a combustion chamber with air cooling using perforations in the chamber walls. A: Flame. B: Hot convective eddies.* ϕ^R*: Radiative heat flux emitted by the flame and hot gases.*

or periodical flows, and another modifies the signals seen by the wall and thus the physics inside it. Moreover, none is compatible with the coupling methodology developed in chapter 4 which allows for an automatic determination of the coupling time step size. For these reasons, a new acceleration method is developed.

5.2.1 Accelerating method with coupling step size control

The method described hereafter addresses the need expressed above. It will be validated against a reference solution and two desynchronized cases (described previously) with $\alpha = 10$ and $\alpha = 100$.

The approach is based on the fact that heat transfer inside walls is a linear phenomenon. All the terms in the heat equation are linear operators. This allows a separation of the temperature field inside the wall into two contributions: A mean and a fluctuating fields.

$$\begin{cases} T_s & = \quad \widehat{T}_s + T'_s \\ 0 & = \quad \nabla \cdot (\lambda_s \nabla \widehat{T}_s) \\ \rho_s c_{p,s} \dfrac{\partial T'_s}{\partial t} & = \quad \nabla \cdot (\lambda_s \nabla T'_s) \end{cases} \tag{5.14}$$

As seen in the system of equations 5.14, the mean temperature component, $\widehat{T}$, follows a Laplace equation, while the fluctuating part, T', verifies a classical heat equation. Using this approach means that the wall heat transfer solver must now solve two equations. One for the steady temperature $\widehat{T}$ and one for the transient temperature fluctuations T'. The real temperature in the wall is simply obtained by summing both contributions.

Boundary conditions are needed for each system. The steady heat transfer solver use a prescribed heat flux as a boundary condition. The value imposed is a mean heat flux, $\widehat{\phi}_{f,bnd}$, computed by the flow solver at the fluid-solid interface:

$$\widehat{\phi}_{f,bnd}(\tau) = \frac{1}{\tau} \int_0^{\tau} \phi_{f,bnd}(t) dt \tag{5.15}$$

The computed sum depends on the total time used for the simulation, τ, meaning that the mean wall heat flux $\widehat{\phi}_{f,bnd}$ which is used by the steady heat transfer solver is actually time-dependent. However, as τ increases $\widehat{\phi}_{f,bnd}(\tau)$ falls in with its statistical steady state, and $\widehat{T}(\tau)$ behaves similarly. The permanent regime is then reached in an accelerated way since the mean solid temperature field will converge once the averaged wall heat flux has. The wall heat flux converges after several periods of the flow, while fully unsteady propagation of the temperature inside the wall will roughly take a time equal to:

$$\tau_s^{cd} = \frac{L_s^2}{a_s} \tag{5.16}$$

which is the diffusive characteristic time of the solid slab of thickness L_s and thermal diffusivity a_s. This approach functions in a similar way to the method developed by He and Oldfield (2011), where the fundamental mode is separated from the others.

The second type of boundary conditions, used by the unsteady heat transfer solver which is used to advance the fluctuating component T', is a Dirichlet boundary condition. This Dirichlet boundary condition is advanced using the hybrid cell interface model combined with the coupling time step control. In this accelerated approach, the interface model is using the heat fluxes provided by the unsteady heat transfer solver, $\phi'_{s,bnd}$, and a second flux, $\phi'_{f,bnd}$, which is the fluctuating part computed at every coupling time step through Eq. 5.19:

$$\phi'_{bnd,f} = \phi_{bnd,f} - \widehat{\phi}_{bnd,f} \tag{5.17}$$

The transient wall heat solver is now only computing the fluctuations around the mean temperature. The two fields inside the wall are initialized as follows:

$$\begin{array}{rcl} \widehat{T}_s(t=0,x) & = & T_s(t=0,x) \\ T'_s(t=0,x) & = & 0 \end{array} \tag{5.18}$$

By doing so, the automatic step size control based on the fluctuations is still adequate, since the unsteady component is still computed. Solving an unsteady heat equation allows the usage of the step size control method. Hence, this method allows an acceleration of the wall's convergence while controlling on the fly the coupling frequency. The new numerical implementation for accelerated coupling is visible in Fig. 5.6: four numerical solvers are now needed, a flow solver, a steady solid heat solver for $\widehat{T}_s$, an unsteady solid heat transfer solver for T'_s as well as the interface temperature solver for T'_{bnd}.

5.2.2 Non-linear extension of the model

If it is impossible to neglect variations of the thermal conductivity with temperature by replacing Eq. 5.14 with:

$$\left\{ \begin{array}{lcl} 0 & = & \nabla \cdot (\widehat{\lambda}_s \nabla \widehat{T}_s) \\ \rho_s c_{p,s} \dfrac{\partial T'_s}{\partial t} & = & \nabla \cdot (\lambda_s \nabla T'_s) + \nabla \cdot \Big((\lambda_s - \widehat{\lambda}_s) \nabla \widehat{T}_s \Big), \end{array} \right. \tag{5.19}$$

where $\widehat{\lambda}_s = \lambda_s(\widehat{T}_s)$. For this kind of coupling the steady heat equation is solved first. Then, the source term, $\nabla \cdot \Big((\lambda_s - \widehat{\lambda}_s) \nabla \widehat{T}_s \Big)$, can be computed and injected into the unsteady heat equation for the fluctuating part of the temperature.

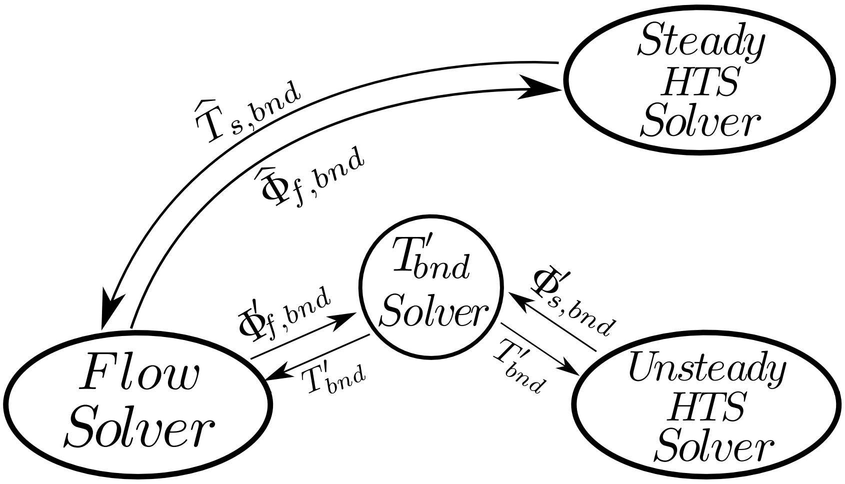

Figure 5.6: *Scheme of the interface model for coupled unsteady conjugate heat transfer when using acceleration of the physical transient heating or cooling.*

5.2.3 1D Validation of the acceleration method

The accelerated coupling method is tested on the same 1D test case series which was presented in section 4.2. It is compared to the reference solution and to the desynchronized cases with $\alpha = 10$ and $\alpha = 100$.

To better compare the methods, the boundary temperature evolution is split into two components. The first is the evolution produced by the fundamental mode of the fluid's outer boundary condition. Tracking its evolution, allows a better vision of the convergence speed of the mean temperature field inside the wall, which is often what is sought for industrial applications.

The second component studied is the fluctuating part of the boundary temperature, generated by the oscillating term in the fluid's outer boundary condition. This component was obtained by computing the difference between the instantaneous and mean solid temperature fields. By doing so, a comparison of the unsteady behaviors of the different methods is possible.

The first component is plotted in Fig. 5.7. As it can be seen, both acceleration methods attain the mean value much faster than the reference solution. Hence, when computing the mean value of the temperature field, both methods produce good results.

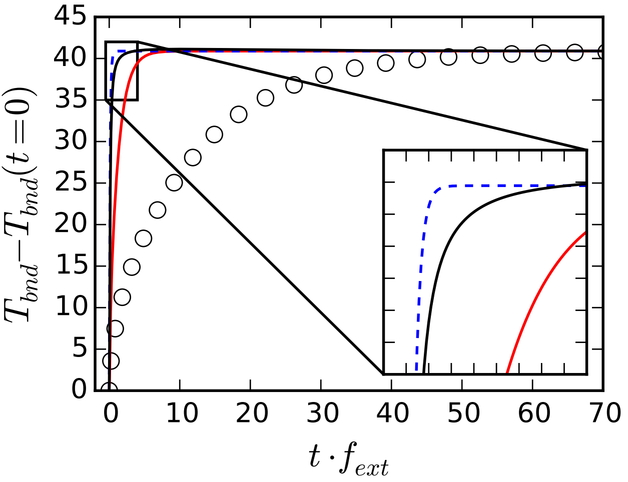

Figure 5.7: *Temporal evolution of the mean component of the boundary temperature. Circles: non-accelerated reference case. Red plain line: Neumann-Dirichlet coupling approach with a desynchronization factor* $\alpha = 10$. *Blue dashed line: Neumann-Dirichlet coupling approach with a desynchronization factor* $\alpha = 100$. *Black plain line: the acceleration method based on the superposition principle. Case conditions:* $f_{ext} = 100$ *Hz and* $\eta = 5\%$ *for the hybrid cell approach.*

Figure 5.8 shows the transient part of the temperature fields. It is possible to see that the desynchronized approach yields a signal which has a too large amplitude. The decomposition approach on the other hand provides excellent agreement for the fluctuations. There is a difference for the first few signal periods, around 5, which is due to the time needed for the convergence of the mean flux used for the computation. This means that the first few values sent for $\phi'_{bnd,f}$ are offset because of the initial non-steady mean flux, until the sampling time is large enough that the statistics are converged. The results show a very satisfying behavior of the derived accelerated coupling for both the mean component and the amplitude of the fluctuating part.

5.3 Conclusion

From these results, the main issue with the desynchronized coupling which arises is the modification of the frequencies seen by the wall. A possible way to fix this drawback is to resynchronize the flow and wall solvers once the mean fields have converged. This is followed by the computation of several flow-through times of the studied flow. Though the flow-wall interface temperature fluctuations are reduced, it is impossible to predict in advance the exact number of flow-through times needed so that the fluctuations re-attain their expected non-desynchronized level. If the statistics inside the wall itself are sought, then the physical time needed is several solid diffusive time scales, τ_s^{cd}, thus rendering the correction too expensive.

Using the acceleration method based on the superposition principle of the heat transfer equation does not change the frequencies seen by the solid wall and thus does not affect the physics inside the wall. The computed fluctuations have the same amplitude as those computed with non-accelerated simulations all the while accelerating the convergence of the mean component towards the permanent regime. Moreover, this approach is compatible with the previously developed coupling step size determination algorithm based on the hybrid-cell interface model. The resulting coupling methodology is hence capable of computing transient heating (or cooling) processes as well as artificially attaining the permanent regime when the transient is not needed, all the while allowing for an automatic determination of the optimal coupling period.

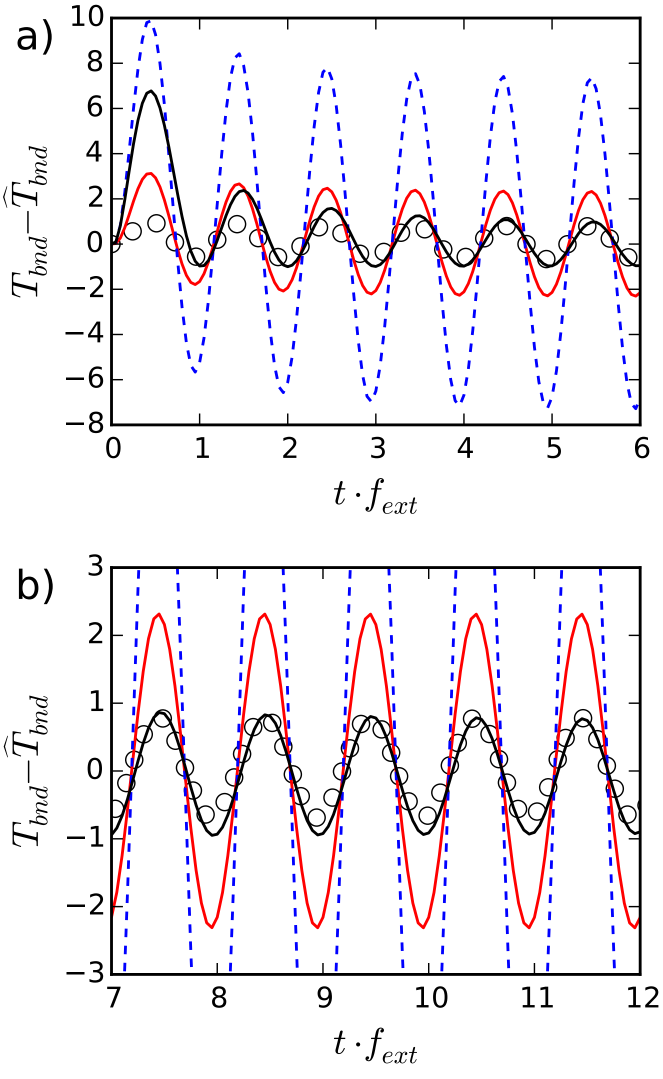

Figure 5.8: *Fluctuating components of the boundary temperature plotted against the time normalized by signal period.*

Chapter 6

Numerical simulation of a three-dimensional configuration of flame-wall interaction

6.1 Simulated configuration 116

6.2 Non-coupled flow simulation 118

6.2.1 Numerical setup 118

6.2.2 3D reactive simulation 119

6.3 Coupled conjugate heat transfer simulations . 124

6.3.1 Numerical setup 124

6.3.2 Coupling procedure 126

6.3.3 Non-accelerated simulation 126

6.3.4 Accelerated simulation 128

6.3.5 Pulsed flow coupled simulations 131

6.4 Conclusion 136

The coupling hybrid-cell based coupling method with an automatic determination of the coupling time step, developed in chapters 3, 4 and 5, is applied here on a configuration of flame-wall interaction experimentally studied by Singh et al. (2013). The experimental configuration consists of a jet flame impinging on a cooled wall made of quartz. The simulations are conducted with the help of the low Mach flow solver YALES2 and a solid heat transfer solver from the YALES2 library. Combustion is accounted for using complex chemistry and the chemical mechanism developed by Coffee (1986).

6.1 Simulated configuration

The experimental setup retained for validation of the coupling strategy is the work conducted by Singh et al. (2013). It consists of a jet flame impinging a solid disc which is cooled on the other side. The experimental setup is visible in Fig. 6.1. The cooled disc is made from quartz, which allowed non-intrusive optical measurements on both of its faces.

The jet is composed of a mixture of air and methane with an equivalence ratio of 0.83. Thus, the studied configuration is that of a premixed flame. The injector's exit diameter is 3 cm and is located at $z = 0$. The disc center point is located at $z = 3$ cm, one injector diameter from the nozzle. The Reynolds number based on the jet's mass flow rate and nozzle diameter is 2 500.

The primary jet is surrounded by a co-flow of pure nitrogen with a bulk velocity which is equal to 20% of the premix's bulk velocity when exiting the injector. The co-flow is used in order to reduce the shear stress of the surrounding air on the main jet, and hence stabilize it. All fresh gases are at 300 K and are not preheated.

The available data consists of the temperature fields on the cold and hot faces of the disc wall (Fig. 6.2), as well as of the temperature field over the centerline axis and the value of the heat flux at the wall's center. The temperature field over the quartz disc were measured using Laser Induced Phosphoresence (LIP) with the help of a special painted strips. The gas temperature was measured using N_2 ro-vibrational CARS.

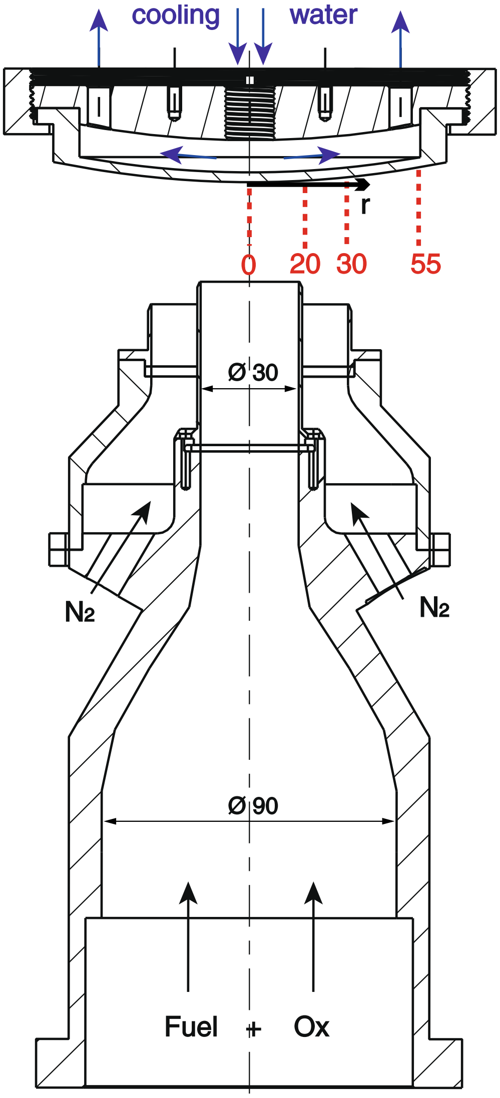
cooling
water
r
0
20
30
55
Ø 30
N2
N2
Ø 90
Fuel + Ox

Figure 6.1: *Experimental setup studied by Singh et al. (2013) Lengths are in mm.*

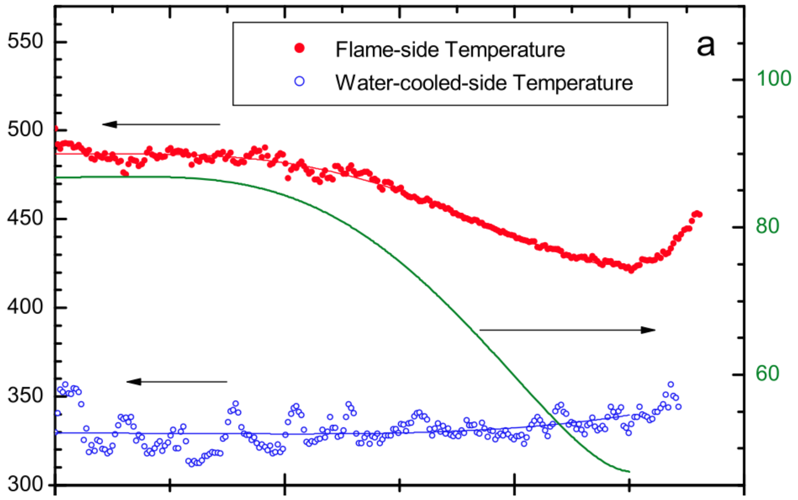

Figure 6.2: *Experimental temperature (in K) measurements along the disc's radius on both hot (red color) and cold (blue color) sides. Circles: Measurements. Lines: data fits Green line: Computed heat flux (in W/m^2) using the temperature fits. Extracted from Singh et al. (2013)*

6.2 Non-coupled flow simulation

Non coupled reactive flow simulations were first conducted in order to assess the capability of the flow solver to correctly solve the flow and predict the wall heat flux.

6.2.1 Numerical setup

Simulations are conducted with the Low Mach solver YALES2 (Moureau et al. (2011), Malandain (2012)), presented in chapter 2. The combustion is taken into account with the help of the chemical mechanism of Coffee (1986).

The numerical schemes used are the fourth order spatial discretization and fourth order time integration scheme TFV4A. The mesh used consists of 38 million tetrahedral elements.

Given the low Reynolds number, no LES model was needed in order to correctly resolve the flow. But to correctly resolve the flame front, an artificial thickening is required. The equations solved are the TFLES equations, written in chapter 2, and which are the following for the mass:

$$\frac{\partial \rho}{\partial t} + \nabla \cdot (\rho \mathbf{u}) = 0 \tag{6.1}$$

Momentum:

$$\frac{\partial \rho \mathbf{u}}{\partial t} + \nabla \cdot ((\rho \mathbf{u}) \otimes \mathbf{u}) = -\nabla p + \nabla \cdot \tau + \mathbf{g} \tag{6.2}$$

A given species k:

$$\frac{\partial \rho Y_k}{\partial t} + \nabla \cdot (\rho \mathbf{u} Y_k) = -\nabla \cdot (\mathcal{F} \rho \mathbf{V_k} Y_k) + \rho \frac{\dot{\omega}_k}{\mathcal{F}} \tag{6.3}$$

And sensible enthalpy:

$$\frac{\partial \rho h_s}{\partial t} + \nabla \cdot (\rho \mathbf{u} h_s) = \frac{\partial p}{\partial t} + \frac{\dot{\omega}_T}{\mathcal{F}} - \nabla \cdot (\mathcal{F} \mathbf{q}) \tag{6.4}$$

$$\dot{\omega}_T = -\sum_{k=1}^{N} \Delta h^0_{f,k} \dot{\omega}_k \tag{6.5}$$

$$\mathbf{q} = \frac{\lambda}{c_p} \nabla h_s - \rho \sum_{k=1}^{N} h_{s,k} Y_k \mathbf{V}_k \tag{6.6}$$

It is important to note that since the main interest is the correct prediction of the boundary temperature and the boundary heat flux, the thickening should not occur at the disc boundary. Otherwise, the thickening will modify the temperature gradient and heat diffusivity on the fluid side, and hence the heat flux. All the results which follow in this section are first obtained from a ***non-coupled*** flow simulation with a prescribed value of $\mathbf{T_{disc}}$ = ***500K*** on the disc surface seen by the flow. The value of 500 K was chosen since it is close to the experimentally measured value in disc center position.

6.2.2 3D reactive simulation

The computation was initialized with all gases at 300 K. The ignition was done by depositing a 10 mm wide hot gases spherical kernel at $z = 15$ mm on the centerline axis, mimicking a spark ignition. A field cut of the temperature field after the sphere deposition is visible in Fig. 6.3.

In Fig. 6.4, a snapshot of the mean temperature is shown. It is possible to see the position of the flame front (A) at about 8 mm from the wall, as

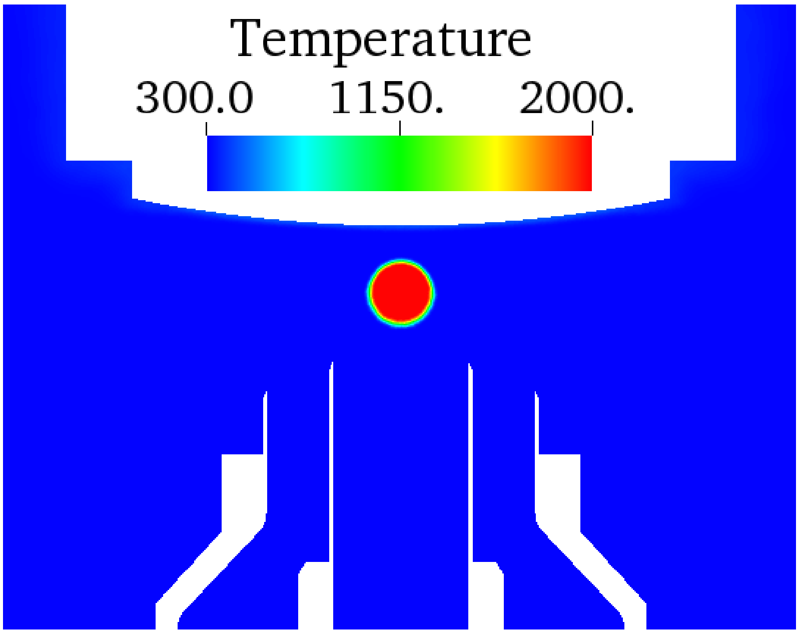

Figure 6.3: *Field cut of the gas temperature for the uncoupled large eddy simulation once the ignition kernel is placed.*

well as the two large green zones (B) where the temperature is approximatively 1000 K. These two zones are due to the nitrogen coflow which dilutes the burnt gases, and hence slows the chemical reactions.

Figure 6.5 shows the mean value of the flame sensor, temperature and progress variable source term along the centerline axis. It can be seen that the thickened zone is about 5 mm large and centered around 7.5 mm from the wall. This means that the last 5 mm, the nearest to the wall, are not thickened. Thanks to this, the thermal diffusivity and the temperature gradient in the near wall region are not modified. The unchanged fields should lead to a non modified heat flux at the wall, and would not corrupt the coupled simulation.

The flame front position, x_{flame}, is defined as the location where the temperature gradient is the largest:

$$\frac{\partial T}{\partial x}(x_{flame}) = max\left(\frac{\partial T}{\partial x}\right) \tag{6.7}$$

The experimentally measured flame front is located at 6.5 mm from the wall while the numerically computed flame is at 7.5 mm. The reason for the numerical flame to be farther downstream from the wall can be explained with the results shown in Chapter 2, where the laminar flame speed obtained with 1D freely propagating premixed flames was slightly larger than the one experimentally measured. Hence, it is logical for the premixed flame to stabilize farther from the wall, in a region where the gases velocity is higher.

The axial profile of CO molar fraction is plotted in Fig. 6.6. It shows a comparison between the standalone computation and the experimental measurements along the centerline axis. This comparison shows an overshoot in the estimated CO molar fraction as well as an offset in the peak value position. The offset in the peak position can be explained by the offset in the flame front position due to the larger numerical laminar flame speed. Similarly, the larger width of the peak is explained by the use of artificial thickening of the flame (TFLES model). The larger peak value could be explained with the fact that the kinetic scheme of Coffee (1986) may not contain enough species and that it was not optimized for the computation of CO mass/molar fractions.

In Fig. 6.7 the experimental and numerical temperature fields near the wall are compared. Since the boundary condition used is not far from the experimentally measured one, there is a very good agreement for this computation between the two fields. The two curves are nearly perfectly superimposed. This agreement also proves that the mesh used is sufficiently refined in order to correctly resolve the thermal boundary layer.

As mentioned earlier, the heat flux in the gas side was measured at the center point of the wall in the work of Singh et al. (2013). This measurement was possible thanks to temperature measurements in the very near vicinity of the wall's surface in flow (CARS measurements). The experimentally measured value is 69.8 kW/m^2 while the numerical value extracted from the simulation is 69.2 kW/m^2. The difference between the two values is less than 1% which is satisfying. The fact that value found numerically is slightly lower than the experimental is predictable since the boundary condition used was of 500K at the boundary while the measured temperature was around 490K. Since the numerically computed temperature field in the fluid part is nearly the same as the experimentally measured one, the numerical temperature gradient is thus lower.

These results show that with a boundary condition not far from the experimentally measured one, good agreement was found between the simulation and the experience. This first simulation also showed that the

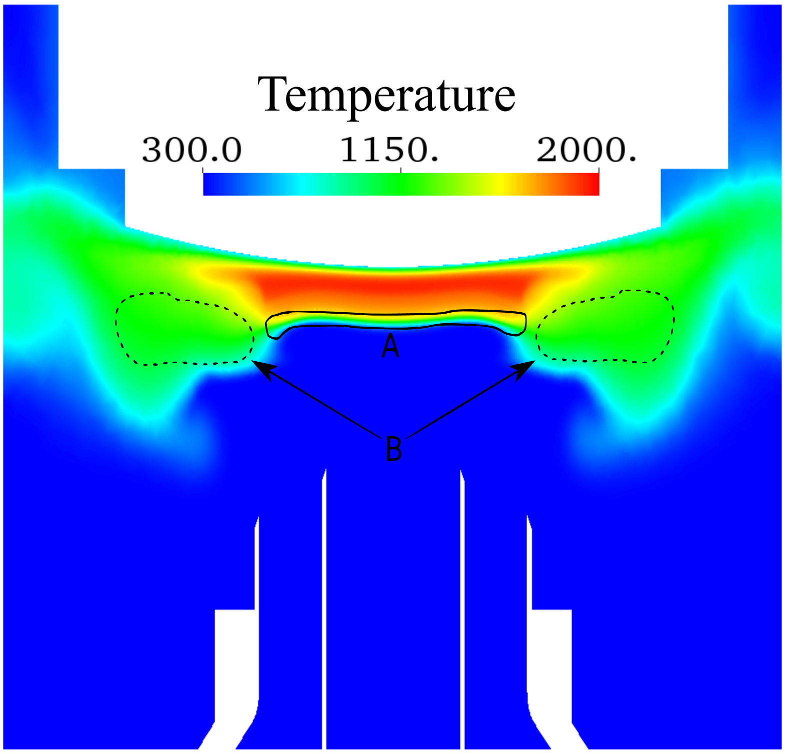

Figure 6.4: *Field cut of the gas mean temperature for the uncoupled simulation. A: Reaction zone delimited by the iso-line* $\dot{\omega}_{Y_c} = 0.1\dot{\omega}_{Y_c}^{max}$*. B: Dilution zones where the hot gases encounter the coflow of* N_2*.*

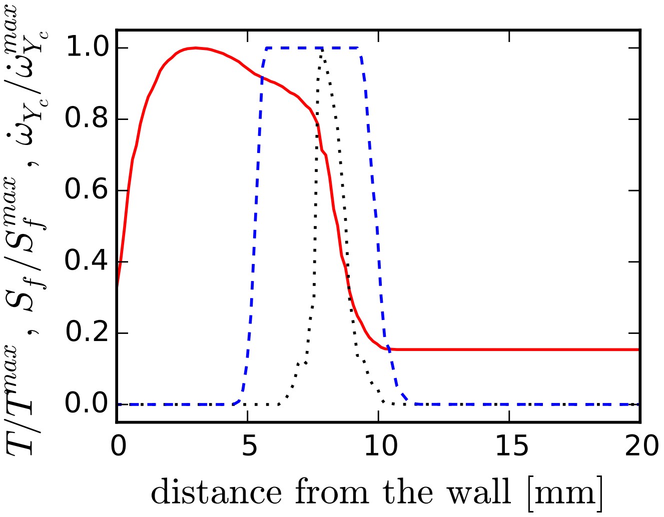

Figure 6.5: *Profile of the normalized temperature (red plain line), flame sensor S_f (blue dashed line) and progress variable source term $\dot{\omega}_{Y_c}$ (black dotted line) along the centerline axis.*

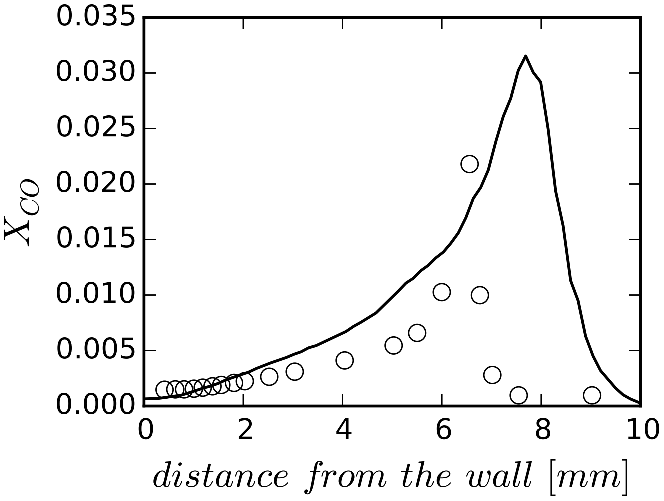

Figure 6.6: *CO molar fraction profile along the centerline axis as a function of the distance from the wall. Black plain line: numerical results. Black circles: Experimental measurements.*

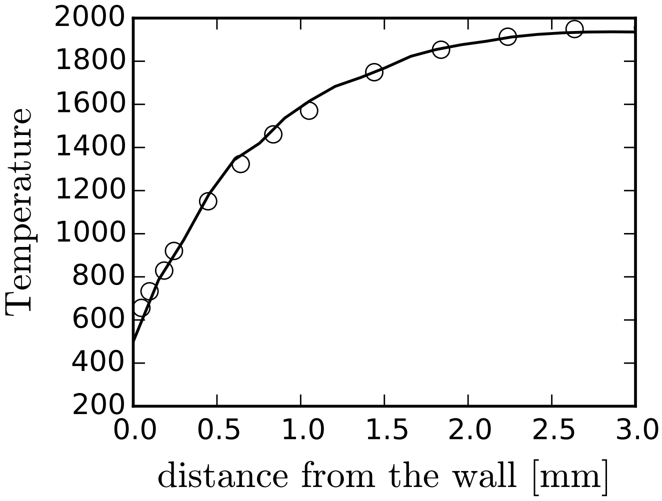

Figure 6.7: *Comparison of the experimental (symbols, Singh et al. (2013)) and numerical (plain line) mean temperature in the near wall region along the centerline axis.*

numerical setup of the reactive flow is well suited for this configuration: The thermal boundary layer is correctly resolved and no thickening is occurring at the near wall vicinity, thus not altering the wall heat flux needed for coupled conjugate heat transfer simulations.
The complete cost of this simulation, including the initialization and computation of flow statistics, is about 275,000 cpu hours on the OCCIGEN supercomputer located at the CINES computing center in Montpellier, France.

6.3 Coupled conjugate heat transfer simulations

The non coupled simulations showed positive results. Especially, the local thickening did not modify the different fields in the near wall vicinity, and the coupled simulation can be carried out.

6.3.1 Numerical setup

The unsteady heat transfer solver is part of the YALES2 framework and uses finite volumes and explicit fourth order schemes for space discretization and time integration. The data structure is the same as for the flow solver as well as the space discretization. The equation solved is:

$$\rho c_p \frac{\partial T}{\partial t} = \nabla \cdot (\lambda \nabla T) + \mathcal{P} \tag{6.8}$$

where $\mathcal{P}$ is a heat source. The time integration used is fourth order explicit Runge-Kutta scheme. The wall's mesh consists of around 8 millions tetrahedra, with cells of the size of 0.25 mm.

The steady part of the heat solver solves the following equation:

$$\nabla \cdot (\lambda \nabla T) = 0 \tag{6.9}$$

This equation is solved with the help of a linear Poisson-solver using a deflated conjugate gradient method (Malandain et al. (2013)). Both heat solvers are applied on the disc heated by the flame on one side and cooled on the other side. A zoom of the zone of interest, showing both fluid and solid meshes is given in Fig. 6.8.

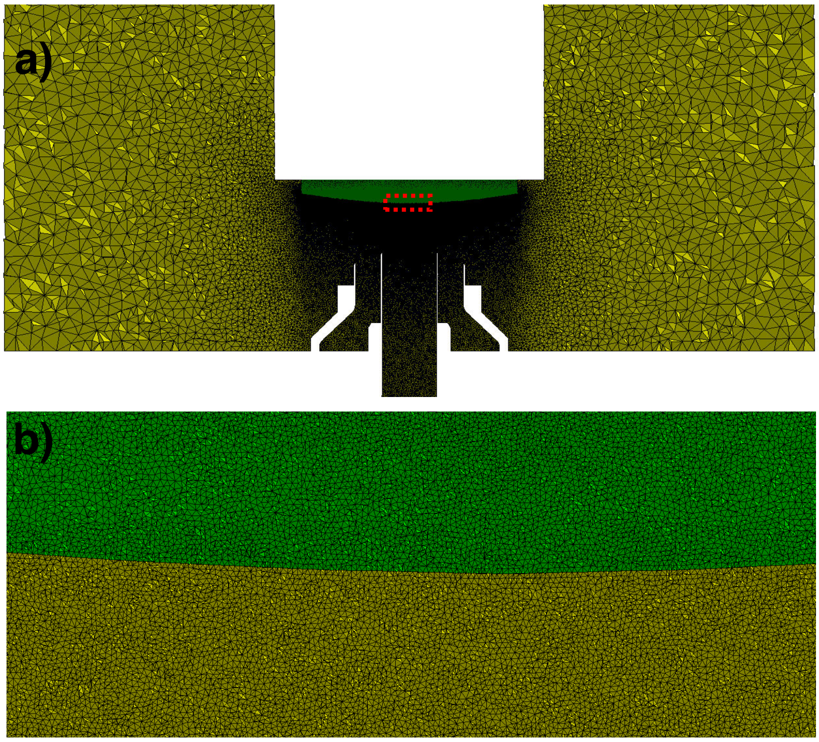

Figure 6.8: *Cuts of fluid (yellow) and solid (green) meshes. (a) Injection burner, coflow and solid disc. (b) Zoom in the interface zone between the solid and fluid domains identified by the red square in Fig.(a).*

6.3.2 Coupling procedure

All codes are coupled with the help of the dynamic coupler OpenPALM Buis et al. (2006). OpenPALM was chosen because it was specifically developed for massively parallel coupled simulations. It allows for generic couplings, since the different data sets are sent to OpenPALM and then dispatched to the correct recipient. It also allows for non conforming meshes by using third order conservative interpolation schemes for the sent data (See chapter 2).

Three different coupling methods are used in this study:

- A Neumann-Dirichlet coupling, using the parallel communication scheme. This approach will also be used in its desynchronized version for the accelerated case tests.
- A hybrid-cell based coupling. Both codes use the same Dirichlet boundary condition and the interface temperature is determined by solving Eq. 3.43. The coupling time step will be determined with the help of the automated step size control algorithm.
- An accelerated hybrid-cell based coupling. Same basics as the previous method, except that the heat transfer solver solves two equations: A Laplace equation for the mean temperature field and an unsteady heat equation for the fluctuating part.

For three-dimensional computations, when the step size control is used, the optimal step size is computed on each cell individually, and the minimal value is chosen as the global value for the entire code.

6.3.3 Non-accelerated simulation

For this coupled simulation, the initial flow field was obtained from a **standalone** uncoupled, **non-reactive** simulation with a boundary condition of **300 K** on the disc surface. The initial temperature field inside the solid disc was taken as a uniform field at 300 K as well. The temperature on the cold side of the disc was imposed using the experimentally measured values. The initial fluid field used is the one available from the non-coupled simulation.

A first run is done without acceleration of the solid temperature field, with a prescribed tolerance $\eta = 5\%$. The physical time simulated is equal to 25 ms, and corresponds to about one flow-through time of the gases through the zone of interest. The evolution of the temperature over time, at the center of the wall, is visible in Fig. 6.9.

This first simulation of a physical time of 25 ms, conducted on GENCI's Bull supercomputer, OCCIGEN located in Montpellier, France, cost around 4 000 CPU hours. To attain the discs thermal mean steady state, at least 30 seconds have to be simulated. Simulating this kind of physical time represents a computational cost of over 4 million CPU hours just for the flow solver in a standalone configuration. A coupled simulation will cost more, since it requires to compute the wall's temperature, and it is likely that the flow solver will be somewhat hindered by the solid solver. Such a computational cost is prohibitive and highlights the need for an acceleration method.

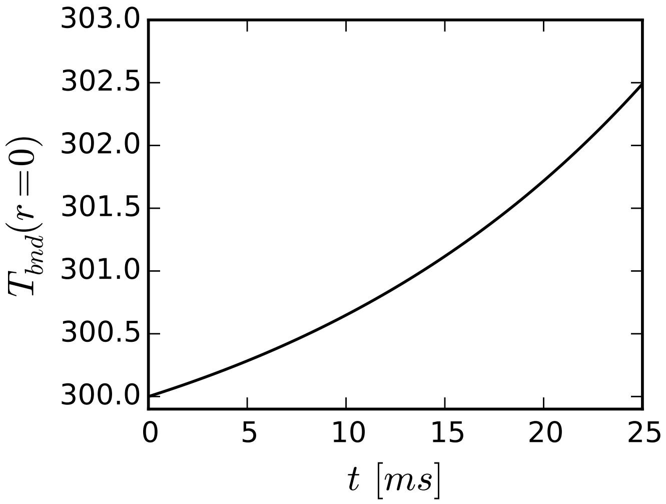

Figure 6.9: *Temporal evolution of the boundary temperature at the disc center for a non-accelerated coupled simulation*

As seen in Fig. 6.10, where the temporal evolution of the coupling time step scaled by the flow solver limiting diffusive time step, the coupling time step is nearly constant. The reason is that the studied case's turbulence is very low, due to the Reynolds number of 2500.

A second run with $\eta = 0.1$ was conducted and the results are also plotted in Fig. 6.10. This second run goal was to see the possible influence of the prescribed error tolerance on the coupling time step. The comparison of

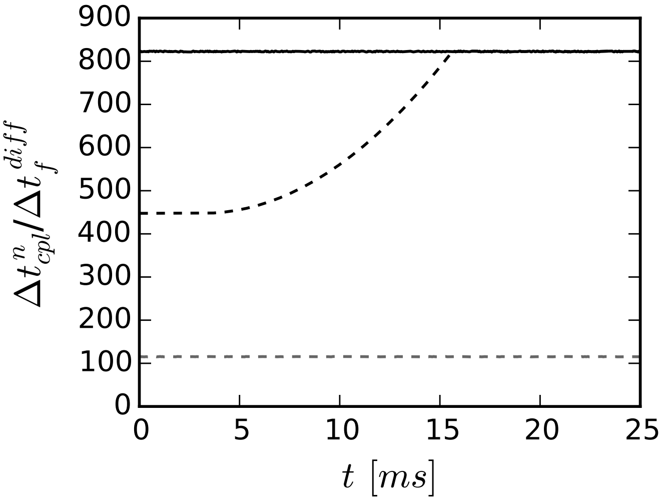

Figure 6.10: *Temporal evolution of the coupling time step scaled by the flow solver limiting diffusive time step for the tolerance η =5% (black plain line) and 0.1% (grey dashed line) without any acceleration. Dashed black line: accelerated simulation from Sec. 5.3.4 with η =5%.*

both cases shows that the automatic coupling step size control is working, though the on the fly control has a low impact. Nevertheless, it is important to take note of the fact that the mean value of the coupling step size was determined by the control algorithm alone, and based on the error tolerance prescribed for each case.

6.3.4 Accelerated simulation

Two computations were done: The first, using a Neumann-Dirichlet coupling with the desynchronized approach, with $\alpha = 1\ 000$. The coupling time step for this Neumann-Dirichlet method is taken equal to the mean value retrieved by the hybrid cell method without acceleration with $\eta = 5\,\%$: 800 times the flow solver limiting diffusive time step. The second was done with the accelerated hybrid-cell based method, with the temperature field divided into mean and fluctuating sub-fields. The error tolerance value chosen is $\eta = 5\%$. The mean heat flux value extracted from the standalone flow simulation is used as the initial condition for the mean heat flux used by the steady heat solver.

The evolution of the coupling time step scaled by the flow solver limiting diffusive time step for the hybrid-cell method combined with acceleration is plotted in Fig. 6.10. The initial value is lower than the one recorded for the non-accelerated computation, which is due to the evolution of the boundary temperature. The coupling time step then increases before attaining the value measured for the non-accelerated simulation once the mean boundary temperature is nearly converged (Fig. 6.11). Figure 6.11 shows the temporal evolution of the temperature's mean contribution. In both accelerated cases, the permanent regime is achieved very fast compared to a non-accelerated simulation. The fact that the duration of the accelerated transient is similar with both acceleration methods is fortuitous with the desynchronization factor $\alpha = 1\,000$. Results for the mean temperature on the wall are available in Fig. 6.12 for the two methods.

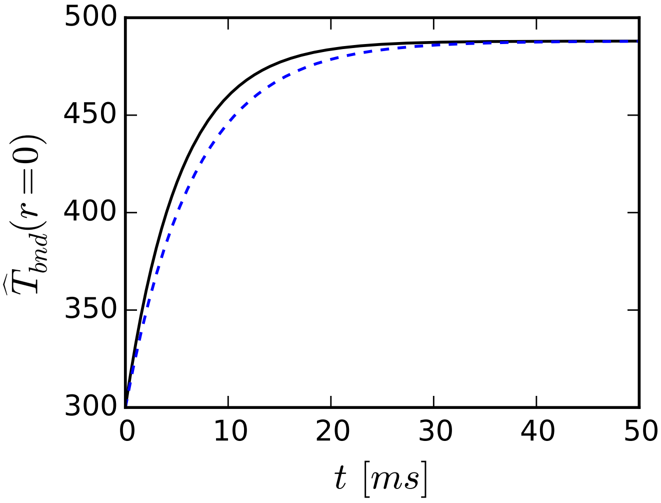

Figure 6.11: *Temporal evolution of the computed mean contribution of the boundary temperature at the disc center for two acceleration methods: Hybrid cell interface model with acceleration based on superposition,* $\eta = 5\%$ *(black plain line); Neumann-Dirichlet coupling approach with a desynchronization factor* $\alpha = 1000$ *(blue dashed line).*

Fig. 6.12 shows that for both coupled simulations, a very good agreement is achieved for the mean temperature field on the wall's hot surface. The local error is around 1%, which indicates a good result. The surface mean temperature field obtained with the hybrid cell based coupling method is given in Fig. 6.13.

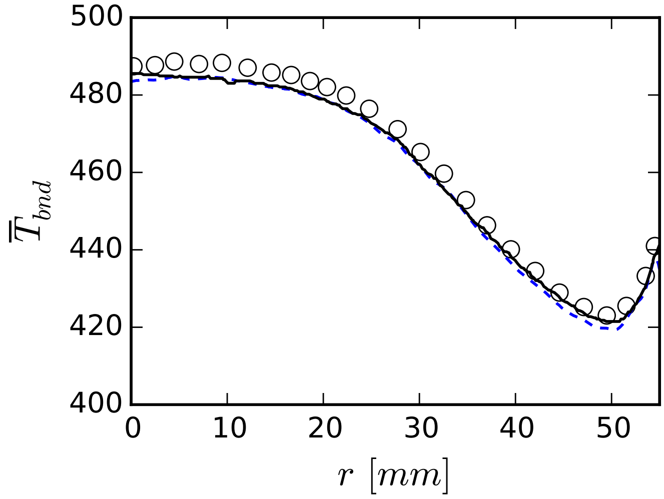

Figure 6.12: *Comparison between experimental and numerical data for the mean boundary temperature as a function of the distance from the center of the disc. Circles: experimental data Singh et al. (2013). Black plain line: Hybrid cell interface model with acceleration based on superposition,* $\eta = 5\%$. *Blue dashed line: Neumann-Dirichlet coupling approach with a desynchronization factor* $\alpha = 1000$.

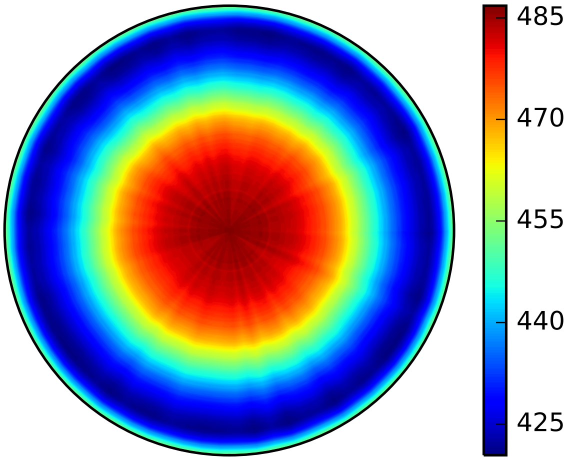

Figure 6.13: *Color map of the mean temperature field over the disc surface for the Hybrid cell interface model with acceleration based on superposition,* $\eta = 5\%$ *case.*

6.3.5 Pulsed flow coupled simulations

The experimental setup presented a low Reynolds number, which leads to a nearly laminar configuration. For this reason, a modified computation was conducted, in order to test the coupling step size control in a configuration which showed more fluctuations. To do so, a pulsed case was computed. It is important to note that no experimental data is available for this kind of flow configuration, and it is only the step size control algorithm which is tested.

The pulsing is done by modifying the entering mass flow-rate of the premixed gases. The mass flow-rate follows the following temporal law:

$$\dot{m}^{premix}(t) = \dot{m}_0^{premix} + \dot{m}' sin(2\pi f_{ext} t) \tag{6.10}$$

Where $f_{ext} = 40$ Hz and:

$$\dot{m}' = 0.15 \dot{m}_0^{premix} \tag{6.11}$$

The forced pulsations of velocity at the inlet, increase the stress in the shear layer between the premixed gases and the nitrogen coflow. The increased stress leads to the creation of vortices in the zone, starting from the injector's tips. Theses vortices modify the form of the flame front, and as consequence, the heat flux in the inner part of the wall. The structures created are visible in Fig. 6.14 which shows a snapshot of the instantaneous N_2 mass fraction field. It is also possible to see that the structures reach the flame front. At some locations of the wall, where the diluted zones seen in Fig. 6.4 begin, an alternation of hot and cold pockets appears. This modification leads to modification of the heat flux at the outer part of the plate (seen in Figures 6.16 and 6.17).

Figure 6.15 shows a snapshot of the temperature field at the same time. It is possible to see that the turbulent structures modify the temperature field near the flame front, as well as the form of the reaction zone delimited by the black line.

Figure 6.16 shows the boundary temperature RMS radial profiles over the disc surface. As expected, the desynchronized method yielded larger temperature fluctuations, up to one order of magnitude, than the hybrid cell based coupling method. A similar trend is seen in Fig. 6.17 concerning the heat flux RMS values normalized by the mean value over the wall's surface.

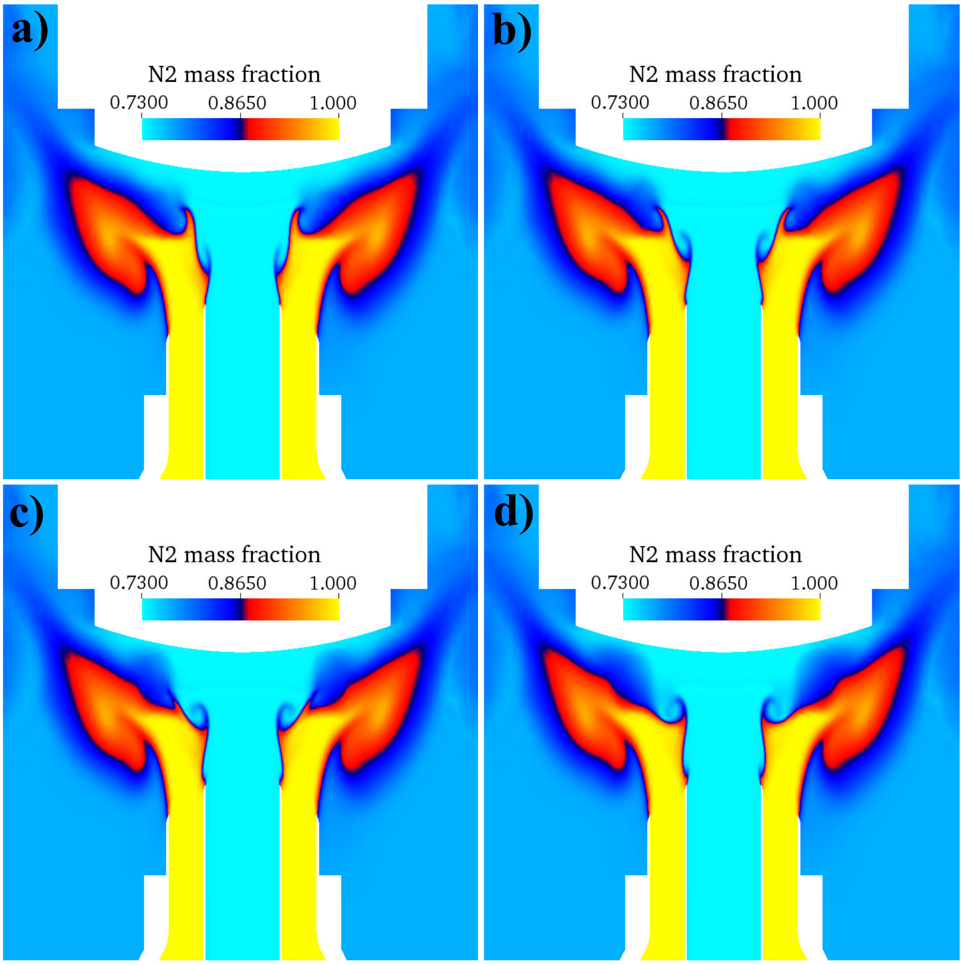

Figure 6.14: *Instantaneous colored maps of N_2 mass fraction in the pulsed configuration simulated with the hybrid cell interface model combined with acceleration, taken at 4 different instants and are spaced every* $5\,ms$.

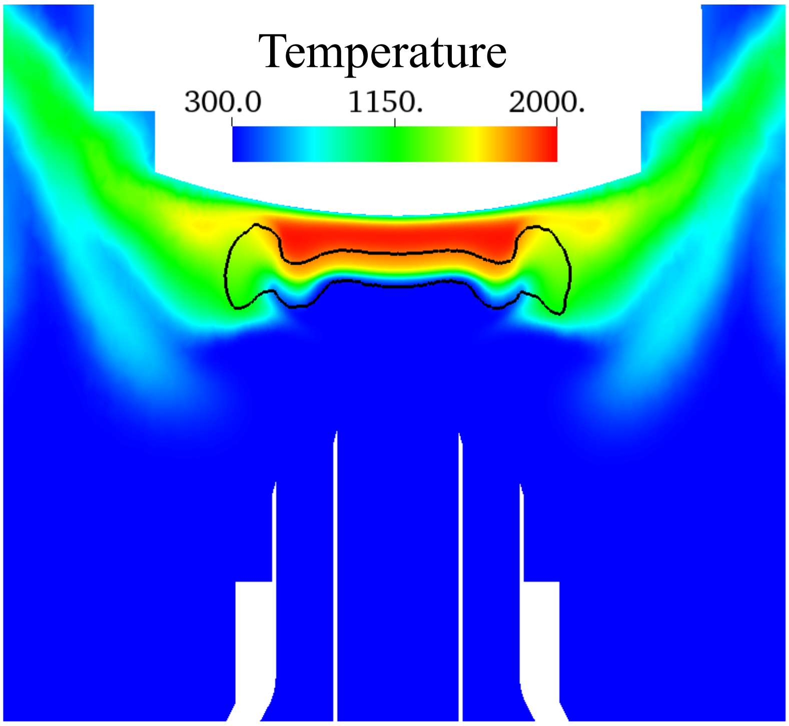

Figure 6.15: *Color map: Temperature field. Black line indicates the flame position as in Fig. 6.4. simulated with the hybrid cell interface model combined with acceleration.*

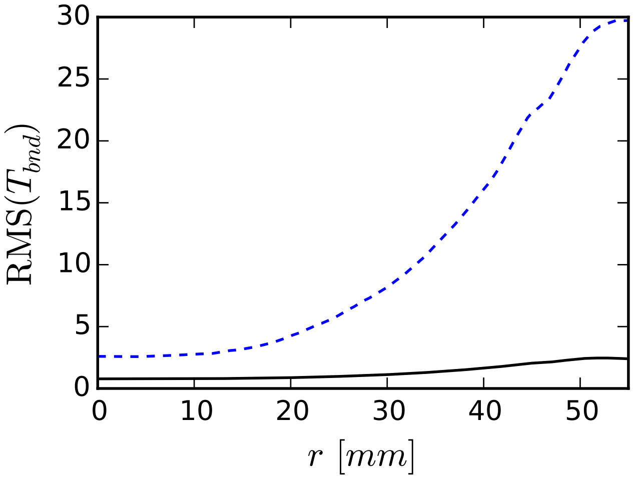

Figure 6.16: *Radial profiles of the disc temperature RMS computed by the accelerated hybrid cell approach (black plain line) and by the accelerated Neumann-Dirichlet coupling with a desynchronization factor* $\alpha = 1000$ *(blue dashed line).*

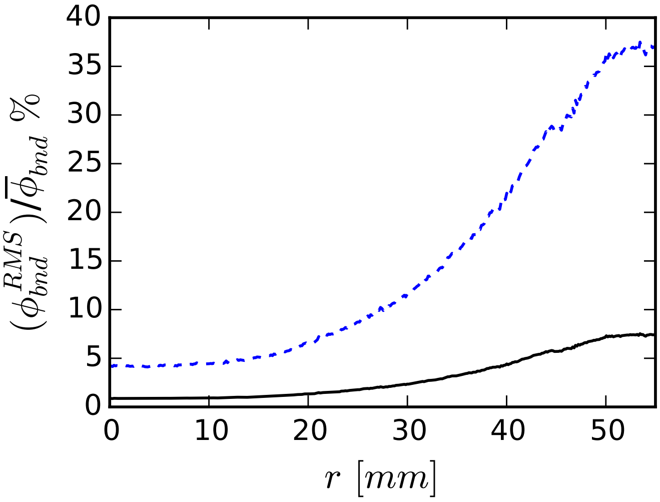

Figure 6.17: *Radial profiles of the relative wall heat flux RMS computed by the accelerated hybrid cell approach (black plain line) and by the accelerated Neumann-Dirichlet coupling with a desynchronization factor* $\alpha = 1000$ *(blue dashed line).*

For both wall temperature and wall heat flux the results show an increase of the heat flux fluctuations towards the extremities, which starts at around 17 mm from the center. This is the position where the alternating hot/cold eddies collide with the disc after being generated in the premix/coflow shear layer. The large difference at the wall's extremities when compared to the center is a function of two parameters: First is the hot/cold eddies aforementioned. The second is that the mean temperature in that zone was lower because of the nitrogen dilution created by the coflow. Thus, the arrival of noticeably hotter gases leads to higher heat flux fluctuations.

In Fig. 6.18 the evolution of the boundary center's temperature is plotted over time. It shows small fluctuations, the maximal value is of about 1 degree. The fluctuations have the same frequency as the mass flow rate's fluctuations.

Figure 6.19 shows the evolution of the coupling time step over time. Three zones can be seen: A first one, which is defined by a constant coupling time step and corresponds to the time needed for the turbulent eddies to arrive at the wall. The second zone is the one which corresponds to a time lapse during which no coherent structure is seen. It starts when

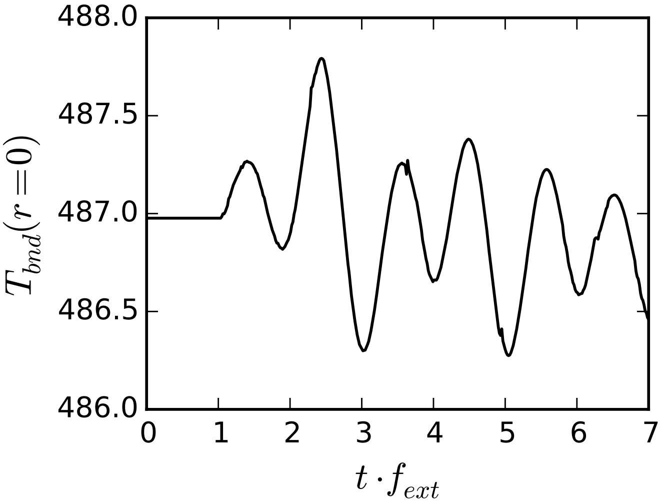

Figure 6.18: *Temporal evolution of the boundary temperature at the center position of the disc computed with the hybrid cell interface model combined with acceleration.*

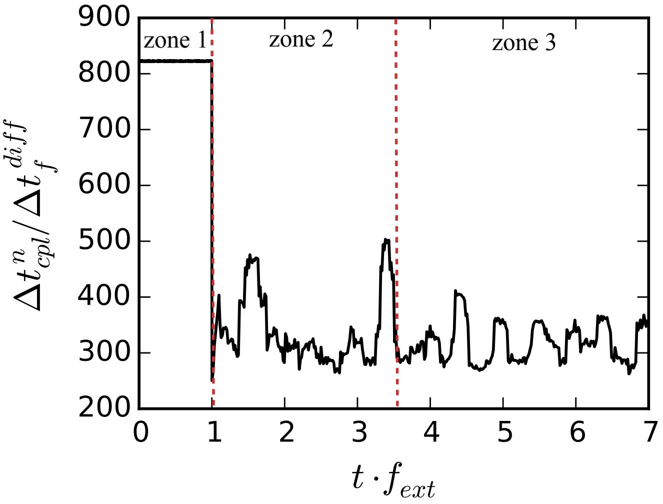

Figure 6.19: *Evolution of the coupling timpte step as a function of time. Time* $t = 0$ *is taken at the moment pulsations of the mass flow rate begin. Time is normalized by the inlet's mass flow rate fluctuation frequency.*

the coupling step size decrease instantly, dropping from 800 to around 300 (6.19), signaling that the turbulent eddies have begun arriving at the wall. Finally, a third zone is seen, for which a repetitive behavior is seen for the coupling time step.

The alternation of peak values in the third zone seems to happen twice during a period of mass flow rate's oscillation. This result can be linked to what was seen in chapter 4, where the sine signal period has two instants where the function is the stiffest. In this case, the peaks are quite evenly spaced and have a similar behavior.

All of these results show that it is the turbulence created by the inlet mass flow-rate pulsation which defines the coupling step size.
As expected, the desynchronized Neumann-Dirichlet coupling method yielded larger temperature and wall heat flux fluctuations at the fluid-solid interface (Figures 6.16 and 6.17), though the mean temperature value remained the same (as in Fig. 6.12 for the non-pulsed configuration.). Moreover, for this more unsteady configuration, the step size control algorithm showed that it was capable of capturing such a phenomenon, and that a modification of the frequencies in the domain is well handled. These results are promising concerning future works on the subject and for turbulent combustion and/or conjugate heat transfer.

6.4 Conclusion

In this chapter, an experimental configuration of flame-wall interaction was studied. A first computation, conducted using only a reactive flow solver allowed a better understanding of the flow behavior and showed that the flow solver was well suited for the investigated configuration.

A second set of simulations has then been conducted. The first coupled run highlighted the need for an artificial acceleration of a coupled flow-wall simulation in order to achieve acceptable computational cost. It allowed nonetheless to test the coupling time step size control algorithm on a three-dimensional test case.

It was followed by two series of accelerated coupled simulations. The first series used a Neumann-Dirichlet coupling with the desynchronization method which is the most common approach for high-fidelity computations. The second series used the hybrid-cell based coupling with an acceleration of the mean field. The comparison of both series showed that results for the mean temperature field on the surface separating flow and wall were similar. This showed that the hybrid-cell methods provides similar results to a well established approach, while providing the possibility to have an automatic control of the coupling frequency.

A last set of computations was conducted in order to test the behavior of the step size control algorithm in a more unsteady configuration. The results showed that the control algorithm is capable of capturing the change in the fluctuations frequency.

All of these results are promising for the future works, where this hybrid-cell based coupling method could be applied to numerical simulations of conjugate heat transfer. This methodology is giving the user a way of finding an optimal step size as a function of the precision required. It is a first of a kind for coupled conjugate heat transfer simulations.

This work has also highlighted the need for experimental measurements of the wall temperature fluctuations in order to further validate the accelerated hybrid cell coupling methodology in turbulent configurations of conjugate heat transfer.

Chapter 7

Application of the Conjugate Heat Transfer methodology to a laboratory-scale combustor

7.1 Experimental test rig and available measurements . . . 141
7.2 Numerical setup . . . 143
7.2.1 Combustion model: F-TACLES . . . 143
7.2.2 Outer boundary condition . . . 149
7.2.3 Applying the outer boundary condition to the steady heat transfer solver . . . 151
7.2.4 Numerical configuration . . . 152
7.3 Results . . . 155
7.3.1 Temperature and velocity fields . . . 155
7.3.2 Flame shape . . . 157
7.3.3 Wall temperature . . . 157
7.3.4 Energy budget . . . 160
7.4 A first quantification of the radiative heat transfer . . . 162
7.4.1 Estimation of the influence of gases radiation inside the EM2C burner using the ERM/OERM methods . . . 162
7.4.2 Results obtained using the OERM method . . . 165
7.4.3 A first assessment of the interaction between wall temperature and gases radiation . . . 167
7.5 Conclusion . . . 168

In this chapter, the previously developed coupling method is applied to the numerical study of a confined flame. This flame was first studied in the PhD theses of Guiberti (2015) and Mercier (2015) and it was shown that the non-adiabaticity of the walls has a great influence on the flame shape and shape transition (Mercier (2015), Guiberti et al. (2015)). In this work, a coupled flow-wall simulation was conducted which showed good agreement in terms of wall temperature predictions. A first quantification of the effects of radiative heat transfer inside the combustion chamber has also been conducted and showed that for an accurate prediction of the wall temperature a full multi-phenomena simulation would be needed.

7.1 Experimental test rig and available measurements

The configuration studied here was used to investigate confined turbulent $CH_4/H_2/$air premixed flames by Guiberti (2015) with low to high dilution ratios by nitrogen (N_2) and carbone dioxyde (CO_2). Such combustion configurations are typical of industrial furnaces in the steel industry where the fuel is diluted with the gaseous by-products of the combustion (Blast Furnace Gas or Coke Oven Gas, see Guiberti (2015)). Figure 7.1 presents the experimental setup. The burner is fed by mixtures of methane(CH_4), air and hydrogen (H_2). The injector has an exit diameter of 14 mm, and the flow is put in rotation by a radial swirling vane. The swirl number $S = 0.4$ was measured using PIV on a non-reacting flow. A central rod of 6 mm of diameter is installed in the center of the injector and help anchoring the flame near the exit. The four quartz windows dimensions are: 250 mm (height) x 92 mm (width) x 12 mm (thickness).

The operating conditions considered here are an equivalence ratio of $\phi = 0.7$ with a corresponding thermal power of $4\,kW$. The injected gases have a temperature of 293 K and a bulk velocity $U_b = 14\,m.s^{-1}$. The fuel volumetric composition is of 60% H_2 and 40% CH_4. The measured flames exhibited a V shape.

In the studies conducted by Guiberti et al. (2015) and Mercier (2015) the measured flame shape was either of a V shape or a M shape (Fig. 7.2). Its shown by **?** that the flame shape depends on the fuel composition. The flame shapes noticed experimentally by Guiberti et al. (2015) were numerically predicted by Mercier (2015) with the help of a non-adiabatic

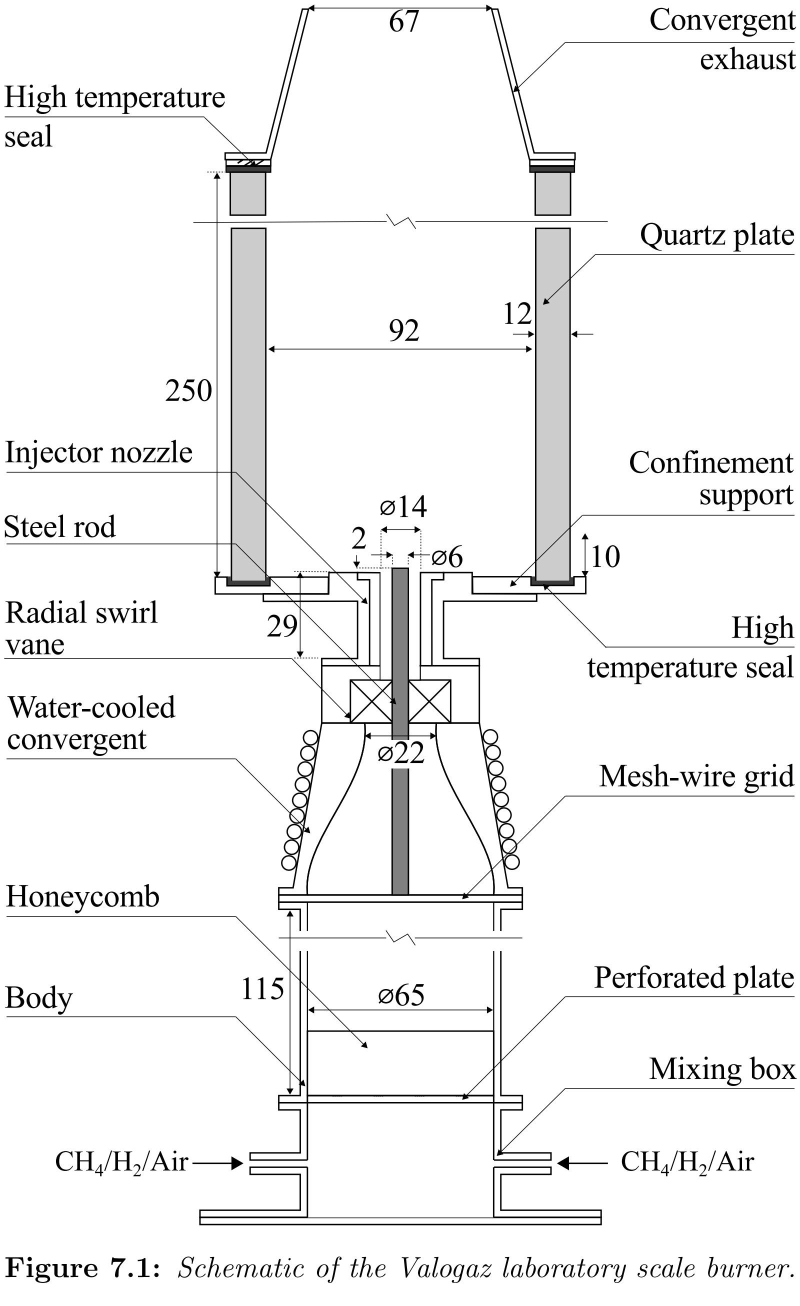
67
Convergent exhaust
High temperature seal
Quartz plate
92
12
250
Injector nozzle
Confinement support
⌀14
Steel rod
2
⌀6
10
Radial swirl vane
29
High temperature seal
Water-cooled convergent
⌀22
Mesh-wire grid
Honeycomb
Body
115
⌀65
Perforated plate
Mixing box
$CH_4/H_2/Air$
$CH_4/H_2/Air$

Figure 7.1: *Schematic of the Valogaz laboratory scale burner.*

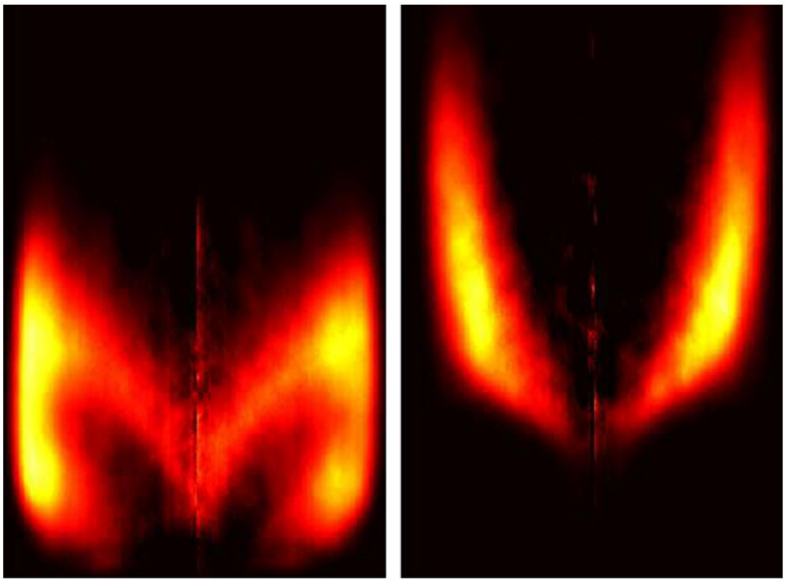

Figure 7.2: *Typical M (left) and V (right) swirling methane/air flames for two different operating conditions. left:* $\phi = 0.62$ *and* $U = 12.2\,m \cdot s^{-1}$*. Right:* $\phi = 0.57$ *and* $U = 12.1\,m \cdot s^{-1}$*. Reproduced from Moeck et al. (2012).*

combustion model. Indeed, using an adiabatic combustion model always leads to an M-flame, while prescribing the experimentally measured wall temperatures with the help of a non-adiabatic combustion model grants access to the V shape when such a flame should exist (Fig. 7.3).

Figure 7.4 exhibits the different measurements locations inside the combustion chamber. Thermocouple measurements are available for the vertical steel bars holding the windows, while Laser Induced Phosphorescence (LIP) measurements were conducted for the windows as for the dump plate.
Examples of the obtained experimental data is available in figures 7.5 and 7.6. Figure 7.5 shows the temperature along the steel bars as a function of the height z, while Fig. 7.6 exhibits a color map of the measured temperature field on the quartz window.

7.2 Numerical setup

7.2.1 Combustion model: F-TACLES

In chapter 6 the combustion phenomena was dealt by explicitly transporting the mass fractions of several species and using a set of chemical

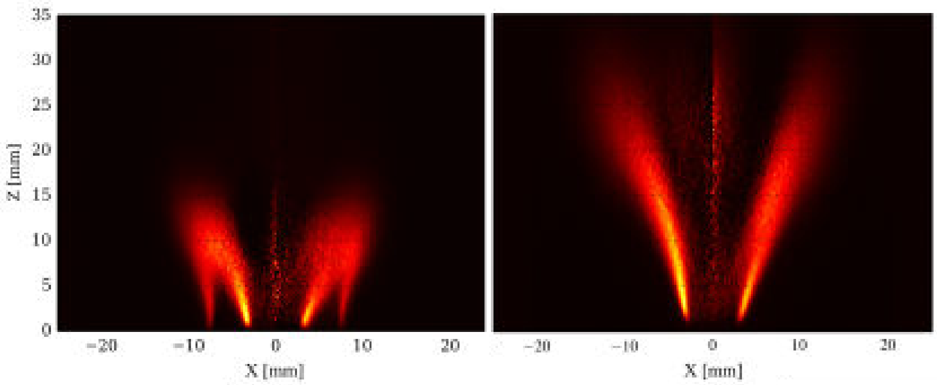

Figure 7.3: *Normalized Abel deconvoluted OH* chemiluminescence corresponding to the zone of heat release. Extracted from Guiberti (2015). Left: M-shape flame. Right: V-shape flame.*

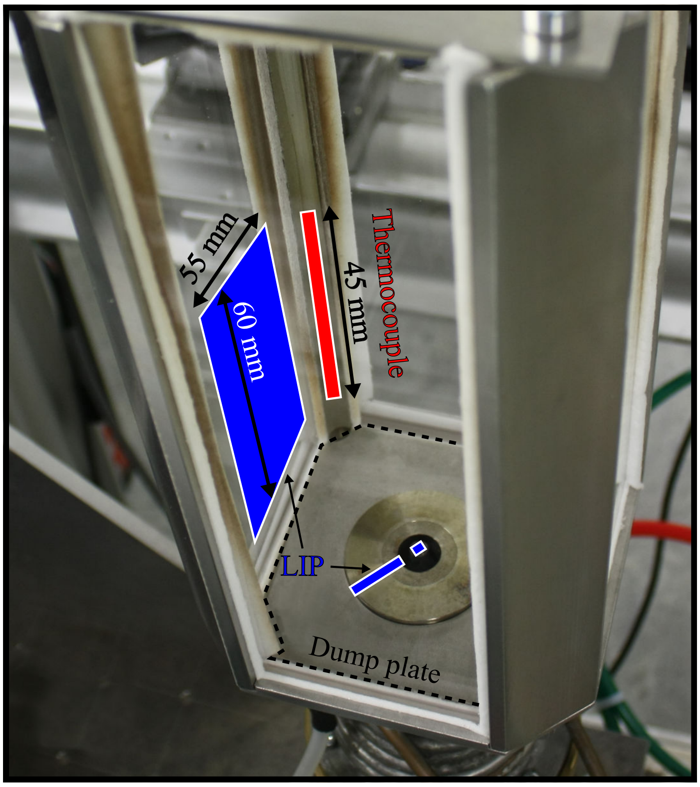

Figure 7.4: *Direct visualisation of the Valogaz burner studied by Guiberti (2015). Blue surfaces: Areas where the temperature was measured by LIP. Red zone: Temperature was measured using thermocouples. Extracted from Guiberti (2015).*

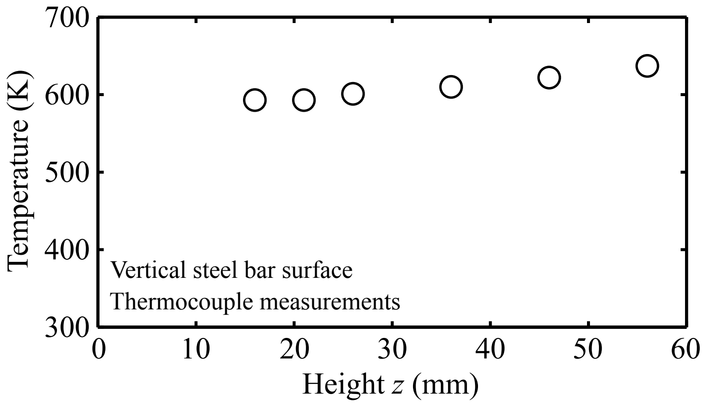

Figure 7.5: *Experimental temperature measurements along the steel bar using thermocouples. Extracted from Guiberti (2015).*

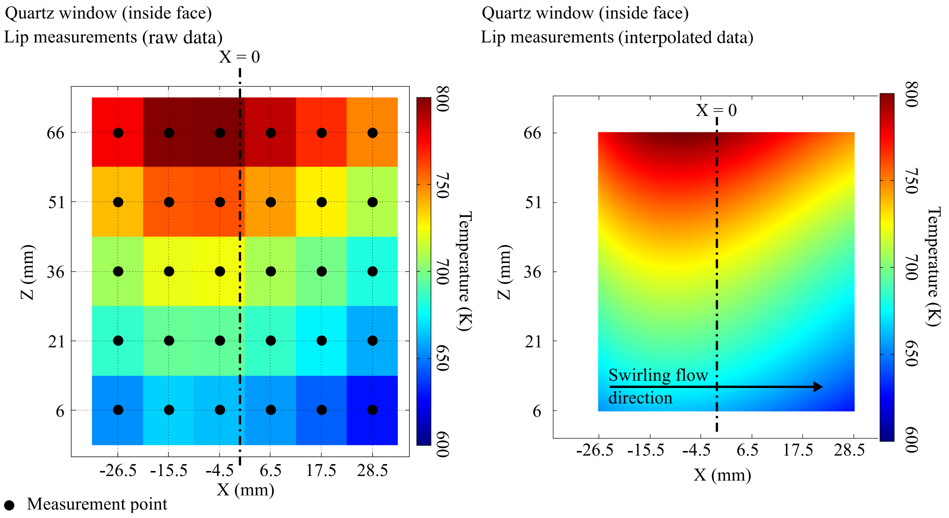

Figure 7.6: *LIP measurements on the quartz windows of the valogaz burner (Large blue zone in Fig. 7.4). Left: raw data with the location of the measurements points. Right: Reconstructed temperature field using linear interpolation. Extracted from Guiberti (2015).*

reactions. In this chapter the combustion model used is the Filtered Tabulated Chemistry for LES (F-TACLES) model (Fiorina et al. (2010),Vicquelin (2010)). The reason behind this choice is that a previous study by Mercier (2015) showed that F-TACLES is well suited for capturing the combustion physics inside the experimental burner.

7.2.1.1 Adiabatic F-TACLES

The first version of the F-TACLES model used a perfectly premixed hypothesis. Considering a mixture with N_{sp} species, a progress variable Y_c is defined:

$$Y_c = \sum_{k=1}^{N_{sp}} n_k Y_k \tag{7.1}$$

Where n_k is the weighting coefficient associated to the species Y_k. The balance equation for Y_c is thus deduced from those of the different species:

$$\frac{\partial Y_c}{\partial t} + \nabla \cdot (\rho \mathbf{u} Y_c) = -\nabla \cdot \left(\sum_{k=1}^{N_{sp}} n_k \rho Y_k V_k \right) + \rho \dot{\omega}_{Y_c} \tag{7.2}$$

And:

$$\dot{\omega}_{Y_c} = \sum_{k=1}^{N_{sp}} n_k \dot{\omega}_k \tag{7.3}$$

For this numerical study, the progress variable Y_c is defined as:

$$Y_c = Y_{CO} + Y_{CO_2} + Y_{H_2O} \tag{7.4}$$

thus leading to:

$$n_k = 1,\ \forall k \in \{CO, CO_2, H_2O\} \tag{7.5}$$

$$n_k = 0,\ \forall k \notin \{CO, CO_2, H_2O\} \tag{7.6}$$

The unresolved subgrid terms needed for the closure of the equations, such as the reaction rate, and thermochemical variables are obtained through the filtering of a database of 1D flames. These 1D flames were computed using the kinetic scheme of Lindstedt (1998). The used filtering is explicit and uses a gaussian filter F_Δ with a kernel of size Δ:

$$F_\Delta(x) = \left(\sqrt{\frac{6}{\pi \Delta^2}} \right) e^{-\dfrac{6x^2}{\Delta^2}} \tag{7.7}$$

thus leading to a space-filtered variable $\overline{\Phi}$:

$$\overline{\Phi} = \int_{-\infty}^{+\infty} \Phi(x')F_\Delta(x - x')dx' \tag{7.8}$$

and favre-filtered $\widetilde{\Phi}$:

$$\widetilde{\Phi} = \frac{1}{\overline{\rho}} \int_{-\infty}^{+\infty} \rho(x')\Phi(x')F_\Delta(x - x')dx' \tag{7.9}$$

The resulting parameters then depend on the progress variable Y_c and on the filter size Δ. The model was later improved by Auzillon et al. (2011) to account for stratified combustion by adding a second tabulated dimension: the mixture fraction Y_z. It was also shown that it is needed to transport the variance of the normalized mixture fraction z: $\widetilde{z"^2}$, which is used to compute the unmixedness of z, S_z. The different thermochemical quantities used in LES are then tabulated as a function of Y_c, Δ, Y_z and S_z:

$$\widetilde{\Phi} = \widetilde{\Phi}\left[Y_c, Y_z, S_z, \Delta\right] \tag{7.10}$$

In this work, conjugate heat transfer is considered, meaning that the adiabatic flame framework is not suitable and the heat losses at the walls must be taken into account. For this reason, the non-adiabatic F-TACLES extended model developed by Mercier et al. (2014) is considered.

7.2.1.2 Non-Adiabatic F-TACLES

Taking into account heat losses in the F-TACLES model is achieved by replacing the initial freely propagating 1D flames used in the original formulation by burner-stabilized flames. The burner is set to a certain temperature which leads to an enthalpy defect Δh. Hence, the enthalpy of the burnt gases can be replaced with the enthalpy h^{eq} which takes into account the defect:

$$h^{eq}(z, \dot{m}) = h(z, \dot{m}) - \Delta h(z, \dot{m}) \tag{7.11}$$

where z is the mixture fraction and $\dot{m}$ is the mass flow rate. The enthalpy defect can be related to the temperature gradient at the burner position:

$$\Delta h(z, \dot{m}) = \left(\frac{\lambda}{\dot{m}}\frac{\partial T}{\partial x}\right)_{burner} \tag{7.12}$$

The thermo-chemical variables are hence also tabulated as a function of the given enthalpy defect Δh along the mixture fraction z and progress variable Y_c. The enthalpy h^{eq} follows a transport equation which is the same as for passive scalars (Mercier et al. (2014)):

$$\frac{\partial \rho h^{eq}}{\partial t} + \nabla \cdot (\rho \mathbf{u} h^{eq}) = \nabla \cdot (\rho D_{th} \nabla h^{eq}) \tag{7.13}$$

Filtering the different equations under the Low-Mach assumptions leads to the following set of equations which need to be solved:

$$\frac{\partial \overline{\rho}}{\partial t} + \frac{\partial}{\partial x_i}(\overline{\rho}\widetilde{u}_i) = 0 \tag{7.14}$$

$$\frac{\partial \overline{\rho}\widetilde{u}_j}{\partial t} + \frac{\partial}{\partial x_i}(\overline{\rho}\widetilde{u}_i\widetilde{u}_j) = -\frac{\partial \overline{p}_2}{\partial x_j} + \frac{\partial(\overline{\tau}_{ij} + \overline{\tau}_{ij}^{sgs})}{\partial x_i} + \overline{\rho}\widetilde{f}_j \tag{7.15}$$

$$\begin{aligned} \frac{\partial \overline{\rho}\widetilde{Y}_c}{\partial t} + \frac{\partial}{\partial x_i}\left(\overline{\rho}\widetilde{u}_i\widetilde{Y}_c\right) = \frac{\partial}{\partial x_i}\Bigg(& \Xi_{\Delta}^{Y_c}\gamma\left[\widetilde{z}, S_z, \Delta\widetilde{h}\right] \\ & \alpha_{Y_c}^{ad}\left[\widetilde{Y}_c, \widetilde{z}, S_z, \Delta\right]\rho_0 D_0 \frac{\partial \widetilde{Y}_c}{\partial x_i}\Bigg) \\ & + \Xi_{\Delta}^{Y_c}\gamma\left[\widetilde{z}, S_z, \Delta\widetilde{h}\right]\Omega_{Y_c}^{ad}\left[\widetilde{Y}_c, \widetilde{z}, S_z, \Delta\widetilde{h}\right] \\ & + \Xi_{\Delta}^{Y_c}\gamma\left[\widetilde{z}, S_z, \Delta\widetilde{h}\right]\overline{\rho}\widetilde{\dot{\omega}}_{Y_c}^{ad}\left[\widetilde{Y}_c, \widetilde{z}, S_z, \Delta\widetilde{h}\right] \end{aligned} \tag{7.16}$$

$$\frac{\partial \overline{\rho}\widetilde{z}}{\partial t} + \frac{\partial}{\partial x_i}(\overline{\rho}\widetilde{u}_i\widetilde{z}) = \frac{\partial}{\partial x_i}\left(\left(\overline{\rho}D_{th} + \frac{\mu_t}{S_{ct}}\right)\frac{\partial \widetilde{z}}{\partial x_i}\right) \tag{7.17}$$

$$\begin{aligned} \frac{\partial \overline{\rho}\widetilde{z''^2}}{\partial t} + \frac{\partial}{\partial x_i}(\overline{\rho}\widetilde{u}_i\widetilde{z''^2}) = \frac{\partial}{\partial x_i}\left(\frac{\mu_t}{S_{ct}}\frac{\partial \widetilde{z''^2}}{\partial x_i}\right) + 2\frac{\mu_t}{S_{ct}}|\nabla\widetilde{z}|^2 \\ - 2C\frac{\mu_t}{S_{ct}\overline{\rho}\Delta^2}\widetilde{z''^2} \end{aligned} \tag{7.18}$$

$$\frac{\partial \overline{\rho}\widetilde{h^{eq}}}{\partial t} + \frac{\partial}{\partial x_i}(\overline{\rho}\widetilde{u}_i\widetilde{h^{eq}}) = \frac{\partial}{\partial x_i}\left(\left(\overline{\rho}D_{th} + \frac{\mu_t}{P_{rt}}\right)\frac{\partial \widetilde{h^{eq}}}{\partial x_i}\right) \tag{7.19}$$

$$p_0 = \overline{\rho}r\widetilde{T} \tag{7.20}$$

Where $\widetilde{z''^2}$ is the subgrid variance of z, $\Xi_{\Delta}^{Y_c}$ is the subgrid wrinkling factor used for a filter size of Δ. γ is the correction coefficient for the laminar flame speed:

$$\gamma\left[\widetilde{z}, S_z, \Delta\widetilde{h}\right] = \frac{\widetilde{S_l}\left(\widetilde{z}, S_z, \Delta\widetilde{h}\right)}{\widetilde{S_l}\left(\widetilde{z}, S_z, \Delta\widetilde{h} = 0\right)} \tag{7.21}$$

where $\widetilde{S}_l$ is the filtered laminar flame speed. $\Omega_{Y_c}^{ad}$ is the unresolved adiabatic tabulated subgrid transport source term. For this simulation, the filter size Δ of the F-TACLES model was taken as: $\Delta = 3.5\,mm$. C is a model constant taken equal to 1 here. P_{rt} and S_{ct} are the turbulent Prandtl and Schmidt numbers which are taken constant for this work $(= 0.71)$.

7.2.2 Outer boundary condition

The available experimental temperature measurements of the chamber walls were done on the inner faces of the chamber. The question which arose is which boundary condition should be imposed at the walls' outer surface? The assumption used in this study is to use a combination of conduction and radiative heat fluxes:

$$\boldsymbol{\phi}_{bnd} = \boldsymbol{\phi}_{bnd}^{cd} + \boldsymbol{\phi}_{bnd}^{R} \tag{7.22}$$

where $\boldsymbol{\phi}_{bnd}$ is the exterior boundary heat flux, $\boldsymbol{\phi}_{bnd}^{cd}$ the convective heat flux and $\boldsymbol{\phi}_{bnd}^{R}$ the radiative heat flux. The temperature of the air surrounding the burner, T_{ext}, is considered constant, and the quartz temperature on its outer face is denoted as T_{bnd}.

First of all, the radiative component is obtained from the radiative heat flux, computed as:

$$\phi_{bnd}^{R} = \epsilon_{bnd}\sigma(T_{bnd}^4 - T_{ext}^4) \tag{7.23}$$

where $\mathbf{n}_{bnd}^{ext}$ is the outgoing boundary normal, ϵ_{bnd} the emissivity of the quartz and σ is the steffan constant.

The conductive component of the exterior heat flux is considered as that of conduction inside the outer air boundary layer and is defined as:

$$\phi_{bnd}^{cd} = h_{ext}(T_{bnd} - T_{ext}) \tag{7.24}$$

while transfer coefficient, h_{ext}, can be determined with the help of the Nusselt number Nu_z defined for a length z:

$$h_{ext} = \frac{Nu_z \lambda}{z} \tag{7.25}$$

By using this formulation, the value of $h_{ext}(z)$ can be found locally along the window in the up going direction, as a function of the z-coordinate on the window:

$$h_{ext}(z) = \frac{Nu_{z-z0}\lambda}{z - z_0} \tag{7.26}$$

where z_0 is the position of the beginning of the window. Considering natural convection and assuming that the flow around the chamber is laminar, it is possible to use the vertical plate correlation of MacAdams (1961), where:

$$Nu_z = 0.39 Ra_z^{1/4} \tag{7.27}$$

and Ra_z is the Rayleigh number, defined with the help of the Prandtl number Pr and Gr the Grashof number:

$$Ra_z = Gr Pr \tag{7.28}$$

The obtained formula for the Rayleigh number is then:

$$Ra_z = g\beta \frac{|T_{bnd} - T_{ext}| z^3}{a\nu} \tag{7.29}$$

where g is the gravity constant, β the thermal dilatation coefficient, which for gases is taken equal to $1/T$, a is the thermal diffusivity of the surrounding flow and ν the kinetic viscosity of the same flow. All of the fluid properties needed for the estimation of the value of the Nusselt number (β, a and ν) are taken at the film temperature T_m which takes into the account the fact that the fluid film is at neither the wall temperature nor the far flow temperature:

$$T_m = 0.5(T_{bnd} + T_{ext}) \tag{7.30}$$

This correlation between Nusselt and Rayleigh numbers is valid for $Gr \leq 10^9$. The maximal value for the Grashof number along the wall, attained at the upper extremity is $Gr \approx 1.25 \cdot 10^9$. This means that the laminar assumption is true for about 93% for the wall length, and can be considered valid for this case.

Using these different relations, the convection coefficient is then equal to:

$$h_{ext}(z) = 0.39\lambda \left(\frac{g|T_{bnd} - T_{ext}|}{T_m a\nu} \right)^{1/4} (z - z_0)^{-1/4} \tag{7.31}$$

For the estimation of the heat transfer coefficient h_{ext}, the approximated film temperature is $T_m = 450\,K$. The different thermal properties are taken for pure air, and the window starts 2 cm after the beginning of the vertical plate. The considered quartz windows are made from the GE-124 quartz, and have an emissivity of $\epsilon_{bnd} \approx 0.75$. The resulting conduction

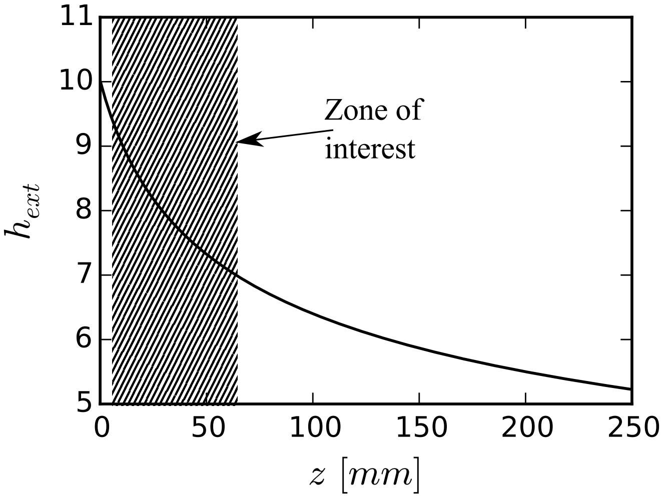

Figure 7.7: *Exterior heat transfer coefficient computed using natural convection correlations, along the the z coordinate on the quartz wall.*

heat transfer coefficient obtained is plotted in Fig. 7.7 for the zone where temperature measurements are available.

For the considered configuration, air temperature and film temperature, the ratio $\phi^{R}_{bnd}/\phi^{cd}_{bnd}$ is approximatively equal to 1.5. This shows that the radiative contribution in this temperature domain is far from negligible and must be taken into account.

7.2.3 Applying the outer boundary condition to the steady heat transfer solver

An issue which arises with the radiative and conduction boundary condition, is that the steady heat transfer problem is no longer linear because of the radiative contribution. Because of this nonlinearity the steady heat equation cannot be solved implicitly as done before. In order to overcome this difficulty, the term T^4_{bnd} in the radiative heat flux is replaced with $T_{bnd} \cdot (T^{est}_{bnd})^3$, where T^{est}_{bnd} is an estimation of the outer boundary temperature T_{bnd}. This leads to the following outer boundary condition:

$$\phi_{bnd} = h_{ext}(T_{bnd} - T_{ext}) + \epsilon_{bnd}\sigma(T_{bnd}(T^{est}_{bnd})^3 - T^4_{ext}) \quad (7.32)$$

Since the temperature estimation T^{est}_{bnd} is different from the obtained boundary temperature T_{bnd}, a fixed point algorithm is used on the outer boundary temperature (Fig. 7.8): the steady heat transfer equation is solved with the new estimation until the convergence is attained for the outer boundary temperature, which corresponds to the solution of the original non-linear heat transfer problem.

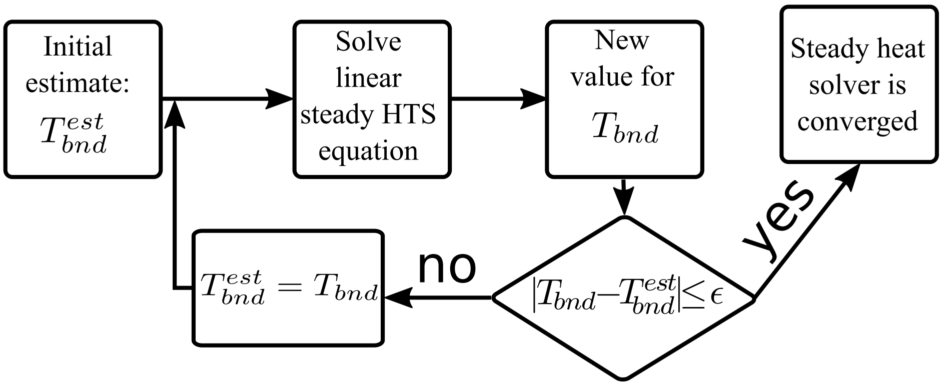
Initial estimate: T_{bnd}^{est}
Solve linear steady HTS equation
New value for T_{bnd}
Steady heat solver is converged
$T_{bnd}^{est} = T_{bnd}$
no
$|T_{bnd} - T_{bnd}^{est}| \leq \epsilon$
yes

Figure 7.8: *Fixed point algorithm used for the resolution of the steady heat transfer equation with a radiative flux boundary condition.* T_{bnd} *is the numerical value obtained for the boundary temperature,* T_{bnd}^{est} *is the temperature estimation and* ϵ *is the numerical tolerance used to check for the convergence.*

Thanks to this approach, the radiative heat flux boundary condition can be applied to the linear steady heat transfer solver with a moderate additional computational cost. Indeed, since the outer boundary temperature does not evolve rapidly, using for each coupling iteration the previous value as the initial estimate leads to a small number of outer-iterations needed inside the fixed point algorithm: the average number is of about 5 outer-iterations for $\epsilon = 0.1\%$.

7.2.4 Numerical configuration

During the study presented in this chapter several numerical solvers are used: A flow solver, a steady and unsteady heat transfer solver which are coupled in the same way as in the previous chapter (Fig. 7.9) with an error tolerance $\eta = 5\%$ for the boundary temperature. The different solvers have been presented in chapter 2. Both the steady and unsteady heat transfer solvers use a mesh of about 41M cells, while the LES flow solver is using a mesh made of 49M cells. A cut of both meshes is shown in Fig. 7.10.

An approximation is made in this study, where the steel bars originally present are replaced with quartz. The resulting configuration is that of a fluid volume which sides are surrounded by a quartz chamber. The

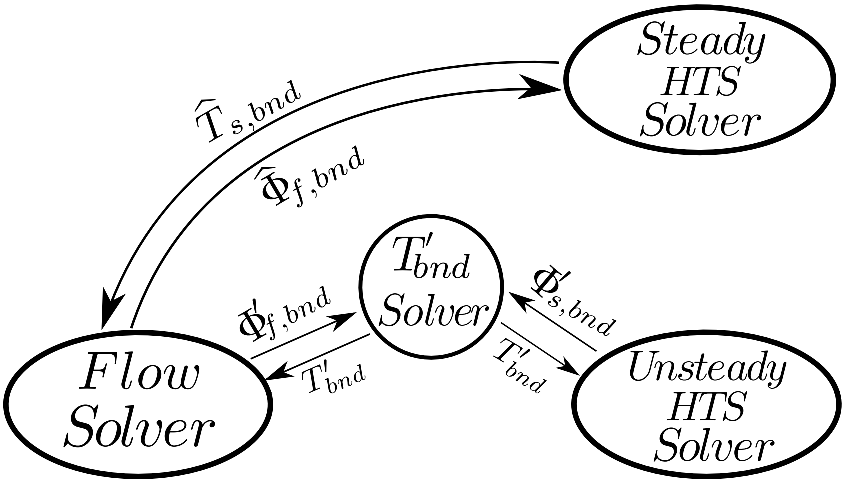

Figure 7.9: *Scheme of the coupling of the different numerical codes used for the simulation of the Valogaz burner. The codes are coupled through the OpenPalm coupler presented in chapter 2.*

bottom plate, injector and converging exhaust on the other hand, use a prescribed temperature boundary condition based on the experimental measurements.

For this configuration, the flow solver was used in combination with the Sigma subgrid scale model (Nicoud et al. (2011)). The time integration used is the fourth order explicit TFV4A scheme. The combustion was dealt with the help of a tabulated chemistry model: F-TACLES which was previously presented. The Large-Eddy simulations conducted here are wall resolved and did not require the use of a wall model for the upper parts of the burner. Indeed, a first standalone flow simulation was conducted using wall laws, which showed a maximal value of $y^+ \approx 1.5$ and hence a wall-resolved LES. For the inside of the injection pipe on the other hand, the wall law was needed because of the high inlet velocity.

An example of the temporal evolution of the coupling time step size is plotted in Fig. 7.11. As seen, it remains close to a mean value of 9.1 times the limiting diffusive time step of the flow solver. The variations encountered are relatively small, of the order of magnitude of 1 diffusive flow time step. The coupling time step obtained here is smaller than the one obtained in chapter 6 because of the turbulent nature of the considered flow and the higher fluctuations present at the wall.

To ensure a minimal computational overcost due to the code coupling, the

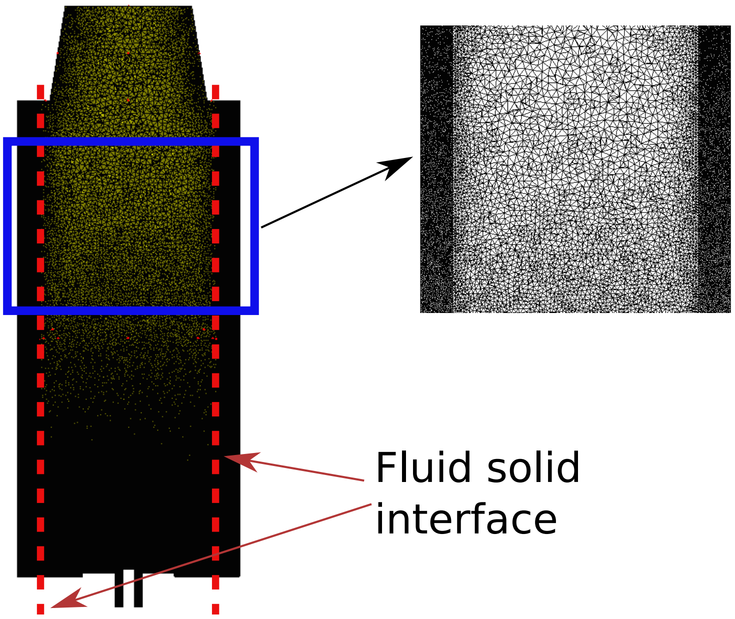

Figure 7.10: *Left: Full meshes for both fluid and solid domain. Yellow is fluid, black is solid and red dashed line symbolize the interface. Right: A zoom on a section of the domain.*

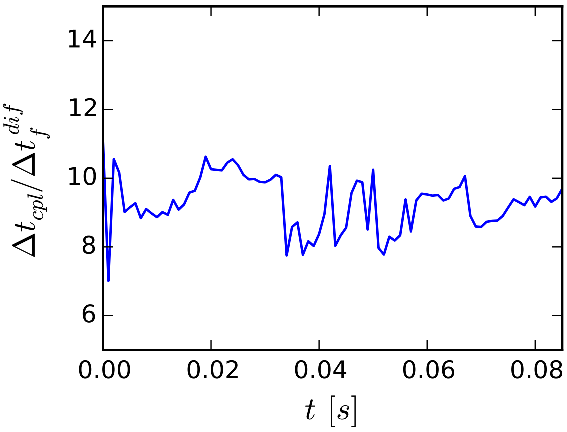

Figure 7.11: *Temporal evolution of the coupling time step during the simulation.*

cores repartition between the different codes needs to be done correctly so that all codes arrive at the coupling point at the same time. Since it is the flow solver which represents the bulk of the cores, the heat transfer solver should have slightly larger percentage of the available CPU cores in order to be sure that the flow solver never has to wait for it. Since a dynamic coupling time step is used in this work, it is impossible to determine beforehand the optimal cores repartition as it was explained in chapter 3. In this work, a first short run was done in order to have a preview of the coupling time step evolution. By studying the minimal and maximal values, a repartition can be found which ensures that the flow solvers never arrives first to the coupling point. The retained cores repartition is given in Tab. 7.1:

Code	LES	U-HTS	S-HTS	OpenPalm	Total
Number of cores	960	47	48	1	1 056

Table 7.1: *Repartition of the available CPU cores between the different numerical codes used. LES stands for the flow solver YALES2, S-HTS for the steady heat transfer solver and U-HTS for the unsteady heat transfer solver.*

7.3 Results

7.3.1 Temperature and velocity fields

Figure 7.12 shows the mean temperature and velocity fields inside the burner. The mean temperature field shows that the gases which interact with the walls are significantly colder than the burnt gases directly issued from the combustion process. This can be explained with the velocity field which shows very large recirculation zones between the hot burnt gases and the walls thus leading to very long residence times. Therefore the gases arriving at the top of the measuring zone exhibit a temperature of about $800K$.

A second, smaller recirculation zone is seen in the bottom of the burner. Because of its position in the lower corners of the chambers, the residence time in this zone are large since the gases are trapped between the larger upper recirculation zone and the burnt gases created by the reaction zone. The larger residence time leads to colder gases and to some unburnt fuel traces ($\leq 0.1\%$) in the zone. This recirculation zone leads to small temperature and heat flux fluctuations in the two lower thirds of the measurement zone because of cooler gases maintained in that zone.

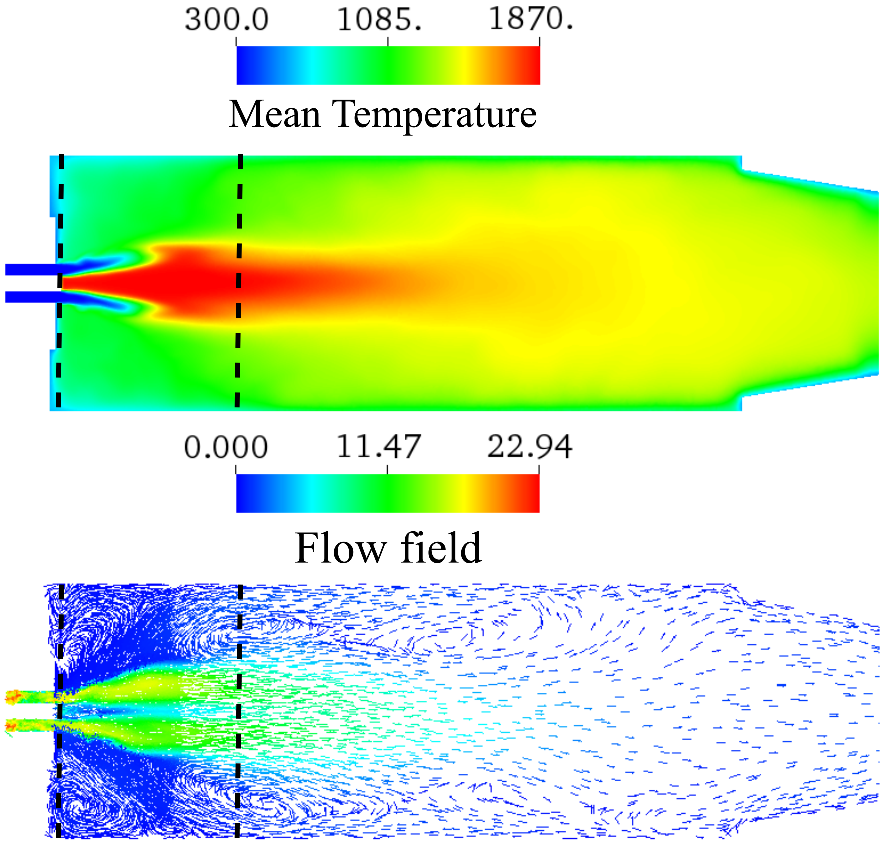

Figure 7.12: *Up: mean temperature field inside the burner. Down: Mean velocity vector field inside the burner. Black dashed lines show the section for which wall temperature measurements are available.*

7.3.2 Flame shape

It was shown in the study of Mercier (2015), where the boundary condition used is the experimentally measured mean wall temperature field, that accounting for heat losses is important in order to correctly predict the shape of the flame in this configuration. In this study the wall temperature was not imposed but computed while the outer faces of the walls were set with a mixed convective and radiative boundary condition.

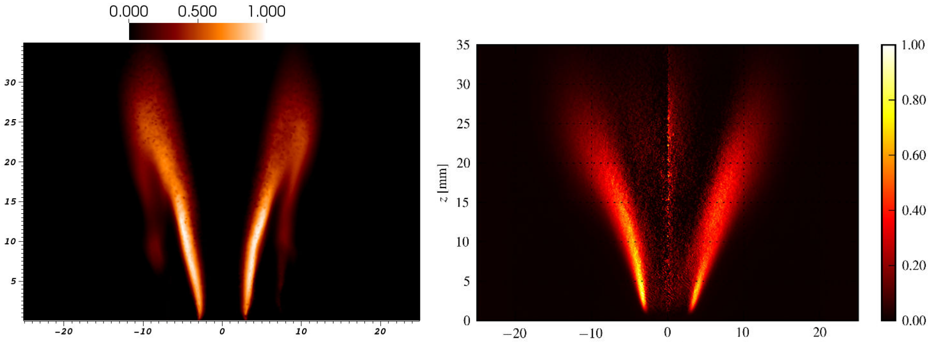

Figure 7.13: *Comparison of the mean normalized heat release field. Left: Mean normalized volumetric heat release. Right: Normalized Abel deconvoluted* OH^* *chemiluminescence corresponding to the zone of heat release.*

Figure 7.13 shows a comparison of the experimental OH^* field which is present in the reaction zone and the numerical heat release rate, while Fig. 7.14 shows the comparison for the mean OH field. These two figures hence show a comparison of the flame position and shape. The numerical results exhibit a V shape flame which is in agreement with the experimental results. Similarly, the predicted flame length is close to the experimental value and the opening angle shows a good agreement as well. These results show that the numerical configuration used is well suited for the simulation of this burner. The obtained results for the flame shape are very similar to the ones obtained by Mercier (2015), including the small tendrils which correspond to a smaller secondary reaction rate in the recirculation zone.

7.3.3 Wall temperature

The obtained mean wall temperature distribution is compared to the experimentally measured one in Fig. 7.15. As it can be seen, a difference exists which is of the order of $100\,K$, as seen in Fig. 7.16(b). Similarly,

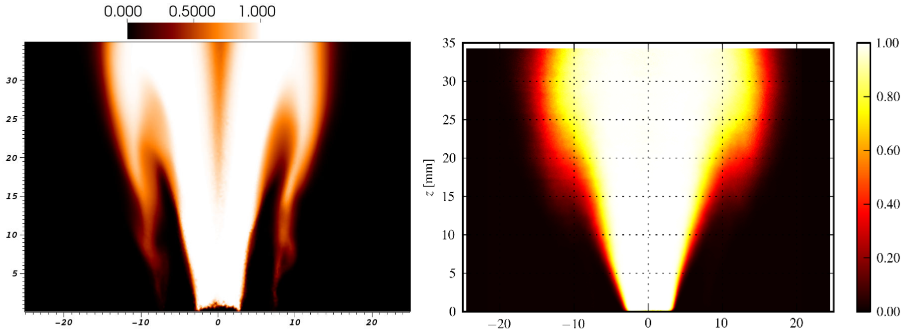

Figure 7.14: *Comparison of the mean normalized OH field. Left: Numerical mean normalized OH molar fraction. Right: Experimentally measured mean normalized OH molar fraction.*

Fig. 7.16 shows the wall temperature deficit, $\Delta T_{bnd} = T_{bnd}^{exp} - T_{bnd}^{num}$, and relative error of the wall temperature, ϵ_T, defined as:

$$\epsilon_T = (T_{bnd}^{exp} - T_{bnd}^{num})/T_{bnd}^{exp} \tag{7.33}$$

The results plotted in Fig. 7.16 show that the maximal relative error is of 10.5% (Fig. 7.16(a)) and that the numerically predicted wall temperature is colder than the experimentally measured one all over the zone of measurements. This difference corresponds to a local absolute difference of up to $\Delta T_{bnd} \approx 90\,K$ (Fig. 7.16(b)).

The shapes of the spatial profiles are very similar, showing that the flow is correctly resolved. Several reasons could explain the colder retrieved wall temperatures. The three main hypotheses are:

- **Full quartz wall approximation:**
  A first explanation is that the approximation of considering the entire wall is made solely from quartz has too large of an influence on considered zone: The metal parts are colder than the quartz and are normally thermally insulated from the latter by a seal. It is possible that by not taking this insulation into account, larger heat losses are computed for the zone of interest and lead to the undershoot in temperature estimation.

- **Outer boundary condition**
  Secondly, an uncertainty exists concerning the outer boundary condition h_{ext}. A first study was conducted using a 1D approximation where a wall heat flux, $\phi_0 = 3.5\,kW/m^2$, is imposed to a quartz layer 12mm thick. The outer boundary condition used is the one

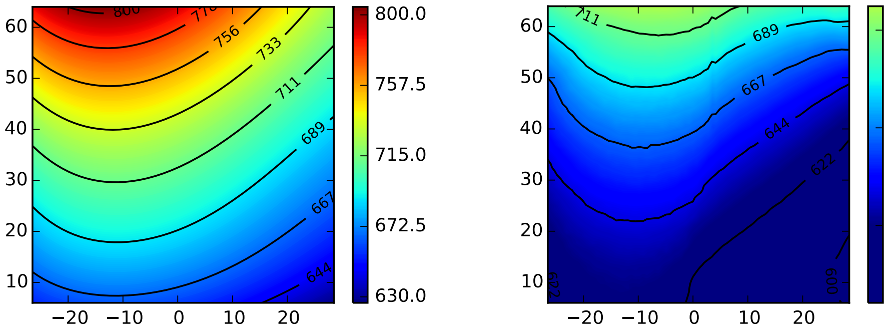

(a) Experimental measurements: LIP results of the mean temperature field on the quartz.

(b) Numerical simulation: Mean temperature field computed from the heat transfer solvers.

Figure 7.15: *Comparison of the mean wall temperature* $\overline{T}_{bnd}$ *field on the quartz. Figure (a) shows the experimentally measured results while Fig. (b) shows the numerically computed field.*

prescribed in the coupled numerical simulation: a combined convective and radiative heat flux. All parameters are set to the same values as in the full 3D coupled simulation except for the convective heat coefficient h_{ext} which is varied. As it can be seen in Fig. 7.17, modifying h_{ext} by 10% only causes a 1% change in the inner wall temperature. Hence, it seems that the possible influence of the convective heat coefficient on the wall temperature is small.

- **Inner wall heat flux value**
  Lastly, the inner wall heat flux computed by the flow solver might be underestimated. This could be due to the fact that the hot gases radiation was not taken into account. Indeed, as it can be seen in Fig. 7.18 the CO_2 and water vapor mole fractions are not negligible and might mean that the gases radiation should be taken into account.

Figure 7.19 shows the scaled temperature and heat flux root-mean-square values on the wall. In terms of numerical value, the obtained root-mean-square values are small: less than one percent for the wall heat flux and less than 3.5% for the wall temperature, but are larger than the ones encountered in chapter 6. The spatial profiles can be explained with the help of the flow patterns. Indeed, in the plotted results in Fig. 7.19, the left side shows larger fluctuations. This is due to the swirled flow which goes from right to left, meaning that the turbulent burnt gases

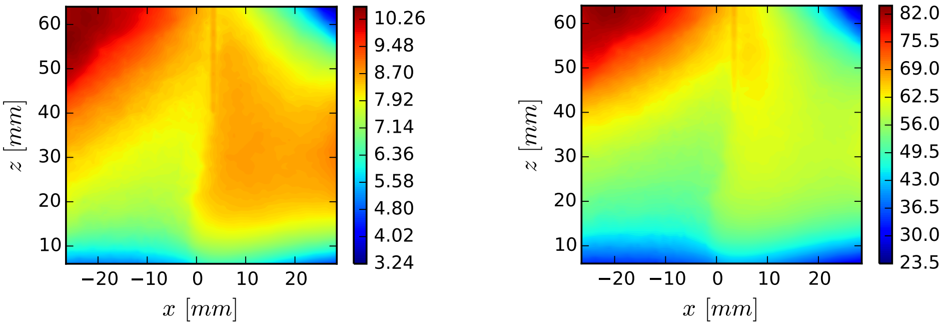

(a) Relative error of the numerical wall temperature ϵ_T in %.

(b) Temperature deficit ΔT_{bnd} in K (Non normalized wall temperature error).

Figure 7.16: *Relative and absolute errors for the wall temperature computed using coupled conjugate heat transfer.*

have more chances at arriving at the left side of the square. Combining this information with the fact that the burnt gases arrive while traveling downwards because of the large recirculation zone (See Fig. 7.12 for the flow patterns) explains why the main zone of fluctuations is in the upper left corner of the studied square.

7.3.4 Energy budget

The energy budget inside the combustion chamber needs to be investigated in order to verify the energy conservation and to study the burner's combustion efficiency. To do so, a sensible enthalpy budget is used, it is obtained by integrating the sensible enthalpy's balance equation over the burner's entire volume:

$$\int_{outlet} \rho u h_s dS - \int_{inlet} \rho u h_s dS + \int_{walls} \phi_w dS - \dot{\Omega}_T = 0 \qquad (7.34)$$

The three integrals of the left hand side can be computed, which grants access to the integrated heat release rate $\dot{\Omega}_T$. Figure 7.20 shows the sensible energy budget with the 4 different terms. As it can be seen, around a third of the thermal energy produced inside the burner is lost through heat losses at the walls, which is far from negligible. The combustion efficiency, defined as $\dot{\Omega}_T/\mathcal{P}$, on the other hand is very good. With $\dot{\Omega}_T = 3.97\,kW$ and $\mathcal{P} = 4.0\,kW$ the efficiency is of 99 % which means that nearly all of the fuel is consumed and that the burnt gases which may exist in the lower recirculation zone represent a very small fraction of the gases created by the flame.

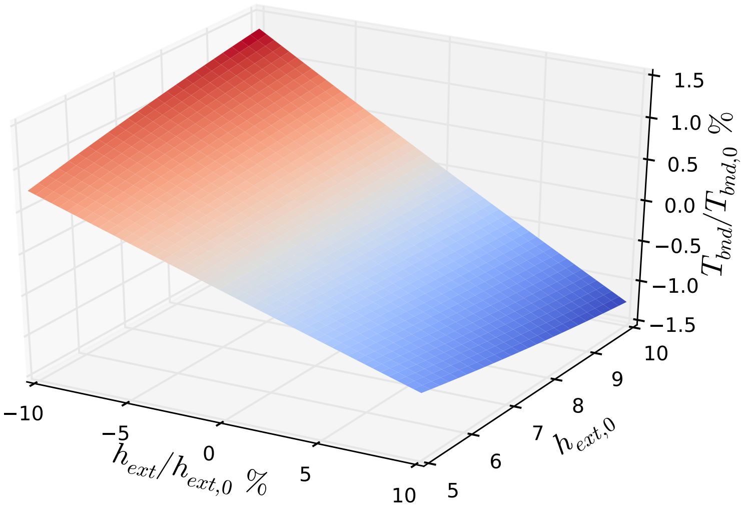

Figure 7.17: *Surface plot of the inner wall temperature T_{bnd} response to a modification of the outer boundary convective coefficient h_{ext}. T_{ext} is set to $293K$ and the radiation is taken into account with $\epsilon = 0.75$ for the quartz wall.*

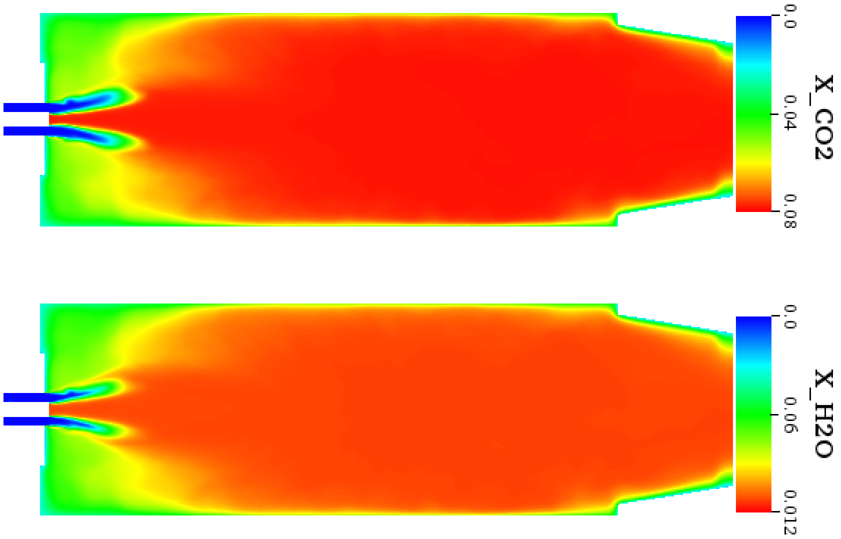

Figure 7.18: *Mean mole fractions of the gaseous CO_2 (top) and water vapor (bottom) inside the studied burner.*

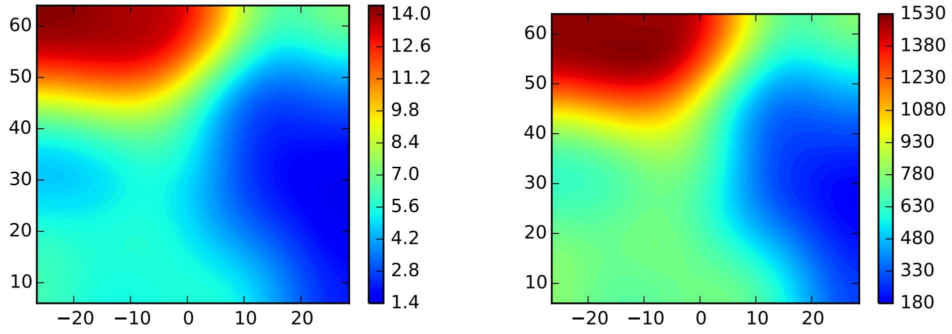

(a) Numerically computed temperature RMS values

(b) Numerically computed heat flux RMS values in $W \cdot m^{-2}$.

Figure 7.19: *Root-mean-square values for the temperature and heat flux inside the measurements zone.*

7.4 A first quantification of the radiative heat transfer

7.4.1 Estimation of the influence of gases radiation inside the EM2C burner using the ERM/OERM methods

As seen with the results of the coupled conjugate heat transfer simulation, the wall temperature is underpredicted. One of the possible reasons for such an undershoot is an error with the estimation of the wall heat flux leading to lower wall temperatures. To better understand the possible influence of the radiative heat transfer, a non coupled simulation is conducted using a gases radiation solver. The code used is the EM2C lab in-house Monte-Carlo method based solver Rainier, presented in chapter 2. For this first estimation, the ERM method (Emission based Reciprocity Monte-carlo method) is used with the same mesh as in the flow computations. The gases spectral properties are computed using the correlated κ-distribution (CK model[1], Goody et al. (1989), Soufiani and Taine (1997), Taine and Soufiani (1999)). Emission coefficients were set to $\epsilon_{bnd} = 0.75$ on all boundaries, and the outlet's visible temperature set to $T_{outlet} = 300\,K$, and emission coefficient $\epsilon_{outlet} = 1.0$, to account for the downstream atmosphere. The temperature, pressure, CO_2 and H_2O molar fractions used are instantaneous values extracted from the flow sim-

---

[1] Dr. Philippe Riviere is acknowledged for providing the database of the Correlated-K model.

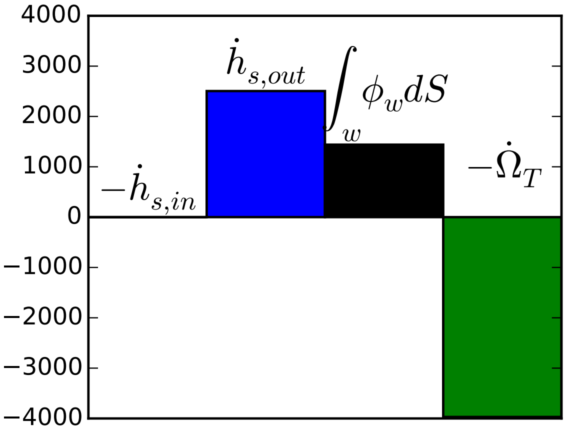

Figure 7.20: *Energy budget of the combustion chamber for the sensible enthalpy. Red: inlet's sensible enthalpy flux. Blue: outlet's sensible enthalpy flux. Black: wall heat flux. Green: Volume integrated heat release rate.*

ulation. The convergence condition of the Monte-Carlo algorithm used is that of an rms lower than 10 % of the mean value.

As seen in Fig. 7.21, most of the domain is in fact emitting energy through radiative heat transfer (negative radiative power) leading to a cooling of the burnt gases. The regions where energy absorption dominates (positive radiative power) are the coldest gas pockets mainly located in thin layers near the walls. Integrating the radiative power over the entire volume shows that the global radiative power is negative and that the portion of absorption-dominated region absorbed power is negligible compared to the emission-dominated region:

$$\int_{burner} P^{rad} dV = -881.15\,W \tag{7.35}$$

$$\int_{burner} P^{rad}_{-} dV = -884.49\,W, \text{ where } P^{rad}_{-} = min(P^{rad}, 0) \tag{7.36}$$

$$\int_{burner} P^{rad}_{+} dV = 3.34\,W, \text{ where } P^{rad}_{+} = max(P^{rad}, 0) \tag{7.37}$$

The third image in Fig. 7.21 shows the root-mean-square of the radiative power scaled by its mean value. It shows that the zones where it is most difficult to attain the convergence criteria of $P^{rad}_{rms}/\overline{P}^{rad} = 0.1$ are the cold zones, which is a known limitation of the ERM method (Zhang (2013), Tessé et al. (2002), Dupoirieux et al. (2006)) and one solution which

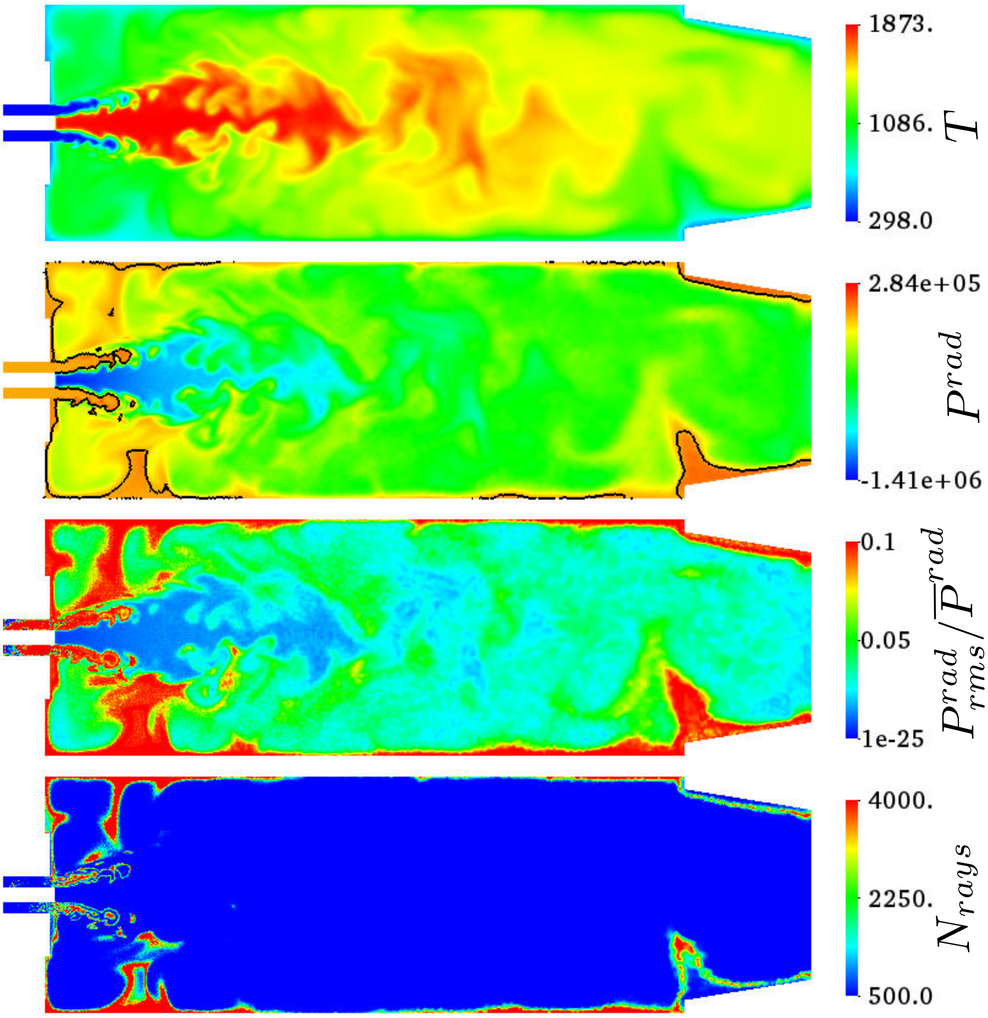

Figure 7.21: *Instantaneous fields extracted from the radiation solver. From top to bottom: Temperature field. Radiative power, black line is the iso-contour for* $P^{rad} = 0$*. Rms radiative power scaled by the mean radiative power. Number of rays used at each point. Values obtained using the ERM method.*

can be used for a faster convergence of the Monte-Carlo algorithm is the OERM method (Zhang et al. (2012)). The fourth image shows the same results for the number of rays used for the statistical convergence of each point, where the maximal possible value is 4 000.

7.4.2 Results obtained using the OERM method

In order to accelerate the convergence speed of the Monte-Carlo algorithm, the OERM method (Zhang et al. (2012)) is used from here on. Using the OERM method yielded speed up factors of around **30** for the wall heat flux and of about **5** for the radiative power. An example of this is given in Fig. 7.22 where the number of rays needed for the convergence of the Monte-Carlo algorithm are compared for both ERM and OERM methods. For both methods the computational parameters are the same: the maximal number of rays is 4 000 and the convergence criterion is a ratio of rms to mean of 10 % for the radiative power. The results show a much faster convergence for the OERM method, where the minimal number of rays needed in the domain is smaller than for the ERM method, and the maximal number of rays used is 2 500, instead of 4 000 for the

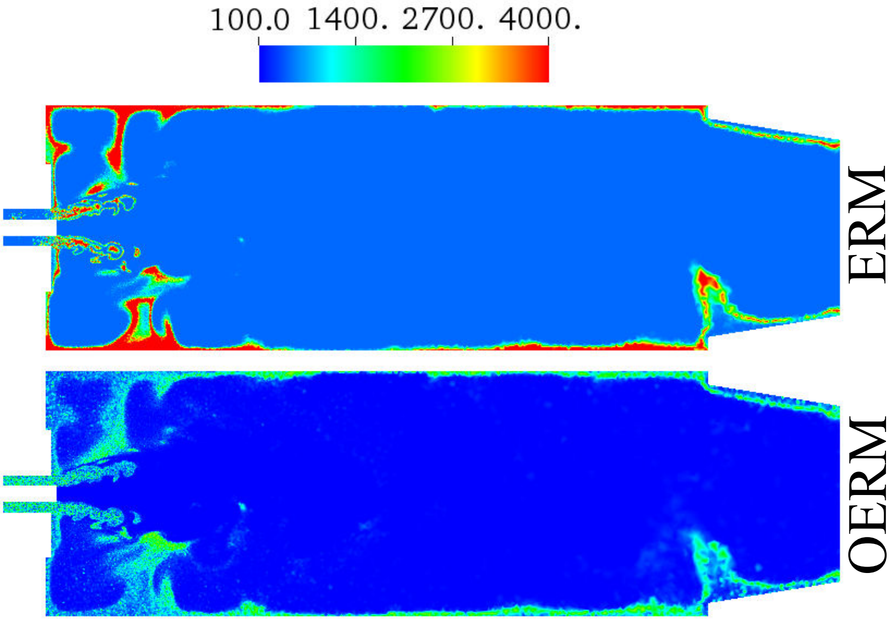

Figure 7.22: *Comparison of the number of rays needed for the Monte-Carlo algorithm for the radiative power using the ERM method (upper figure) and the OERM method (lower figure).*

ERM algorithm. These results outline the advantages of using the OERM method for turbulent combustion configurations where both cold and hot gases co-exist.

It is also important to verify that the radiative heat transfer budget is indeed closed. Since the radiative power is defined as:

$$P^{rad} = -\nabla \cdot (\boldsymbol{\phi}^{rad}) \tag{7.38}$$

the following relation should be verified:

$$\int\int\int P^{rad} dV = -\int\int \boldsymbol{\phi}^{rad} \mathbf{n}_{ext} dS \tag{7.39}$$

Numerically, the value obtained for the surface integrated radiative wall heat flux is:

$$\int\int \boldsymbol{\phi}^{rad} \mathbf{n}_{ext} dS = 879.63\, W \tag{7.40}$$

the small difference between the two computations, 0.17% is due to the statistical nature of the Monte-Carlo method, and shows that the radiative energy budget is indeed closed. The radiative wall heat flux over the walls surface is shown in Fig. 7.23: The radiative wall heat flux is larger in the spots which were already the hotter in the simulation. It also shows that the radiative heat flux is of the same order of magnitude as the convective wall heat flux computed with the coupled conjugate heat transfer simulation and thus cannot be neglected: The ratio of radiative heat flux over convective heat flux is approximately 61 %.

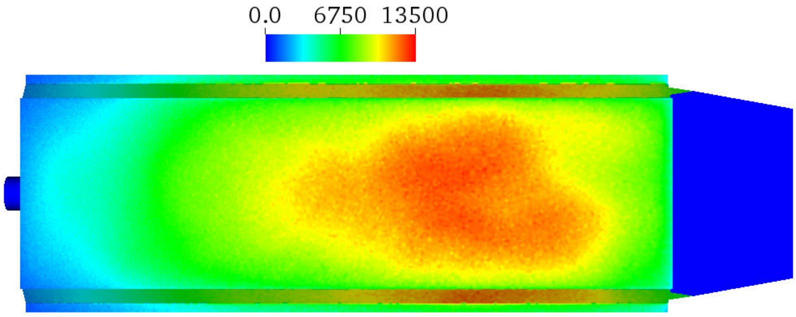

Figure 7.23: *Instantaneous radiative wall heat flux color map over the quartz walls. Flux showing is deactivated for the other walls.*

Furthermore, post-processing a non-coupled reactive flow simulation of the burner, from Mercier (2015), where the wall temperature is imposed to the experimentally measured ones, leads to a total integrated wall heat flux of $\Phi_{non\,coupled} = 2114\,W$. Summing both the conductive and the radiative integrated wall heat fluxes which were precedentely computed leads to a total wall flux:

$$\begin{aligned} \Phi_{tot} &= \Phi^{rad} + \Phi_w \\ &= 2319.6\,W \end{aligned} \tag{7.41}$$

meaning that the difference between the two is less than 10%. It appears hence that the missing wall heat flux is due to the radiation inside the the combustion chamber.

7.4.3 A first assessment of the interaction between wall temperature and gases radiation

In order to assess the radiation importance a 1D analytic case is studied, and the configuration is shown in Fig. 7.24. The value of T_w was computed analytically for two cases: a first one where $\phi^{rad} = 0.0$ and a second where the value of ϕ^{rad} is approximatively the average value of the radiative wall heat flux computed using the Rainier solver in the upper limit of the zone where experimental temperature measurements are available ($\phi^{rad} = 5000\,W \cdot m^{-2}$). With $T_c = 1400\,K$, $h_c = 18\,W \cdot K^{-1} \cdot m^{-2}$ and $h_{ext} = 9.0\,W \cdot K^{-1} \cdot m^{-2}$, two value are obtained for the wall temperature

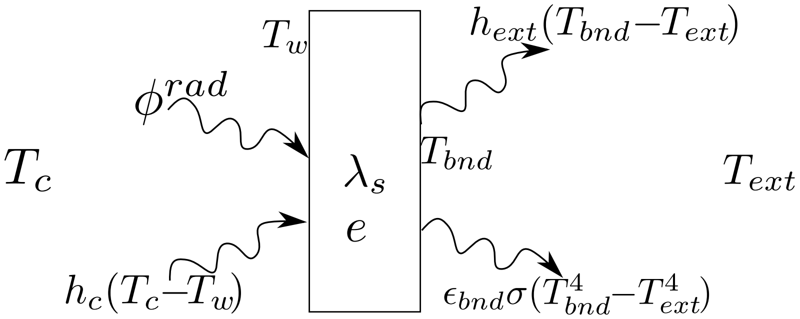
T_w
$h_{ext}(T_{bnd} - T_{ext})$
ϕ^{rad}
T_c
λ_s
e
T_{bnd}
T_{ext}
$h_c(T_c - T_w)$
$\epsilon_{bnd}\sigma(T_{bnd}^4 - T_{ext}^4)$

Figure 7.24: *1D configuration representative of the EM2C burner. The wall has a thickness e, and a thermal conductivity* λ_s. T_c *is the bulk temperature of the hot gases near inner walls,* h_c *is the heat transfer coefficient inside the chamber,* T_w *the wall temperature and* ϕ^{rad} *the radiative wall heat flux.* T_{bnd} *is wall's outer temperature,* T_{ext} *the atmosphere temperature,* h_{ext} *is the heat transfer coefficient outside the chamber and* ϵ_{bnd} *is the emissivity of the wall.*

T_w:

$$\begin{aligned} T_w(\text{No rad}) &= 744.37\,K \qquad (7.42) \\ T_w(\text{With rad}) &= 827.74\,K \qquad (7.43) \end{aligned}$$

As it can be seen, the wall temperature obtained without the radiative wall heat flux is not far from the values obtained in the upper limit of the comparison zone, while the estimated value accounting for radiation is close to the experimentally measured value. Hence, accounting for radiation in a fully coupled simulation seems to be the missing link for an accurate estimation of the wall temperature.

7.5 Conclusion

In this chapter a laboratory scale swirled confined burner was studied using the coupling methodology developed in chapters 3, 4 and 5. The combustion phenomenon was dealt using the tabulated chemistry model F-TACLES accounting for thermal heat losses. It was shown that this numerical configuration is well suited for the study of the considered combustor: The numerically computed flame showed a good agreement with the experimentally measured one in terms of flame length, shape and opening angle.

Moreover, it was also seen that the predicted wall temperature profile has a similar shape to that of the experimental measurements. Even though the retrieved values are smaller than the experiment's, the difference ($\leq 90\ K$) remains within a 10% error margin. A first estimation of the radiation heat transfer inside the studied burner showed that the undershoot in wall temperatures seems to be a result of not taking the radiation into account and that for a better estimation a fully coupled flow-wall-radiation simulation is needed.

The results obtained here show that the coupling methodology developed in this thesis is capable of correctly accounting for conjugate heat transfer in turbulent combustion configurations. It also showed that for an accurate prediction of wall temperatures it is important to have a good estimation of the outer boundary condition as well as to take into account the different phenomena responsible for heat transfer inside the combustion chamber.

Conclusion

Main achievements

During this work an **interface model** intended for the study of **unsteady conjugate heat transfer** with the help of high fidelity numerical solvers was developed. The interface model is based on a Dirichlet-Dirichlet coupling: Both the flow solver and solid heat transfer solver use the same imposed temperature boundary condition. In order to update the shared coupling boundary condition, an energy balance equation is solved over a control volume around the interface nodes. Thanks to the energy balance equation the energy conservation is ensured.

Solving an energy balance equation has another advantage: the interface temperature's temporal evolution then depends on a first order differential equation. Since the integration time step used for the numerical resolution of the differential equation is the coupling time step Δt_{cpl}, an **automatic determination algorithm of the optimal coupling time step size** is derived. The determination algorithm is based on PID controllers (Hairer et al. (2008), Gustafsson et al. (1988), Söderlind (2003)), and uses the Adamas-Bashforth explicit multi-step integration schemes (Hairer et al. (2010)). The use of PID controllers for the automatic coupling time step size determination provides an additional advantage: a better robustness. Indeed, the error control done by the PID controller ensures a stability of the coupling method since numerical instabilities lead to larger integration errors and hence to a time step size reduction by the controller, and thus a stable coupling procedure.

The issue of obtaining the **permanent regime statistics** of a conjugate heat transfer configuration is dealt with the development of an **artificial acceleration method** for the solid walls which has much larger physical time scales than the turbulent reactive flow. This acceleration technique is based on the linearity of the heat equation in solids and uses a steady/unsteady decomposition of the temperature field inside the walls.

The combined coupling method, coupling time step determination and steady state acceleration, was first validated on unsteady 1D configurations. It was afterwards implemented in the YALES2 low-Mach number flow solver and used to simulate two different configurations: first, a **flame wall interaction** experimentally studied by Singh et al. (2013) and secondly a **confined turbulent flame** studied experimentally by Guiberti (2015) and numerically by Mercier (2015) where it was shown that the wall boundary conditions have a strong influence on the flame shape. In both cases the coupling method showed satisfying results and appears as a promising methodology for future studies of conjugate heat transfer in multi-physics configurations such as those which exist in industrial combustion chambers. The obtained **quantitative comparisons** in terms of mean wall temperature for both configurations is also an important milestone since such results are still rare in the existing literature.

Future perspectives

The different points developed in this thesis open the way to further developments and analyses:

- The coupling method developed in this thesis was validated on unsteady 1D cases and 3D unsteady reactive flow configurations. Though the results are satisfying, the comparison were only made against statistically mean measurements. It is hence still needed to validate this coupling approach using unsteady measurements such as fluctuations or temporal evolutions at the wall.

- The automatic determination of the coupling time step arises a new issue: how to correctly manage the cores allocation? Since the coupling time step can change over time, it is not possible to predict precisely an optimal repartition of the available CPU-cores as it is possible with coupling methods where the coupling time step is set to a constant. The optimal cores-repartition should thus be further investigated.

- In high pressure combustion chambers, the radiative heat exchange has an important role, but even in atmospheric pressure combustion chambers the gases radiation effects can be important (see chapter 7). Due to a lack of time it was not possible to thoroughly study the interaction between the gases radiation and the other heat transfer mechanisms. Its addition to the global numerical simulation tool will allow for more accurate numerical simulations. Yet, in order to maintain a reasonable computational cost a determination method for the optimal coupling time step between the radiative heat transfer solver and the other solvers should be developed.

Appendix A

$0D$ ODE solver for the coupling time step determination

A.1 Adams-Bashforth integration schemes 174
A.2 0D test case 175

In this appendix, the variable step size integration algorithm is presented and validated on a 0D configuration, and the optimal orders of accuracy to use are chosen.

A.1 Adams-Bashforth integration schemes

For the variable step size integrator, explicit multi-step methods were chosen, which are also known as the Adams-Bashforth integration schemes. The Adams-Bashforth integration schemes are called multi-step since the integration requires information concerning the integrated function at several instants, hence steps (Hairer et al. (2008)).

These schemes are derived from approximating the function to integrate with the help of interpolation polynomials. This implies, that for the method of order k, k points need to be used. For the ordinary differential equation,

$$\frac{df}{dt}(t) = g_{rhs}(t) \tag{A.1}$$

the right hand side function is approximated as follows:

$$g_{rhs}(t) \approx \sum_{i=0}^{k-1} g_{rhs}(t_{n-i}) P_{n-i}^{k}(t) \tag{A.2}$$

Where $P_n^k(t)$ is the Lagrange interpolation polynomial defined as:

$$P_{n-j}^{k}(t) = \prod_{i=0,\ i\neq j}^{k-1} \frac{t - t_{n-i}}{t_{n-j} - t_{n-i}} \tag{A.3}$$

Integrating an approximation with k points is of order k (Hairer et al. (2008)), and leads to following integration scheme:

$$f_{[k]}^{n+1} = f^{n} + \sum_{i=0}^{k-1} g_{rhs}(t_{n-i})\alpha_i \tag{A.4}$$

where:

$$\alpha_i = \int_{t_n}^{t_{n+1}} P_{n-i}^{k}(t)dt \tag{A.5}$$

It is interesting to take note that when applying this solver to an array of differential equations, as it is done for the hybrid cell interface model where an ODE is solved for each cell, the most expensive part of the computation which is the evaluation of the integration coefficients α_i is only done once since these coefficients depend only on the integration step sizes.

A.2 0D test case

The 0D test case chosen is the one where the result is the error function $erf(t)$. The error function is the solution of the following ordinary differential equation:

$$y'(t) = A \cdot e^{-(t-t_0)^2/\sigma^2} \tag{A.6}$$

where the error function is centered around t_0 and σ is a parameter which allows to control the stiffness of the problem. For this test, three variable step solvers are used: $AB12$, $AB23$ and $AB34$ where the $ABij$ solver is using two Adams-Bashforth integration schemes, of orders i and j, in order to solve the differential equation and to estimate the numerical integration error of the method of lesser order.

The results for the three solvers are plotted in Fig. A.1 for the integration time step size and for the solution over time. For this case, the parameters used are $t_0 = 1.0$ and $\sigma = 0.125$. The numerical results show that all three solvers are capable of correctly solving the differential equation and to adapt the integration time step to the local stiffness of the equation.

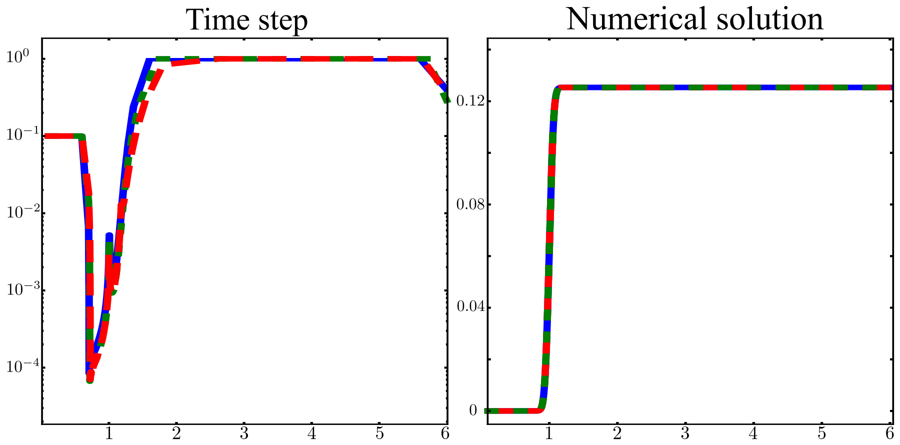

Figure A.1: *Left: Temploral evolution of the integration time step size. Right: Temporal evolution of the computed numerical solution. Blue plain line: $AB12$ solver. Green dotted line: $AB23$ solver. Red dashed line: $AB34$ solver.*

It is important to note that all three solvers have nearly-identical time steps, while normally the a method of higher order should be able to use larger time steps all the while providing the same accuracy. The reason for this behavior is that contrary to the Runge-Kutta integration schemes, the Adams-Bashforth integration schemes' stability region is getting smaller

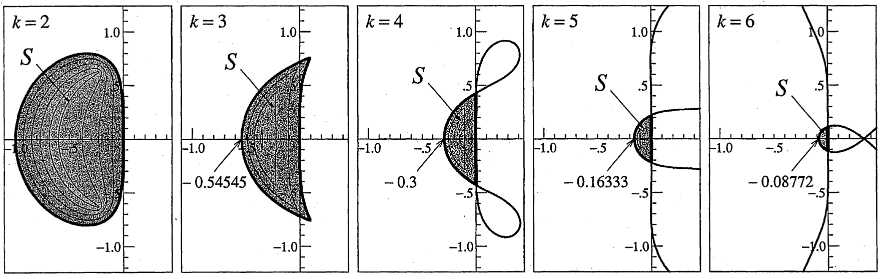

Figure A.2: *Stability regions of the explicit Adams-Bashforth integration schemes, extracted from Hairer et al. (2008)*

when the order increases (Fig. A.2).

The higher order methods are hence obliged to decrease their integration time step in order to ensure an acceptable accuracy which enforces the stability of the integrator. The conclusion of this study is that for a variable step integrator, based on the Adams-Bashforth schemes, it is better suited to use the $AB12$ solver since it has the lowest computational cost while providing the same integration step size for a given wished accuracy.

References

Abe, H., H. Kawamura, and Y. Matsuo (2004). Surface heat-flux fluctuations in a turbulent channel flow up to re_τ= 1020 with pr= 0.025 and 0.71. *International Journal of Heat and Fluid Flow 25*(3), 404–419. *(p. xv, 13)*

Amaya, J. (2010). *Unsteady coupled convection, conduction and radiation simulations on parallel architectures for combustion applications*. Ph. D. thesis, Université de Toulouse. *(p. 13, 47, 105)*

Amaya, J., E. Collado, B. Cuenot, and T. Poinsot (2010). Coupling les, radiation and structure in gas turbine simulations. In *Proceedings of the Summer Program*. *(p. 50, 56, 105)*

Auzillon, P., B. Fiorina, R. Vicquelin, N. Darabiha, O. Gicquel, and D. Veynante (2011). Modeling chemical flame structure and combustion dynamics in les. *Proceedings of the Combustion Institute 33*(1), 1331 – 1338. *(p. 147)*

Baqué, B. (2012). *Couplage aéro-thermo-mécanique pour la prédiction de la déformation d'une plaque soumise à une flamme*. Ph. D. thesis, Ecole Nationale Supérieure des Mines de Paris. *(p. 50)*

Baque, B., M.-P. Errera, A. Roos, and F. Feyel (2013). Simulation of transient conjugate heat transfer via a temporal multiscale approach. *International Journal for Multiscale Computational Engineering 11*(4), 333–345. *(p. 50)*

Benteboula, S. (2006). *Résolution des équation de Navier-Stokes à faible nombre de Mach : Application à l'étude de l'anneau de vorticité à masse volumique variable*. Ph. D. thesis, Université de Marne-la-Vallée. *(p. 21)*

Berger, S., S. Richard, G. Staffelbach, F. Duchaine, and L. Gicquel (2015). Aerothermal prediction of an aeronautical combustion chamber based on the coupling of large eddy simulation, solid conduction and radiation solvers. In *ASME Turbo Expo 2015: Turbine Technical Conference and Exposition*, pp. V05AT10A007–V05AT10A007. American Society of Mechanical Engineers. *(p. 47, 49, 50)*

Biagioli, F. and F. Güthe (2007). Effect of pressure and fuel–air unmixedness on no x emissions from industrial gas turbine burners. *Combustion and Flame 151*(1), 274–288. *(p. 9)*

Birken, P., K. Quint, S. Hartmann, and A. Meister (2010). A time-adaptive fluid-structure interaction method for thermal coupling. *Computing and visualization in science 13*(7), 331–340. *(p. 49)*

Buis, S., A. Piacentini, and D. Déclat (2006). Palm: a computational framework for assembling high-performance computing applications. *Concurrency and Computation: Practice and Experience 18*(2), 231–245. *(p. 42, 126)*

Butler, T. and P. O'Rourke (1977). A numerical method for two dimensional unsteady reacting flows. *Symposium (International) on Combustion 16*(1), 1503 – 1515. *(p. 30)*

Chemin, S. (2006). *Etude des Interactions Thermiques Fluide-Structure par un Couplage de Codes de Calcul.* Thèse de doctorat, Université de Reims Champagne-Ardenne. *(p. xx, 47, 49, 50, 55, 101)*

Chorin, A. (1986). Vortex methods for the study of turbulent combustion at a low mach number. In *Dynamics of reactive systems*, Volume 1, pp. 14–21. *(p. 22)*

Coffee, T. (1986). Kinetic mechanisms for premixed, laminar, steady-state hydrogen nitrous-oxide flames. *Combustion and Flame 65*(1), 53–60. *(p. 28, 31, 116, 118, 121)*

Colin, O., F. Ducros, D. Veynante, and T. Poinsot (2000). A thickened flame model for large eddy simulations of turbulent premixed combustion. *Physics of Fluids 12*(7), 1843–1863. *(p. 30)*

Dorey, L.-H., N. Bertier, L. Tessé, and F. Dupoirieux (2011). Soot and radiation modeling in laminar ethylene flames with tabulated detailed chemistry. *Comptes Rendus Mécanique 339*(12), 756–769. *(p. 47)*

Duarte, M. (2011). *Méthodes numériques adaptatives pour la simulation de la dynamique de fronts de réaction multi-échelles en temps et en espace.* Ph. D. thesis, Ecole Centrale Paris. *(p. 56, 59, 78)*

Duchaine, F., A. Corpron, L. Pons, V. Moureau, F. Nicoud, and T. Poinsot (2009). Development and assessment of a coupled strategy for conjugate heat transfer with large eddy simulation: Application to a cooled turbine blade. *International Journal of Heat and Fluid Flow 30*(6), 1129 – 1141. *(p. xvii, 50, 52, 53, 55, 56, 102)*

Duchaine, F., S. Jauré, D. Poitou, E. Quémerais, G. Staffelbach, T. Morel, and L. Gicquel (2015). Analysis of high performance conjugate heat transfer with the openpalm coupler. *Computational Science & Discovery 8*(1), 015003. *(p. 41, 42)*

Duchaine, F., N. Maheau, V. Moureau, G. Balarac, and S. Moreau (2013, June 3-7). Large Eddy Simulation and conjugate heat transfer around a low-mach turbine blade. In *Proceedings of ASME Turbo Expo 2013*, pp. GT2013–94257. *(p. 50, 103)*

Dupoirieux, F., L. Tessé, S. Avila, and J. Taine (2006). An optimized reciprocity monte carlo method for the calculation of radiative transfer in media of various optical thicknesses. *International Journal of Heat and Mass Transfer 49*(7), 1310–1319. *(p. 163)*

ec.europa.eu/clima/policies/strategies/2030/ (2015, 10). European commission: 2030 climate & energy framework. *(p. 2)*

Egolfopoulos, F., P. Cho, and C. Law (1989). Laminar flame speeds of methane-air mixtures under reduced and elevated pressures. *Combustion and flame 76*(3), 375–391. *(p. xiii, 28)*

Errera, M.-P. and B. Baque (2013). A quasi-dynamic procedure for coupled thermal simulations. *International Journal for Numerical Methods in Fluids 72*(11), 1183–1206. *(p. 50)*

Errera, M.-P. and S. Chemin (2013). Optimal solutions of numerical interface conditions in fluid–structure thermal analysis. *Journal of Computational Physics 245*, 431 – 455. *(p. 50, 56, 101)*

Estep, D., S. Tavener, and T. Wildey (2009). A posteriori error analysis for a transient conjugate heat transfer problem. *Finite Elements in Analysis and Design 45*(4), 263 – 271. The Twentieth Annual Robert J. Melosh Competition. *(p. 78)*

Fiorina, B., R. Vicquelin, P. Auzillon, N. Darabiha, O. Gicquel, and D. Veynante (2010). A filtered tabulated chemistry model for {LES} of premixed combustion. *Combustion and Flame 157*(3), 465 – 475. *(p. 146)*

Flageul, C., S. Benhamadouche, É. Lamballais, and D. Laurence (2015). Dns of turbulent channel flow with conjugate heat transfer: Effect of thermal boundary conditions on the second moments and budgets. *International Journal of Heat and Fluid Flow 55*, 34–44. *(p. 47)*

Fleck, J. (1961). The calculation of nonlinear radiation transport by a monte carlo method: statistical physics. *Methods in Computational Physics 1*, 43–65. *(p. 40)*

Fourcher, B. and K. Mansouri (1997). An approximate analytical solution to the graetz problem with periodic inlet temperature. *International Journal of Heat and Fluid Flow 18*(2), 229 – 235. *(p. 12)*

Geiser, J. and S. Güttel (2012). Coupling methods for heat transfer and heat flow: Operator splitting and the parareal algorithm. *Journal of Mathematical Analysis and Applications 388*(2), 873 – 887. *(p. 49)*

Germano, M. (1992). Turbulence: the filtering approach. *Journal of Fluid Mechanics 238*, 325–336. *(p. 24)*

Giles, M. B. (1997). Stability analysis of numerical interface conditions in fluid-structure thermal analysis. *Iternational Journal for Numerical Methods in Fluids 25*(4), 421–436. *(p. 48, 55, 66, 68)*

Goody, R., R. West, L. Chen, and D. Crisp (1989). The correlated-k method for radiation calculations in nonhomogeneous atmospheres. *Journal of Quantitative Spectroscopy and Radiative Transfer 42*(6), 539–550. *(p. 162)*

Guiberti, T. (2015, February). *Analysis of the topology of premixed swirl-stabilized confined flames*. Theses, Ecole Centrale Paris. *(p. xxiii, 141, 144, 145, 170)*

Guiberti, T. F., D. Durox, L. Zimmer, and T. Schuller (2015). Analysis of topology transitions of swirl flames interacting with the combustor side wall. *Combustion and Flame 162*(11), 4342–4357. *(p. 15, 141)*

Gustafsson, K. (1991). Control theoretic techniques for stepsize selection in explicit runge-kutta methods. *ACM Transactions on Mathematical Software (TOMS) 17*(4), 533–554. *(p. xiii, 80, 82, 83, 86)*

Gustafsson, K., M. Lundh, and G. Söderlind (1988). A pi stepsize control for the numerical solution of ordinary differential equations. *BIT 28*(2), 270–287. *(p. 80, 83, 88, 169)*

Hairer, E., S. Norsett, and G. Wanner (2008). *Solving Ordinary Differential Equations I*. Springer series in computational mathematics. *(p. xxv, 46, 77, 78, 82, 84, 169, 174, 176)*

Hairer, E., S. Norsett, and G. Wanner (2010). *Solving Ordinary Differential Equations II*. Springer series in computational mathematics. *(p. 77, 78, 81, 169)*

He, L. (2013). Fourier spectral modelling for multi-scale aero-thermal analysis. *International Journal of Computational Fluid Dynamics 27*(2), 118–129. *(p. 50, 102)*

He, L. and M. Oldfield (2011). Unsteady conjugate heat transfer modelling. *ASME Journal of Turbomachinery 133*(3), 031022. *(p. 47, 49, 102, 108)*

Howell, J. R. and M. Perlmutter (1964). Monte carlo solution of thermal transfer through radiant media between gray walls. *Journal of Heat Transfer 86*(1), 116–122. *(p. 40)*

IEA (2010). *World Energy Outlook*. OECD. *(p. 4)*

Jauré, S. (2012). *Methodology for conjugate heat transfer simulations relying on Large Eddy Simulations in massively parallel environ-*

ments. Ph. D. thesis, Institut National Polytechnique de Toulouse - INPT. *(p. 13, 53, 56, 103)*

Jaure, S., F. Duchaine, G. Staffelbach, and L. Y. M. Gicquel (2013). Massively parallel conjugate heat transfer methods relying on large eddy simulation applied to an aeronautical combustor. *Computational Science and Discovery 6*(1), 015008. *(p. 56, 103, 105)*

Kasagi, N., Y. Tomita, and A. Kuroda (1992). Direct numerical simulation of passive scalar field in a turbulent channel flow. *Journal of heat transfer 114*(3), 598–606. *(p. xvi, 25, 27)*

Kawamura, H., H. Abe, and Y. Matsuo (1999). Dns of turbulent heat transfer in channel flow with respect to reynolds and prandtl number effects. *International Journal of Heat and Fluid Flow 20*(3), 196 – 207. *(p. 13)*

Kawamura, H., K. Ohsaka, H. Abe, and K. Yamamoto (1998). Dns of turbulent heat transfer in channel flow with low to medium-high prandtl number fluid. *International Journal of Heat and Fluid Flow 19*(5), 482 – 491. *(p. 13)*

Kazemi-Kamyab, V., A. van Zuijlen, and H. Bijl (2013). A high order time-accurate loosely-coupled solution algorithm for unsteady conjugate heat transfer problems. *Computer Methods in Applied Mechanics and Engineering 264*, 205 – 217. *(p. 50)*

Kim, J. and P. Moin (1989). Transport of passive scalars in a turbulent channel flow. In *Turbulent Shear Flows 6*, pp. 85–96. Springer. *(p. 25)*

Kimmerlin, G. (2010). Gaz naturel. *Techniques de l'ingénieur*. *(p. 5)*

Kraushaar, M. (2011). *Application of the compressible and low-Mach number approaches to large-eddy simulation of turbulent flows in aero-engines*. Theses, Institut National Polytechnique de Toulouse - INPT. *(p. 22)*

Kuenne, G., A. Ketelheun, and J. Janicka (2011). Les modeling of premixed combustion using a thickened flame approach coupled with fgm tabulated chemistry. *Combustion and Flame 158*(9), 1750 – 1767. *(p. 31)*

Légier, J.-P., T. Poinsot, and D. Veynante (2000). Dynamically thickened flame les model for premixed and non-premixed turbulent combustion. In *Proc. of the summer program*, pp. 157–168. Citeseer. *(p. 31)*

Lindstedt, P. (1998). Modeling of the chemical complexities of flames. In *Symposium (International) on Combustion*, Volume 27, pp. 269–285. Elsevier. *(p. 146)*

Lindstrom, J. and J. Nordstrom (2010). A stable and high-order accurate conjugate heat transfer problem. *Journal of Computational Physics 229*(14), 5440–5456. *(p. 49)*

MacAdams, V. (1961). Heat transfer [russian translation]. *Metallurgizdat, Moscow*. *(p. 150)*

Majda, A. and J. Sethian (1985). The derivation and numerical solution of the equations for zero mach number combustion. *Combustion science and technology 42*(3-4), 185–205. *(p. 21)*

Malandain, M. (2012). *Simulation massivement parallèle des écoulements turbulents à faible nombre de Mach*. Ph. D. thesis, Institut National des Sciences Appliquées de Rouen. *(p. 20, 22, 118)*

Malandain, M., N. Maheu, and V. Moureau (2013). Optimization of the deflated conjugate gradient algorithm for the solving of elliptic equations on massively parallel machines. *Journal of Computational Physics 238*, 32 – 47. *(p. 37, 125)*

Marchuk, G. (1968). Some applications of splitting-up methods to the solution of mathematical physics problems. *Applications of Mathematics 13*(2), 103–132. *(p. 56)*

Mensch, A. and K. A. Thole (2015). Conjugate heat transfer analysis of the effects of impingement channel height for a turbine blade endwall. *International Journal of Heat and Mass Transfer 82*, 66 – 77. *(p. 13)*

Mercier, R. (2015). *Turbulent flame modeling for Large Eddy Simulations of industrial combustion chambers*. Theses, Ecole Centrale Paris. *(p. 15, 141, 146, 157, 167, 170)*

Mercier, R., P. Auzillon, V. Moureau, N. Darabiha, O. Gicquel, D. Veynante, and B. Fiorina (2014). LES Modeling of the Impact of Heat Losses and Differential Diffusion on Turbulent Stratified Flame Propagation: Application to the TU Darmstadt Stratified Flame. *Flow Turbulence and Combustion 93*(2), 349–381. *(p. 147, 148)*

Moeck, J. P., J.-F. Bourgouin, D. Durox, T. Schuller, and S. Candel (2012). Nonlinear interaction between a precessing vortex core and acoustic oscillations in a turbulent swirling flame. *Combustion and Flame 159*(8), 2650–2668. *(p. xxii, 143)*

Moser, R. D., J. Kim, and N. N. Mansour (1999). Direct numerical simulation of turbulent channel flow up to re= 590. *Phys. Fluids 11*(4), 943–945. *(p. xv, xvi, 25, 26)*

Moureau, V., P. Domingo, and L. Vervisch (2011). Design of a massively parallel cfd code for complex geometries. *Comptes Rendus Mecanique 339*(2-3), 141–148. *(p. 20, 118)*

Nicoud, F. and F. Ducros (1999). Subgrid-scale stress modelling based on the square of the velocity gradient tensor. *Flow, turbulence and*

Combustion 62(3), 183–200. *(p. 24)*

Nicoud, F., H. B. Toda, O. Cabrit, S. Bose, and J. Lee (2011). Using singular values to build a subgrid-scale model for large eddy simulations. *Physics of Fluids (1994-present) 23*(8), 085106. *(p. 24, 153)*

Noh-Pat, F., J. Xamán, G. Álvarez, M. Gijón-Rivera, I. Hernández-Pérez, J. Arce, and E. Villanueva-Vega (2015). Unsteady-rans simulation of conjugate heat transfer in a cavity with a vertical semi-transparent wall. *Computers & Fluids 117*, 183 – 195. *(p. 13)*

Nordstrom, J. and J. Berg (2013). Conjugate heat transfer for the unsteady compressible navier-stokes equations using a multi-block coupling. *Computers & Fluids 72*, 20–29. *(p. 47)*

Oran, E. and J. Boris (2001). *Numerical Simulation of Reacting Flows* (Second ed.). Cambridge University Press. *(p. 56)*

Pozzi, A. and M. Lupo (1988). The coupling of conduction with laminar natural convection along a flat plate. *International Journal of Heat and Mass Transfer 31*(9), 1807 – 1814. *(p. 12)*

Pozzi, A. and M. Lupo (1989a). The coupling of conduction with forced convection in a plane duct. *International Journal of Heat and Mass Transfer 32*(7), 1215 – 1221. *(p. 12)*

Pozzi, A. and M. Lupo (1989b). The coupling of conduction with forced convection over a flat plate. *International Journal of Heat and Mass Transfer 32*(7), 1207 – 1214. *(p. 12)*

Radenac, E. (2006). *Développement et validation d'une méthode numérique pour le couplage fluide/structure en aérothermique instationnaire.* Ph. D. thesis, Ecole Nationale Supérieure de l'Aéronautique et de l'Espace. *(p. 47, 49, 53, 61, 64)*

Radenac, E., J. Gressier, and P. Millan (2014). Methodology of numerical coupling for transient conjugate heat transfer. *Computers & Fluids 100*, 95 – 107. *(p. 50, 56)*

Refahi, S. (2013). *Development of a radiative transfer code and its coupling with a LES code.* Theses, Ecole Centrale Paris. *(p. 40)*

Refloch, A., B. Courbet, A. Murrone, P. Villedieu, C. Laurent, P. Gilbank, J. Troyes, L. Tesse, G. Chaineray, J. Dargaud, E. Quemerais, and F. Vuillot. (2011). Cedre software. *Aerospace Lab Journal.* *(p. 42)*

Roache, P. (2002). Code verification by the method of manufactured solutions. *Journal of fluids engineering 124.* *(p. 34)*

Roe, B., R. Jaiman, A. Haselbacher, and P. H. Geubelle (2008). Combined interface boundary condition method for coupled thermal simulations. *International Journal for Numerical Methods in Flu-*

ids 57(3), 329–354. *(p. 50)*

Salari, K. and P. Knupp (2000). Code verification by the method of manufactured solutions. Technical report, Sandia National Laboratories, Albuquerque (U.S.A). *(p. 34, 71)*

Santos, R. G. D., M. Lecanu, S. Ducruix, O. Gicquel, E. Iacona, and D. Veynante (2008, 2). Coupled large eddy simulations of turbulent combustion and radiative heat transfer. *Combustion and Flame 152*(3), 387–400. *(p. 47)*

Schwer, D., P. Lu, W. Green, and V. Semiao (2003). A consistent-splitting approach to computing stiff steady-state reacting flows with adaptive chemistry. *Combustion Theory and Modelling 7*(2), 383–399. *(p. 56)*

Singh, A., M. Mann, T. Kissel, J. Brübach, and A. Dreizler (2013). Simultaneous measurements of temperature and co concentration in stagnation stabilized flames. *Flow Turbulence and Combustion 90*(4), 723–739. *(p. xxi, xxii, 15, 116, 117, 118, 121, 124, 130, 170)*

Smagorinsky, J. (1963). General circulation experiments with the primitive equations: I. the basic experiment*. *Monthly weather review 91*(3), 99–164. *(p. 24)*

Söderlind, G. (2002). Automatic control and adaptive time-stepping. *Numerical Algorithms 31*(1-4), 281–310. *(p. 82, 83)*

Söderlind, G. (2003). Digital filters in adaptive time-stepping. *ACM Trans. Math. Softw. 29*(1), 1–26. *(p. xiii, 83, 86, 88, 169)*

Soufiani, A. and J. Taine (1997). High temperature gas radiative property parameters of statistical narrow-band model for h 2 o, co 2 and co, and correlated-k model for h 2 o and co 2. *International journal of heat and mass transfer 40*(4), 987–991. *(p. 162)*

Statistics, I. (2014, July). Co2 emissions from fuel combustion-highlights. *IEA, Paris*. *(p. xv, 3, 4)*

Taine, J. and A. Soufiani (1999). Gas ir radiative properties: from spectroscopic data to approximate models. *Advances in heat transfer 33*, 295–414. *(p. 162)*

Tessé, L., F. Dupoirieux, and J. Taine (2004). Monte carlo modeling of radiative transfer in a turbulent sooty flame. *International journal of heat and mass transfer 47*(3), 555–572. *(p. 47)*

Tessé, L., F. Dupoirieux, B. Zamuner, and J. Taine (2002). Radiative transfer in real gases using reciprocal and forward monte carlo methods and a correlated-k approach. *International Journal of Heat and Mass Transfer 45*(13), 2797–2814. *(p. 163)*

Tiselj, I., R. Bergant, B. Mavko, I. Bajsić, and G. Hetsroni (2001, 03).

Dns of turbulent heat transfer in channel flow with heat conduction in the solid wall. *Journal of Heat Transfer 123*(5), 849–857. *(p. 13, 47, 68, 70)*

Tiselj, I. and L. Cizelj (2012). Dns of turbulent channel flow with conjugate heat transfer at prandtl number 0.01. *Nuclear Engineering and Design 253*, 153 – 160. *(p. 47, 70)*

Tiselj, I., J. Oder, and L. Cizelj (2013). Double-sided cooling of heated slab: Conjugate heat transfer dns. *International Journal of Heat and Mass Transfer 66*(0), 781 – 790. *(p. xviii, 47, 68, 69, 70)*

Total (2015, 10). lacq-pilot-project. *(p. xv, 6, 7)*

Ulber, D. (2015). A guide to: Methane reforming. *Chemical Engineering 122*(1), 40. *(p. 5, 7)*

Vicquelin, R. V. (2010, June). *Tabulated chemistry for turbulent combustion modeling and simulation.* Theses, Ecole Centrale Paris. *(p. 146)*

Wu, Y., D. Haworth, M. Modest, and B. Cuenot (2005). Direct numerical simulation of turbulence/radiation interaction in premixed combustion systems. *Proceedings of the Combustion Institute 30*(1), 639–646. *(p. 47)*

www.coria cfd.fr (2015). coria-cfd. *(p. 20)*

www.topac.com. topac-instruments. *(p. xv, 10)*

Zel'Dovich, Y. (1946). The oxidation of nitrogen in combustion explosions. *Acta Physicochimica U.S.S.R* (21), 577–628. *(p. 9)*

Zhang, Y. (2013, September). *Coupled convective heat transfer and radiative energy transfer in turbulent boundary layers.* Theses, Ecole Centrale Paris. *(p. xvii, 40, 41, 163)*

Zhang, Y., O. Gicquel, and J. Taine (2012). Optimized emission-based reciprocity monte carlo method to speed up computation in complex systems. *International Journal of Heat and Mass Transfer 55*(25), 8172–8177. *(p. 165)*

Zhang, Y., R. Vicquelin, O. Gicquel, and J. Taine (2013). Physical study of radiation effects on the boundary layer structure in a turbulent channel flow. *International Journal of Heat and Mass Transfer 61*, 654 – 666. *(p. 47)*

université
PARIS-SACLAY

ÉCOLE DOCTORALE
Sciences mécaniques et
énergétiques, matériaux
et géosciences (SMEMAG)

Titre: Modélisation des transferts de chaleur couplés pour la simulation multi-physique des chambres de combustion.

Mots-clés: Transferts de chaleur couplés, Interaction flamme-paroi, Combustion, Couplage, Contrôle du pas de temps.

Résumé: Dans un souci d'optimisation des fours industriels et de réduction des émissions de gaz à effet de serre, l'oxy-combustion est considérée comme l'une des solutions d'avenir. Les conditions existantes dans les chambres d'oxy-combustion créent une interaction forte entre les différents phénomènes : Combustion, turbulence et transferts de chaleur. Pour mieux dimensionner les configurations futures il est nécessaire de pouvoir étudier la physique qui y règne, et ce pour un coût et un temps de retour raisonnables. De tels études nécessitent l'emploi d'outils de simulation de haute-fidélité, et afin de modéliser les interactions inter-phénomènes à un coût acceptable le couplage de codes est utilisé. C'est avec cet objectif que les travaux présentés dans ce manuscrit se concentrent sur la mise au point d'une méthodologie de couplage entre codes d'écoulements réactifs et de transfert de chaleur dans les parois pour la réalisation de simulations de haute-fidélité massivement parallèles prédictives des chambres futures.

Title: Modeling conjugate heat transfer phenomena for multi-physics simulations of combustion applications.

Keywords: Conjugate Heat Transfer, Flame wall interaction, Combustion, Coupling, Time step control.

Abstract: Oxycombustion is seen as one mean to attain the wished goals in terms of efficiency optimisation and Greenhouse Effect Gases emissions reduction for industrial furnaces. The extreme operating conditions, high pressure and temperature, lead to a strong interaction between the different phenomena which take place inside the combustion chamber: Combustion, turbulence and heat transfer. To better design these futur oxy-fuel processes, a mean to study the related physics with a reasonable computational cost and return time. Such studies require the use of high-fidelity numerical resolution tools, and in order to model the multi-physics interaction in a cost efficient way, code coupling. The operating conditions being extreme : High pressure and temperature, a strong interaction exists between the different phenomena occuring inside the chamber. To better understand the physics inside oxycombustion chambers, a multiphysics high-fidelity simulation methodology is developped.